University of Pardubice

Faculty of Transport Engineering

DYNAMIC FRACTURE BEHAVIOUR OF HIGH STRENGTH STEELS

Ing. Fatih Bozkurt

Doctoral Thesis

2018

Programme of Study:

P3710 Technique and Technology in Transport and Communications

Branch of Study:

3706V005 Transport Means and Infrastructure

Supervisor: Prof. Ing. Eva Schmidová, Ph.D.

Doctoral dissertation has arisen at the supervising: Educational and Research Centre in Transport (ERCT)

Author's Declaration

I hereby declare:

This thesis was prepared individually. All the literary sources and the information I used in the thesis are listed in the bibliography.

I was familiar with the fact that rights and obligations arising from the Act No. 121/2000 Coll., the Copyright Act, apply to my thesis, especially with the fact that the University of Pardubice has the right to enter into a license agreement for use of this thesis as a school work pursuant to § 60, Section 1 of the Copyright Act, and the fact that should this thesis be used by me or should a license be granted for the use to another entity, the University of Pardubice is authorized to claim from me a reasonable contribution to cover the costs incurred during the making of the thesis, according to the circumstances up to the actual amount thereof.

I agree with the reference-only disclosure of my thesis in the University Library. This diploma thesis was realized by using of ERCT technologies.

In Pardubice on the 12.10.2018

Prohlašuji:

Tuto práci jsem vypracoval samostatně. Veškeré literární prameny a informace, které jsem v práci využia, jsou uvedeny v seznamu použité literatury.

Byl jsem seznámen s tím, že se na moji práci vztahují práva a povinnosti vyplývající ze zákona č. 121/2000 Sb., autorský zákon, zejména se skutečností, že Univerzita Pardubice má právo na uzavření licenční smlouvy o užití této práce jako školního díla podle § 60 odst. 1 autorského zákona, a s tím, že pokud dojde k užití této práce mnou nebo bude poskytnuta licence o užití jinému subjektu, je Univerzita Pardubice oprávněna ode mne požadovat přiměřený příspěvek na úhradu nákladů, které na vytvoření díla vynaložila, a to podle okolností až do jejich skutečné výše.

Souhlasím s prezenčním zpřístupněním své práce v Univerzitní knihovně.

V Pardubicích dne 12.10.2018

Acknowledgement

First and foremost, I would like to express my sincere gratitude to my supervisor Prof. Ing. Eva Schmidová, Ph.D. for her patience, enthusiasm and continuous support during my doctoral study.

In particular, I would like to thank Prof. Ing. Bohumil Culek, CSc. for his guidance, help and effort during conducting of my experiments.

My acknowledgements would not be complete without thanking Ing. Jakub Zajíc for his friendship and moral support throughout my study.

My special thanks go to my colleague Sunil Kumar who has always encouraged me to write this thesis and for his invaluable support.

My heartfelt thanks go to my father, mother and sister for the support provided me through my entire life.

I would like to thank my precious father-in-law and mother-in-law. They motivate me all the time of my study.

I owe also thanks to my friends from military service Fırat Altunhan and Murat Sencer Akyüz. I enjoyed the most pleasant moments with them in Czechia.

Special thanks to Council of Higher Education, Anadolu University and Eskişehir Technical University for financial support.

Last but not the least, I would like to express my deepest thanks and appreciations to my wife. Any word cannot express her support and help.

Abstract

In accordance with the current trend towards the lightweight railway transport means, this dissertation work is focused on the use of advanced high-strength steels. Their mechanical response is based on specific material and technology processes. Application of steels with improved strength generally means increased sensitivity to internal defects, together with increased requirements for precise determination of all material parameters. Hence the investigation through fracture mechanics aspects is an inevitable precondition for the reliable and optimized design of railway structural parts.

In this dissertation work, the experimental analyzes of fracture behavior in connection with structural evaluation were conducted. The plane strain fracture toughness (K_{IC}) of Strenx 700MC steel compared to standardly used S355 steel in rail vehicles were determined with two different nonstandardized test methods. The new methodology for evaluation of dynamic response at different loading rates near to crash conditions was used and validated in the experimental part of the work. In order to specify the dynamic fracture toughness (K_{Id}) value, uniaxial impact tensile tests and three-point dynamic fracture tests were performed and evaluated with emphasis on crack propagation mode. Vehicle crashworthiness of high strength steel is greatly influenced by the welded joints because of high energy input during welding. The microstructural changes during the experimental welding process were analyzed and hardness measurements were performed. According to identified critical changes and considering used welding parameters, the weld thermal cycle simulation was applied to Strenx 700MC specimen to evaluate the effect of heat input on fracture behaviour at static and dynamic loading conditions. Lastly, in order to find out the fracture mode depending loading conditions of tested steels, fractography analysis was performed using scanning electron microscopy (SEM).

Keywords: Fracture mechanics, plane strain fracture toughness, dynamic fracture toughness, impact tensile test, fatigue crack growth rate, high strength steel, railway, rail vehicle.

Souhrn

Disertační práce je v souladu s aktuálními trendy v konstrukci odlehčených kolejových vozidel zaměřena na použití pokročilých vysocepevných ocelí, kterých mechanická odezva je založena na specifických materiálových a technologických procesech. Aplikace těchto materiálů znamená zvýšenou citlivost k vnitřním defektům, rovněž zvýšené požadavky na přesné stanovení mechanických parametrů. Vyhodnocení na základě principů lomové mechaniky je proto nevyhnutnou podmínkou pro spolehlivý a optimalizovaný návrhu konstrukcí kolejových vozidel.

V disertační práci byly provedeny experimentální analýzy lomového chování v propojení se strukturními analýzami. Analyzována byla lomová houževnatost (K_{IC}) vysocepevné oceli Strenx 700MC ve srovnání se standardně aplikovanou ocelí S355, a to použitím dvou nestandardních metod. Použita a ověřena byla nová metoda pro hodnocení dynamické odezvy při různých rychlostech zatížení, blízkých crashovým podmínkám. Ke stanovení dynamické lomové houževnatosti (K_{Id}) byly použity jednoosé tahové rázové zkoušky a rázové zkoušky 3-bodovým ohybem se zaměřením na mód rozvoje trhlin. Lomová odolnost vysocepevných ocelí daného typu je výrazně ovlivňována svařováním. Provedeny byly analýzy strukturních změn a měření tvrdosti vlivem experimentálního svařování. S uvažováním zjištěných kritických změn při daných technologických parametrech byla provedena simulace svařovacího cyklu u oceli Strenx 700MC, která umožnila vyhodnocení vlivu tepelného cyklu při statickém a dynamickém zatěžování. Fraktografické analýzy použitím rastrovací elektronové mikroskopie (SEM) byly provedeny pro hodnocení lomových mechanizmů testovaných ocelí v závislosti na podmínkách zatěžování.

Klíčové slova: lomová mechanika, lomová houževnatost při rovinné deformaci, dynamická lomová houževnatost, rázové tahové zkoušky, rychlost růstu únavových trhlin, vysocepevné oceli, kolejová vozidla.

Table of Contents

List of Figures

List of Tables

Nomenclature

Symbols

a_0	(mm)	Length of the fatigue precrack
a_b	(mm)	Crack length due to the brittle fracture
a_f	(mm)	Length of the fatigue precrack
a_i	(mm)	Length of the average initial fatigue precrack
a_m	(mm)	Machined notch depth
a_s	(mm)	Length of the average steady crack
CVN	(J)	Charpy impact energy
D	(mm)	Diameter of unnotched section of the specimen
d	(mm)	Diameter of notched section of the specimen
d_{eff}	(mm)	Effective diameter
G	(J/m^2)	Energy release rate
G_C	(J/m^2)	Critical energy release rate
HV	(kgf/mm^2)	Vickers Pyramid Number
I	(A)	Current
K_I	(MPa√m)	Stress intensity factor, Mode I
K_{IC}	(MPa√m)	The critical stress intensity factor, plane strain fracture toughness
K_{Id}	(MPa√m)	Dynamic fracture toughness
K_{max}	(MPa√m)	Maximum stress intensity factor
K_{min}	(MPa√m)	Minimum stress intensity factor
K_t	(-)	Stress concentration factor
K_Q	(MPa√m)	Conditional fracture toughness
KV_0	(J)	Charpy impact energy from the analogue scale
L	(mm)	Specimen length
L_0	(mm)	Gauge length of the specimen
N_f	(-)	Total number of cycles till failure
P_{dmax}	(N)	Maximum force during the impact tensile test
P_f	(N)	Maximum force during the static tensile test
Q	(kJ/mm)	Heat input
R_{stress}	(-)	Stress ratio ($\sigma_{min}/ \sigma_{max}$)
R	(mm)	Radius of unnotched section of the specimen

r	(mm)	Radius of notched section of the specimen
t	(μs)	Measured physical time
t'	(μs)	Modified time
t_f	(μs)	Time to fracture
T_p	(°C)	Peak temperature
U	(V)	Voltage
V	(mm/min)	Welding speed
V_0	(m/s)	Impact velocity
V_{0s}	(m/s)	Impact velocity corresponding to the maximum potential energy
W	(mm)	Width of the single edge notch bend specimen
ΔK	(MPa√m)	Stress intensity factor range
ΔK_{th}	(MPa√m)	Fatigue crack growth threshold
$\Delta t_{8/5}$	(°C/s)	Time to cool material from 800°C to 500°C
σ_B	(MPa)	Bending stress acting on the specimen
σ_f	(MPa)	Failure stress

Abbreviations

AHSS	Advanced high strength steel
ASTM	American Society for Testing and Materials
AWS	American Welding Society
CCRB	Circumferentially cracked round bar
CCT	Continuous cooling transformation
CE	Carbon equivalent
CNRB	Circumferentially notched round bar
CT	Compact tension
CTOD	Crack tip opening displacement
FCGR	Fatigue crack growth rate
GMAW	Gas metal arc welding
HAZ	Heat affected zone
ISO	International Organization for Standardization
LEFM	Linear elastic fracture mechanics
MAG	Metal active gas
MIG	Metal inert gas

MMA	Manual metal arc
SEM	Scanning electron microscopy
SENB	Single edge notch bend
TMCP	Thermo-mechanical control processing

1. Introduction

Rail transport has been a vital issue to the humanity over the centuries, it has shaped the transportation system from past to now and it will definitely shape the future. It covers heavy rail, light rail, tram, funicular and monorail means. They provide numerous advantages, varying from economic to social and energetic to environmental, which makes rail transport the best land transportation option for passengers and freight. When we look at the railway sector for the transport of passengers and freight, there is an increasing use of this mode in almost every country due to the safety, rapidity, cost effectiveness and environmentally friendly. The growth in the field of rail transport is expected to be doubled in the next decade by considering economic growth in fast developing countries including China, India and Turkey [1].

Rail vehicles are relatively heavy in comparison to other transportation modes. There is a competition among transport industry, especially in rail vehicle manufacturers and operators. They are constantly looking for ways to increase payload and improve energy efficiency. Freight wagons and passenger carriages need to become lighter without compromising on performance, safety and service life. This is possible by examining and improving the design of rail vehicles. The most common procedure is using advanced high strength steel (AHSS) with thinner dimensions [2–9]. It improves the final product and it brings benefits along the way. Experience in using AHSS in other transport sector shows that doubling the strength of the steel can lead to weight reductions of about 30% for up-graded parts [10]. Another important advantage of AHSS is having good energy absorption properties. The crashworthiness of rail cars has been substantially improved by using AHSS [11].

The application of welding process in the production of rail transportation vehicles is essential for structural parts. Many metallurgical changes that take place in the welded area because of high heat input. The region outside the welded joint which is thermally affected by the welding process is known as the heat affected zone (HAZ) and it significantly affects the welded steels. The formation of various HAZ sub-zones depends on various factors, e.g., the metallurgical composition of base metal and weld metal, thermal and mechanical treatments before welding and welding procedures [12–14]. But the investigation of the HAZ of real welded joints is not easy because of the narrowness and heterogeneous structure which is formed in the HAZ. The HAZ can be geometrically extended by welding simulation method in order to determine the different microstructures which can be formed in real welded joints. A

considerable amount of literature has been published on weldability investigations using weld thermal cycle simulation for the identification of the microstructure types in the HAZ [15–27]. The change of microstructural and mechanical properties due to the welding process or welding simulation method can be evaluated by material characterization techniques and investigated on fracture mechanics basis. It is important to know that material behavior during its service life. Taking into consideration of the fracture mechanics, the service life of the structural part can be estimated, and precautions can be taken for safety.

This doctoral dissertation dealt with the measurement of plane strain fracture toughness (K_{IC}) of S355 steel and Strenx 700MC steel which is planned to use in rail vehicles with two different nonstandardized test methods. Additionally, the fracture toughness of experimental high strength steel was also determined as a comparative steel. The new approach was used for determination of dynamic fracture toughness (K_{Id}) at two different loading rates near to crash conditions and the result was compared with standardized test method (ISO 26843:2015(E), three-point dynamic fracture test). As the vehicle crashworthiness of high strength steel is greatly influenced by the welded joints because of high energy input during the welding process, the microstructural changes during welding process were evaluated and hardness measurements were performed in heat affected zone. According to these changes and considering welding parameters, the weld thermal cycle simulation was applied to Strenx 700MC specimen to examine the effect of heat input on fracture behaviour in static and dynamic loading conditions. Lastly, in order to find out the fracture mode of tested steels, fractography analysis was performed using scanning electron microscopy (SEM).

2. Theoretical Background of Fracture Mechanics

Contrasts of the fracture mechanics approach and the traditional approach to structural design and material selection are shown in Figure 2.1. In the latter case, the anticipated design stress is compared to the flow properties of candidate materials; a material is assumed to be adequate if its strength is greater than the expected applied stress. This approach may attempt to guard against brittle fracture by imposing a safety factor on stress, combined with minimum tensile elongation requirements on the material. The fracture mechanics approach has three important variables as shown in Figure 2.1b. The additional structural variable is flaw size and fracture toughness replaces strength as the relevant material property. Fracture mechanics quantifies the critical combinations of these three variables [28].

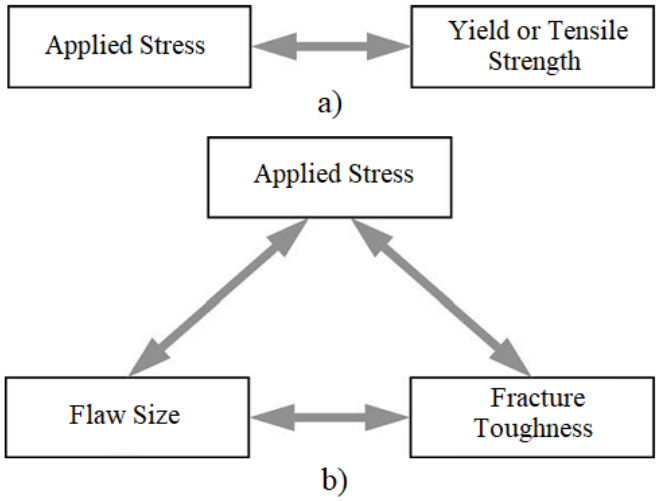

Figure 2.1 Comparison of the fracture mechanics approach and traditional strength of materials approach [28]

Figure 2.2 shows brief family tree for the field of fracture mechanics. Most of the early work was applicable only to linear elastic materials under quasistatic conditions, while subsequent advances in fracture research incorporated other types of material behavior. Elastic-plastic fracture mechanics considers plastic deformation under quasistatic conditions, while dynamic, viscoelastic and viscoplastic fracture mechanics include time as a variable. Dashed line is drawn because some early research considered dynamic linear elastic behavior.

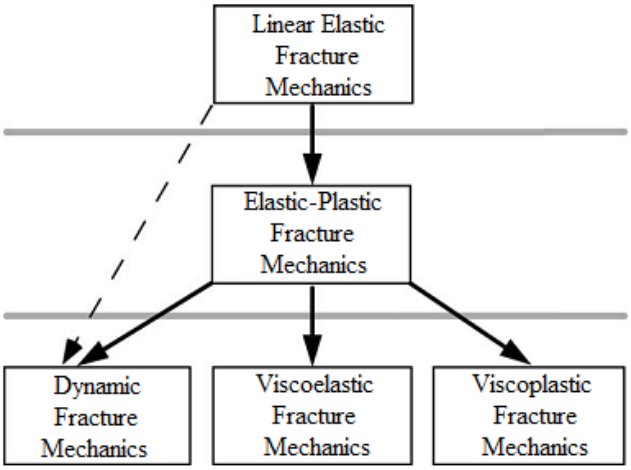

Figure 2.2 Simplified family tree of fracture mechanics [28]

Considered a cracked plate that is loaded to failure. Figure 2.3 is a schematic plot of failure stress vs. fracture toughness K_{IC}. For low toughness materials, brittle fracture is the governing failure mechanism and critical stress varies linearly with K_{IC}. At very high toughness values, linear elastic fracture mechanics is no longer valid and failure is governed by the flow properties of the material. At intermediate toughness levels, there is a transition between brittle fracture under linear elastic conditions and ductile overload.

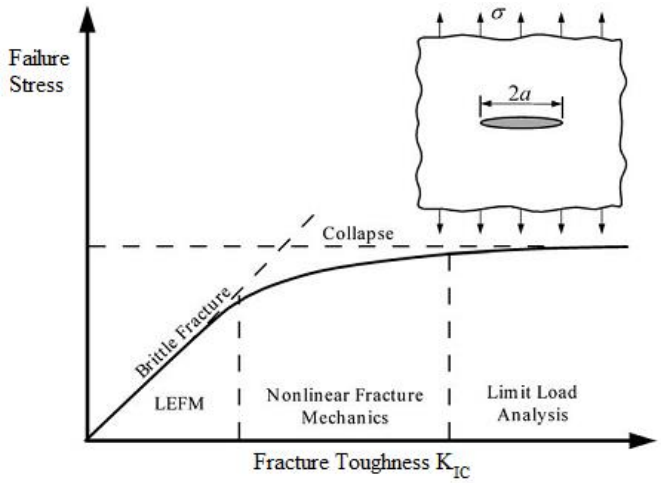

Figure 2.3 Effect of fracture toughness on the governing failure mechanism [28]

2.1. Linear Elastic Fracture Mechanics

Linear elastic fracture mechanics (LEFM) deals with the material which exhibits linear elastic behavior and also consist of crack or crack like flaw. Some theories have been developed from the past to today and two important approaches are the energy criterion and stress intensity parameters. Fundamentals of LEFM is essential to an understanding of fracture mechanics.

2.1.1. The Energy Criterion

The energy approach states that crack extension occurs when the energy available for crack growth is sufficient to overcome the resistance of the material. The material resistance may include the surface energy, plastic work or other types of energy associated with propagating crack.

Griffith was the first to propose the energy criterion for fracture, but Irwin is primarily responsible for developing the present version of this approach: the energy release rate G which is defined as the rate of change in potential energy with the crack area for a linear elastic material. At the moment of fracture $G = G_C$ the critical energy release rate, which is a measure of fracture toughness.

For a crack of length 2a in an infinite plate subject to a remote tensile stress as shown in Figure 2.4, the energy release rate is given by

$$G = \frac{\pi\sigma^2 a}{E} \tag{2.1}$$

where E is Young's modulus, σ is the remotely applied stress and a is the half crack length. At fracture $G = G_C$ and Equation 2.1 describes the critical combinations of stress and crack size for failure:

$$G_C = \frac{\pi\sigma_f^2 a}{E} \tag{2.2}$$

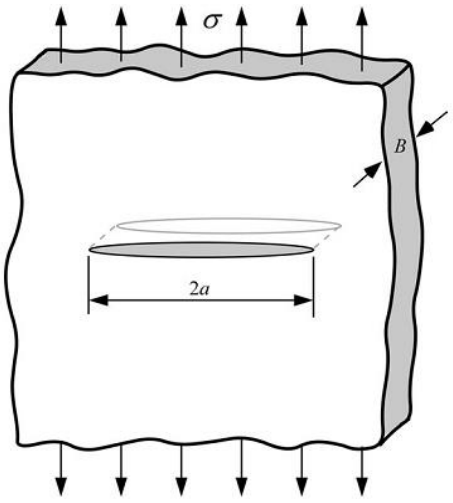

Figure 2.4 Through-thickness crack in an infinite plate subject to a remote tensile stress. In practical terms, infinite means that the width of the plate is >> 2a [28]

For a constant G_C value, failure stress σ_f varies with $1/\sqrt{a}$. The energy release rate G is the driving force for fracture, while G_C is the material's resistance to fracture. To draw analogy to the strength of materials approach of Figure 2.1a, the applied stress can be viewed as the driving force for plastic deformation, while the yield strength is a measure of the material's to deformation [28].

The tensile stress analogy is also useful illustrating the concept of similitude. Yield strength value measured with a laboratory specimen should be applicable to a large structure; yield strength does not depend on specimen size, provided the material is reasonably homogeneous. One of the fundamental assumptions of fracture mechanics is that fracture toughness (G_C in this case) is independent of the size and geometry of the cracked body; a fracture toughness measurement on a laboratory specimen should be applicable to a structure. As long as this assumption is valid, all configuration effects are taken into account by driving force G. The similitude assumption is valid as long as the material behavior is predominantly linear elastic [28].

2.1.2. Stress Concentration Factor – k_t

Nearly all structural members have discontinuities like holes, fillets, notches etc. When a structure is loaded, distribution of load varies at different regions of the structure, due to cross sectional changes in the structure. If these discontinuities are well defined geometries, it is usually possible to determine a stress concentration factor k_t for these geometries. Then, the engineer can account for the local elevation of stress using the well-known relation between the local maximum stress and applied nominal stress:

$$\sigma_{max} = k_t \sigma_{nom} \tag{2.3}$$

For most structures, the engineer usually relies on the ductility of the material to redistribute the load around a stress concentration. The effects of stress concentrations (holes, smooth fillets, etc.) in ductile materials are addressed in various codes and standards. However, if the stress concentration is severe, approaching a sharp crack in which the radius of the crack tip approaches zero, the use of fracture mechanics becomes necessary to analyze structural performance [29].

To illustrate this point, the stress concentration at the edge of an ellipse (point A) as shown in Figure 2.5. This is given as:

$$k_t = \frac{\sigma_{max}}{\sigma_{nom}} = \left(1 + 2\frac{a}{b}\right) \tag{2.4}$$

Rearranging Equation 2.4 gives σ_{max} for an ellipse

$$\sigma_{max} = \sigma_{nom}\left(1 + 2\frac{a}{b}\right) \tag{2.5}$$

For very sharp cracks

$$a >> b \therefore \sigma_{max} \; ; \; \sigma_{nom}\left(1 + 2\frac{a}{b}\right) \tag{2.6}$$

In Figure 2.5, k_t becomes very large as a/b becomes large. The radius at the end of the major axis can be approximated by $\rho = b^2 / a$. For sharp cracks,

$$a >> \rho, \sigma_{max}; \sigma_{nom} 2\sqrt{\frac{a}{\rho}} \tag{2.7}$$

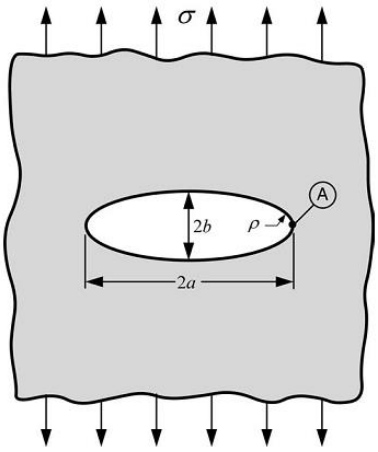

Figure 2.5 Stress concentration factor for an elliptical hole [28]

For sharp cracks, $\rho \rightarrow 0$ and $k_t \rightarrow 0$. Thus, the use of the stress concentration approach becomes meaningless. The determination of the stress concentration around a sharp crack cannot be possible using stress concentration concept and a different approach, namely stress factor is introduced [29].

2.1.3. Stress Intensity Factor – K_I

Linear elastic fracture mechanics is based on analytical procedure. This procedure relates the stress field magnitude and distribution in the vicinity of a crack tip, the nominal stress applied to a test specimen or structural member and also the size, shape and orientation of a crack or crack like discontinuity.

The fundamental principle of fracture mechanics is that the stress field ahead of a sharp crack in a test specimen or a structural member can be characterized as a single parameter, K, which is the stress intensity factor. The parameter K is related with the nominal stress (σ) in the member and the size of the crack and has units of MPa√m. Thus, all structural members or test samples that have flaws can be loaded to various levels of K.

To establish methods of stress analysis for cracks in elastic solids, it is convenient to define three types of relative movements of two crack surfaces. These displacement modes represent the local deformation ahead of a crack as shown in Figure 2.6 [29].

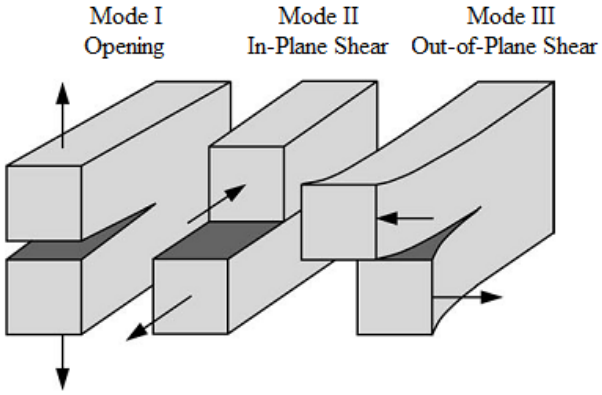

Figure 2.6 The three basic modes of crack surface displacements [28]

The stress intensity factor is usually given a subscript to denote the mode of loading, K_I, K_{II} and K_{III}. The opening mode, Mode I, is characterized by local displacements that are symmetric and the two fracture surfaces are displaced perpendicular to each other in opposite directions. In plane shear mode, Mode II, the two fracture surfaces slide over each other in a direction perpendicular to the line of the crack tip. In out of plane also called tearing mode, Mode III, the two fracture surfaces slide over each other in a direction parallel to the line of the crack front. Each of these modes of deformation corresponds to a basic type of stress field in the vicinity of crack tips. In any analysis, the deformations at the crack tip can be treated as one or a combination of these local displacement modes. Moreover, the stress field at the crack tip

can be treated as one or a combination of the three basic types of stress fields [28,29]. By using a method developed by Westergaard and Irwin found that the stress fields in the vicinity of crack tips subjected to three modes are given in Table 2.1 according to coordinate system in Figure 2.7.

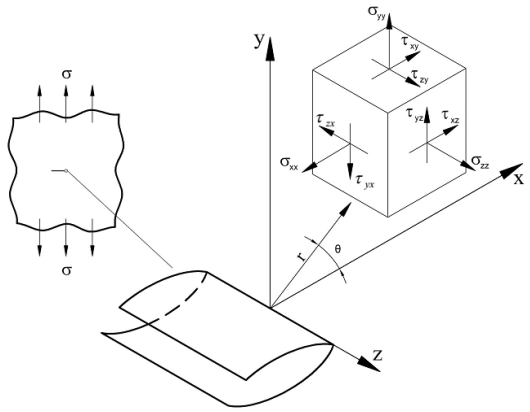

Figure 2.7 Components of stress field near a crack tip and coordinate system

Table 2.1 Stress field ahead of a crack tip for Mode I, Mode II and Mode III

Mode I	$\sigma_{xx}=\frac{K_I}{\sqrt{2\pi r}}\cos\left(\frac{\theta}{2}\right)\left[1-\sin\left(\frac{\theta}{2}\right)\sin\left(\frac{3\theta}{2}\right)\right]$ $\sigma_{yy}=\frac{K_I}{\sqrt{2\pi r}}\cos\left(\frac{\theta}{2}\right)\left[1+\sin\left(\frac{\theta}{2}\right)\sin\left(\frac{3\theta}{2}\right)\right]$ $\tau_{xy}=\frac{K_I}{\sqrt{2\pi r}}\cos\left(\frac{\theta}{2}\right)\sin\left(\frac{\theta}{2}\right)\cos\left(\frac{3\theta}{2}\right)$ $\sigma_{zz}=\upsilon\left(\sigma_{xx}+\sigma_{yy}\right),\tau_{xz}=\tau_{yz}=0$
Mode II	$\sigma_{xx}=-\frac{K_{II}}{\sqrt{2\pi r}}\sin\left(\frac{\theta}{2}\right)\left[2+\cos\left(\frac{\theta}{2}\right)\cos\left(\frac{3\theta}{2}\right)\right]$ $\sigma_{yy}=\frac{K_{II}}{\sqrt{2\pi r}}\sin\left(\frac{\theta}{2}\right)\cos\left(\frac{\theta}{2}\right)\cos\left(\frac{3\theta}{2}\right)$ $\tau_{xy}=\frac{K_{II}}{\sqrt{2\pi r}}\cos\left(\frac{\theta}{2}\right)\left[1-\sin\left(\frac{\theta}{2}\right)\sin\left(\frac{3\theta}{2}\right)\right]$ $\sigma_{zz}=\upsilon\left(\sigma_{xx}+\sigma_{yy}\right),\tau_{xz}=\tau_{yz}=0$
Mode III	$\tau_{xz}=-\frac{K_{III}}{\sqrt{2\pi r}}\sin\left(\frac{\theta}{2}\right)$ $\tau_{yz}=\frac{K_{III}}{\sqrt{2\pi r}}\cos\left(\frac{\theta}{2}\right)$ $\sigma_{xx}=\sigma_{yy}=\sigma_{zz}=\tau_{xy}=0$

Considering the Mode I singular field on the crack plane, where θ = 0. According to Table 2.1, the stresses in the x and y direction are equal:

$$\sigma_{xx} = \sigma_{yy} = \frac{K_I}{\sqrt{2\pi r}} \tag{2.8}$$

When θ = 0, the shear stress is zero, which means that the crack plane is a principal plane for pure Mode I loading. Figure 2.8 is plot of σ_{yy}, the stress normal to the crack plane vs. distance from the crack tip. Equation 2.8 is valid only near the crack tip, where the 1/r singularity dominates the stress field [28].

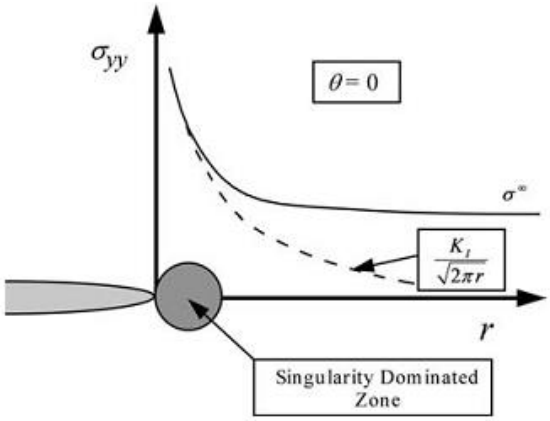

Figure 2.8 Stress normal to the crack plane in Mode I [28]

The stress intensity factor defines the amplitude of the crack tip singularity. That is, stresses near the crack tip increase in proportion to K. Moreover, the stress intensity factor completely defines the crack tip conditions; if K is known, it is possible to solve for all components of stress, strain and displacement as a function r and θ. This single parameter description of crack tip conditions turns out to be one of the most important concepts in fracture mechanics [28,29].

2.1.4. The Critical Stress Intensity Factor

A crack can be loaded up to some limiting value until total fracture in the structural member occurs. Before the fracture, the stress intensity factor reaches a critical value and it is treated as a material property called fracture toughness, K_C. For sufficiently thick materials, the plane strain fracture toughness K_{IC} measures the crack resistance. The fracture criterion by

K_{IC} states that crack propagation occurs when $K_I \geq K_{IC}$, which defines a failure criterion [28–30].

If mode I loading system is considered, then it is important to determine the applied stress intensity factor K_I and the plane strain fracture toughness K_{IC} for a specific geometry in order to assess the safety factor for the cracked body. Mode I (opening) loading system is the most studied and evaluated mode for determining the mechanical behavior of solids having specific geometries exposed to a particular environment [30].

Fracture toughness of a material is dependent on temperature, loading rate and size of the specimen. Of the three primary factors that affect the fracture toughness of a given structural material, size of the specimen is the most difficult to establish quantitatively [29].

It can be seen that in Figure 2.9 how fracture toughness is strongly dependent on the material thickness up to a limiting value. For a thin plate, plane stress condition (σ_{zz}=0) governs the fracture process because the plate is too thin to sustain through the thickness stress [30].

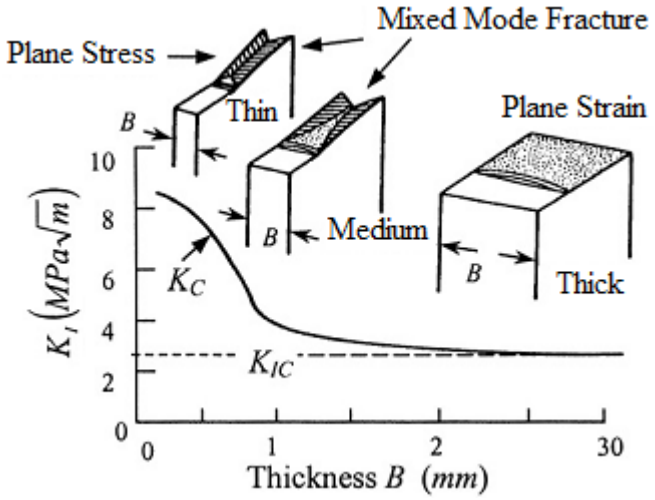

Figure 2.9 Effect of specimen on fracture toughness (K_C and K_{IC}) [30]

Plane strain fracture toughness of a structural member or a material, denoted as K_{IC}, has the lowest value and hence it is more critical. Most of the fracture mechanics designs are considered with plane strain fracture toughness.

2.1.5. Crack Tip Plasticity

On the crack plane ($\theta = 0$), the nominal stress σ_{yy} in a linear elastic material is given by Equation 2.8. As a first approximation, it can be assumed that the boundary between elastic and

plastic behaviour occurs when the stresses given by Equation 2.8 satisfy a yield criterion. For plane stress conditions, yielding occurs when $\sigma_{yy} = \sigma_{YS}$, the uniaxial yield strength of the material. Substituting yield strength into the left side of Equation 2.8 and solving for r gives a first order estimate of the plastic zone size:

$$r_y = \frac{1}{2\pi}\left(\frac{K_I}{\sigma_{YS}}\right) \tag{2.9}$$

In plane strain, yielding is suppressed by the triaxial stress state and plastic zone is smaller by a factor of 3:

$$r_y = \frac{1}{6\pi}\left(\frac{K_I}{\sigma_{YS}}\right) \tag{2.10}$$

The difference in the size and shape of the Mode I plastic zones for plane stress and plane strain is shown in Figure 2.10. The latter condition suppresses yielding, resulting in a smaller plastic zone for a given K_I value.

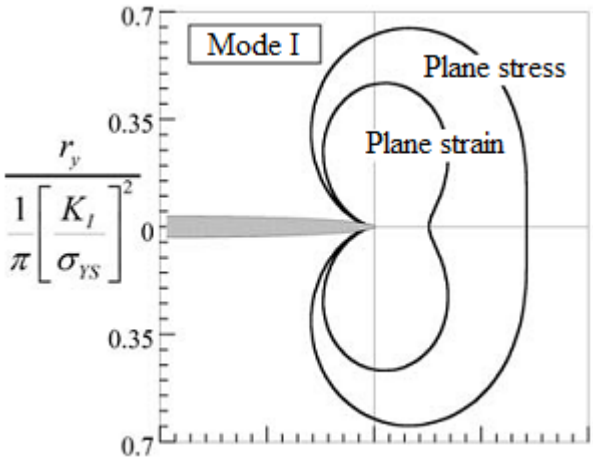

Figure 2.10 Crack tip plastic zone shapes estimation for Mode I [28]

2.2. Elastic – Plastic Fracture Mechanics

The mechanism of fracture is related with plastic deformation at the crack tip where high stresses are developed. Therefore, elastic – plastic fracture mechanics applies to materials that exhibit time – independent, nonlinear behavior. Two elastic parameters are commonly used in literature: the crack tip opening displacement and J contour integral.

2.2.1. Crack Tip Opening Displacement

When Wells tried to measure K_{IC} values for structural steels, he found that these kinds of materials were too tough to characterize with LEFM. While examining fractured test specimens, Wells noticed that the crack faces had moved apart prior to fracture and plastic deformation had blunted an initially sharp crack as shown in Figure 2.11. The degree of crack blunting increased in proportion to the toughness of the material. After this observation, Wells propose the opening at the crack tip as a measure of fracture toughness. Today, this parameter is known as crack tip opening displacement (CTOD) [28].

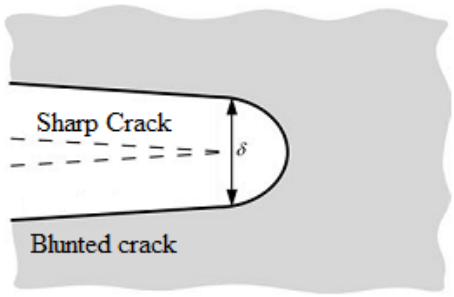

Figure 2.11 An initially sharp crack blunts with plastic deformation [28]

Wells performed an approximate analysis that related CTOD to the stress intensity factor in the limit of small scale yielding. Consider a crack with small plastic zone as shown in Figure 2.12. Irwin postulated that crack tip plasticity makes the crack behave as if it were slightly longer. CTOD can be estimated by solving for the displacement at the physical crack tip. The displacement r_y behind the effective crack tip is given by

$$u_y = \frac{\kappa+1}{2\mu} K_I \sqrt{\frac{r_y}{2\pi}} = \frac{4}{E'} K_I \sqrt{\frac{r_y}{2\pi}} \tag{2.11}$$

where E' is the effective Young's modulus, $\kappa = 3\text{-}4\nu$ (plane strain) and $\kappa = (3\text{-}\nu)/(1+\nu)$ plane stress, μ is the shear modulus. The Irwin plastic zone correction for plane stress is

$$r_y = \frac{1}{2\pi}\left(\frac{K_I}{\sigma_{YS}}\right) \tag{2.12}$$

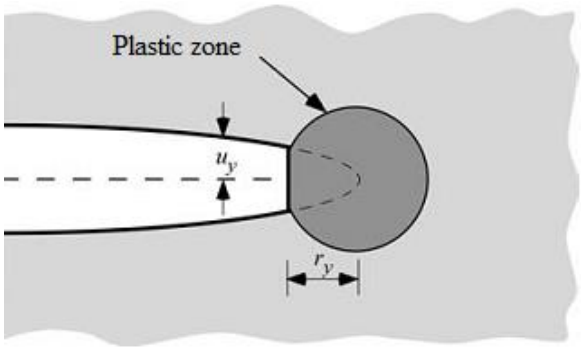

Figure 2.12 Estimation of CTOD from the displacement of the effective crack in the Irwin zone correction

Substituting Equation 2.12 into Equation 2.11 gives

$$\delta=2u_y=\frac{4}{\pi}\frac{K_I^2}{\sigma_{YS}E} \tag{2.13}$$

where δ is the CTOD.

There are several alternative definitions of CTOD. The two common definitions are illustrated in Figure 2.13 and these are the displacement at the original crack tip and the 90º intercept. The latter definition is used in generally finite element measurements. These two definitions are equivalent if the crack blunts in semicircle.

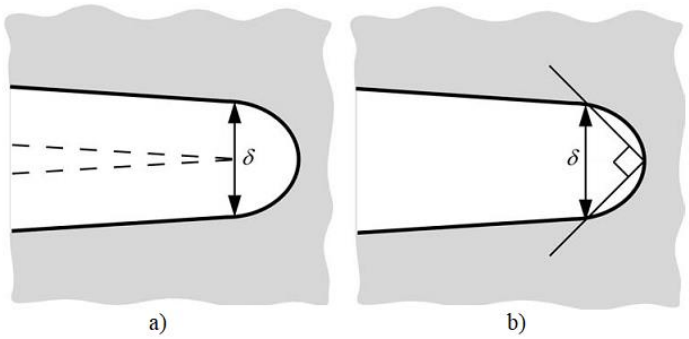

Figure 2.13 Alternative definitions of CTOD, a) displacement at the original crack tip and b) displacement at the intersection of a 90º vertex with the crack flanks [28]

The displacement V at the crack mouth is measured with three-point bending test method and CTOD is inferred by assuming the specimen halves are rigid and rotate about a hinge point as shown in Figure 2.14. Referring to this figure, CTOD is estimated from a similar triangles construction:

$$\frac{\delta}{r(W-a)}=\frac{V}{r(W-a)+a} \tag{2.14}$$

Therefore

$$\delta = \frac{r(W-a)V}{r(W-a)+a} \tag{2.15}$$

where r is the rotational factor, a dimensionless constant varies between 0 and 1.

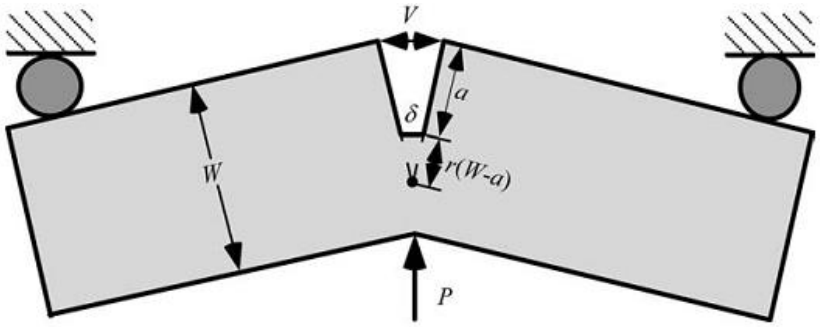

Figure 2.14 The hinge model for estimating CTOD from three-point bend specimen [28]

Standard methods for CTOD testing, adopting a modified hinge model, in which displacements are separated into elastic and plastic components. Hinge assumption is applied only to plastic displacements. Typical load (P) vs. displacement (V) curve from CTOD test is shown in Figure 2.15. The CTOD in this specimen is calculated by this formula:

$$\delta = \delta_{el} + \delta_p = \frac{K_I^2}{m\sigma_{YS}E'} + \frac{r_p(W-a)V_p}{r_p(W-a)+a} \tag{2.16}$$

Equation 2.14 consists of two parts, elastic and plastic components. In generally, elastic part can be negligible.

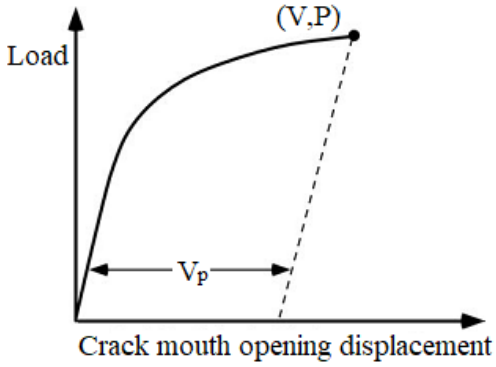

Figure 2.15 Determination of the plastic component of the crack mouth opening displacement [28]

2.2.2. J Integral

Consider an arbitrary counterclockwise path (Γ) around the tip of a crack as shown in Figure 2.16. The J integral is given by

$$J=\int_{\Gamma}\left(wdy-T_i \frac{\partial u_i}{\partial x} ds \right) \tag{2.17}$$

where

w = strain energy density

T_i = components of the traction vector

u_i = displacement vector components

ds = length increment along the contour (Γ)

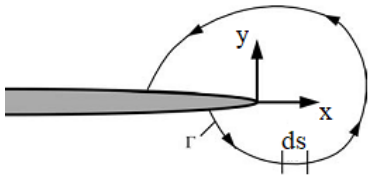

Figure 2.16 Arbitrary contour around the tip of a crack [28]

The strain energy density is defined as

$$w=\int_0^{\varepsilon_{ij}} \sigma_{ij} d\varepsilon_{ij} \tag{2.18}$$

where σ_{ij} and ε_{ij} are the stress and strain tensors, respectively. The traction is a stress vector at a given point on the contour. That is, if a free body diagram of the material inside of the contour, T_i would define the stresses acting at the boundaries. The components of the traction vector are given by

$$T_i = \sigma_{ij} n_j \tag{2.19}$$

where n_j are the components of the unit vector normal to Γ [28].

Generally, J is calculated with using three-point bend test method. For the single edge bend specimen, J is estimating as follows;

$$J = J_{el} + J_{pl} \tag{2.20}$$

where J_{el} is elastic component of J and J_{pl} is plastic component of J. At a point corresponding to force versus displacement record, J integral is calculated as;

$$J=\frac{K^2\left(1-\nu^2\right)}{E}+\frac{\eta_{pl}A_{pl}}{B_N b_o} \tag{2.21}$$

where:

A_{pl} = area under force versus displacement record as shown in Figure 2.17

η_{pl}= 1.9 if the load line displacement is used for A_{pl}, $3.667 - 2.199(a_0/W) + 0.437(a_0/W)^2$ if the crack mouth opening displacement record is used for A_{pl}

B_N = net specimen thickness

$b_o = W - a_0$.

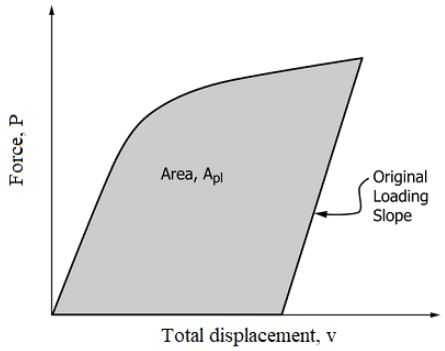

Figure 2.17 Definition of area for J calculation [28]

2.3. Standard Test Methods

All standardized fracture toughness test methods have several common features. Test specimen geometries are almost similar. The cracks in test specimens are introduced by fatigue tests. The instrumentation is required to measure load and displacement and some of the tests needs additional instrumentation to monitor crack growth.

There are many types of specimen bend, compact tension, arc, disk etc. as shown in Figure 2.18 however, in the literature the most common specimen geometries are single edge notch bending (SENB) and compact tension (CT).

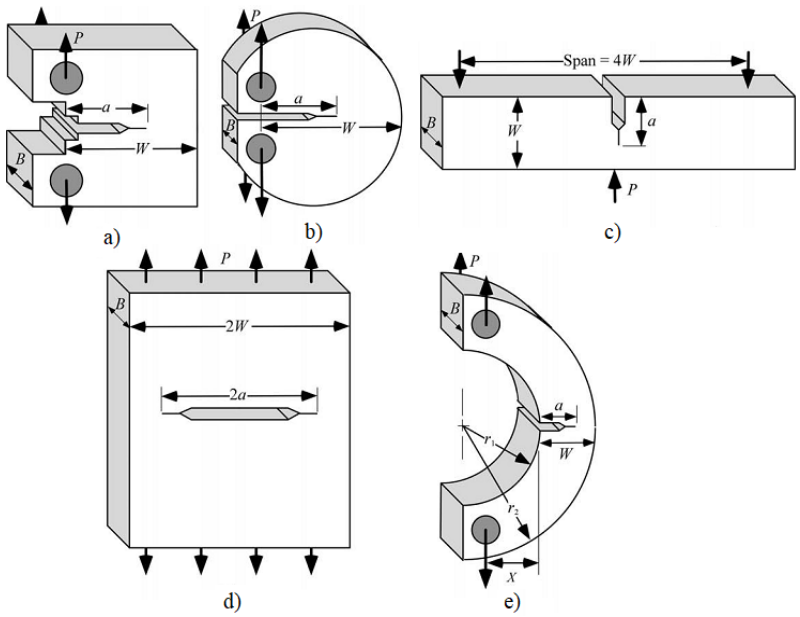

Figure 2.18 Standardized fracture mechanics test specimens: a) Compact specimen, b) disk shaped compact specimen, c) Single edge notched bend specimen d) Middle tension specimen and e) Arc shaped specimen [28]

Theory of fracture mechanics applies to cracks that are infinitely sharp prior to loading. While laboratory specimens invariably fall short of this approach, it is possible to introduce cracks which are sufficiently sharp for tests. The most efficient way to produce such a crack is through cyclic loading. Figure 2.19 illustrates the precracking procedure in a specimen, where a fatigue crack initiates at the tip of a machined notch and propagate to the desired size through control of the cyclic loads. This procedure is completed by modern servo-hydraulic test machines. To produce cyclic loading, generally sinusoidal loading is chosen. To reflect the true material properties in terms of fracture toughness measurement, the fatigue crack must satisfy these conditions:

- The crack tip radius at failure must be much larger than the initial radius of fatigue crack,

- The plastic zone produced during fatigue cracking must be small compared to the plastic zone at fracture.

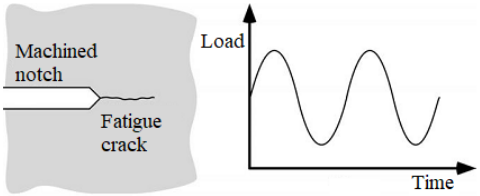

Figure 2.19 A fatigue crack is introduced at the tip of a machined notch by means of cyclic loading [28]

Load measurement during a conventional fracture toughness test is relatively straightforward, since nearly all test machines are equipped with load cells. For displacement measurement, clip gage is used as shown in Figure 2.20. The clip gage is attached to the mouth of the crack and consists of four resistance strain gages bonded to a pair of cantilever beams. Deflection of the beams result in a change in voltage across the strain gages, which varies linearly with displacement.

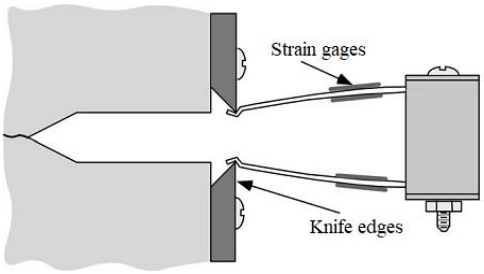

Figure 2.20 Measurement of the crack mouth opening displacement with a clip gage [28]

ASTM has proposed the test methods E1820 – 17a and E399 – 17 for determination of fracture toughness of metallic materials using fatigue pre-cracked specimens having specified dimensions subjected to increasing crack displacement force [31,32]. In order to summarize the general concept of test procedures, E399 – 17 is explained briefly for single edge bend specimen configuration.

Specimens for K_{IC} tests usually are prepared ratio between width (W) and thickness (B), $1 \leq W/B \leq 4$. The support span (S) is nominally equal to four times the specimen width and B_N is the specimen thickness between the roots of the side grooves. Most standardized tests lead to valid results as long as the technician follows all of the procedures outlined in the standard. Sometimes, K_{IC} tests, produces invalid results through no fault of the technician. If the plastic zone at fracture is too large, it is not possible to obtain a valid K_{IC}, regardless of how skilled the technician is. In order to ensure valid K_{IC} test results, the size requirements are prepared as:

$$W\text{-}a \geq 2.5\left(\frac{K_{IC}}{\sigma_{YS}}\right)^2 , \; 0.45 < \frac{a}{w} < 0.55$$

where a is crack length of the precracked specimen. Single edge bend specimen is shown in Figure 2.21.

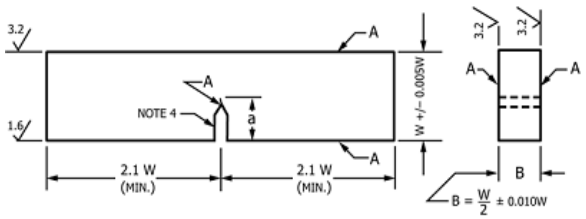

Figure 2.21 Dimensions of single edge bend specimen [32]

In order to determine required specimen dimensions, the user should make a rough estimate of the anticipated K_{IC} for the material. Such an estimate can be from data for similar materials. If these data are not available, the ASTM standard provides table of recommended thickness for various strength levels.

When a precracked test specimen is loaded to failure, load vs. displacement graph is recorded. Three types of load vs. displacement are shown in Figure 2.22. The critical load P_Q is defined depending on the type of curve. One must construct a 5% secant line (a line from the origin with a slope equal to 95% of the initial elastic loading slope) to determine P_5. P_{max} is shown for three type of curves.

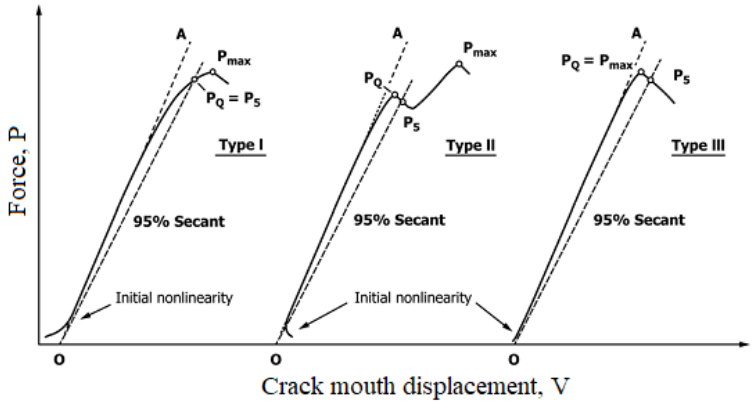

Figure 2.22 Three types of load-displacement behavior in standardized test [32]

The crack length must be measured from the fracture surface. Since there is a tendency for the crack length variation, the crack length is defined as the average of three evenly spaced measurements. After P_Q and the crack length are determined, a provisional (conditional) fracture toughness K_Q is calculated as:

$$K_Q = \frac{P_Q S}{\sqrt{BB_N}W^{3/2}} f\left(\frac{a}{W}\right) \tag{2.22}$$

where f(a/W) is a dimensionless function of a/W. This function is tabulated in ASTM E399 – 17. The K_Q value calculated from Equation 2.20 is a valid K_{IC} result only if all validity requirements in the standard met, including

$$W\text{-}a \geq 2.5\left(\frac{K_{IC}}{\sigma_{YS}}\right)^2,\ 0.45<\frac{a}{w}<0.55,\ P_{max} \leq 1.10P_Q$$

If the test meets all of the requirements which are specified in the standard, then $K_Q = K_{IC}$.

Because the size requirement of ASTM E 399 – 17 is very stringent, sometimes impossible to measure a valid K_{IC}.

Researchers are seeking to determine fracture toughness values with easy and reliable test methods. In Chapter 5 and 6, the methodologies are summarized, and important points are highlighted. This methodology is also a part of the doctoral dissertation.

3. Welding Processes and Metallurgy

Welding is defined by The American Welding Society (AWS) as "a localized coalescence of metals or nonmetals produced either by heating the materials to the required welding temperatures, with or without the application of pressure or by the application of pressure alone, and with or without the use of filler materials." Depending upon the combination of temperature and pressure, a wide range of welding processes has been developed. Welding processes can be classified as follows; gas welding, arc welding, resistance welding, solid-state welding, thermo-chemical welding and radiant welding [13]. In this chapter, metal active gas welding which is one of the arc welding methods is briefly explained.

3.1. Metal Active Gas (MAG) Welding

Until the 1970s, manual metal arc (MMA) was the dominant method of welding process. Today metal inert gas (MIG) and metal active gas (MAG) is the leading welding process in most industrial countries. Both MIG and MAG welding are described by the term gas metal arc welding (GMAW). Only inert gases or gas mixtures are used for the shielding gas when MIG welding is applied. Typical inert gases used for MIG welding are argon and helium. These gases are usually used for MIG welding of aluminum and other non-ferrous metals. Active gas mixtures are developed primarily for welding steels. Typical shielding gases are mixtures argon, carbon dioxide and oxygen. The composition of the shielding gas has a substantial effect on the stability of the arc, metal transfer and the amount of spatter. The shielding gas also affects the behaviour of the weld pool, particularly its penetration and the mechanical properties of the welded joint [12].

Although every manufacturer's welding equipment is designed differently, it is almost in a similar manner. One of the typical welding equipment is shown in Figure 3.1. This welding technique uses a solid welding wire that is fed automatically at a constant speed as an electrode. An arc is generated between the wire and the base metal and the resulting heat from the arc melts the welding wire and base metal to join the parts together as shown in Figure 3.2. This is semiautomatic arc welding process because wire is fed automatically at a constant rate and you provide gun movement. During the welding process, shielding gas protects the weld from the atmosphere and prevents oxidation of the base metal [33].

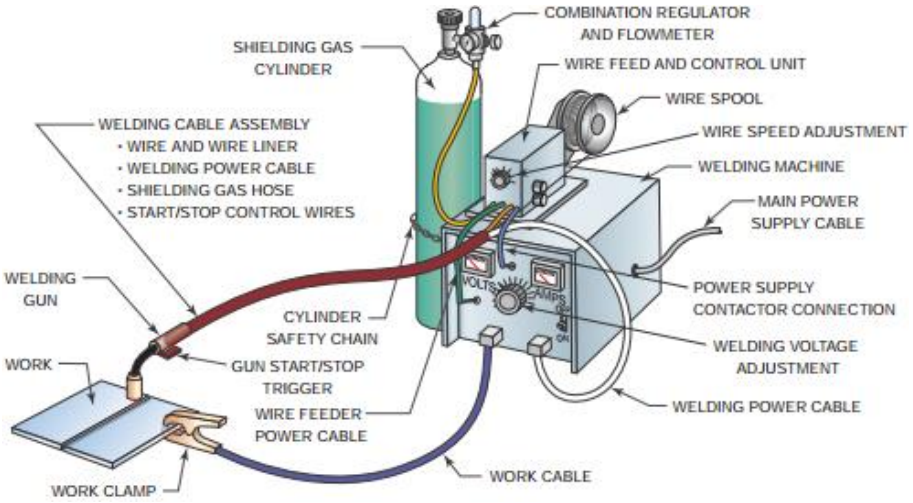

Figure 3.1 Typical welding equipment [33]

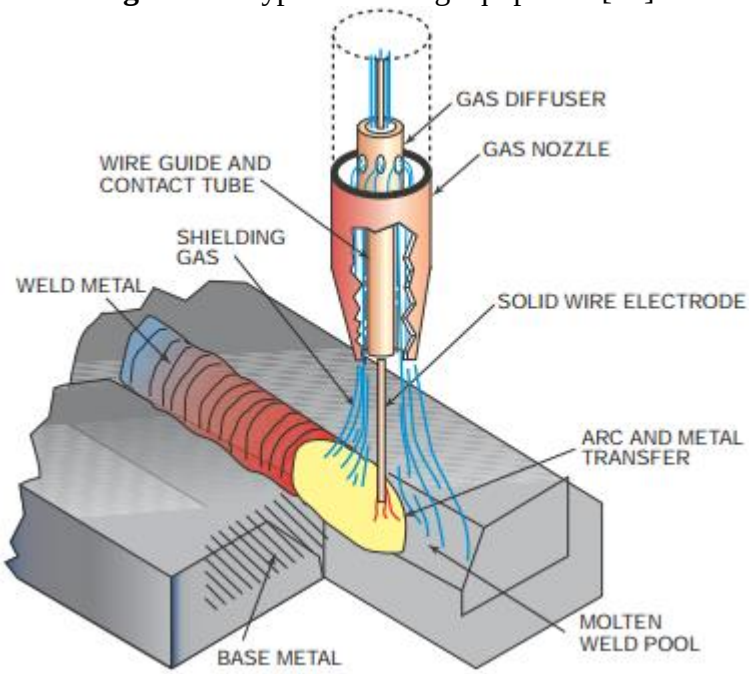

Figure 3.2 Gas metal arc welding [33]

The success of the MAG welding process is dependent on many welding parameters: voltage, wire size, wire feed speed and current, wire stick-out length, inductance, choice of shielding gas, flow rate of gas, torch and joint position. Most of these parameters must be matched to each other for optimum welding performance. The working point must be within the working range or tolerance box for the particular welding situation [12].

3.2. The Weldability of Steel and Heat Affected Zone

Weldability describes how far the materials affected by the weld retain the same strength, corrosion resistance, oxidation resistance etc. as the base material after welding.

First important parameter during welding is heat input. It has great importance for the rate of cooling of the weld. It can be calculated from the formula:

$$Q=\frac{U\times I\times 60}{V\times 1000}\times \text{Efficiency} \tag{3.1}$$

where Q is heat input (kJ/mm), U is voltage (V), I is current (A), V is welding speed (mm/min) and efficiency depends on the welding technology (for MIG/MAG is 0.8) [12].

Another important parameter is carbon equivalent (CE), a measure of the hardenability of the steel, how easily martensite is formed upon cooling of a given steel. The CE expresses the joint effect of addition of several alloying elements on the martensite transformation by weighing the presence of the alloying elements relative to that of carbon, as if the steel were to be a plain carbon steel. The CE can be calculated according to Equation (3.2) [12].

$$CE=C+\frac{Mn}{6}+\left(\frac{Cr+Mo+V}{5}\right)+\left(\frac{Ni+Cu}{15}\right) \tag{3.2}$$

A high CE value is equivalent to a steel having high hardenability and therefore low CE values are desired for steels to be considered weldable. Steel is generally considered weldable if the CE of the steel is below 0.45.

The welded joint can be divided into two main regions, the fusion zone and the heat affected zone (HAZ). During welding, the material in the fusion zone is heated up to the melting point followed by rapid cooling. The HAZ is that area of the base metal not melted during welding operation but whose microstructural properties are altered by the heat input. A change in microstructure leads to different mechanical properties in the HAZ compared to the base material. The HAZ consists several regions with different microstructural features depending on the heat input experienced during one or several weld passes. The peak temperature T_p and cooling rate $\Delta t_{8/5}$ (the time to cool material from 800°C to 500°C) are important parameters that determines the final microstructure [12].

The HAZ can consist characteristic regions for a single pass weld process and it depends on the T_p experienced during weld thermal cycle. Figure 3.3 shows the names of the various zones obtained after welding process.

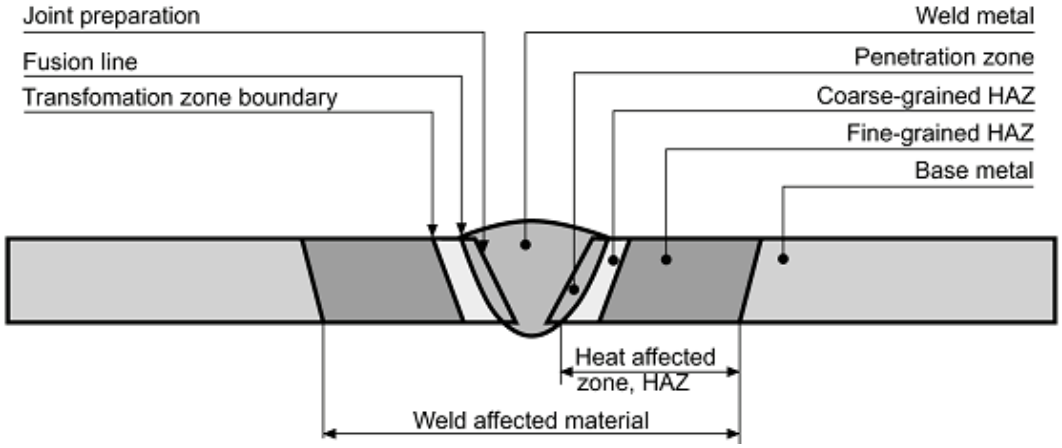

Figure 3.3 Different zones and boundaries in heat affected zone [12]

Metallurgical changes in the HAZ are inevitable. Figure 3.4 relates the T_p to the resulting zones and microstructures in welded steels after cooling to the phase diagram of steels. The closest zone to the fusion line is heated above the A_3 temperature where the microstructure transforms to austenite. This region is called as the coarse grained HAZ, where the microstructure consists of large grained austenite due to annealing during heating beyond A_3. As the distance from the fusion line increases, the grain size of the austenite decreases. This zone is called as the fine-grained zone and usually exhibit good mechanical properties compared to coarse grained HAZ. Further away from the fusion line, the microstructure is only partially transformed to austenite, as the T_p obtained in this region lies between the A_1 and A_3 temperatures. The austenite that forms in this region has a high carbon content, as the solubility of carbon in austenite increases with decreasing temperature. The parts of the HAZ that does not transform fully or partially to austenite are tempered. When the cooling rate of welding is high, the coarse grain HAZ consists of mainly martensite and bainite [34].

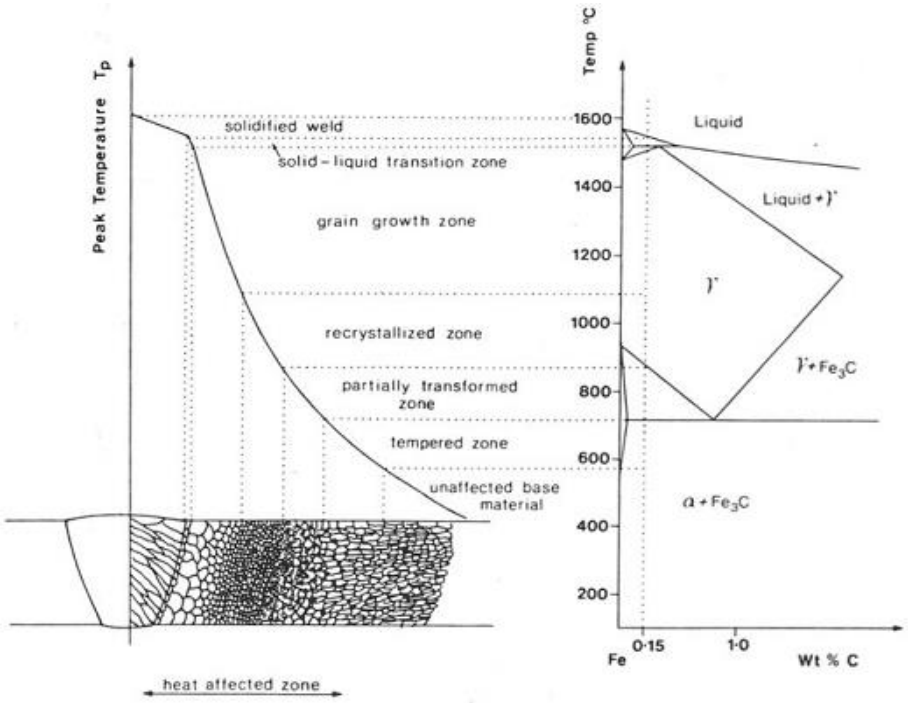

Figure 3.4 Weld zones in welded steel [34]

In the literature, several continuous cooling transformation (CCT) diagrams have been sketched schematically to explain and understand the development of the weld metal microstructure of low carbon steels. One of them is shown in Figure 3.5. The hexagon represents the transverse cross sections of columnar austenite grains in the weld metal. As austenite is cooled down from high temperature, ferrite nucleates at the grain boundary and started to grow inward and it is called grain boundary ferrite. At lower temperatures the mobility of the planar growth front of the grain boundary ferrite decreases and Widmanstatten ferrite (side plate ferrite) forms instead. At even lower temperature it is too slow for Widmanstatten ferrite to grow to the grain interior and it is faster if new ferrite nucleates ahead of the growing ferrite. The new ferrite, that is, acicular ferrite, nucleates at inclusion particles and has randomly oriented short ferrite needles with a basket weave feature. Figure 3.6 shows the microstructures of the weld metal of a low carbon low alloy steel. Possible microstructures are grain boundary ferrite (A), polygonal ferrite (B), Widmanstatten Ferrite (C) and acicular ferrite (D). It is possible to observe upper bainite and lower bainite but examination with transmission electron microscopy is usually needed to identify of them. The most desirable of all these possible microstructures is acicular ferrite because it improves the toughness of the weld metal. The factors of affecting the developed microstructures are cooling time, alloying additions, grain size and weld metal oxygen content [14].

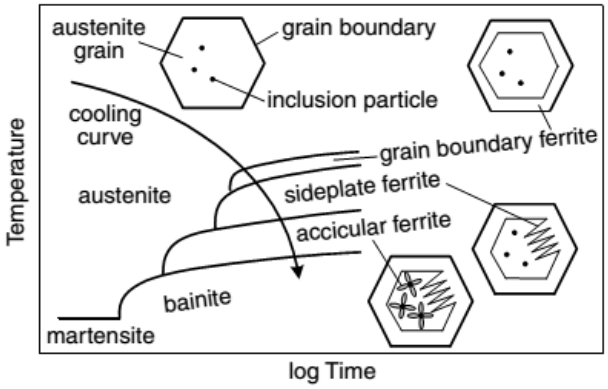

Figure 3.5 Continuous cooling transformation diagram for weld metal of low carbon steel [14]

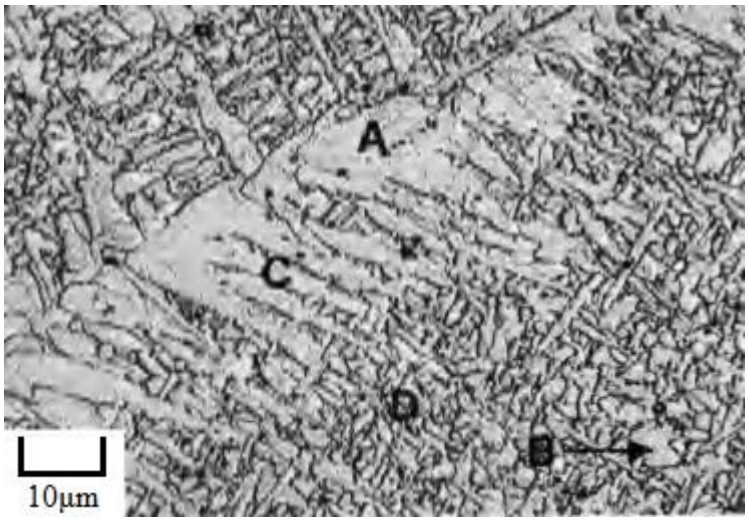

Figure 3.6 Typical weld metal microstructures in low carbon steels [14]

3.3. Weld Defects

During welding process, discontinuities like flaws or cracks are introduced and they act as a stress raiser. These small imperfections cause some mechanical properties variation of the welded metal. When the discontinuity is large enough to affect the function of the joint it is termed a defect. Typical weld defects are undercut, cracks, porosity, slag inclusions, lack of fusion and lack of penetration as shown in Figure 3.7 [13]. They are divided into three categories: crack like discontinuities (lack of fusion and lack of penetration), volumetric discontinuities (porosity and slag inclusions) and geometric discontinuities (undercut) [30].

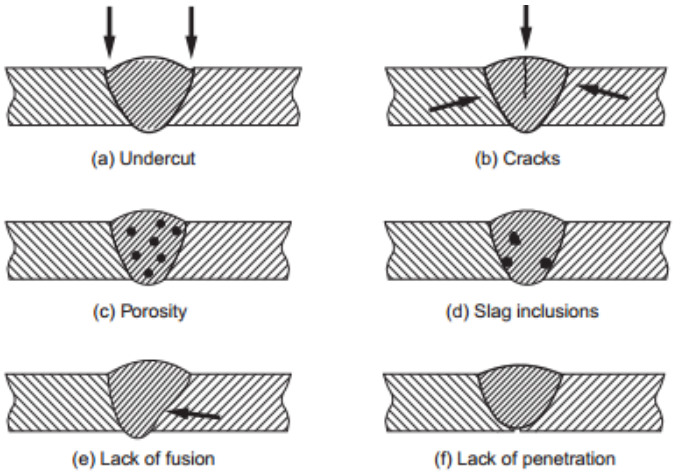

Figure 3.7 Typical weld defects [13]

In general, these weld discontinuities may be caused by improper design that restricts accessibility for welding, incorrect selection of a welding process or welding parameters, improper care of electrode or flux or both and other causes including welder performance. The severity of a discontinuity is governed by its size, shape and orientation and by the magnitude and direction of the design and fabrication stresses. Generally, the severity of discontinuities increases as the size increases and the geometry becomes more planar and the orientation more perpendicular to the direction of tensile stresses. Thus, volumetric discontinuities are usually less injurious than crack like discontinuities. Also, crack like discontinuities whose orientation is parallel to the tensile stress would be innocuous. Furthermore, for a given size and shape, a surface discontinuity whose plane is perpendicular to the tensile stresses is more severe than embedded [29].

In summary, geometric discontinuities are caused by the weld operator or the weld procedure. They act as stress raisers that intensity the local stresses in their immediate vicinity. Their effect on the fracture behaviour of a component is directly related to their severity as stress raisers.

3.4. Weld Simulation and Simulators

Extensive research has shown that the thermal cycles experienced in a workpiece during welding can be replicated in specimens more convenient for mechanical testing, using so called weld thermal cycle simulators or more generally thermal simulators. It has been used for weldability investigations and for the identification of the microstructures types which are

developed in the HAZ. There are two main reasons for using weld thermal cycle simulation method [20,21]:

1) The identification of the microstructures types in the HAZ is complex because it consists many fine regions having different structures.
2) The HAZ of welded joint is very narrow in width.

Weld thermal cycle simulation is appropriate method to prepare specimens to identify and examine the various HAZ sub-zones. With using this methodology, the HAZ can be geometrically extended and the mechanical properties of each sub-zones which are developed in the HAZ can be evaluated. In Figure 3.8 the thermal cycle simulator TCS 1405 Smitweld is presented. The power sources are made on electro resistant and electro induction principles that facilitate enough and controlled heat input during heating. Sometimes it is needed for gas shielding during simulation. After connecting all sensors rapid heating and cooling follows in controlled conditions (determined start temperature, heating and cooling rate, peak temperature, cooling time between 800°C and 500°C). The thermal cycle simulation process is monitored by a computer and all data are recorded for further processing and application. With this procedure, controlled heat input in base material is applied and it possible to expect same effect during real welding in workshop in case of controlled welding parameters (heat input achieved by means of welding current, voltage and weld travel speed). Weld thermal simulation can be performed as single or multi cycle [26].

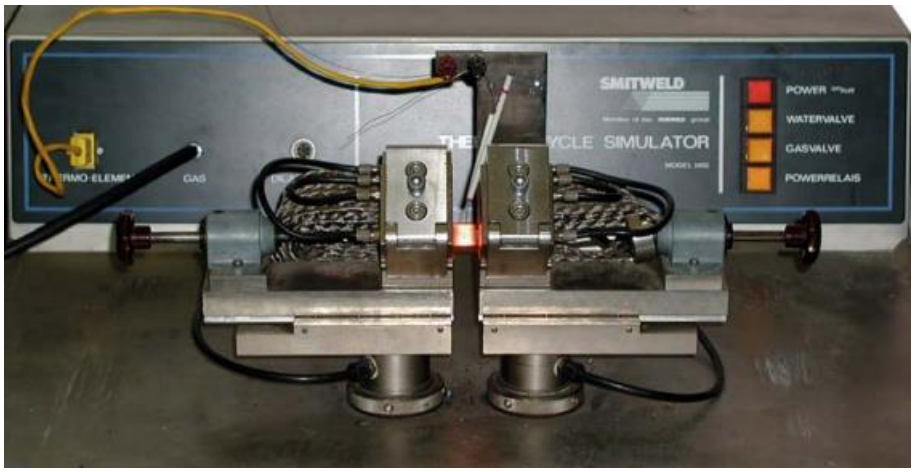

Figure 3.8 Thermal cycle simulator type Smitweld TCS 1405 [19]

The weld thermal cycle simulation technique has some disadvantages like other procedures. For instance, the grain size of simulated sample is slightly larger than that of real

welded joint when applying same thermal profile. The reason of this case is the thermal pinning is not considered in the thermal simulation process. Nevertheless the result of weld thermal cycle simulator may not fully reflect the true welded joint, the thermal simulation technique becomes a key tool in the field of current weld physical metallurgy and steel rolling [21].

4. Objectives of the Doctoral Dissertation

The dissertation aims to contribute the knowledge of advanced high strength steel (AHSS) application for lightweight constructions. It is necessary to understand two main weak points of prospective application:

i. The influence of the welding process: Because of the primary strengthening process (based on thermomechanical treatment), the chosen steel is sensitive to heat input in sense of the drop of primary strength.
ii. The sensitivity to imperfection: In direct connection with welding, the safety requirements are based on reliable non-destructive diagnostic. Fracture mechanics approach is necessary for the determination of the sensitivity of stable crack propagation.

The following set of experimental techniques and analyses were carried out in accordance with the objectives of the dissertation:

1. Three kinds of materials were selected for experimental study:
   - S355 steel is a referential steel which is commonly used for structural part of railway transport means,
   - Strenx 700MC attributes to the prospective high strength steel for lightweight structures,
   - Experimental high strength steel (with increased static and dynamic strength in comparison to Strenx 700MC) was used for extending the experimental scope and validation of used methodology for fracture toughness.

   Standard tensile tests were performed using all mentioned steels, results were used for the design of parameters for the next study of sensitivity to internal defects under different structural and loading conditions. Metallography evaluation was focused on S355 steel and Strenx 700MC steel.
2. Using nonstandardized test methodologies, the static and the dynamic fracture toughness of Strenx 700MC steel, and referential S355 steel were compared.
3. In order to assess the effect of loading rate on dynamic fracture toughness, S355 steel and Strenx 700MC steel were tested at two different impact speeds.
4. In order to evaluate the welding process on the crack sensitivity of Strenx 700MC steel, set of experiments and material analyses were applied:

- Experimental welding of Strenx 700MC defined the structural and mechanical degradation,
- The weld simulation of HAZ enabled testing of homogeneous critical sublayer,
- Static and dynamic tests were conducted by the same (CCRB) method.

5. Dynamic fracture toughness of high strength experimental steel was compared by ISO 26843:2015(E) and CCRB test methodologies.

5. Used Methods of the Fracture Toughness Evaluation

5.1. Static Fracture Toughness Determination with Nonstandardized Test Methods

As mentioned in Chapter 2, the determination of the fracture toughness of the materials with using standardized test methods is quite tedious and time-consuming because of the specimen preparation and test procedures. A large and growing body of literature has investigated the nonstandardized test method using round notched and precracked tensile specimens [35–47]. Wilson and Landes summarized the problems in fracture toughness test methods which are prepared by ASTM [47]:

- The user can estimate the material response in advance or at least having an educated guess is necessary.
- The standard specimens have planar geometries and stress triaxiality is ignored. Plane stress condition exists on the lateral surfaces of the thin planar specimens and the stress triaxiality is nearly uniform through the thickness. For thick planar specimens, plane stress condition exists on the lateral surfaces of the specimen and transitions toward plane strain condition in the middle of the specimen. If the specimen is thick enough, a state of plane strain will exist in the middle. Since therefore, the stress triaxiality will always vary from plane stress to plane strain in planar specimens.
- There are many inconsistencies between the practices described in proposed tests.
- The tests are complicated and expensive than standard tension testing. These complications may even discourage some industries from performing qualitative fracture toughness testing.

In addition to these problems, the standard test procedures have these following disadvantages [35,39]:

- Require specific geometric configuration of test specimens
- To obtain valid fracture toughness value (K_{IC}) requires large specimens
- Special fixtures are necessary for mounting these specimens
- Fatigue precracking must be done with utmost care
- If the fatigue precracking is not appropriate, the fracture toughness test is invalid.

The researchers have tried to find out the methods for determination of fracture toughness in rapid and at the same time reliable way. In the literature, there are two different approaches, using round bar specimens to determine the fracture toughness of metallic materials.

The first approach uses a notched round bar that is allowed to rotate under bending fatigue load in R. R. Moore four-point fatigue testing machine, then precracked specimen is loaded in tensile universal testing machine and pulled till failure. Next step, crack lengths are measured with suitable optical measuring devices and fracture toughness is calculated using proposed equations which depend on fracture load, crack lengths and dimensions of the specimens. This methodology is called as circumferentially cracked round bars (CCRB).

The second approach uses a notched round bar that is directly loaded in universal tensile testing machine and pulled till failure. During the tensile test, fracture load is recorded. Depending upon the fracture load and dimensions of the specimen, fracture toughness is determined according to proposed equations. This methodology is named as circumferentially notched round bars (CNRB).

According to summarized experimental works, the researchers concluded that these two kinds of nonstandardized test methods (CCRB and CNRB) are reliable, rapid and easy in comparison with standardized test methods. The advantages of using these two nonstandardized test methods can be summarized as follows:

- The geometry of the specimen is simple
- The specimens are easy to prepare, machining requires an ordinary lathe
- The plane strain condition which is the most important point can be obtained because the circumferential crack has no end in the plane stress region compared with the standard specimen geometries
- Less time-consuming in specimen preparation and precracking for CCRB method
- It is not necessary any special fixtures for mounting specimens and any costly instrumentation
- Fatigue testing machine and universal tensile testing machine are sufficient to conduct tests.

In Experimental Procedure Chapter, every detail of CCRB and CNRB methodologies are explained.

5.2. Determination of Dynamic Fracture Toughness

Actually, to this day, use of the term “dynamic fracture toughness” is quite confusing. ASTM does not clearly define this mechanical parameter. In the literature, the term K_{Id} appears and it might mean K_{IC} or values that are converted from data developed from notched bar impact tests. A nearly true K_{Id} value probably comes from impacting the precracked Charpy specimen [48].

The significance of the conventional (static) K_{IC} properties also applies to the case of rapid loading. The plane strain fracture toughness of certain materials (bcc, for example) is sensitive to loading rate. Generally, these kinds of materials also show a pronounced dependence of K_{IC} on test temperature. It is possible to measure dynamic toughness with using a quasi-static fracture test, which basically involves applying a fast loading rate to conduct an ordinary K_{IC} test. Procedures for this rapid load K_{IC} test are given in special Annex A10 to ASTM E399 – 17 for plane strain fracture testing. For conventional tests, the loading rate of the specimen is limited between 0.55 and 2.75 MPa√m/s. Any loading rate faster than that is considered rapid load fracture toughness. There is a general perception that three fracture parameters, static K_{IC}, K_{Id} and V – notch impact energy, are connected in some way so that correlation among any two parameters is feasible [48].

Several empirical attempts have tried to correlate the Charpy impact energy (CVN) with K_{IC} and K_{Id} to allow a quantitative assessment of critical flaw size and permissible stress levels. Most of these proposed correlations are dimensionally incompatible, ignore differences between the two measures of toughness and are valid only for limited types of materials and ranges of data. Furthermore, these correlations can be widely scattered. However, some correlations can provide a useful guide to estimating fracture toughness. Some of the more common correlations are listed in Table 5.1 (1 ksi = 6.8948 MPa, 1 ksi√in = 1.099 MPa√m, 1 ft.lbf = 1.356 J) [49].

Table 5.1 Typical Charpy, K_{IC} and K_{Id} correlations for steels [49]

Correlation Name	Proposed Equation	Units
Barson	$\frac{K_{Id}^2}{E}=5(CVN)$	K_{IC}, K_{Id} = Psi$\sqrt{in}$ E=Psi CVN = ft.lbf
Barsom – Rolfe	$\frac{K_{IC}^2}{E}=2(CVN)^{3/2}$	
Sailors – Corten	$\frac{K_{IC}^2}{E}=8(CVN)$	
	$\frac{K_{Id}^2}{E}=15.873(CVN)^{3/8}$	K_{Id} = ksi$\sqrt{in}$ CVN = ft.lbf

ISO 26843:2015(E) specifies requirements for performing and evaluating instrumented precracked Charpy impact tests on metallic materials using fracture mechanics approach. The Charpy specimen which has V type notch at the middle point is subjected to cyclic loading. With using instrumented Charpy pendulum impact tester, precracked specimen is loaded in three-point impact bending. During the impact test, force – time or force – displacement curve is recorded. The obtained curve is evaluated and the dynamic fracture toughness value K_{Id} is calculated with proposed equations [50]. The details of the calculation method are explained in the Experimental Procedure Chapter.

6. Current Results of The Related Research

In this chapter, important and related with this dissertation of published studies which are focused on determination of fracture toughness with using non-standardized test methods and dynamic behavior of high strength steels are reviewed.

Bayram et al. investigated three types of material whose fracture toughness tests were previously performed by using circumferentially notched round bars, namely 1) a dual-phase steel with three different morphologies, 2) an Al-Zn-Mg-Cu wrought alloy and 3) Al-si cast alloys with three different Si contents, in terms of accuracy and reliability of the testing method. With using stress concentration factors, which were associated with the bluntness of the notch, correction factors for the fracture toughness calculations were derived. They have concluded that the corrected fracture toughness values were found to be close to the uncorrected ones. Furthermore, they also have emphasized that circumferentially notched cylindrical specimens can be readily used for rapid determination of fracture toughness of metallic materials because the specimen preparing and the test procedures are straightforward [35].

Bayram et al. studied 0.1 %C steel which has three different microstructures (using three different heat treatment procedures) and aimed to correlate these microstructures with mechanical properties especially focusing on fracture toughness values of the respective materials. Fracture toughness testing was performed on circumferentially notched round bar method. Two notch diameter 6 mm and 8 mm and three notch angles of 45°, 60° and 75° were employed so that the effect of these parameters on fracture toughness values could be observed. The results indicated that the notch strength and fracture toughness of specimens with a 2 mm notch depth were found to be higher than those with a 1 mm notch depth because of the higher plastic constraint present in the thinner cross-section. The notch strength and fracture toughness of all the materials were found to increase in the notch angle for both notch depths. Finally, it was concluded that obtaining a fine fibrous microstructure resulted to optimized mechanical properties in tested steel [36].

Nath and Das examined the effect of microstructure and notches on the fracture toughness of medium carbon steel with using circumferentially notched round bar method. Two notch diameters (5.6 mm and 4.2 mm) and three notch angles namely 45°, 60° and 75° were used and the microstructure of the tested steel was also varied by heat treatment and its effect

on the fracture toughness was observed. It was found that samples with lower notch diameter showed higher (K_{IC}) for same notch angle as compared to higher notch diameter. This could be explained on the basis of plastic constraint present at notch root. Plane stress condition prevailed rather than plane strain condition. It is observed that plane strain fracture toughness (K_{IC}) decreased, as notch angle decreased. Lastly, the microstructure of the steel had a strong influence on the value of K_{IC}. A fine-grained structure was found to have higher value of K_{IC} than a coarse-grained structure, because of it gave better resistance to crack propagation due to higher grain boundary area per unit volume [37].

Neelakantha et al. tested EN8 (low carbon unalloyed steel) and EN31 (high carbon alloy steel) steels for determination of fracture toughness with using circumferentially cracked round bar method. The method was based on samples which were machined in round bar shape with "V" type notch at the center was subjected to bending load using R. R. Moore rotating bending fatigue testing machine in order to initiate and propagate the crack inside the specimens. After completion of fatigue precracking, tensile test was performed on fatigue precracked specimens. With measuring the crack dimensions and diameters, fracture toughness values were calculated according to proposed equations which depended on maximum load during tensile test. It was concluded that the experimentally obtained fracture toughness values were within the comparable range of K_{IC} values of low and medium carbon steels. And they also determined the stress intensity factor range ΔK through fatigue tests [38].

Neelakantha et al. explained the use of circumferentially cracked round bar specimens of high strength Al2014T651 alloy for determination of K_{IC} and fatigue crack growth rate. The methodology was same as previously mentioned [38]. The pre-cracked round bar specimen was loaded in tensile in a universal testing machine and pulled till failure. Using suitable stress intensity factor equations, the fracture toughness could be calculated. The experimentally obtained fracture toughness values were very close to K_{IC} values reported in the literature which were obtained using standard compact tension and single edge notched bend specimen configurations. It was concluded that the methodology of determination of fracture toughness and fatigue crack growth rate using circumferentially cracked round bar specimens was relatively simple, reliable, fast and economical. Lastly, the applied methodology was recommended as a standard test method for fracture toughness as well as crack growth tests by researchers [39].

Manesh et al. investigated St37 (S235) and St52 (S355) steel plates which were tested in uniaxial tension at room temperature over various strain rates ranging from 0.001 s^{-1} to 0.1 s^{-1}. The static and earthquakes-type dynamic loadings were conducted using a servo-hydraulic testing machine. It was found that St52 steels showed higher yield values and flow stress under static and dynamic loading conditions as compared to St37 as shown in Figure 6.1. An increase in the loading rate from 0.001 s^{-1} to 0.1 s^{-1} led to 30% increase in the lower yield strength of St37 steel and an increase of 6% for St52. The ductile dimple fracture was observed in static and dynamic conditions; however, increasing the strain rate resulted in a pronounced cleavage type fracture in both steel [51].

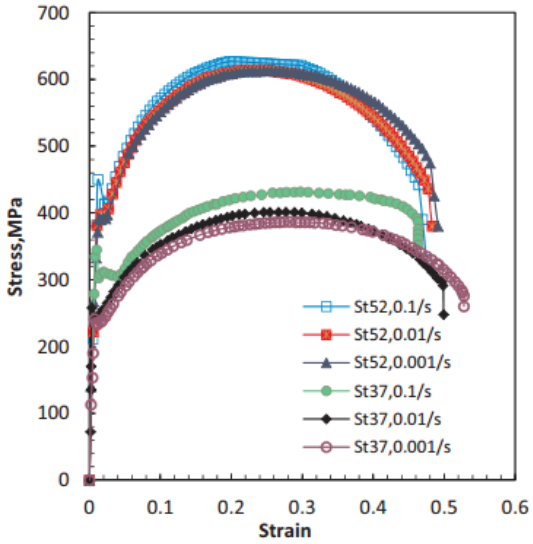

Figure 6.1 The engineering stress – strain curves of St37 and St52 at different strain rates [51]

Boyce and Dilmore examined the strain rate sensitivity of four high strength steels at strain rates varying from 0.002 s^{-1} to 200 s^{-1}: AerMet 100, modified 4340, modified HP9-4-2- and Eglin AFB alloy. New developed dynamic servo-hydraulic method was employed to perform tensile tests over the entire range from quasi-static to near split-Hopkinson strain rates. They highlighted that tested alloys only exhibited a 10% increase in yield strength when strain rates were increased from quasistatic to 200 s^{-1} as shown in Figure 6.2 and their work hardening rate was essentially unaffected by strain rate. The Aermet 100 and HP9-4-20M alloys still retain more ductility at 200 s^{-1} than other two alloys and material selection would still favor these alloys in spite of their strain-rate dependent loss in ductility. The fracture surfaces were inspected by scanning electron microscopy (SEM) and in all cases, the cylindrical tensile bars resulted in a cup and cone fracture morphology [52].

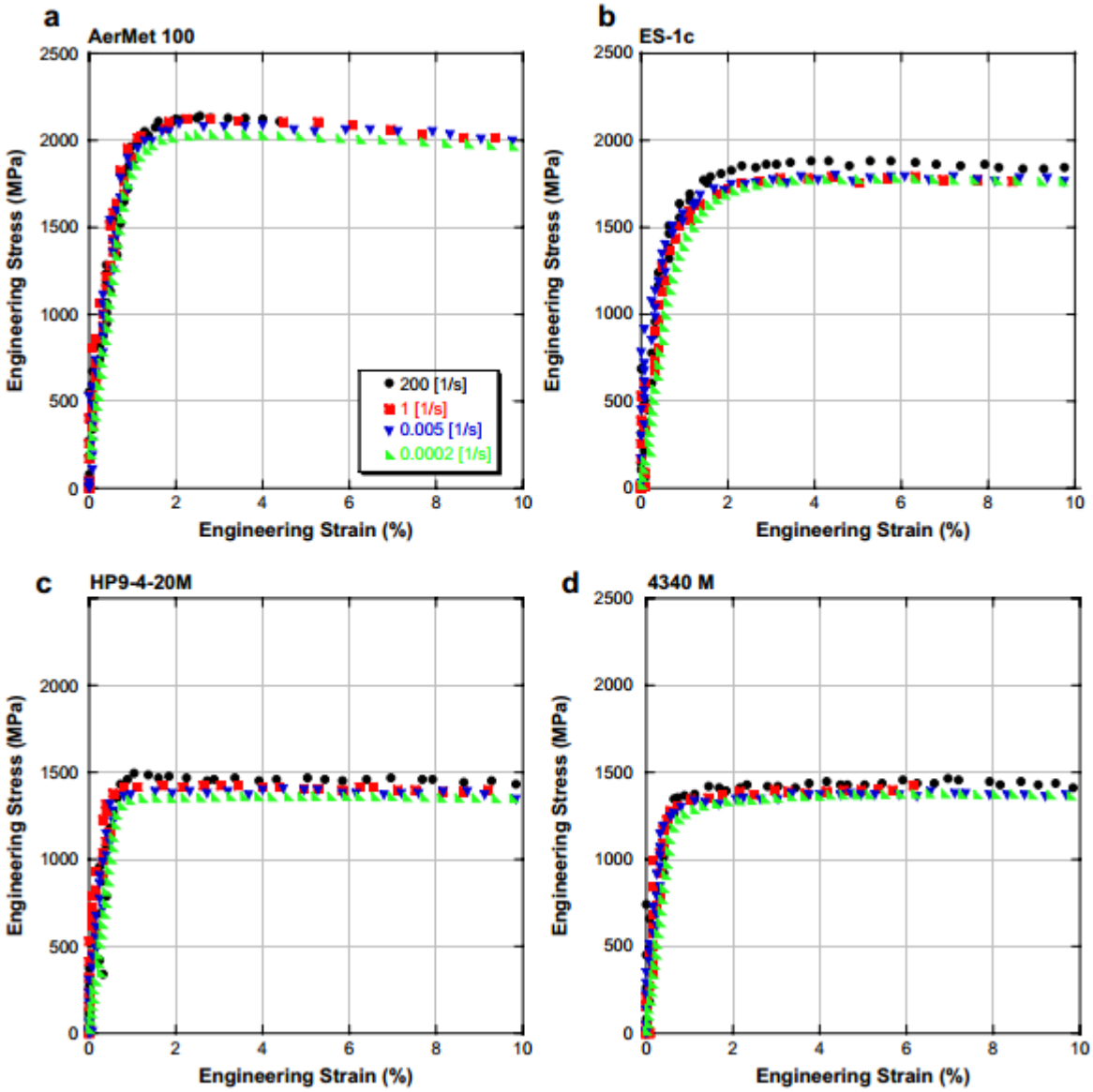

Figure 6.2 Engineering stress-strain curves for the four high strength alloys under evaluation at strain rates ranging from 0.0002 s^{-1} to 200 s^{-1} [52]

Tsuchida et al. studied the effect of grain size which varied between 0.47 μm and 13.6 μm on tensile deformation behavior of ferrite – cementite (FC) low carbon steel. They performed tensile test with strain rates of 10^3, 10^0 and 3.3 x 10^{-4} s^{-1} at room temperature. They concluded that the effect of ferrite grain size on flow stress was almost independent of strain rate and the strain rate sensitivity depends on ferrite grain size little as shown in Figure 6.3. The yield-drop and the Lüders elongation were observed at the early stage of the deformation. Their experimental evidence implied that the grain refinement strengthening mainly contributed to an increase in the athermal stress [53].

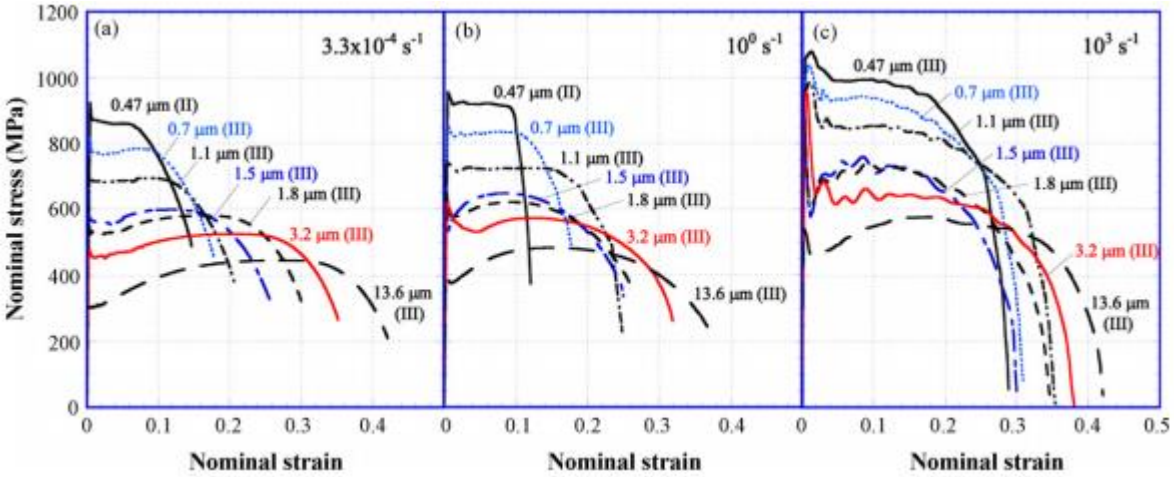

Figure 6.3 Nominal stress – nominal strain curves of the FC specimens obtained by tensile tests with strain rates of 3.3 x 10^{-4} s^{-1} a), 10^{0} s^{-1} b) and 10^{3} s^{-1} [53]

Singh et al. were reported that results of uni-axial tensile testing of multi-phase 800 High Yield strength steel (MP800HY) at different strain rates (0.001-750 s^{-1}). The quasi-static tests (0.001 s^{-1}) were performed on electromechanical universal testing machine whereas hydro-pneumatic machine and modified Hopkinson bar apparatus were used for testing at intermediate (5 s^{-1} and 25 s^{-1}) and high strain rates (250 s^{-1}, 500 s^{-1} and 750 s^{-1}) respectively. The experimental data were compared to the engineering stress versus engineering strain curves and the true stress versus true strain curves as shown in Figure 6.4. The results showed that the strain hardening of MP800HY was found to increase with increasing strain rate. MP800HY was moderately sensitive to strain rate. However, it was a poor strain rate sensitive material in the strain rate range from 0.001 s^{-1} to 750 s^{-1}. As the area under the stress-strain curve is more at high strain rates, the fracture energy and toughness of the material was more at high strain rates compared to that at quasi-static and intermediate strain rates. Study of the fracture surfaces by scanning electron microscope showed that ductile fracture mode was observed [54].

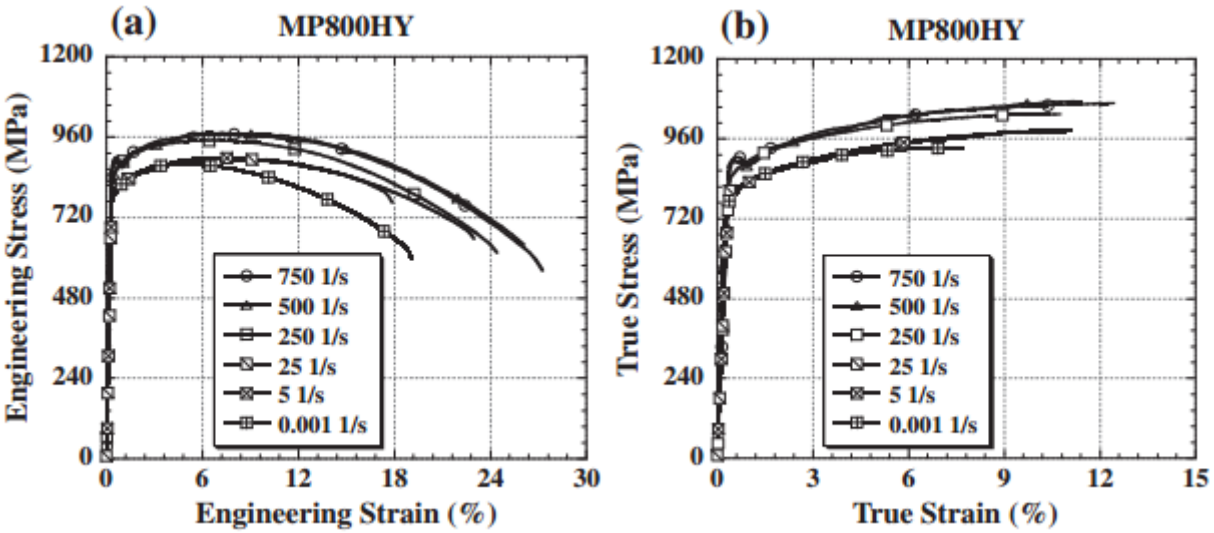

Figure 6.4 Comparison of stress versus strain curves of MP800HY steel at different strain rates, a) Engineering stress versus engineering strain and b) true stress versus true strain [54]

Fang presented the work which was focused on dynamic properties of HSLA steel with using instrumented impact tensile testing method. The specific type of specimens were prepared from X80 pipeline steel (transverse and longitudinal orientation). The researcher emphasized that dynamic properties could be evaluated with using instrumented impact testing machine Zwick Roell RKP 450 by means of mounting special instrumentation as shown in Figure 6.5 instead of servo system or the Split Hopkinson Pressure Bar method which were used for decades. The nominal stress-strain curve of miniature bar specimen under dynamic and quasi-static loading was recorded as Figure 6.6. The results showed that the strength of X80 steel was sensitively dependent on the strain rate change. With increasing strain rate from 10^{-2} s^{-1} to 10^{2} s^{-1}, the strength values rose by nearly 100 MPa [55].

Figure 6.5 Illustration of the impact equipment and specimen [55]

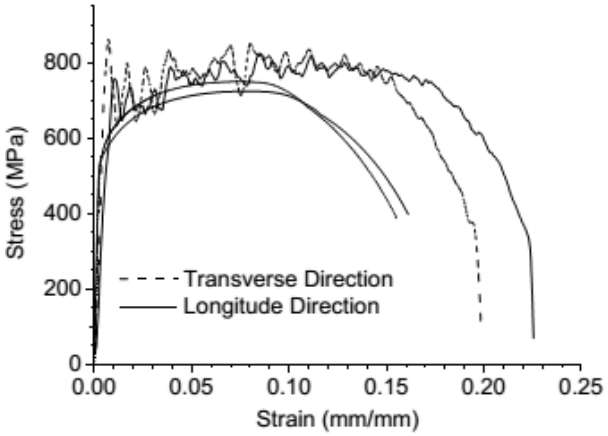

Figure 6.6 Stress – strain curves obtained by tensile testing under dynamic and quasi – static loading conditions [55]

Daud et al. conducted three-point bend impact experiments using an instrumented impact testing machine by Charpy V notch in accordance to ASTM E24.03.03 on AZ61 magnesium alloy. In this test method, a sharp fatigue pre-crack was initiated and propagated to half of the specimen at a constant crack propagation rate and after that, the specimen was loaded by the impact force until the maximum force was reached, finally rapid fracture occurred. In order to determine dynamic fracture toughness, specimens were prepared five different thickness of 2, 4, 6, 8 and 10 mm. The Charpy V notch test was performed at an impact velocity of 3.85 m/s. The dynamic fracture toughness was determined from the force-displacement history of the load point from measurements of input and reflected strain profiles on the incident specimen. Based on the obtained results, they concluded that the fracture toughness value K_d for AZ61 magnesium alloy decreased with increasing of the specimen thickness. The highest dynamic fracture toughness was 31.2 MPa√m and the lowest fracture toughness 21.7 MPa√m for specimens thickness of 2 mm and 10 mm, respectively. Cleavage fractures with river making seen predominantly in the fracture surface of shear – lip for all samples [56].

7. Experimental Procedure

In this chapter, the mechanical tests and evaluation methods carried out within the scope of the doctoral dissertation were introduced in all details.

7.1. Tested Materials

Nowadays, the manufacturers of transport mean implement new design solutions and new materials with the aim of reducing carbon dioxide emissions, decreasing energy consumption, improving the strength and reducing vehicles weight while increasing its capacity. These efforts are possible with using high strength steels and these kinds of steels are widely used in particularly heavy vehicles such as trucks, trailers, semi-trailers, rail vehicles including wagons and tramcars. An example is the latest grade of steel Strenx 700MC which is introduced by SSAB Company to the world market. The new grade of steel Strenx 700MC is originally produced as Domex 700MC and classified by the manufacturer to a thermomechanically rolled steel even though properties of the steel are at the level of the quenched and tempered steels. However, the manufacturer does not disclose the details of the manufacturing process of these steels. In general, the new high strength, micro-alloyed and fine-grained steels are manufactured by means of a complex technology of Thermo-Mechanical Control Processing (TMCP). Thanks to complex TMCP technology, two-phase microstructures consisting of very fine ferrite grains and bainite and/or martensite, depending on the process parameters and also the chemical composition, is produced as shown in Figure 7.1. High strength and micro-alloyed steels have a low carbon equivalent value and are therefore considered to be well weldable with low susceptibility to cracking. The micro-alloying elements control the microstructure. Trace amounts of elements such as niobium and titanium in concentrations on the order of 0.01 mass % allow the microstructure to be refined from the slab-reheating to controlled-rolling and accelerated-cooling processes and enhance the strength of the final products [2,3,6,57]. In this study, one of the evaluated steels was Strenx 700MC and its chemical composition is given in Table 7.1.

Table 7.1 Chemical composition of Strenx 700MC steel (in weight %)

C	Mn	Nb	P	S	V	Al	Ti
0.047	1.75	0.061	0.009	0.0026	0.016	0.041	0.0091

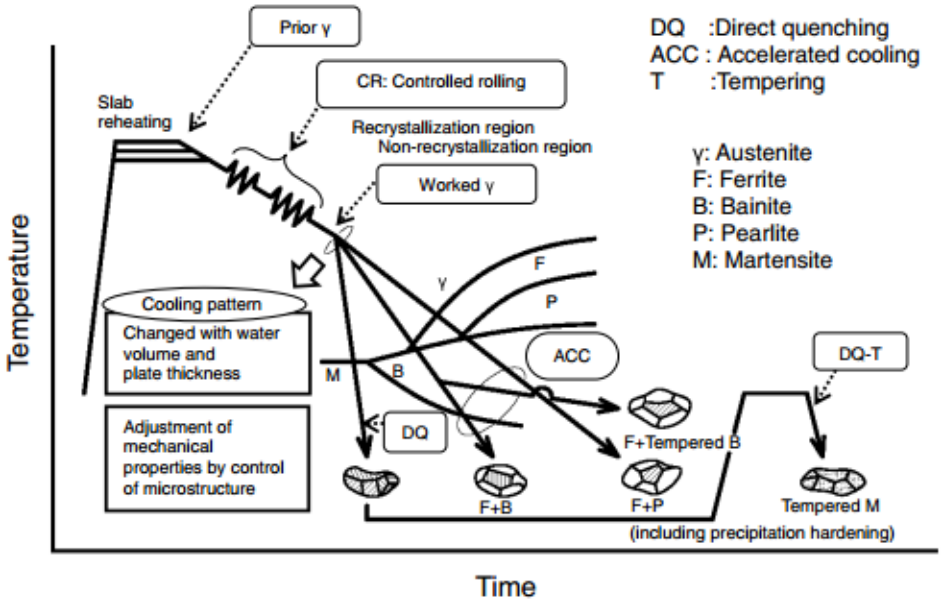

Figure 7.1 Concept of microstructure control by TMCP [57]

Another evaluated steel in this study was S355 structural steel, widely used in the construction and general engineering applications [40]. In the railway industry, the typical application of the S355 steel is for the passenger and freight cars. They are mainly made of S355 steel [58]. The chemical composition of the S355 steel is given in Table 7.2.

Table 7.2 Chemical composition of S355 steel (in weight %)

C	Mn	Si	P	S	V	Al	Ti
0.15	1.32	0.18	0.017	0.0056	0.0016	0.035	0.001

The last evaluated steel was experimental high strength steel for railway application.

The mechanical properties of all tested steels are given in Table 7.3.

Table 7.3 Mechanical properties of tested steels

Materials	Yield Strength (MPa)	Tensile Strength (MPa)
S355	516	550
Strenx 700MC	623	683
Experimental	874	1041

7.2. Welding of Strenx 700MC Plates

Because of the application of Strenx 700MC is a prospective material for lightweight construction in railway, only this kind of steel was examined and evaluated after the welding process. The steel plates were received as 120x300x10 mm^3 in dimensions. Before welding

process, steel plates were prepared “V” type groove as shown in Figure 7.2. The butt joint was used for bringing two steel plates together. Kempact 253R welding equipment was used to weld by metal active gas (MAG) method (shielding gases were mixtures of CO_2 and Ar) with three welding passes using Böhler UNION NiMoCr Ø1 (diameter 1 mm) filler wire. The chemical composition of the filling wire is given in Table 7.4. In order to prevent the distortion during the welding process, steel plates were fixed with four clamping apparatus as shown in Figure 7.3.

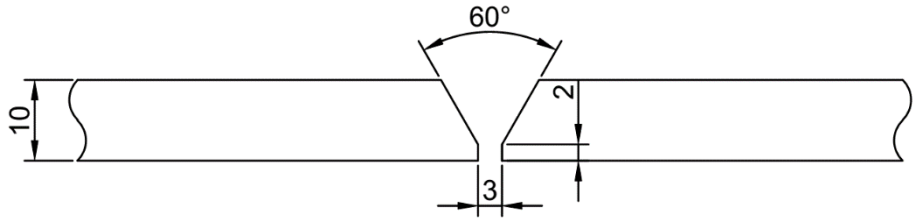

Figure 7.2 Details of V type configuration and dimensions of Strenx 700MC plate

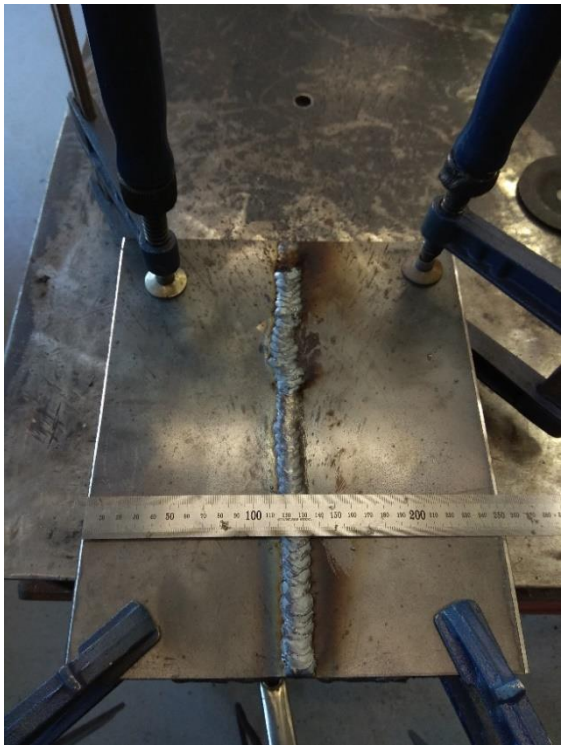

Figure 7.3 Welding of Strenx 700MC plates with clamping apparatus

Table 7.4 Chemical composition of filler wire Böhler UNION NiMoCr Ø1

C	Si	Mn	Cr	Mo	Ni
0.08	0.60	1.70	0.20	0.50	1.50

Heat input was calculated according to Equation 3.1 and all welding parameters for each welding pass are given in Table 7.5 (efficiency of MAG welding process is 0.8). After or before the welding process, no heat treatment process such as stress relieving was carried out.

Table 7.5 Welding parameters of MAG

Welding Pass	U (Voltage)	I (Current)	Travel speed (mm/min)	Energy (KJ/mm)
1	18.5	140	112	1.1
2	18.5	140	81	1.5
3	18.5	140	102	1.2

7.3. Weld Simulation of Strenx 700MC Specimens

There are two main reasons applying weld simulation method for Strenx 700MC specimens. First, no matter how precautions are taken during the welding process, at least one type of typical weld defects can be seen e.g. undercut, cracks, porosity, slag inclusions, lack of fusion and lack of penetration. These small imperfections act as a stress raiser for specimens or cause some mechanical properties variation of the welded specimen. Second, by using weld simulation method, the HAZ can be geometrically extended and the mechanical properties of each sub-zones which are developed in the HAZ can be evaluated. In order to compare the welding simulation method with the real welding method in an appropriate way, the parameter to be considered is the hardness. At first, the lowest hardness value of real welding specimen was measured, according to this value, welding simulation parameters were specified.

Welding simulation was conducted using WTU 315-3 welding equipment. The prepared specimen was heated by electric arc which was transferred with using copper rings were placed on the specimen. During the welding simulation process, time – temperature (from heating to cooling) was recorded by Omega HH309A four-channel data logger thermometer as shown in Figure 7.4a. Before and after the weld simulation process of the specimen are shown in Figure 7.4b and Figure 7.4c, respectively.

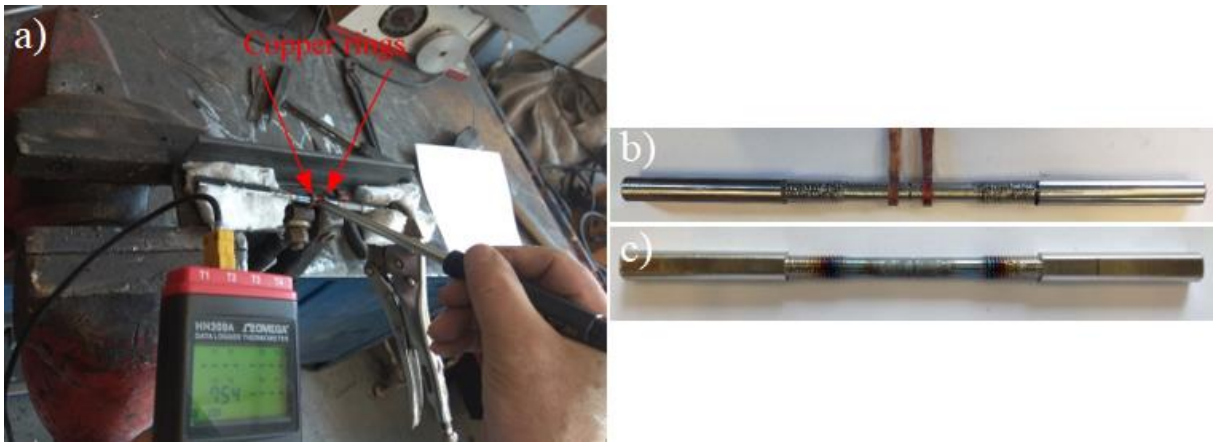

Figure 7.4 a) During the weld simulation process of Strenx 700MC specimen, b) Before weld simulation process of specimen c) After weld simulation process of specimen

For evaluating the effect of heat input on fracture toughness of Strenx 700MC steel, samples were prepared only weld simulation method. As mentioned above, after the real welding process, the preparation of samples from welded plates are not possible due to consisting of weld defects.

7.4. Hardness Test

In order to determine the hardness, the specimen was cut and prepared from suitable regions. The prepared samples were ground with SiC abrasive papers (120, 240, 600, 800 and 1000 grit number) and finally polished using 3 µm diamond paste. If it was necessary to reveal the microstructure, the surface of the specimen was etched with 2% nital solution. The tests were conducted on Nexus 4300 Serie hardness tester using Vickers indenter (according to EN ISO 6507-1). The load and the dwell time was kept at a constant value of 1 kgf – 9.807 N load and 10 seconds, respectively. Hardness measurements were evaluated in Vickers Scale (HV1).

7.5. Metallography

Metallographic examinations were carried out on the samples cut from suitable positions of the tested steels and welded steel plates. Except for welded steel plates, the other steels were molded with bakalite resin to grind and polish easily with utmost care. To begin with, SiC papers with grit number of 120, 240, 600, 800 and 1000 were used respectively for grinding. On the next step, 3 and 1 µm diamond pastes were used for polishing. Finally, the specimens were etched with 2% nital solution, cleaned with alcohol and dried carefully. To observe the

complete microstructure, Carl Zeiss Jena Neophot 32 and scanning electron microscope TESCAN VEGA 5130SB were used.

7.6. Analysis of Fracture Surfaces

In order to calculate the values of fracture toughness, it is necessary to measure dimensions and crack lengths precisely. For this reason, macro photos of fracture surfaces were captured using SMZ800 zoom stereomicroscope. The SMZ800 offers 1 – 8x zoom range and enables high-resolution observation.

Another device for analyzing the fracture surfaces was the Scanning Electron Microscopy (SEM). It has unique capabilities for giving details of fracture surfaces. Microscale of fracture surfaces can give information e.g. crack initiation side, crack propagation direction, mechanism of cracking and type of fracture. In this study, TESCAN VEGA 5130SB was used for analysis of fracture surfaces.

7.7. Methods of Determination of Plane Strain Fracture Toughness

7.7.1. Circumferentially Cracked Round Bar (CCRB) Test Method

In this methodology, the round bar specimen which had a notch at the midpoint was fatigue precracked and loaded in uniaxial tensile test machine till failure. After failure, fractured surface of the specimen was investigated with optical instruments and the measurement of diameters and crack lengths were specified. In order to calculate the fracture toughness of the materials, proposed equations which depend on the fracture load and specified dimensions were used.

The technical drawing and illustration of the prepared round bar test specimen for CCRB test method are shown in Figure 7.5 and in Figure 7.6, respectively. The specimen was prepared "V" type notch of 60° with 1 mm radial depth (mean notch radius was 0.225) at the midpoint as shown in Figure 7.7. The important dimensions of the specimen were the diameter of unnotched section (D) was 8 mm, the diameter of notched section (d) was 6 mm, specimen length (L) was 226 mm and gauge length (L_0) was 96 mm. The specimen was prepared from steel plates parallel to the rolling – longitudinal direction. During the machining process in a lathe, smooth surface quality at the specimen surface and also at the notch section were

obtained. The reason of choosing “V” type notch, during reversed bending fatigue test, stress at the tip of the notch would be very high and the crack started to propagate at this point as shown in Figure 7.8.

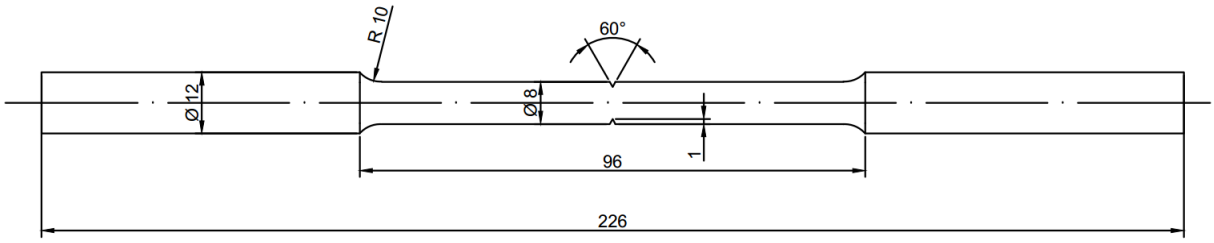

Figure 7.5 Technical drawing of round bar test specimen for CCRB test method

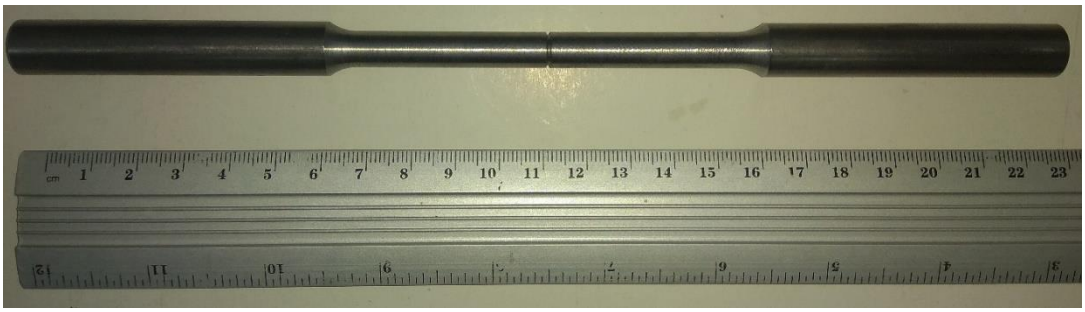

Figure 7.6 Illustration of the prepared of round bar test specimen for CCRB test method

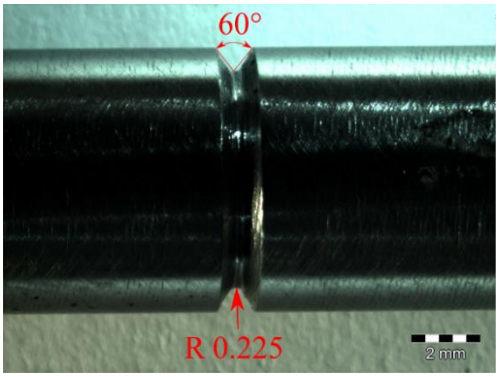

Figure 7.7 “V” type notch at the midpoint of the specimen

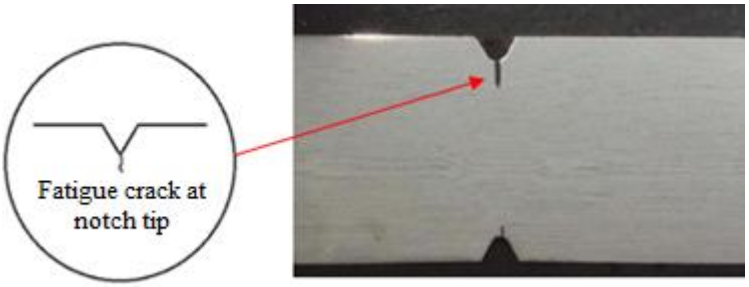

Figure 7.8 Crack propagation at the notch tip

In order to ensure initial fatigue crack in the specimen, R. R. Moore four-point rotating beam fatigue testing machine was used as shown in Figure 7.9. During the precracking procedure, the specimen was subjected to cyclic tensile – compressive loads of equal amplitude were applied with the stress ratio R_{stress} equal to minus 1 (R_{stress} = -1). With choosing suitable bending load (M), the selected load was such that the maximum stress intensity factor K_{max} should not exceed 60% of the minimum expected fracture toughness K_{IC} of tested material. The mounted round bar specimen on the fatigue machine for precracking procedure is shown in Figure 7.10.

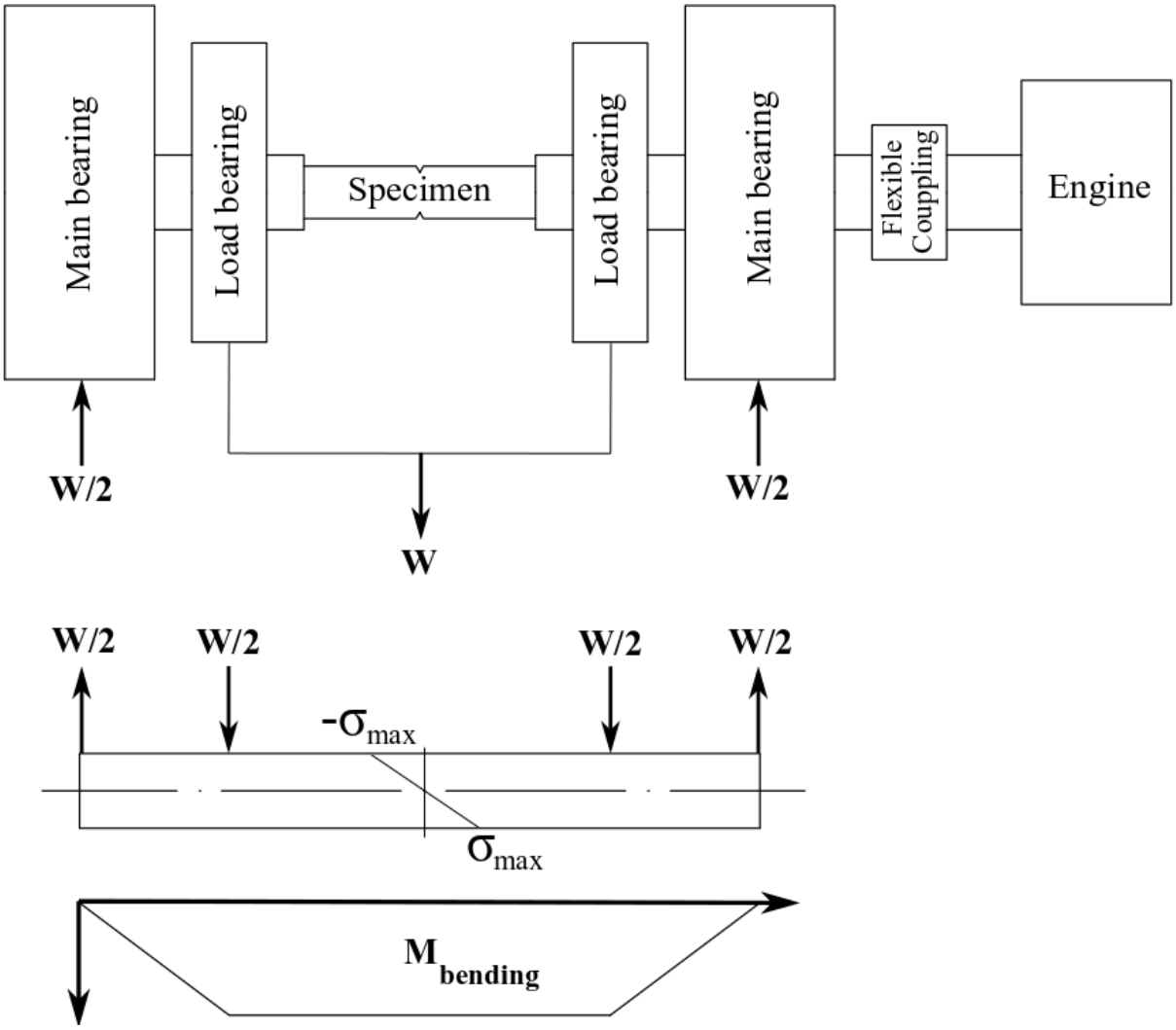

Figure 7.9 R. R. Moore four-point fatigue testing machine

Figure 7.10 Mounted round bar specimen on fatigue machine

During fatigue precracking process, estimation of crack propagation was very important for determination of fracture toughness. In order to succeed it, the length of crack was estimated by using JK – 1 Crack Depth meter device as shown in Figure 7.11a. Determination of crack depth with this device was based on the measurement of the electrical resistance between two points on the surface of the specimen which had a notch at the middle point. If there was a crack between measured two points, the electrical resistance was higher than for a crack-free surface. The probe had four pins, two pins of the probe were positioned to the left side of the notch and the other two pins of the probe were positioned to right side of the notch as shown in Figure 7.11b. The next step, the probe was slightly pressed on the specimen by hand force. Before the fatigue tests, each of the specimens was calibrated and set to zero according to the upper blue scale as shown in Figure 7.11a. After the completion of the fatigue test at a specific time, the crack length of the specimen was measured again. If there was a crack in the specimen, the scale showed a value higher than zero. But with using this approach, the exact length of the crack could not be specified, it was only predicted that a crack existed in the specimen.

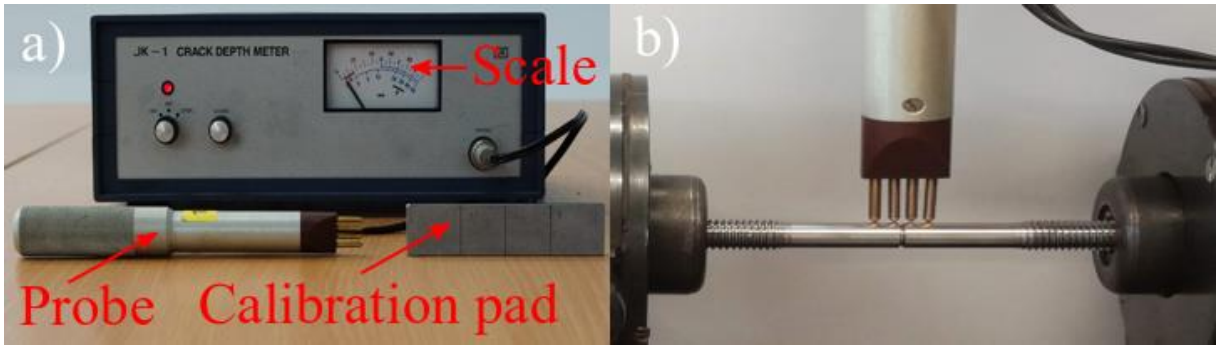

Figure 7.11 a) JK – 1 crack depth meter device, b) Position of the probe during measurement

For mode – I loading condition, the precracked specimen was loaded in tension on a universal tensile tester device which was ZD 10/90 as shown in Figure 7.12. Crosshead displacement rate of 0.5 mm/min was used until failure. During the tensile tests, load and crosshead displacements were recorded. All specimens were tested at room temperature. A minimum of three specimens of the materials were tested for fracture toughness calculation. The maximum loads of all the specimens were specified.

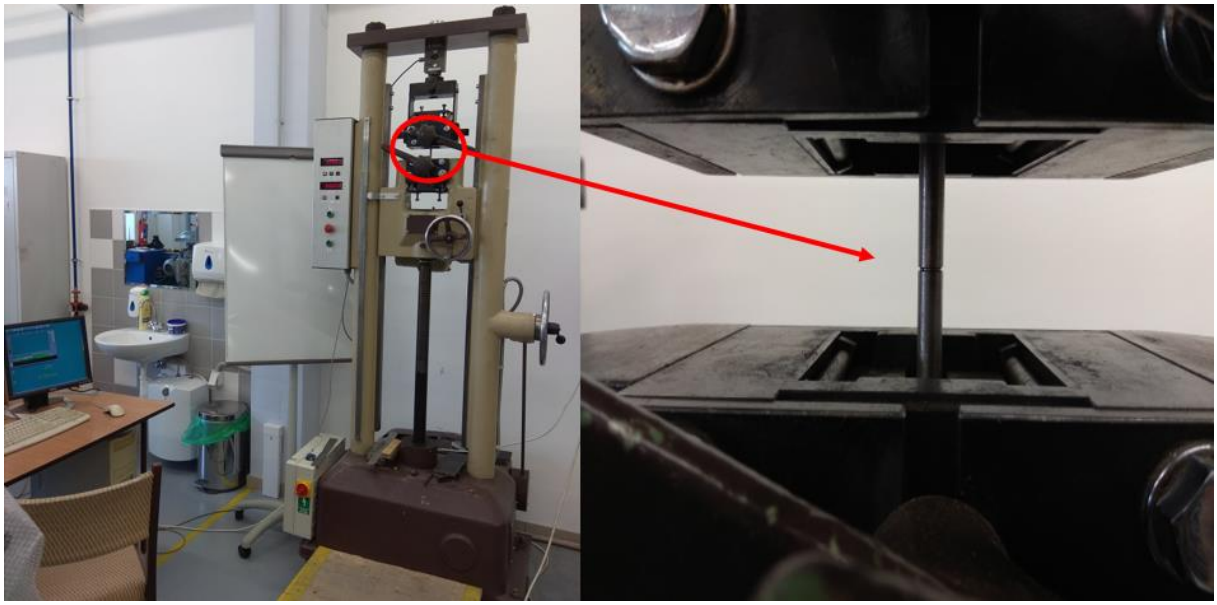

Figure 7.12 Universal tensile tester device ZD 10/90 and mounted specimen

After completion of the uniaxial tests, the fracture surface of the specimen was investigated, and specified dimensions were measured with a stereo optical microscope. For calculation of fracture toughness, defined dimensions were machined notch depth (a_m), length of fatigue precrack (a_f), crack length due to brittle fracture (a_b) and total crack length (a). The mentioned dimensions were distinct with captured figures as shown in Figure 7.13 and they were specified according to these regions: Region A was the cross-sectional view of the machined notch, Region B was the result of steady crack propagation and Region C was the zone of sudden unstable fracture due to the tensile test.

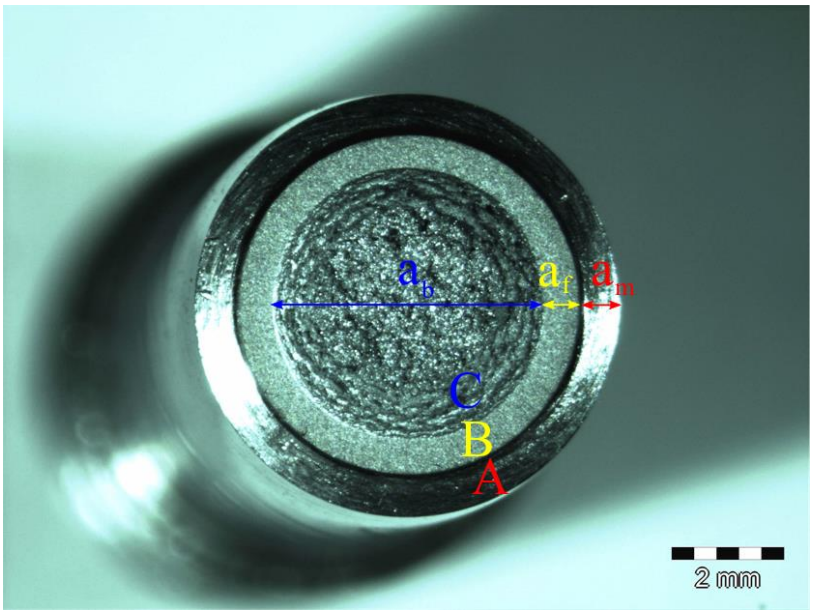

Figure 7.13 Image of the fracture surface of the specimen and defined dimensions according to regions

For determination of the fracture toughness of the material, the effective diameter (d_{eff}) was calculated by the sum of machined notch depth and the length of the fatigue precrack as in Equation 7.1

$$d_{eff} = D-2(a_m + a_f) \tag{7.1}$$

Equation 7.1 was used for calculation of fracture toughness as in Equation 7.2 [39],

$$K_{IC} = \frac{P_f}{D^{3/2}}\left[1.72\frac{D}{d_{eff}}-1.27\right] \tag{7.2}$$

where P_f was the maximum fracture load and D was the diameter of the unnotched section. The valid range of Equation 7.2 was $0.46<(d_{eff}/D)<0.86$. For CCRB test method, the fracture toughness of each specimen was calculated according to this proposed equation.

In the fracture mechanics approach to fatigue crack growth rate is correlated with the stress intensity parameter K. This approach makes it possible to estimate the useful safe lifetime of machine elements and components. da/dN is the fatigue crack growth rate and $\Delta K=K_{max}-K_{min}$ is the stress intensity factor range. An idealized da/dN versus ΔK curve is shown in Figure 7.14. In region I, ΔK_{th} is the fatigue crack growth threshold where crack growth rate approaches to zero. In region II is called as Paris region because it is introduced by Paris and Erdogan in

1963. In this region the crack growth rate is almost stable and has linear characteristic and it can be modeled by power law equations:

$$da/dN=C(\Delta K)^m \tag{7.3}$$

where C and m are constant material parameters and related to type of material, environment, temperature and fatigue stress conditions. Finally, in Region III, the crack growth rate accelerates and sudden failure occurs at the final stage [59].

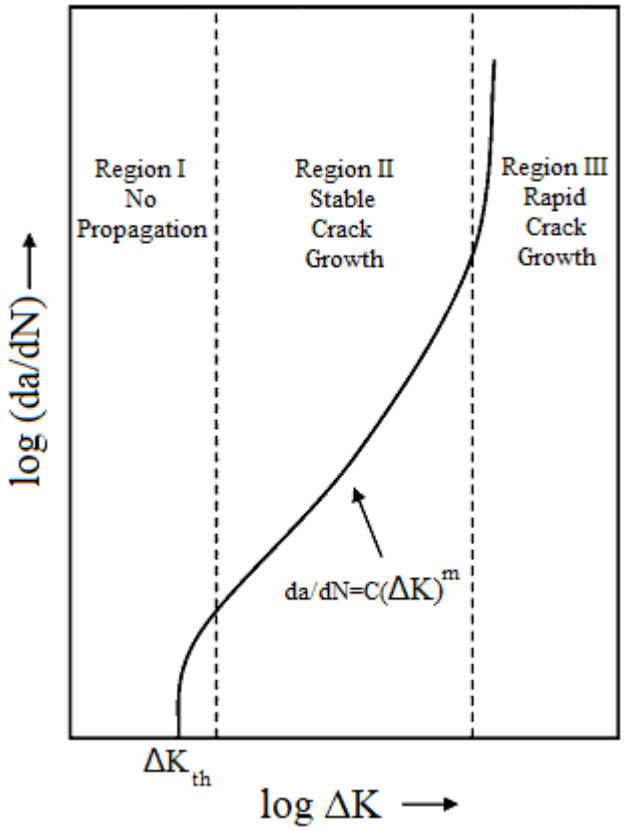

Figure 7.14 An idealized crack propagation curve for fatigue loading [59]

According to Neelakantha et. al, in addition to fracture toughness, determination of fatigue crack growth rate (FCGR) is possible with using notched round bar specimen [38,39]. On a R. R. Moore four-point rotating beam fatigue testing machine, the specimen which had a notch at the midpoint was mounted and allowed to rotate under suitable bending load till failure and total number of fatigue cycles (N_f) were specified. (Actually, this procedure was completed at the first stage of the work. With taking into consideration (N_f) values, the required number of cycles (which was lower than N_f) to propagate crack was specified for calculation of fracture toughness of the specimen.) The radial crack started to propagate from notch root to inward of

specimen center. There were three distinct regions existed in the fracture surface as shown in Figure 7.15. Defined crack lengths were (a_i) was the average initial fatigue precrack, (a_s) was the average steady crack length. Final ligament at the time of final sudden fracture was also seen at the center of the specimen but during the calculation procedure was not necessary to consider. Using this methodology, the fatigue crack growth rate was calculated as:

$$\frac{da}{dN} = \frac{a_s}{N_f} \tag{7.4}$$

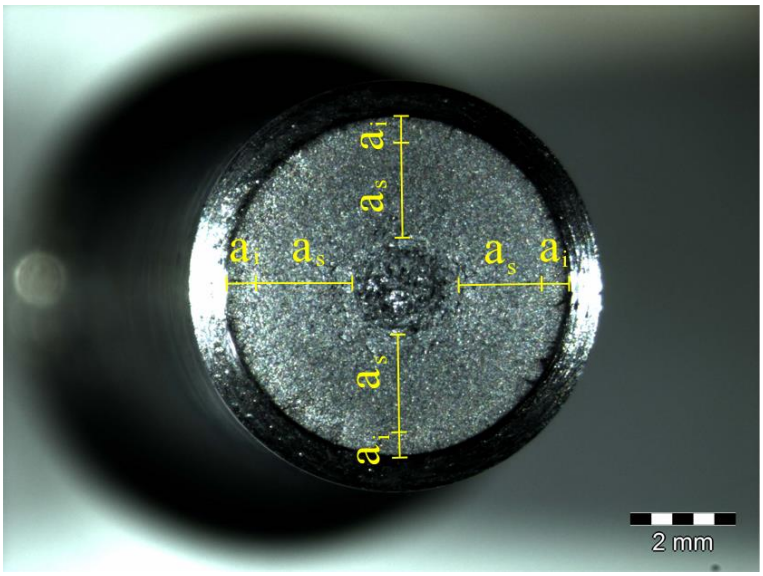

Figure 7.15 Image of the fracture surface of the specimen for determination of fatigue crack growth rate

The following equations were used to calculate the stress intensity factors K_{min} and K_{max} at the notch root of round bar specimen in fatigue bending [39]:

$$\alpha_{min,max} = \frac{r\text{-}a_{i,s}}{R} \tag{7.5}$$

$$F(\alpha_{min,max}) = G(\alpha_{min,max})\sqrt{(1-\alpha_{min,max})} \tag{7.6}$$

$$G(\alpha_{min,max}) = \frac{3}{8}\left[1+\frac{1}{2}(\alpha_{min,max})+\frac{3}{8}(\alpha_{min,max})^2+\frac{5}{16}(\alpha_{min,max})^3+\frac{35}{128}(\alpha_{min,max})^4+\frac{537}{1000}(\alpha_{min,max})^5\right] \tag{7.7}$$

$$\sigma_{B\,min,max} = \frac{4M}{\pi(r-a_{i,s})^3} \tag{7.8}$$

$$K_{min,max} = \sigma_{Bmin,max} \sqrt{\pi\left(r\text{-}a_{i,s}\right)} F(\alpha_{min,max}) \quad (7.9)$$

where r was the radius of the notched section of the specimen, R was the radius of unnotched section of the specimen, M was the bending moment and σ_B was the bending stress acting on the specimen. At least three different bending moments were applied to specimens to plot da/dN (m/cycle) versus ΔK (MPa$\sqrt{m}$) graph.

7.7.2. Circumferentially Notched Round Bar (CNRB) Test Method

Circumferentially notched round bar (CNRB) methodology is less complicated and simple than circumferentially cracked round bar (CCRB) methodology because of there is no precracking procedure like using four-point rotating beam fatigue test.

The round bar specimen was prepared "V" type notch of 60° with 1 mm radial depth at the midpoint and defined dimensions were same as in CCRB test method. Representative of prepared specimen is shown in Figure 7.16. The important dimensions were diameter of unnotched section (D), diameter of notched section (d) and gauge length (L_0).

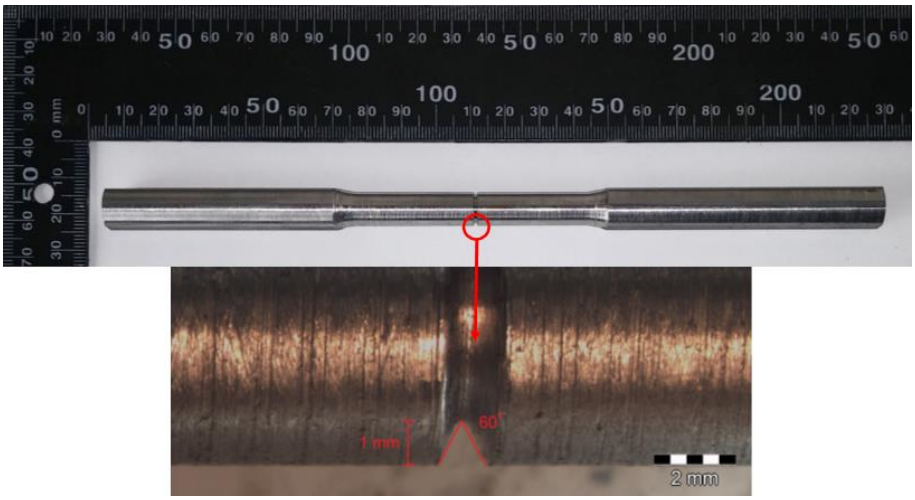

Figure 7.16 Representative prepared of the round bar test specimen for CCRB test method

The prepared specimen was directly loaded in tensile test and the fracture load was recorded during the experiment. After completion of the tensile test, the fracture toughness was calculated using the dimensions and fracture loads.

In the literature, K_{IC} was calculated and formulated using CNRB method by different researchers.

First equation for determining fracture toughness from the notched tensile specimen was given below [37]:

$$K_{IC} = \frac{P_f}{D^{3/2}}\left[1.72\frac{D}{d}\text{-}1.27\right] \tag{7.10}$$

This suggested equation was valid for the D/d ratio between 1 and 1.25.

The second proposed equation was based on notch tensile strength. Notch tensile strength was calculated as [35],

$$\sigma_{NTS} = \frac{4P_f}{\pi d^2} \tag{7.11}$$

Using Equation 7.11, the fracture toughness of the materials was calculated by using the following equation,

$$K_{IC} = 0.454\sigma_{NTS}D^{1/2} \tag{7.12}$$

The last suggested equation was proposed by the researcher as follows [43],

$$K_{IC} = \frac{0.932P_f\sqrt{D}}{d^2\pi} \tag{7.13}$$

This assumption needs a requirement which was $1.2 \leq D/d \leq 2.1$.

7.8. Determination of Dynamic Fracture Toughness with Nonstandardized Test Method

The methodology of the determination of the dynamic fracture toughness is very similar to CCRB method in terms of material preparation and fatigue precracking procedures. The specimen used for dynamic fracture toughness (K_{Id}) test was round bar which had "V" type notch of 60° with 1 mm radial depth (mean notch radius is 0.225) at the midpoint and it had also M10 thread. The specimens were prepared longitudinal orientation according to the rolling direction. The technical drawing and illustration of the prepared threaded round bar test specimen are shown in Figure 7.17 and in Figure 7.18, respectively. The reason of machining M10 thread was the necessity of screwing samples to the tups during the impact tensile test.

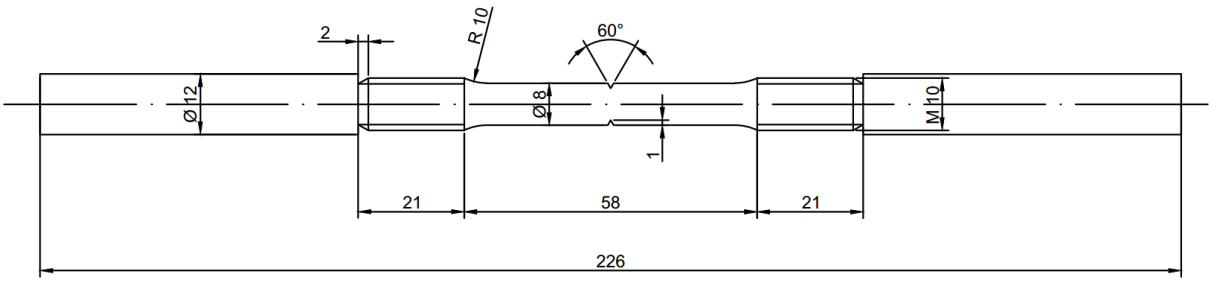

Figure 7.17 Technical drawing of round bar test specimen for dynamic fracture toughness

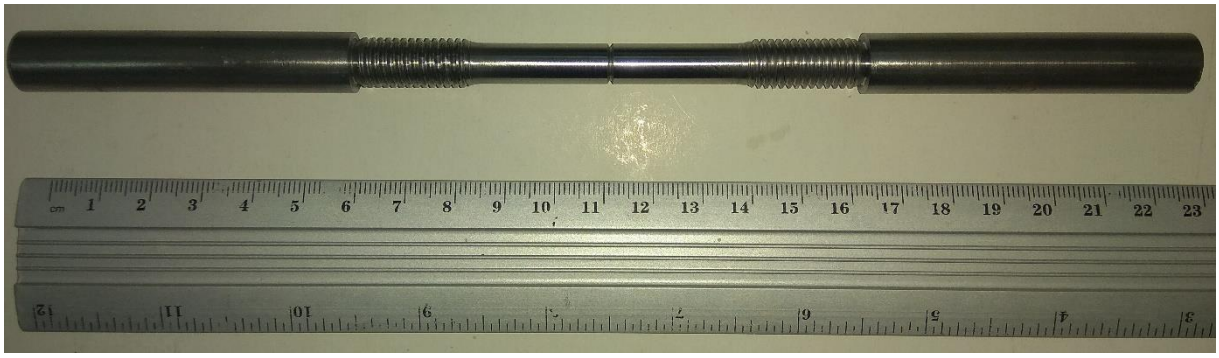

Figure 7.18 Illustration of the prepared of the thread round bar test specimen for dynamic fracture toughness

The procedures which were conducted in CCRB method had also been applied to the threaded round bar specimen for determination of dynamic fracture toughness. With using R. R. Moore four-point rotating beam fatigue testing machine, precrack was initiated and propagated radially towards the center of the specimen. Each specimen was rotated to a finite number of fatigue cycles (less than N_f). When a crack was detected in the specimen using JK – 1 Crack Depth Meter device, the specimen was ready for the dynamic tensile test. Before conducting dynamic tensile test, the specimen was cut from end positions of both M10 thread.

In present study, Zwick/Roell RKP 450 with PC connected with testXpert testing software was chosen to conduct the instrumented impact tensile testing. To perform the impact tensile tests, special instrumentation and accessories were needed e.g. anvil, pendulum hammer, tailor block and tup as shown in Figure 7.19. The specimen was screwed and fixed between the tup and tailor block. During the impact tensile test, the hammer was started to swing from the specified height, the tup with the screwed specimen transited through the central gap of the anvil. While the tailor block was impeded by the end wall of the stiff anvil, which led to the impact loading transferred onto the specimen and induced braking. All tests were conducted at

room temperature and during the impact, force – displacement or force – time graph was recorded.

Figure 7.19 a) Pendulum hammer, b) Screwed specimen between tailor block and tup, c) General view of Zwick/Roell RKP 450 pendulum impact tester and d) Anvil

In order to investigate the effect of loading rate on the dynamic fracture toughness of the materials, the tests were conducted at two different impact velocities. The first group of material was tested at 5.23 m/s and the second group was tested at 3.48 m/s. While calculating the reduced impact velocity, it can be determined as follows: the pendulum hammer was released from the appropriately reduced height, without a specimen on the anvil. The energy KV_0 (J) was read from the indication of the analog scale. Finally, the reduced impact velocity was calculated for a 450 J pendulum as,

$$V_0 = V_{0s}\sqrt{\frac{450\text{-}KV_0}{450}} \tag{7.14}$$

where V_{0s} was the impact velocity corresponding to the maximum potential energy of the pendulum impact tester. If the maximum available energy of the pendulum impact tester is different from 450 J, it is necessary to replace 450 with the actual available energy [50].

After completion of the impact tensile test, the fracture surface of the specimen was investigated and specified dimensions were measured with stereo optical microscope. For calculation of dynamic fracture toughness, defined dimensions were same as in CCRB test method: a_m was the machined notch depth, a_f was the length of fatigue precrack and a_b was the crack length due to unstable sudden fracture. For determination of dynamic fracture toughness of the material, the effective diameter (d_{eff}) was necessary to calculate by the sum of machined notch depth and the length of the fatigue precrack as in Equation 7.1. Depending on the effective diameter (d_{eff}), unnotched section diameter (D) and maximum force (P_{dmax}) during the impact tensile test, dynamic fracture toughness (K_{Id}) was calculated as follow [39]:

$$K_{Id} = \frac{P_{dmax}}{D^{3/2}} \left[1.72 \frac{D}{d_{eff}} - 1.27 \right] \tag{7.15}$$

In the literature, the proposed equation was used only static loading condition to specify the fracture toughness (K_{IC}). This approach provided a novel method to determine the dynamic fracture toughness of the metallic materials using pendulum impact tester.

7.9. Determination of Dynamic Fracture Toughness with Standardized Test Method

It is possible to determine the dynamic fracture toughness of metallic materials using precracked Charpy type test specimen which is explained in ISO 26843:2015(E) (Metallic materials – Measurement of fracture toughness at impact loading rates using precracked Charpy-type test pieces) [50].

The specimen used for dynamic fracture toughness test was single edge notch bend (SENB or 3-point bending) as shown in Figure 7.20 and Figure 7.21. Precracking was carried out on fatigue testing machine at a constant ΔK level to obtain constant crack growth rate.

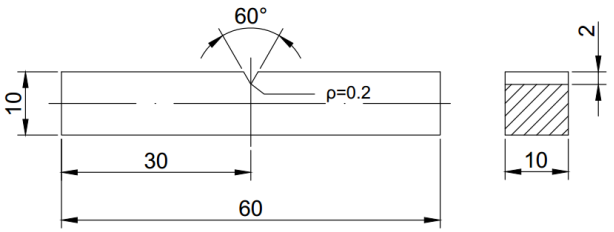

Figure 7.20 Technical drawing of the SENB specimen

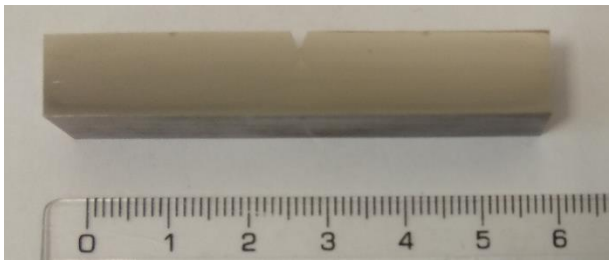

Figure 7.21 Illustration of the prepared of the SENB specimen

According to ISO 26843:2015(E), the dynamic fracture K_{Id} can be calculated with using instrumented pendulum impact tester. In this study, Zwick/Roell RKP 450 by choosing suitable accessories and instrumentation was preferred to conduct the instrumented impact 3-point bending testing. In this section, the evaluation of test records and calculation of results were explained in detail. The impact response curve method was a fully dynamic measuring technique. After impact testing, it was necessary to evaluate the force – time curve and the characteristics of this curve was shown in Figure 7.22. First important parameter in this graph was time to fracture (t_f) which was indicated with arrow. Using the measured (t_f), the dynamic fracture toughness K_{Id} was determined as:

$$K_{Id} = K_I^{dyn} (t=t_f) \tag{7.16}$$

$$K_I^{dyn} = RV_0 f(t') \tag{7.17}$$

where the constant R= 301 GN/$m^{5/2}$, V_0 was impact velocity (5.23 m/s) and the correction factor f(t') was found in Table A1 (in Appendix A) with

$$t'=t\left[1-0.62\left(\frac{a}{W}-0.5\right)+4.8\left(\frac{a}{W}-0.5\right)^2\right] \tag{7.18}$$

where (t) was the measured physical time and (t') was a modified time which compensated for variations of the initial crack length in the range 0.45<a/W<0.55. To determine the crack length of the SENB specimen, the crack surfaces were examined with stereo optical microscope. The specified crack lengths were a_m was machined notch depth, a_0 was the length of fatigue precrack and a was the total crack length (a_m+ a_0) as shown in Figure 7.23.

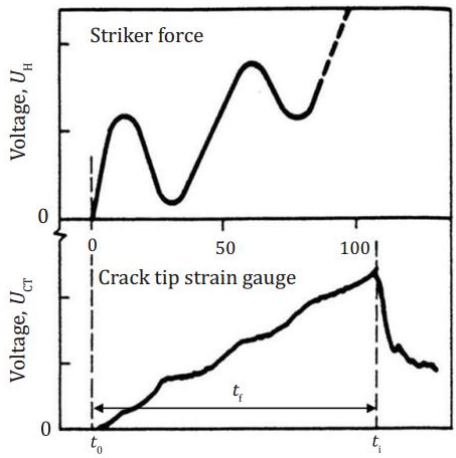

Figure 7.22 Typical force and strain gauge signals during impact [50]

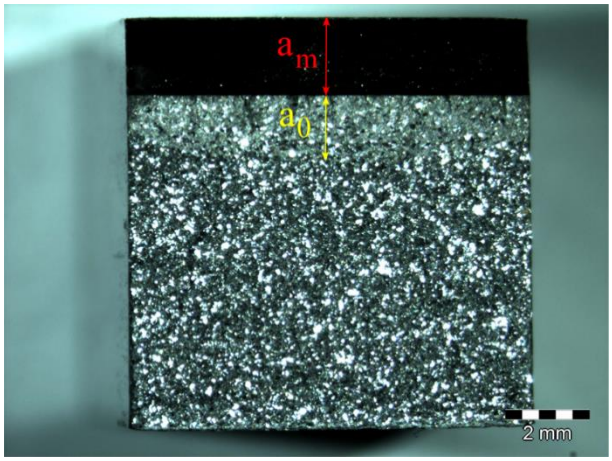

Figure 7.23 The fracture surface of the SENB specimen and specified crack lengths

8. Results and Discussion

8.1. Structural Characterization of Tested Steels

Metallography evaluation was performed to find out the primary structural parameters of the high strength steel (Strenx 700MC) and reference S355 steel.

The microstructures of S355 steel in the longitudinal rolling direction were characterized by optical microscopy, as can be seen in Figure 8.1. It was visible that typical ferrites and pearlites were apparent in both figures (500x and 1000x). The dark regions refer to pearlite whereas light-colored regions refer to ferrite. The mechanical properties of pearlitic are specified by the thickness of the ferrite and cementite layers. The thickness of these layers can be controlled by carbon content and cooling rate during the stage of steel production. Slow diffusion at low temperatures leads to fine-grained microstructure and it is called as fine pearlite. At higher temperatures, high diffusion rate allows for grain growth and pearlite is formed in thick layered structure, it is known as coarse pearlite. As a result, smaller inter lamellar spacing give higher strength for these kinds of steels.

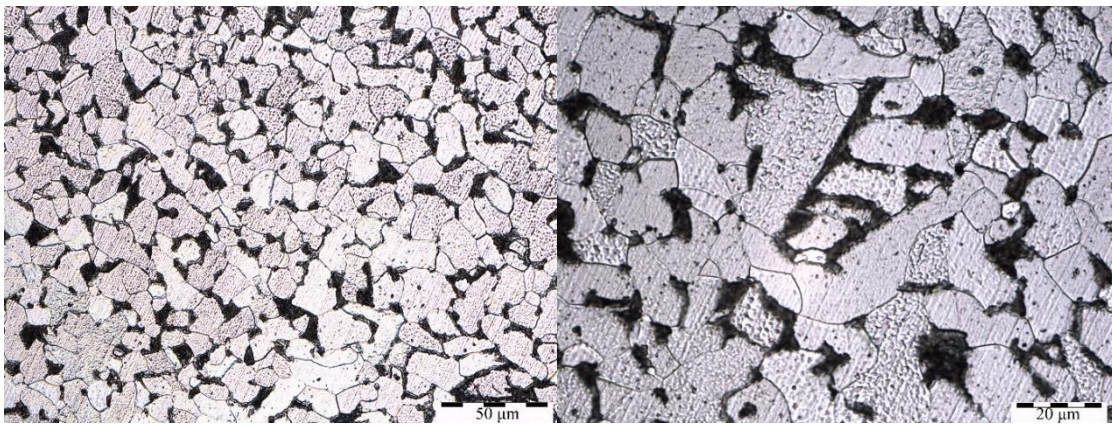

Figure 8.1 The microstructures of S355 steel, left 500x and right 1000x

The microstructural observation of Strenx 700MC steel sample is shown in Figure 8.2. It was characterized by a fine-grained microstructure. This kind of microstructure can be formed by microalloying elements. Trace amounts of elements such as niobium and titanium (in concentrations on the order of 0.01 mass %) resulted in the microstructure to be refined during the thermomechanical control process. The main heterogeneity of Strenx 700MC steel was carbide distribution as shown in Figure 8.3. This heterogeneity affected the fracture behaviour of the material which was explained in the following chapters. Chemical micro analyzes were

performed to identify the micro impurities. EDX1 was complex oxides and EDX2 was TiN with no decisive influence. The observed carbide distribution has crucial effect on fracture response.

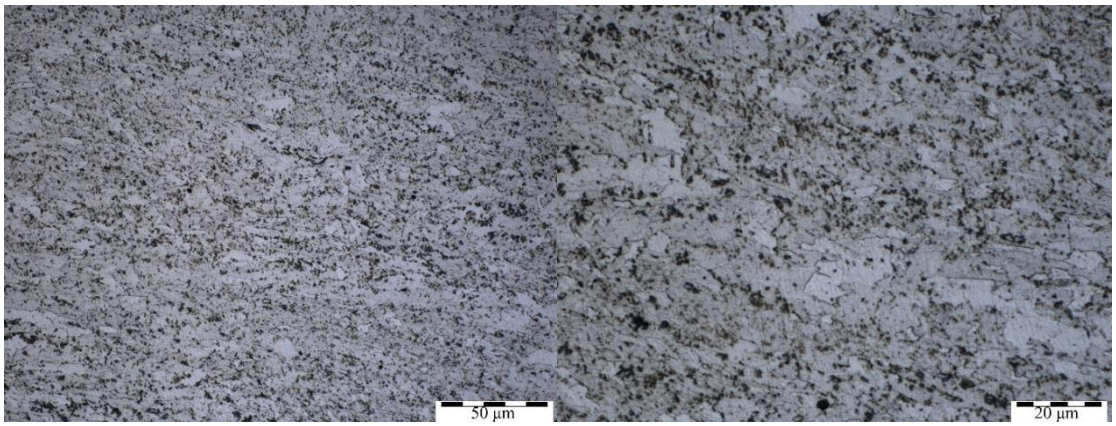

Figure 8.2 The microstructures of Strenx 700MC steel, left 500x and right 1000x

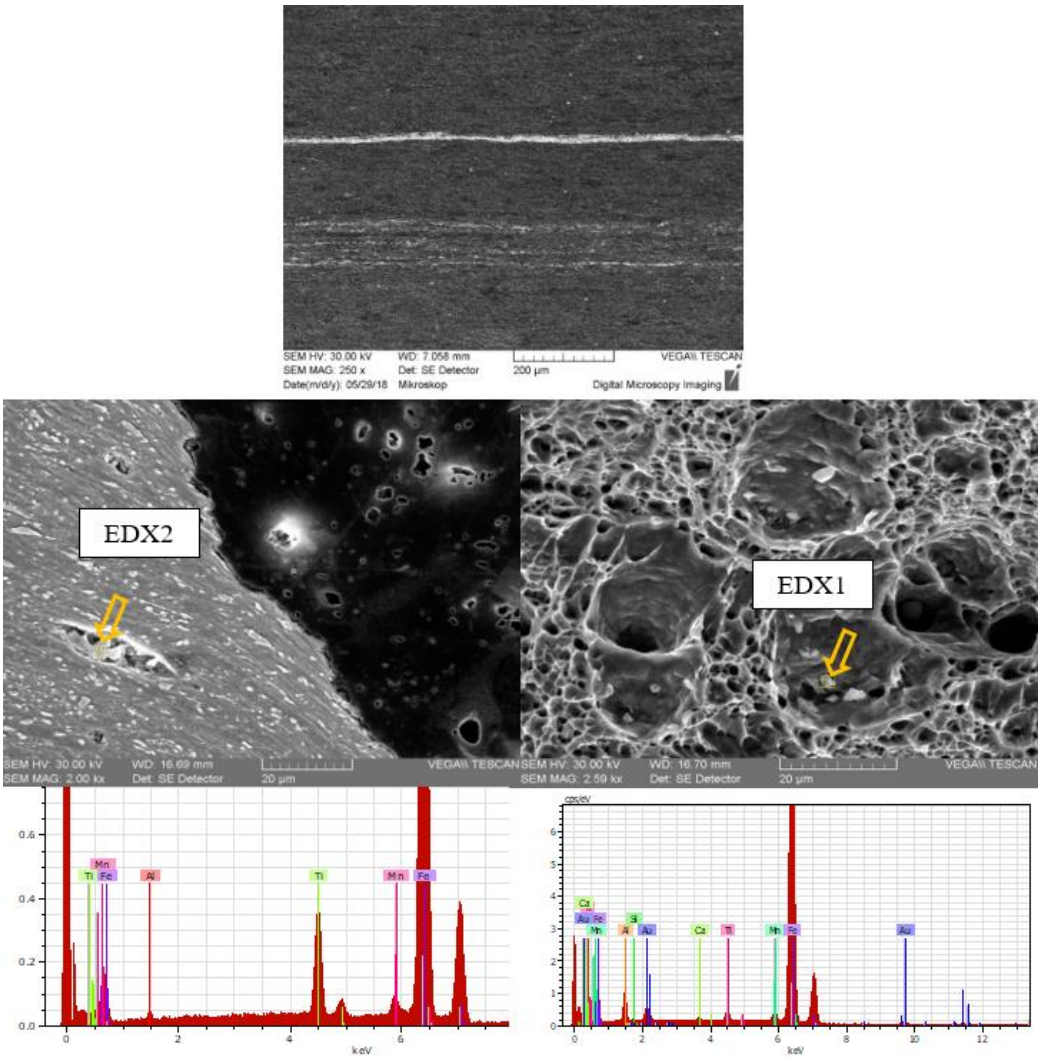

Figure 8.3 The carbide distribution in Strenx 700MC

8.2. Analyzes of the Welding Process Influence

8.2.1. Metallography Evaluation

Complex structural characterization of the experimental welding was conducted to:

- Identify the critical sublayer of HAZ in terms of structural degradation
- Describe the involved degradation process
- Enable suitable simulation process of welding influence.

The cross-sectional macro photo and microstructure of Strenx 700MC weld joints are displayed in Figure 8.4. The first noticeable observation in macrographs which is in the middle of Figure 8.4, macro porosities were observed in the welding pool. These weld defects affected the mechanical properties of the welded steel in negative way. These defects confirmed that the weld thermal simulation was a better approach than real welding method for investigating the effect of heat input on the tested steel. Four regions with significant influence on fracture resistance were visible in macrograph: welding pool, grain coarsening zone, grain refinement zone and base metal. These formed regions were dependent on heat energy input during welding, heat treatment before and post welding process and the number of welding pass. In the welding pool, during weld metal solidification, grains tend to grow in the direction of maximum heat extraction. A typical columnar shape of grains in the welding pool is shown in the upper position of Figure 8.4. Next to the welding pool, grain coarsening is visible compared to the zone of base metal. The high cooling rate and large grain size stimulate the ferrite to form side plates from the grain boundaries. In the lower position of Figure 8.4, the zone of grain refinement is presented. Observed intensity of grain size refinement was an effective strengthening mechanism. Finally, a rolling effect was visible in the zone of base material. Irregular, locally rough inclusions were observed.

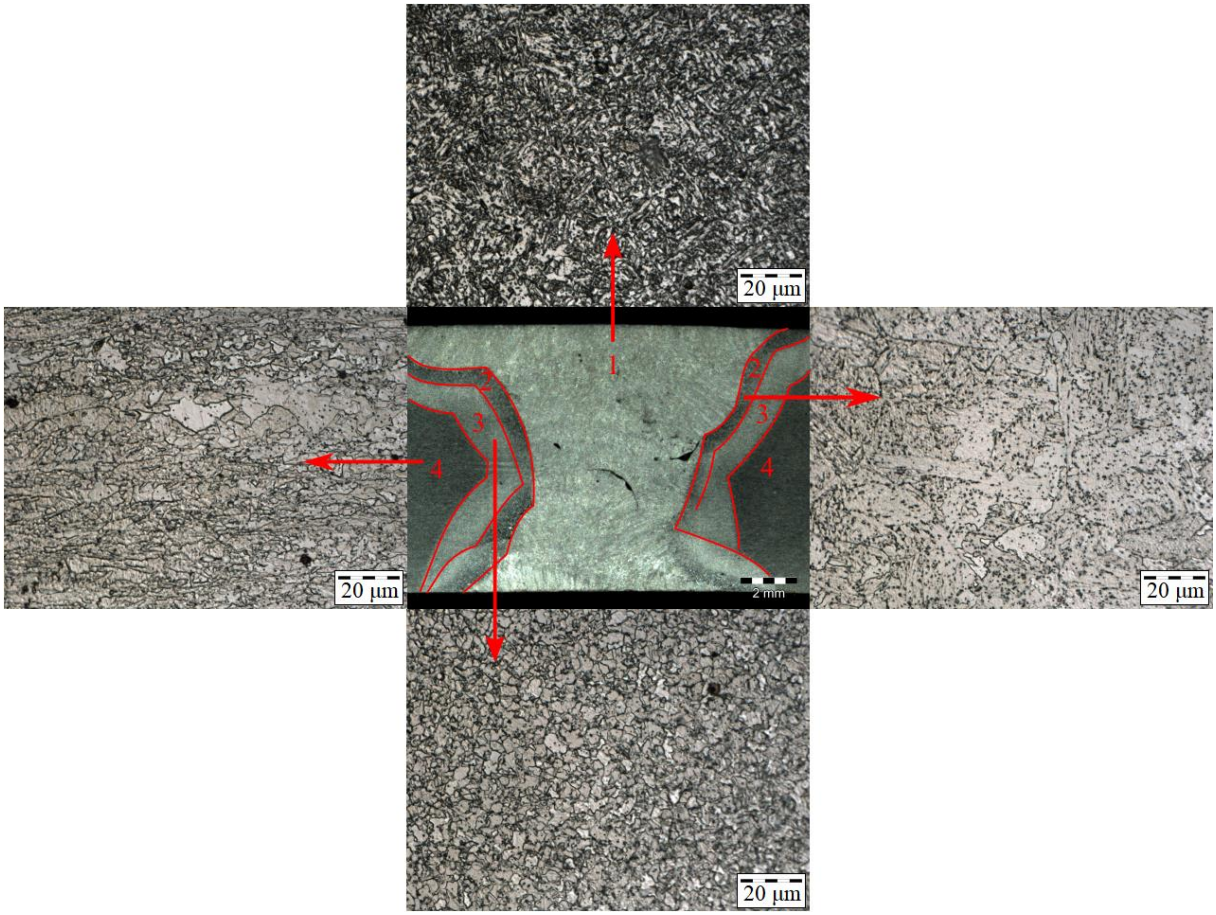

Figure 8.4 The cross-sectional macro photo and microstructures of Strenx 700MC weld joints, 1) welding pool, 2) grain coarsening zone, 3) grain refinement zone and 4) base metal

The structural evaluation was also conducted with scanning electron microscopy as shown in Figure 8.5. The microstructure of uninfluenced metal consisted of a fine-grained polygonal ferrite with a limited amount of pearlite. An increased heat input resulted in a broader coarse-grained zone. Primary grain morphology (Figure 8.5a) was not completely polygonal and effect of deformation during rolling was essentially maintained. The same effect was the reason for the lamellar morphology of fracture response during mechanical testing. The secondary phases dissolution was found as the most effective degradation process. It was followed by reprecipitation which led to the creation of reduced count and increased size mainly carbides (Figure 8.5c), hence the final effect in terms of mechanical behavior was measured as a significant decrease of hardness. An increased heat input in the zone adjacent to the fusion line resulted in a broader coarse-grained zone (Figure 8.5b).

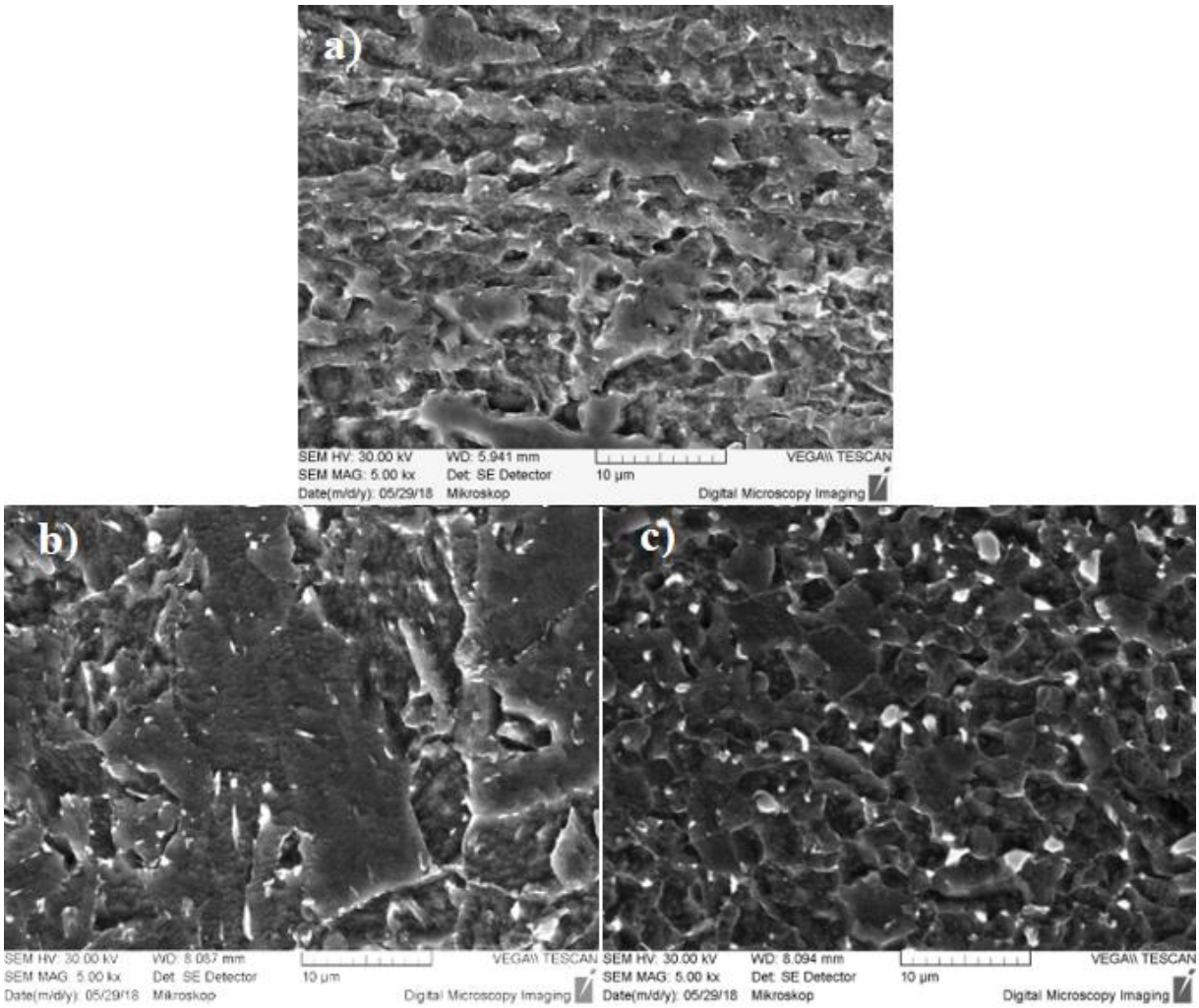

Figure 8.5 a) Uninfluenced steel, b) Fusion zone and c) Over A_3 of welded Strenx 700MC steel

8.2.2. Hardness Test Result of Welded Strenx 700MC

Hardness testing is an essential part of the evaluation of the welded specimen. The local differences in hardness have shown the weakest point of welding influence on the used type of high strength steel. Identification of the most degraded sublayer has provided information about the critical temperature level for the design of the weld thermal cycle simulation.

In order to achieve Vickers hardness values in HV1 scale, the measurements were conducted with 0.2 mm interval from the left side to the right side of the welded specimen. The exact positions and hardness values of the welded specimen are shown in Figure 8.6. Hardness values vs. distance from weld center is also plotted in Figure 8.7. The hardness value of the received base metal was approximately 295 HV1. In the region of the grain refinement zone, the hardness values varied from 245 HV1 to 266 HV1. Some sharp peaks were observed in the

region between grain refinement and grain coarsening zone. The reason of high hardness value could be heterogeneity of the heat affected zone or small inclusions. The hardness measurement indicated that the lowest value in the sublayer of the outer part of the grain refinement zone (236 HV1). This result seemed to be in contradiction with generally known grain refining effect. Based on detail microstructure evaluation, it could be concluded that it was a result of partially austenitization process, together with lost both of primary strengthening processes – dislocation hardening and precipitation hardening. The latter one was more effective hence the reprecipitation of carbides has led to a substantial decrease of hardness. This value (236 HV1) had great importance because parameters of the weld thermal cycle simulation (maximum temperatures, heating and cooling time) were specified according to lowest hardness value. In the region of grain coarsening was very narrow and the hardness values were changing from 259 HV1 to 272 HV1. Common effect of grain coarsening – i.e. the decreasing of hardness, was overcome by partial transformation to acicular ferrite and bainite. The welding pool had almost stable hardness value which was approximately 258 HV1. As a result, the analysis of the measurement of hardness test showed that Strenx 700MC was strongly influenced by metal active gas welding method. With choosing optimum welding parameters and method, variation of the hardness values can be decreased.

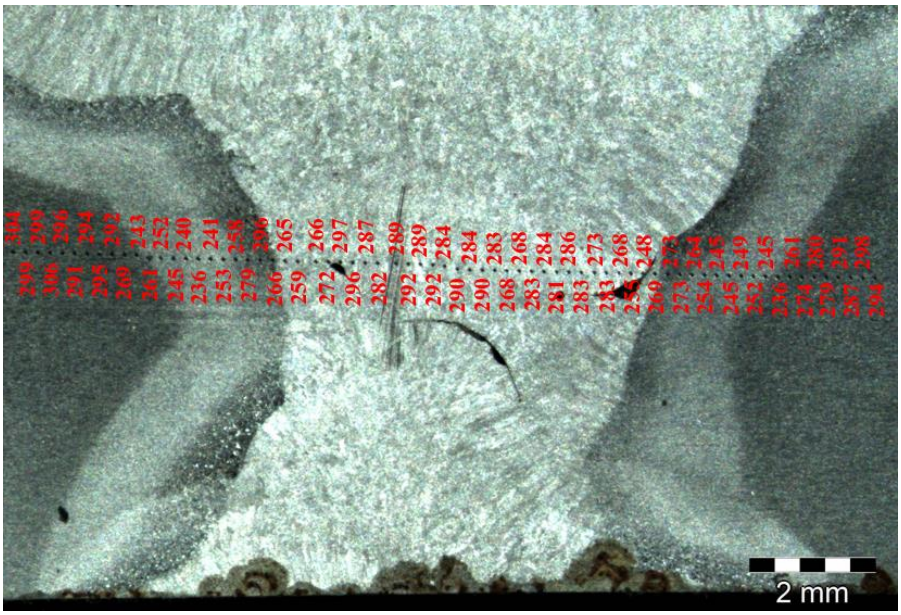

Figure 8.6 HV1 hardness survey across the cross-section of the welded Strenx 700MC

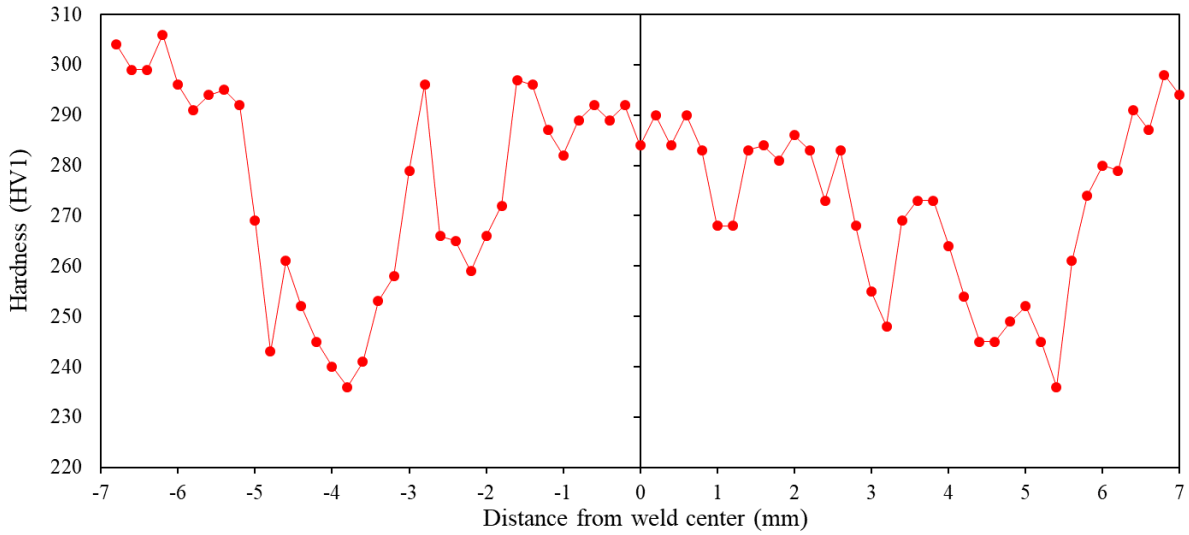

Figure 8.7 HV1 hardness vs. distance from weld center for welded Strenx 700MC specimen

8.3. Simulation of Welding Degradation Process

Simulation of degradation process was designed based on analyses of experimental welding process influence. During the thermal cycle simulation, the specimen was rapidly heated to a maximum temperature of 800°C and held at this temperature for 5 seconds, the temperature was recorded as a function of time as shown in Figure 8.8. For validation of the used simulation, the thermal cycle influence was evaluated by metallography analyses and hardness measurement.

After completion of the thermal cycle, the sample for metallographic examination was prepared from circumferential notched round bar specimen. The microstructure of the sample which was subjected to thermal cycle simulation is shown in Figure 8.9a. In the microstructure, side plate ferrite which is also called Widmanstatten ferrite was formed. The reason of forming this kind of phase was side plate ferrite can grow faster because of carbon, instead of piling up at the planar growth front, it was pushed to the sides of the growing tips. In the microstructure, acicular ferrite was also formed because at lower temperatures it was too slow for Widmanstatten ferrite to grow into the grain interior. The acicular ferrite is desirable because it improves toughness of the metal. The interlocking nature of acicular ferrite and with its fine grain size, provides the maximum resistance to crack propagation. Based on results of metallography evaluation of the real welding influence, the carbide reprecipitation process was found out as the most effective degradation process. In terms of that, the dissolution and recreation of carbides was also important validation of performed simulation process. As shown

in Figure 8.9b, coarsening of the primary carbides was induced. This observation was in required accordance with the previous structural analyses results of real welding joints. The initiation of microcracks along the localized coarsened carbides during mechanical testing was also visible.

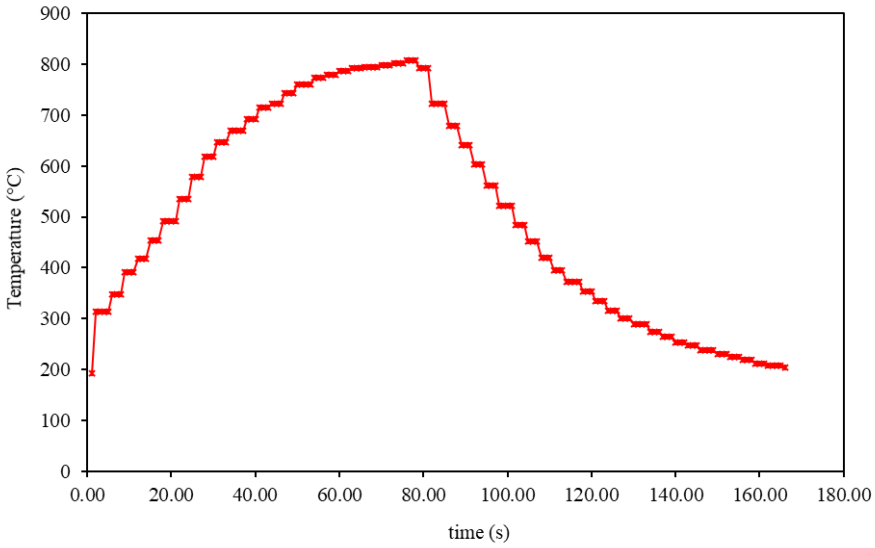

Figure 8.8 Weld thermal cycle profile for Strenx 700MC specimen

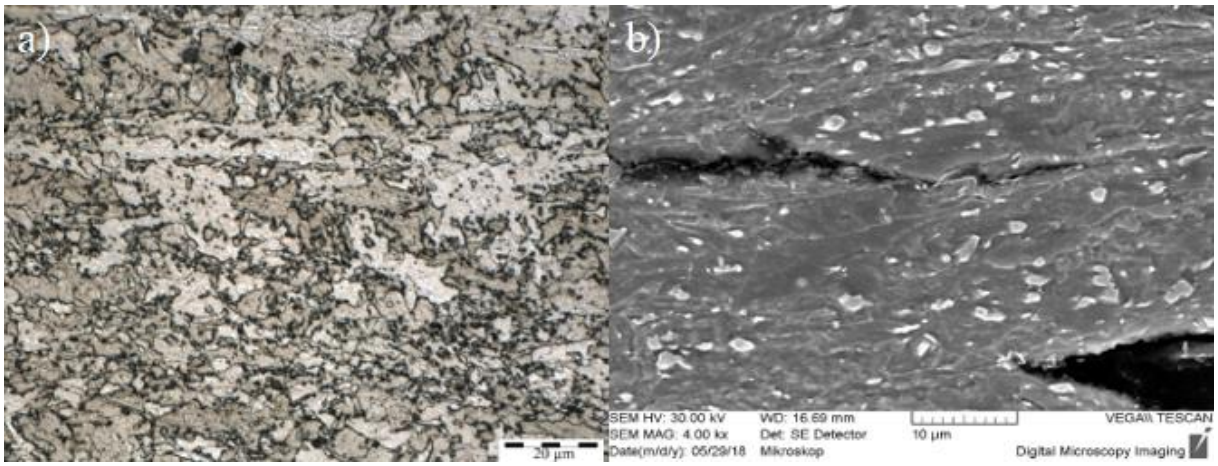

Figure 8.9 a) Microstructure and b) SEM image of Strenx 700MC specimen subjected to thermal cycle simulation

Hardness measurements were also performed on the sample which was subjected to weld thermal cycle simulation. The studied sample was extracted from the longitudinal axis of the circumferentially round bar specimen. As it can be seen in Figure 8.10, the hardness measurements started from notch tip and continued to the other notch tip with 0.25 mm interval.

Macro photo of the measured sample documented the values in exact positions. Almost stabile values in all cross section presented very important result in terms of simulation. It enabled to evaluate the change of fracture behaviour using both parameters – the fracture toughness and also the crack propagation resistance. Figure 8.11 shows the hardness vs. distance from notch to notch of the Strenx 700MC specimen subjected thermal cycle simulation. The hardness values of this specimen varied from 216 HV1 to 233 HV1 and mean value was approximately 225 HV1. As mentioned above, the main aim was approaching the lowest value (236 HV1) which was observed in the real welding sample of Strenx 700MC. In this way, it was possible to make an appropriate evaluation between real welding method and weld thermal cycle simulation.

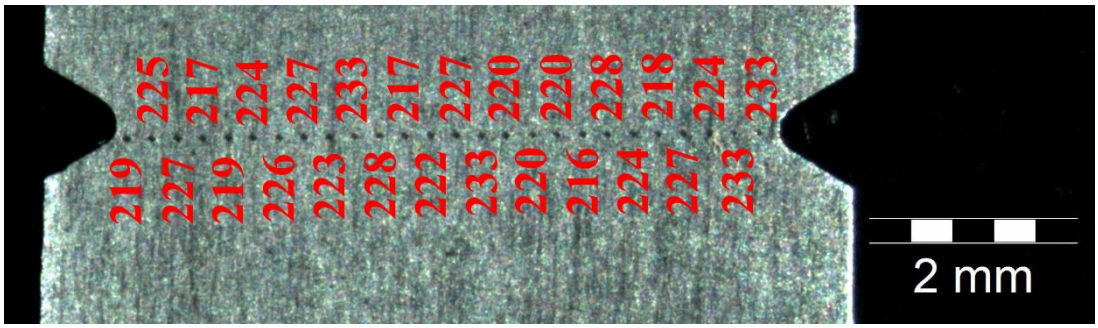

Figure 8.10 HV1 hardness survey across the cross-section of the Strenx 700MC specimen subjected to weld thermal cycle simulation

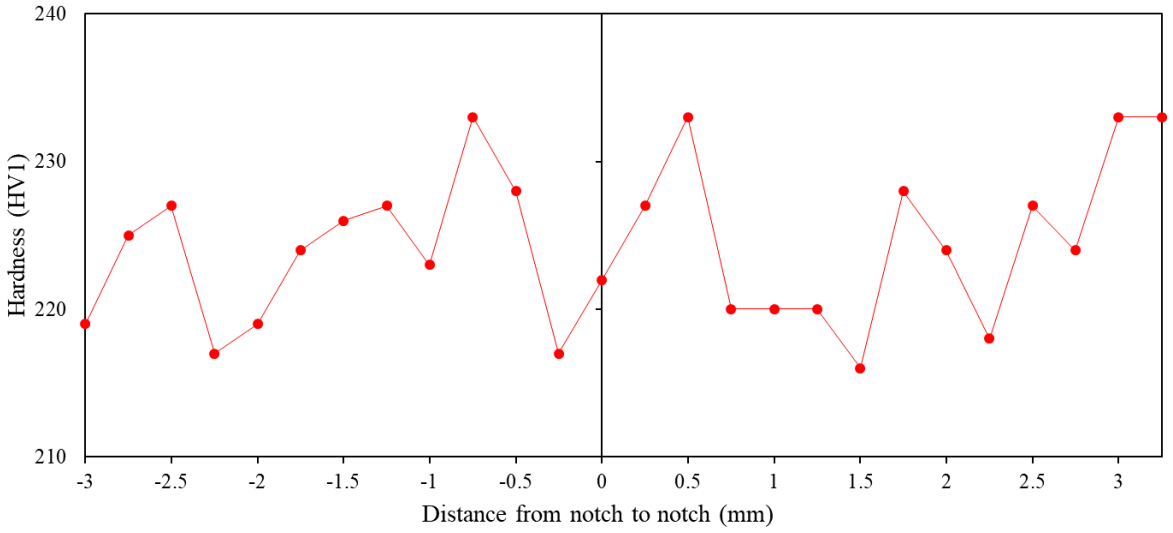

Figure 8.11 HV1 hardness vs. distance from notch to notch of Strenx 700MC specimen subjected to weld thermal cycle simulation

8.4. Result of CNRB Test Method

The materials inspected in this methodology were S355 and Strenx 700MC steels whose mechanical properties and chemical compositions are given in Chapter 7. Each sample were tested at least three times. The maximum load, diameters of unnotched and notched sections, notch tensile strength and fracture toughness values which were calculated with three proposed equations are given in Table 8.1. In the table, S355 and Strenx 700MC steel specimens were denoted as SNCRB and StxCNRB, respectively.

Table 8.1 Fracture toughness (K_{IC}) and notch tensile strength values of the tested steels

Sample No	P_f (N)	D (mm)	d (mm)	σ_{NTS} (MPa)	K_{IC} (MPa√m) Equation 7.10	K_{IC} (MPa√m) Equation 7.12	K_{IC} (MPa√m) Equation 7.13	NSR
SCNRB-01	58190	11.56	9.58	807.29	39.41	37.71	35.85	1.47
SCNRB-02	59880	11.69	9.64	820.42	40.27	38.65	36.63	1.49
SCNRB-03	58710	11.66	9.68	797.76	39.11	37.39	35.58	1.45
StxCNRB-01	47440	8.71	6.68	1353.64	57.35	56.77	52.17	1.98
StxCNRB-02	47240	8.84	6.78	1308.46	55.85	55.28	50.81	1.92
StxCNRB-03	50500	8.96	6.94	1335.00	57.37	56.60	52.19	1.95

* (P_f) fracture load, (D) diameter of unnotched section, (d) diameter of notched section, (σ_{NTS}) notch tensile strength, (K_{IC}) fracture toughness, (NSR) notch strength ratio.

The notch tensile strength of the tested specimens was defined as the maximum load divided by the original cross-sectional area at the notch. The relationship between the notch tensile strength and the fracture toughness of the S355 and Strenx 700MC steels was plotted in Figure 8.12. It could be seen that because of the fracture toughness values were calculated by the fracture load of the notched specimen, an increase in fracture load was resulted with the increase in fracture toughness. The calculated fracture toughness values with Equation 7.12 were found to be in close agreement with those of Equation 7.10 and Equation 7.13. The fracture toughness values of Strenx 700MC steel were higher than those of S355 steel because of having a fine microstructure of Strenx 700MC. Bayram et al. concluded that fine grain microstructure gives better resistance to crack propagation and higher strength to the materials [36]. The obtained results with respect to microstructure were consistent with the work of Bayram et al.

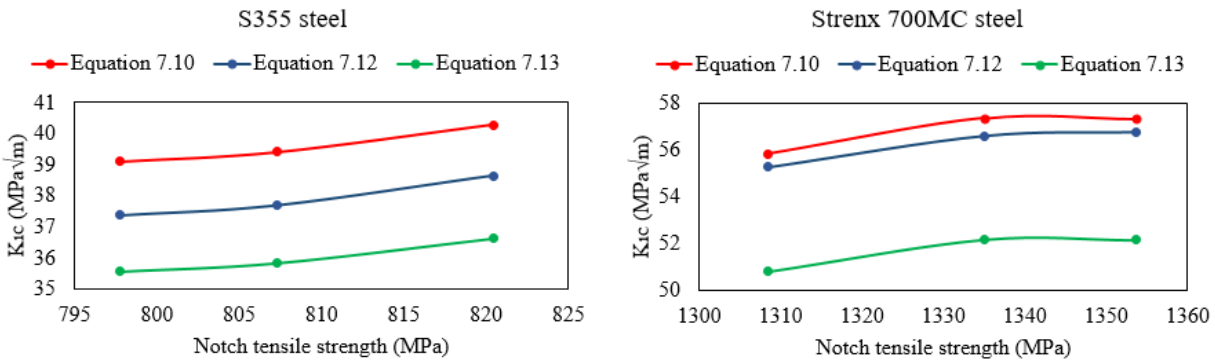

Figure 8.12 The relationship between the notch tensile strength and the fracture toughness values of S355 and Strenx 700MC steels calculated by three different equations

The tensile strength of notched specimens of both materials was higher than that of the unnotched specimen. This was caused by the constraint of plastic flow, because the material possessed ductility. At the notched sections, when the stress reaches the yield strength, the material in the reduced section tries to stretch plastically in the direction parallel to the loading direction. Concurrently, the material at the notch root attempts to contract but is constrained by the rest of the material, which is still encountering an elastic stress. The developed tensile stress which is in the other two principal directions makes it necessary to increase the axial stress to initiate plastic deformation [36]. Due to this reason, the higher tensile strength was seen in the notched specimen. The common way of detecting notch brittleness or high notch sensitivity was by determining the notch strength ratio (NSR). It was calculated as the ratio of notch tensile strength to the yield strength. If the NSR was less than 1, the material was considered to be notch brittle [59]. The NSR values of the tested materials are given in Table 8.1. Because the NSR values were higher than 1, the tested materials were considered to be notch insensitive.

8.5. Result of CCRB Test Method

The fatigue precracked specimens of S355, experimental high strength and Strenx 700MC steels were used as test materials to determine the fracture toughness values with using CCRB test methodology. K_{IC} of S355 steel was tested for two different unnotched (D) and notched (d) diameters with constant D/d ratio as 1.2 to investigate the effect of diameters on fracture toughness. Strenx 700MC steel was selected to observe the effect of heat input which was conducted by weld thermal cycle simulation on fracture toughness. In this methodology, the measurement of crack length has great importance for calculation procedures. The figure of the cross-sectional and side view of the fractured all samples are given in Appendix B. While calculating the length of the fatigue precrack (a_f), at least 16 measurements were performed on

the fractured surface of the samples and mean value was considered for each tested steel. The measured of crack lengths, fracture load, diameter of the tested specimen and the fracture toughness values which were calculated using Equation 7.2 were tabulated as shown in Table 8.2. During the calculation process, the eccentricity of the ligament did not take into consideration. In the table, the marking of S355 steel, experimental high strength steel, Strenx 700MC steel specimen and Strenx 700MC specimen which was subjected to weld thermal simulation were denoted as SCCRB, ECCRB, StxCCRB and StxWSCCRB, respectively.

When the results of the fracture toughness values were evaluated for S355 steel, it can be seen from the data in Table 8.2, the diameter of the unnotched and notched sections had a significant effect on fracture toughness even if (D/d) ratio was kept constant as 1.2. For higher diameter, the fracture toughness of S355 steel varied from 35.78 MPa√m to 40.44 MPa√m and for lower diameter it varied from 51.01 MPa√m to 54.92 MPa√m. These results showed that as the unnotched diameter along with notch diameter increased, the fracture toughness values decreased. As mentioned before, the specimen thickness had a significant amount of effect on the fracture toughness value.

Table 8.2 Fracture toughness values (K_{IC}) of the tested materials

Sample No	P_f (N)	D (mm)	a_m (mm)	a_f (mm)	d_{eff} (mm)	d_{eff}/D	K_{IC} (MPa√m)
SCCRB-01	51433	11.72	0.99	0.18	9.36	0.80	35.78
SCCRB-02	47644	11.80	0.98	0.50	8.84	0.75	38.13
SCCRB-03	46603	11.85	0.99	0.67	8.53	0.72	40.44
SCCRB-04	27284	7.77	0.76	0.50	5.24	0.67	51.01
SCCRB-05	24250	7.89	0.72	0.75	4.93	0.63	51.23
SCCRB-06	17957	8.05	0.75	1.28	3.98	0.49	54.92
ECCRB-01	20028	7.79	0.71	0.47	5.45	0.70	34.62
ECCRB-02	19931	7.72	0.71	0.45	5.40	0.70	34.94
ECCRB-03	22147	8.28	0.77	0.42	5.90	0.71	33.62
StxCCRB-01	28744	7.70	0.70	0.64	5.02	0.65	58.21
StxCCRB-02	31953	7.65	0.69	0.47	5.32	0.70	57.46
StxCCRB-03	32243	7.61	0.69	0.38	5.47	0.72	54.54
StxWSCCRB-01	34183	7.67	0.73	0.21	5.78	0.75	51.52
StxWSCCRB-02	24784	6.98	0.74	0.35	4.80	0.69	52.32
StxWSCCRB-03	24972	7.26	0.73	0.43	4.94	0.68	50.78

* (P_f) fracture load, (D) diameter of unnotched section, (a_m) machined notch depth, (a_f) length of fatigue precrack, (d_{eff}) effective diameter, (K_{IC}) fracture toughness

The fracture toughness of Strenx 700MC steel were found to be highest value with using CCRB test methodology. It was expected result because it had fine grain microstructure and gave better resistance to crack propagation due to higher grain boundary area per unit volume. In the microstructure, grain boundary acted as a barrier to the crack growth mechanism. The fracture toughness of received Strenx 700MC steel specimen was found to be slightly higher than that of the specimen which was exposed to weld thermal cycle simulation. K_{IC} value was found to be in a range of 54.54 MPa√m to 58.21 MPa√m for received Strenx 700MC steel whereas it varied from 50.78 MPa√m to 52.32 MPa√m for same material after weld thermal cycle simulation. This difference can be explained on the basis of microstructures. The microstructure of Strenx 700MC specimen subjected to thermal cycle simulation was a combination of acicular and Widmanstatten ferrite whose grain size was slightly larger than that of heat untreated steel. The suppression of the heterogeneity after weld simulation process can be a second reason for decreasing in K_{IC} value.

The lowest fracture toughness value was obtained for experimental high strength steel. It did not exhibit a significant amount of plasticity. As the experimental steel had lowest K_{IC} value, it displayed completely brittle cleavage cracking. The mean value of fracture toughness was obtained as 34.39 MPa√m for experimental high strength steel.

In order to compare the fracture behavior of all tested materials, the macro photos of the fractured surface are shown in Figure 8.13. Generally, the length of fatigue precrack (from notch tip to unstable region) was almost equal in circumferentially for S355 steel but the eccentricity was observed in some samples. The possible reasons of eccentricity could be surface quality of the notch and mainly internal heterogeneity of tested steels. That was the case of Strenx 700MC steel in uninfluenced stage (Figure 8.13c). According to Neelakantha et al., the eccentricity may start during pre-cracking or at the time of tensile loading [39]. The side view of the fractured S355 specimen was nearly flat but in the outer side of the surface was seen 45° shear lips in Figure 8.14a. This angle represents the direction of maximum shear stress that causes shear lip final stage. Strenx 700MC steel exhibited unusual fatigue precracking pattern and this behavior was related with material heterogeneities which were formed during the thermo-mechanical control processing. There were very sharp macro hills were existed in the side view of the fractured specimens as shown in Figure 8.14c. It was the natural form of forming effect for Strenx 700MC steel. But after weld thermal cycle simulation, not only fatigue precracking pattern but also side view of the fractured specimen was completely changed. The sharp macro hills did not existed in the specimen and the length of fatigue precracking was nearly equal in the circumferential direction. The annealing process was activated by applying the weld thermal cycle and it eliminated the negative effect of heterogeneous carbide distribution. Figure 8.13b shows the top view of the fractured experimental high strength steel. In comparison to other materials, the region of stable crack propagation was too hard to identify in macro scale, but it was observed by detail fractographic analyses. Brittle fracture was observed as a dominant failure mechanism because of shiny appearance. As in S355 steel, experimental high strength steel had also almost flat fractured surface for all tested specimens.

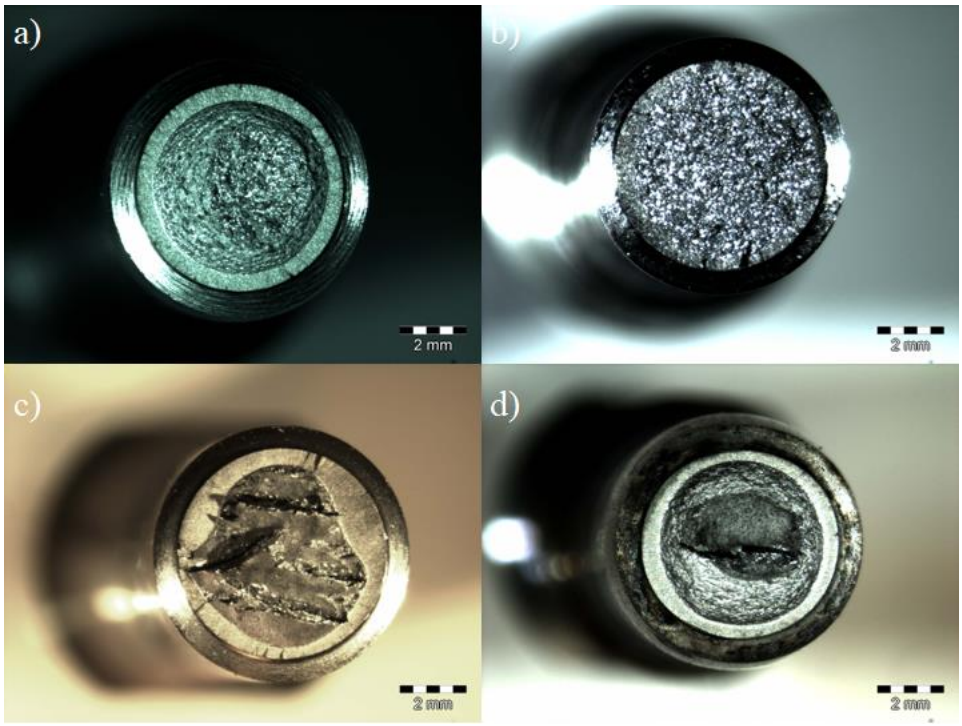

Figure 8.13 Sectional view of fractured tested specimens a) S355 steel, b) Experimental high strength steel, c) Strenx 700MC steel, d) Strenx 700MC steel exposed to weld thermal cycle simulation

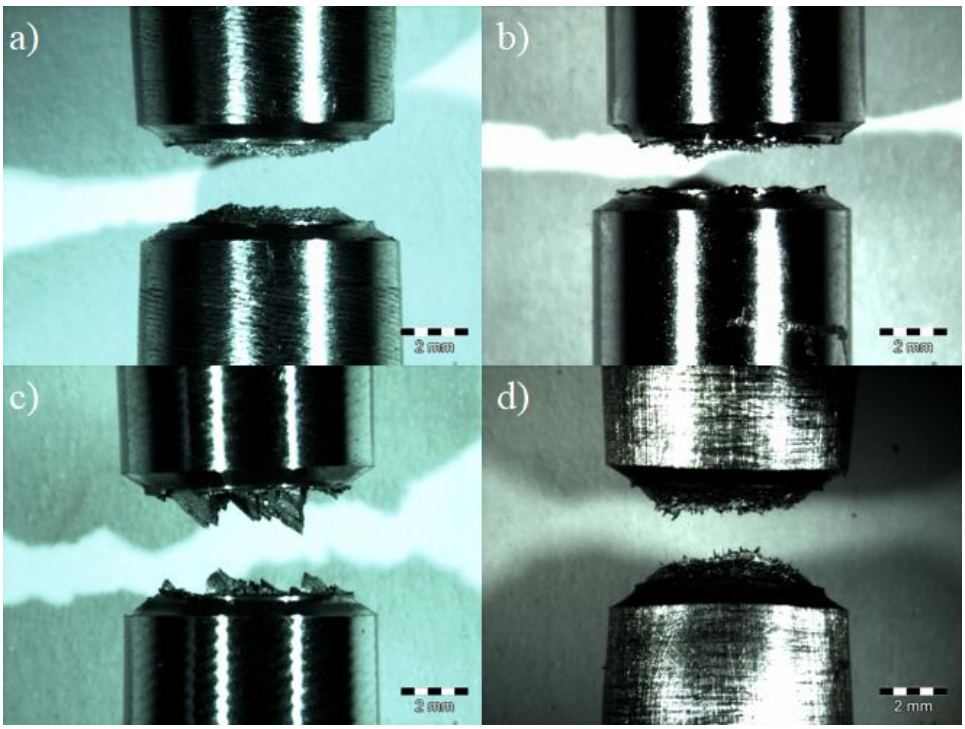

Figure 8.14 Side view of the fractured specimens a) S355 steel, b) Experimental high strength steel, c) Strenx 700MC steel, d) Strenx 700MC steel exposed to weld thermal cycle simulation

This study showed a correlation between d_{eff}/D ratio and K_{IC} value. It can be clearly seen in Figure 8.15, as the d_{eff}/D ratio increased, the fracture toughness value decreased. These observations were in agreement with the study of Neelakantha et al. [39]. In that study, the valid range of Equation 7.2 was $0.46<(d_{eff}/D)<0.86$. This wide interval caused variations for calculation of fracture toughness values with using CCRB test methodology. In order to prevent the variations in fracture toughness value, this proposed interval limit can be reduced to lower values.

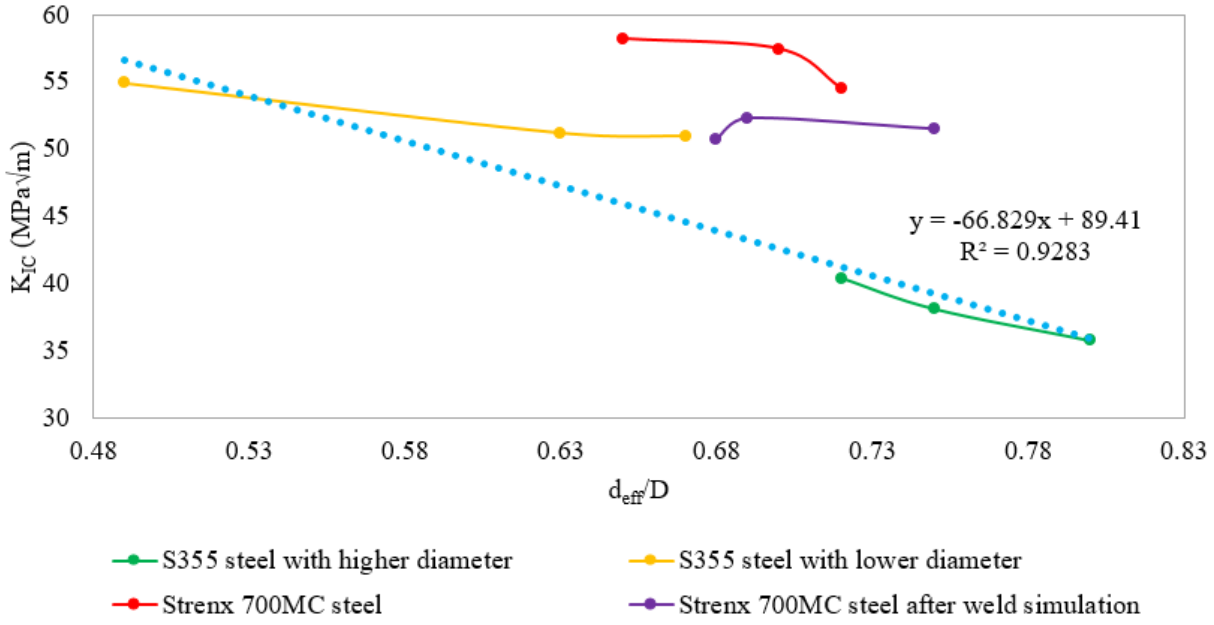

Figure 8.15 Correlation between d_{eff}/D and K_{IC} value

Based on the calculation of fracture toughness of tested steels, CCRB test method vs. CNRB test method gave acceptable results and the difference between two different proposed methods were very close to each other. According to Nath and Das, the fracture toughness value of medium carbon steel was found to be 50 MPa√m, low carbon steel was found to be 25 MPa√m in the literature [37]. It was also reported that plane strain fracture toughness values of low carbon steels were in the range of 41 MPa√m to 82 MPa√m [60]. The used comparison was too general and it was necessary to accept the effect of notch sharpness, the constraint factor as a substance of the fracture mechanics approach. The reasons of the high difference value of K_{IC} depend on the production method and the heat treatment process. Bozkurt and Schmidová reported that as the notch angle increased, the value of the fracture toughness increased [61]. The similar tendency of increasing K_{IC} value as the notch increases was observed by Bayram et al. [36]. The reason of this observation was attributable to as the notch angle decreases, the

triaxiality of stresses at the notch root increased and plastic deformation was increasingly suppressed. In this study, the obtained values were in the range of K_{IC} values reported in the literature.

8.6. Result of Fatigue Crack Growth Test

Fatigue crack growth tests were conducted at room temperature with using R. R. Moore rotating bending fatigue machine. All specimens were allowed to rotate under three different suitable bending loading till failure. During fatigue crack growth test, the value of stress ratio (R_{stress}) was kept constant as -1 (minus one) in order to get steady crack propagation. One advantage of the keeping R_{stress}=-1, it gives rise to more severe state of stress condition. In order to calculate the K_{min} and K_{max}, initial fatigue precrack (a_i) and average steady crack length (a_s) were measured at least four points in the circumferential direction as shown in Figure 8.16 and mean values were calculated. In figures and in tables, the marking of S355 steel and Strenx 700MC steel were denoted as S-FCGR and Stx-FCGR, respectively. Using a set of equations (from Equation 7.5 to 7.9) which were proposed by Neelakantha et al., the stress intensity factors K_{min} and K_{max} were calculated and tabulated in Table 8.3 and Table 8.4 [39]. The difference between stress intensity factors (K_{min} and K_{max}) gives the ΔK values which are given in Table 8.5 for S355 steel and Strenx 700MC steel. Graph of da/dN versus ΔK is plotted for S355 steel and Strenx 700MC steel in Figure 8.17 and in Figure 8.18, respectively.

It can be clearly seen that as the da/dN increases, ΔK value also increases for both steels as shown Figure 8.17 and Figure 8.18. In the Paris law regime, the linear part of each fatigue crack growth rate data was fitted to best fit line (curve) in MS Office Excel software and exponential equations were obtained with regression values (R^2). If one can characterize the crack growth in Paris law regime, it is possible to estimate the service life or inspection intervals required under specific loading conditions and service environment. Stable crack propagation equations were specified for S355 steel as $da/dN=4x10^{-9}\Delta K^{0,888}$ with $R^2 = 0.9659$ and for Strenx 700MC steel as $da/dN=3x10^{-17}\Delta K^{6,467}$ with $R^2 = 0.9743$. It can be deducted that the crack growth rate is higher for higher applied stresses. The range of ΔK value was smaller for Strenx 700MC steel compared to S355 steel because of during the fatigue crack growth test, the applied moment was varied from 3.4335 Nm to 3.924 Nm. In order to achieve wider ΔK value ranges, the applied moments can be started from the small values and it can be gradually increased.

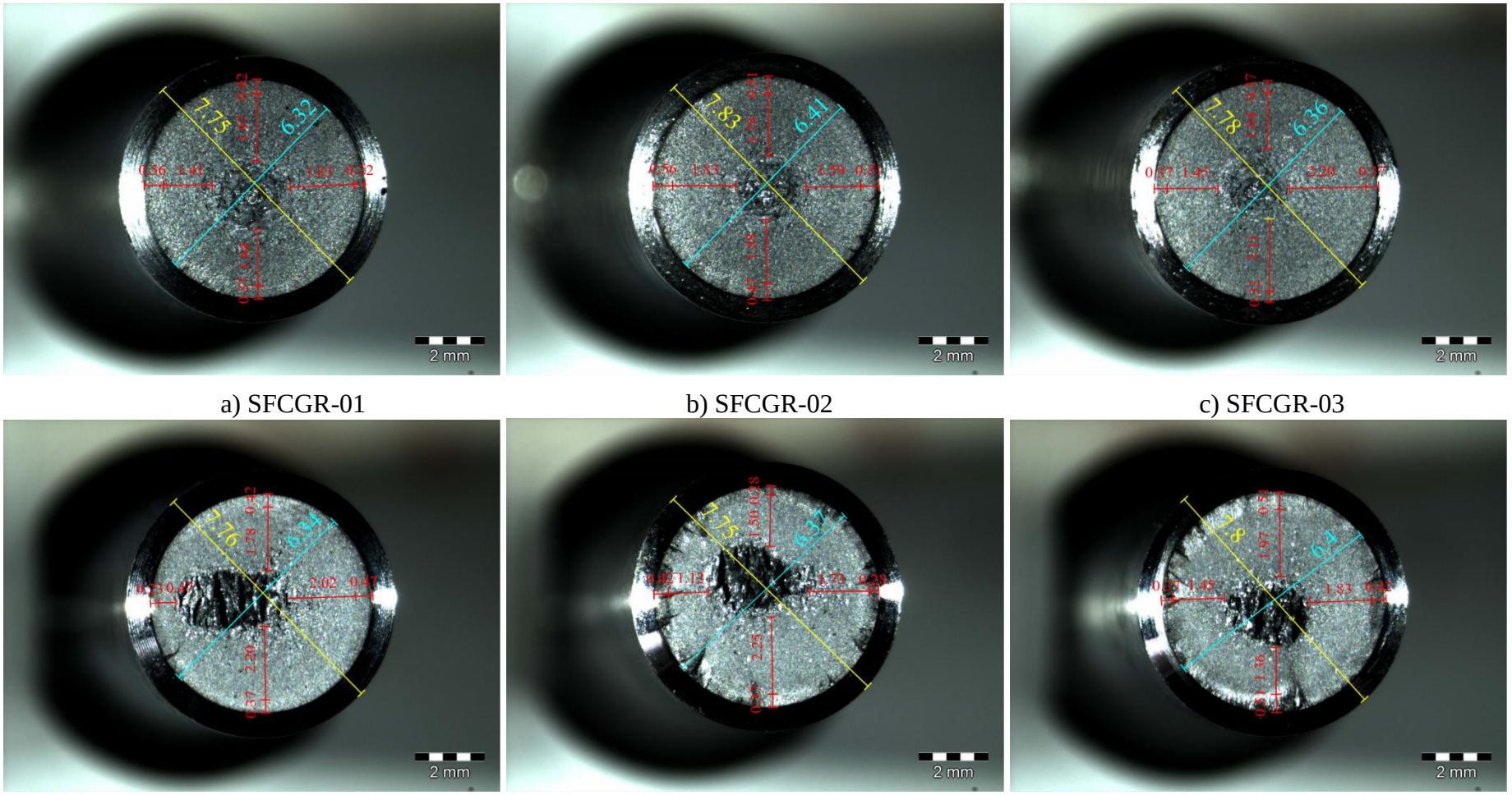

a) SFCGR-01 b) SFCGR-02 c) SFCGR-03

d) StxFCGR-01 e) StxFCGR-02 f) StxFCGR-03

Figure 8.16 Sectional view of the fractured specimens for calculation of fatigue crack growth rate

Table 8.3 Calculated K_{min} values for fatigue crack growth rate

Sample No	R (m)	r (m)	a_i (m)	r-a_i (m)	α (r-a_i)/R	G(r/R)	F(r/R)	Moment (Nm)	σ_B (MPa)	K_{min} (MPa√m)
SFCGR-01	0.003875	0.00316	0.00042	0.00274	0.7071	0.68015	0.3681024	2.943	182.158	6.22
SFCGR-02	0.003915	0.00320	0.00051	0.00269	0.6871	0.66193	0.3702661	1.962	128.337	4.37
SFCGR-03	0.003890	0.00318	0.00036	0.00282	0.72494	0.69811	0.3661358	0.981	55.697	1.92
StxFCGR-01	0.003880	0.00317	0.00037	0.0028	0.72165	0.69481	0.366573	3.924	227.596	7.82
St-FCGR-02	0.003875	0.003185	0.00034	0.002845	0.73419	0.7076	0.3648109	3.67875	203.406	7.02
StxFCGR-03	0.003900	0.0032	0.00045	0.00275	0.70513	0.67867	0.3685312	3.4335	210.208	7.20

Table 8.4 Calculated K_{max} values for fatigue crack growth rate

Sample No	R (m)	r (m)	a_s (m)	r-a_s (m)	α (r-a_s)/R	G(r/R)	F(r/R)	Moment (Nm)	σ_B (MPa)	K_{max} (MPa√m)
SFCGR-01	0.003875	0.00316	0.00171	0.00145	0.37419	0.47446	0.3753378	2.943	1229.13	31.14
SFCGR-02	0.003915	0.0032	0.00177	0.00143	0.36526	0.47108	0.3753107	1.962	854.282	21.49
SFCGR-03	0.00389	0.00318	0.00185	0.00133	0.3419	0.46256	0.375244	0.981	530.914	12.88
StxFCGR-01	0.00388	0.00317	0.00162	0.00155	0.39948	0.48445	0.3754175	3.924	1341.66	35.15
StxFCGR-02	0.003875	0.003185	0.00165	0.001535	0.39613	0.48309	0.3754068	3.67875	1295.05	33.76
StxFCGR-03	0.0039	0.0032	0.00165	0.00155	0.39744	0.48362	0.375411	3.4335	1173.96	30.75

Table 8.5 Fatigue crack growth rate for S355 and Strenx 700MC steel

Sample No	ΔK (MPa√m)	N_f (Cycle)	da/dN (m/cycle)
SFCGR-01	10.96	49700	3.72E-08
SFCGR-02	17.12	35900	4.93E-08
SFCGR-03	24.92	22000	7.77E-08
StxFCGR-01	23.55	62400	2.64E-08
StxFCGR-02	26.75	30400	5.43E-08
StxFCGR-03	27.32	22000	7.36E-08

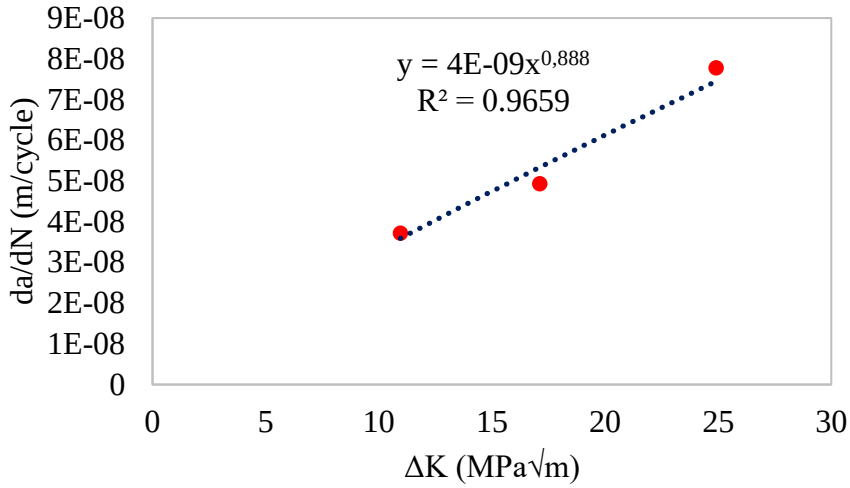

Figure 8.17 da/dN vs. ΔK plot for S355 steel

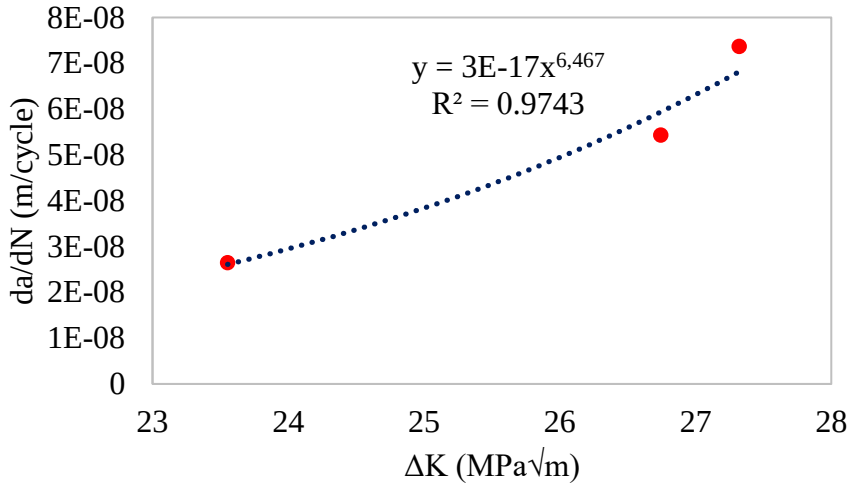

Figure 8.18 da/dN vs. ΔK plot for Strenx 700MC steel

In Region II (Paris law region), the crack growth occurs when the Stage I changes the direction and the crack path is perpendicular to the applied stress direction. On a microscopic scale, the most characteristic patterns are striations which are occurred during Region II crack growth and with each striation representing one cycle of fatigue. Striations can only be seen as suitable magnifications. In Figure 8.19, the accelerated crack growth near to final crack propagation was documented in this case.

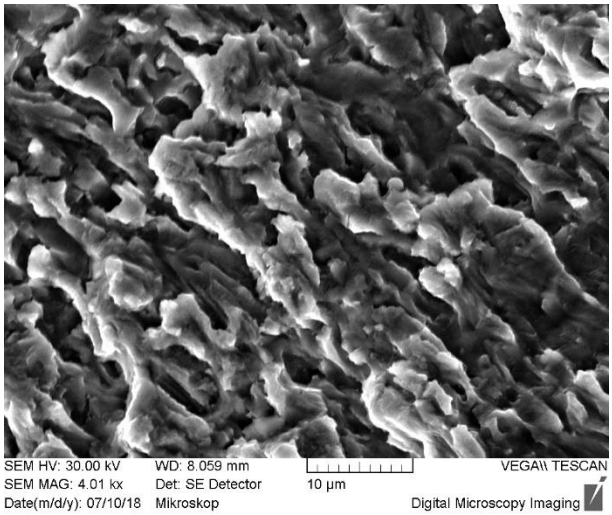

Figure 8.19 SEM image of showing fatigue striations

The crack growth rate is affected by several parameters. Generally, these parameters divided into two categories: intrinsic and extrinsic factors. The intrinsic factors are e.g. mechanical properties of materials, microstructure and grain size as shown in Figure 8.20 and the extrinsic factors are e.g. environmental effects and the loading system [62].

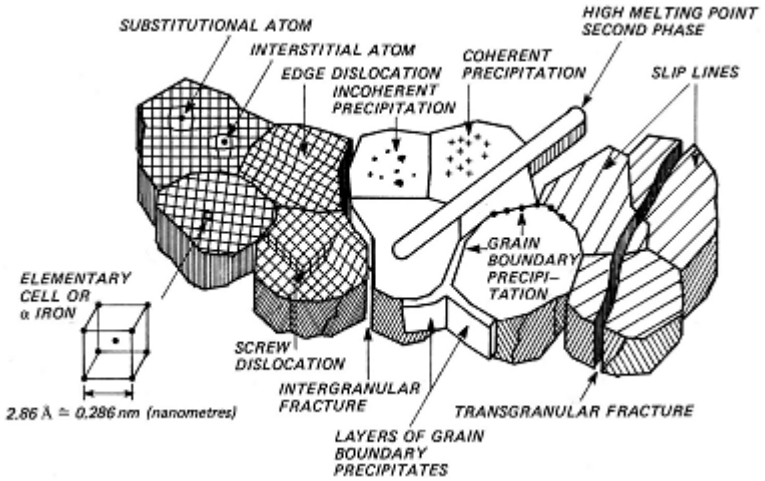

Figure 8.20 The intrinsic factors are mechanical properties of materials [62]

8.7. Result of Dynamic Fracture Toughness with Nonstandardized Test Methods

The impact tensile tests were performed using circumferentially cracked round bar specimens after the fatigue precracking procedure to obtain the value of dynamic fracture toughness, K_{Id}. Three different kinds of steels S355, Strenx 700MC and experimental high strength, were examined at room temperature using instrumented impact testing machine Zwick/Roell RKP 450 equipped with a personal computer. For S355 and Strenx 700MC steels, the impact tensile tests were performed with two different pendulum speeds 5.23 m/s and 3.48 m/s to investigate the effect of loading rate on dynamic fracture toughness value. The difference in loading conditions can be expressed only as a difference in speed of the pendulum. In order to evaluate the heat effect on dynamic fracture toughness, Strenx 700MC steel specimens exposed to weld thermal cycle simulation were tested with 5.23 m/s pendulum speed. For calculating the dynamic fracture toughness value, the same procedures which were used also for determining plane strain fracture toughness (K_{IC}) were followed. Firstly, it was necessary to measure the defined dimensions with using stereomicroscope after conducting the impact tensile tests. The figure of the cross-sectional and side view of the fractured all samples are given in Appendix C. Secondly, another important parameter for determining the K_{Id} values was maximum dynamic force (P_{dmax}). Thanks to the instrumentation, dynamic force against displacement or time were recorded during the impact tensile test. Each data set was processed and filtered with testXpert testing software. Although all force – displacement data was filtered, the oscillation of the signal was still existed in the plot because of the inertia effect between the tail block and stiff anvil. The force – displacement graph of all tested steels is given in Appendix D. In order to specify the maximum value of P_{dmax}, considering the first peak of the filtered force – displacement curve was fitted by using "curve fitting tool" in MS Office Excel software as shown in Figure 8.21. Depending on the effective diameter (d_{eff}), unnotched section diameter (D) and maximum force (P_{dmax}) during the impact tensile test, dynamic fracture toughness (K_{Id}) was calculated using Equation 7.15 and all results are tabulated in Table 8.6. In figures (Appendix C) and in Table 8.6, the marking of S355 and Strenx 700MC steel for higher and lower speed impact tensile tests were denoted as "S355D", "S355LSD", "StxD" and "StxLSD" respectively and experimental high strength steel were denoted as "ED". Lastly, Strenx 700MC specimen which was subjected to weld thermal simulation was denoted as "StxWSD".

Table 8.6 Dynamic fracture toughness values of tested all steels

Sample No	P_{dmax} (N)	D (mm)	a_m (mm)	a_f (mm)	d_{eff} (mm)	d_{eff}/D	K_{Id} (MPa√m)
S355D-01	38012	7.65	0.72	0.625	4.96	0.65	78.56
S355D-02	38032	7.77	0.73	0.72	4.87	0.63	81.86
S355D-03	37988	7.57	0.745	0.49	5.1	0.67	74.00
S355D-04	36756	7.79	0.735	0.99	4.34	0.56	97.15
S355D-05	35649	7.59	0.785	0.63	4.76	0.63	79.39
S355D-06	35389	7.76	0.72	0.81	4.70	0.61	81.27
S355D-07	30446	7.80	0.715	1.26	3.85	0.49	97.88
S355D-08	34854	7.79	0.735	1.03	4.26	0.55	95.06
S355LSD-01	35879	8.13	0.765	0.81	4.98	0.61	75.27
S355LSD-02	33794	8.23	0.745	0.88	4.98	0.61	71.18
S355LSD-03	32284	8.19	0.78	1.00	4.63	0.57	77.21
StxD-01	41484	7.59	0.695	0.32	5.56	0.73	67.71
StxD-02	40534	7.78	0.66	0.38	5.70	0.73	63.65
StxD-04	43833	6.95	0.535	0.21	5.46	0.79	69.61
StxD-05	38764	7.84	0.725	0.49	5.42	0.69	68.09
StxD-08	43510	7.80	0.72	0.49	5.38	0.69	77.29
StxLSD-01	43676	7.62	0.69	0.20	5.84	0.77	63.97
StxLSD-02	41164	8.11	0.75	0.42	5.77	0.71	64.68
StxLSD-03	44534	8.11	0.73	0.25	6.15	0.76	60.86
StxWSD-01	36057	7.22	0.83	0.45	4.66	0.65	81.98
StxWSD-02	22769	7.74	0.805	1.68	2.77	0.36	118.24
StxWSD-03	32839	7.20	0.575	0.67	4.71	0.65	73.06
ED-01	30694	7.76	0.725	0.68	4.95	0.64	64.05
ED-02	31853	7.82	0.75	0.57	5.18	0.66	61.11
ED-03	33836	7.89	0.75	0.51	5.37	0.68	60.69

* (P_f) fracture load, (D) diameter of unnotched section, (a_m) machined notch depth, (a_f) length of fatigue precrack, (d_{eff}) effective diameter, (K_{Id}) dynamic fracture toughness.

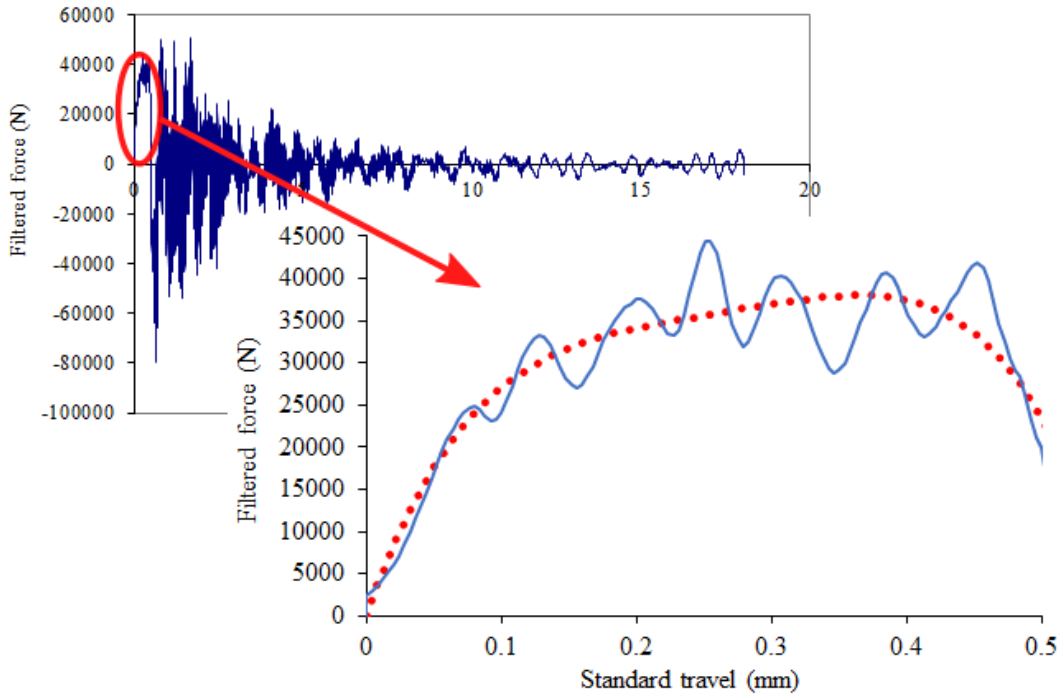

Figure 8.21 Curve fitted plot of force – displacement graph

For S355 steel, totally 8 specimens were tested at higher speed and 3 specimens were tested at lower speed in order to ensure reliability and repeatability of this test methodology. The first notable result was the plot of force – displacement curve had lots of vibrations during the impact event. But these vibrations did not existed when the impact tensile was conducted with lower speed (from FigureD1 to Figure D11, in Appendix D) and generally exhibited a smooth curve for considering the first peak. As can be seen from the table (above), the fracture toughness values varied between 74 MPa√m and 97.88 MPa√m. The first reason for this high interval could be during the impact tensile test, existing of large amplitudes in force – displacement graphs. It was mathematically evident that large vibrations were resulted with higher dynamic fracture toughness value for S355D-04, S355D-07 and S355D-08 specimens. The second reason for higher K_{Id} value was a correlation between d_{eff} and dynamic fracture toughness. It can be clearly seen from the table, as the d_{eff} decreased, K_{Id} value increased and the same behaviour was also seen while calculating the plane strain fracture toughness (K_{IC}) of S355 steel. The K_{Id} values of the rest samples were in range from 74 MPa√m to 81.86 MPa√m. A comparison of higher and lower speed impact tensile test revealed that S355 steel was typically sensitive to the loading rate. With the speed of pendulum decreased from 5.23 m/s to 3.48 m/s, the value of dynamic fracture toughness decreased approximately 12% for the calculated mean value. As the K_{Id} value was calculated with Equation 7.15, higher loading rate

did not allow time for stress redistribution and it was resulted with higher maximum dynamic force (P_{dmax}). Generally, by increasing strain rate, the yield strength and tensile strength of the steels increase. But this strain hardening process, some of the steels are strongly depended while some of the steels has less strain sensitivity. It depends on chemical composition, heat treatment, grain size of the materials and the test temperature. Macro photo of the fractured specimens had clearly exhibit two discrete regions for all tested materials from Figure C1 to C11 in Appendix C. It was visible that fatigue fracture region has macro beach marks while unstable fracture region had shiny appearance granular structure due to impact tensile test. The side view of all specimens was almost flat, and any macro groove or hill was not observed.

For Strenx 700MC steel, at higher pendulum speed totally 8 and at lower speed totally 3 of impact tensile test was conducted. During the fatigue precracking procedure, even though the same bending moment and number of cycle was applied to all specimen, StxD-03, StxD-06 and StxD-07 specimens were not fractured from the cross-sectional alignment of the notched section. Because of this reason, the dynamic fracture toughness values of the mentioned specimens could not be calculated. The side view of these specimens is shown in Figure C14, Figure C17 and Figure C18 in Appendix C. They had unique fracture appearance in terms of fracture mechanics. Half part of the specimen had one macro hill and the other part of the specimen had macro valley and tearing of the specimen was also observed. Considering force – displacement graphs which are given in Appendix D (Figure D3, Figure D6, Figure D7) gradual response is the supporting of the unique fracture appearance. The possible reason of this behavior, the material heterogeneity which was caused by the manufacturing process was more dominant than fatigue precracking. From the cross-sectional view of all fractured specimens (in Appendix C), length of fatigue precrack was not propagated equidistantly. As can be seen from the figures, the crack was not initiated in some points from machined notch tip and it was resulted with one side or nonhomogeneous crack propagation. The calculated dynamic fracture toughness for higher loading rate varied between 63.65 MPa√m and 77.29 MPa√m, and for lower loading rate in the range from 60.86 MPa√m to 64.68 MPa√m. Considering the calculated mean values, K_{Id} values of the lower loading rate decreased approximately 8% in comparison to a higher loading rate. These results showed that Strenx 700MC steel less sensitive than S355 steel. The response of the force – displacement graph was smoother, and less vibration was observed during the impact tensile test. After conducting the weld thermal cycle simulation, the value of the calculated dynamic fracture toughness increased

but ratio of d_{eff}/D was not in valid range which was suggested as $0.46<(d_{eff}/D)<0.86$ for only StxWSD-02 specimen. One interesting finding was the length of fatigue precrack was propagated almost in equidistantly and the crack was initiated along every point of the circumferential machined notch tip. After weld thermal cycle simulation process, almost flat surface was observed instead of the macro hill and valley. With heat supplying to the specimens, they have gained resistance to crack propagation and it exhibited higher dynamic fracture toughness value in comparison to the non-heat-treated specimens.

The experimental high strength steel specimens were tested only at 5.23 m/s pendulum speed. The lowest value was obtained for dynamic fracture toughness K_{Id} value as well as for the plane strain fracture toughness K_{IC} value. Taking into account with the mean value of K_{Id} was higher approximately 44% that of K_{IC}. This percentage value was 38% for S355 steel and 18% for Strenx 700MC steel. It was apparent that the experimental high strength steel was the most sensitive for the loading rate among the examined all specimen. The characteristic of force – displacement graph had very sharp peak, but less oscillation was observed for the first peak. The cross-sectional view of the fractured specimens had shiny appearance which was the proof of brittle fracture mechanism and the side view was completely flat. These findings were supported by having the lowest value of experimental high strength steel.

8.8. Validation of Novel Methodology

8.8.1. Result of Dynamic Fracture Toughness with Standardized Test Methods

Experimental high strength steel was chosen as referential steel for validation of novel methodology. Low initial plasticity enables to apply the limited dimensions of tested samples, i.e. comparative with CCRB method. The specimen used for dynamic fracture toughness according to ISO 26843:2015(E) was single edge notch bend (SENB or 3-point bending). The precracking was carried out on Vibrophores Amsler 50 – 250 HFP 5100 testing machine and it was performed at frequencies 75 Hz, using sinusoidal loading maximum 4.5 kN and number of cycles was approximately 30000. The fatigue precracking was started from the machined notch tip and propagate constant crack growth rate. The impact testing was conducted after the fatigue precracking procedure to obtain the value of dynamic fracture toughness. All of the testing procedures were performed at room temperature. The calculation procedure of dynamic fracture toughness was explained in Chapter 7.9. First important parameter was time to fracture (t_f)

which could be obtained from force – time plot and second one was the total crack length (a) which was algebraic sum of the machined notch depth (a_m) and the length of fatigue precrack (a_0). The force – time plots are given in Appendix E and the measured crack lengths are given in Appendix F. While calculating the length of fatigue precrack (a_0), totally 11 measurements were performed on the surface and mean values were considered for the calculation of dynamic fracture toughness.

The defined dimensions, time to fracture and calculated dynamic fracture toughness values are tabulated in Table 8.7. The results of K_{Id} values obtained by the standardized test method were consistent with that of the nonstandardized test method. It has to be mentioned that ratio of (a/W) is not in valid range which is suggested as ($0.45<a/W<0.55$) by ISO standard. Despite this possible influence, very close results were obtained (the calculated mean value of standard method was 56.69 MPa√m while that of nonstandardized method was 61.95 MPa√m). In conclusion, the novel method provides the possibility of acquiring the dynamic fracture toughness for metallic materials.

Table 8.7 Calculated dynamic fracture toughness value according to ISO 26843:2015(E)

Sample No	a (mm)	W (mm)	a/W	t' (μs)	f(t) (μs)	K_{Id} (MPa√m)
ESD-01	3.18	9.82	0.32	21.36	35.43	55.77
ESD-02	3.29	9.84	0.33	25.94	38.98	61.36
ESD-03	4.07	9.62	0.42	22.89	33.63	52.94

For determination of dynamic fracture toughness, ASTM E399 – 17 standard suggests using force parameter. As the brittle material has very little observable plastic deformation and minimal absorption of energy, crack propagation is very fast. At high strain rates, the force signal has large amplitudes due to the inertia of test equipment and it is too hard to specify the maximum dynamic force. In order to eliminate this problem; loading rate can be decreased, less brittle material can be used or holding system of the specimen can be changed. The methodology of ISO 26843:2015(E) standard considers the time to fracture (t_f) parameter and it is more reliable method in comparison to that of ASTM E399 – 17. This is the reason why the methodology of ISO 26843:2015(E) standard is chosen for determination of dynamic fracture toughness.

The macroscopic figures of fracture surfaces of the tested experimental high strength specimens clearly showed three discrete regions in Appendix F. These were machined notch depth, fatigue precracking and dynamic fracture region. The direction of the crack propagation was visible.

The characterization of fracture mechanism was essential step of the experimental study for comprehensive understanding of materials fracture response and for true interpretation of obtained results. Detailed examination of fractured surfaces was carried out at suitable magnifications and resolution using scanning electron microscopy (SEM).

8.8.2. Fracture Analysis of Experimental High Strength Steel

SEM image of ECCRB-02 experimental high strength steel specimen which was fatigue precracked and following static tensile loaded is shown in Figure 8.22. It can be clearly seen that fractured specimen had three distinctive regions which were machined notch, steady crack propagation and sudden unstable fracture due to static tensile loading. According to K_{IC} results, the experimental high strength steel had the lowest fracture toughness values in comparison to other tested steels. In the zone of sudden unstable fracture mode was completely brittle fracture and the cleavages were visible. These findings confirmed that the experimental high strength steel specimen had lowest K_{IC} value. Because, if the material exhibits almost total brittle cleavage, it should have lowest resistance to crack propagation. In region of steady crack propagation was characterized by the occurrence of striations which were the proof of the fatigue process.

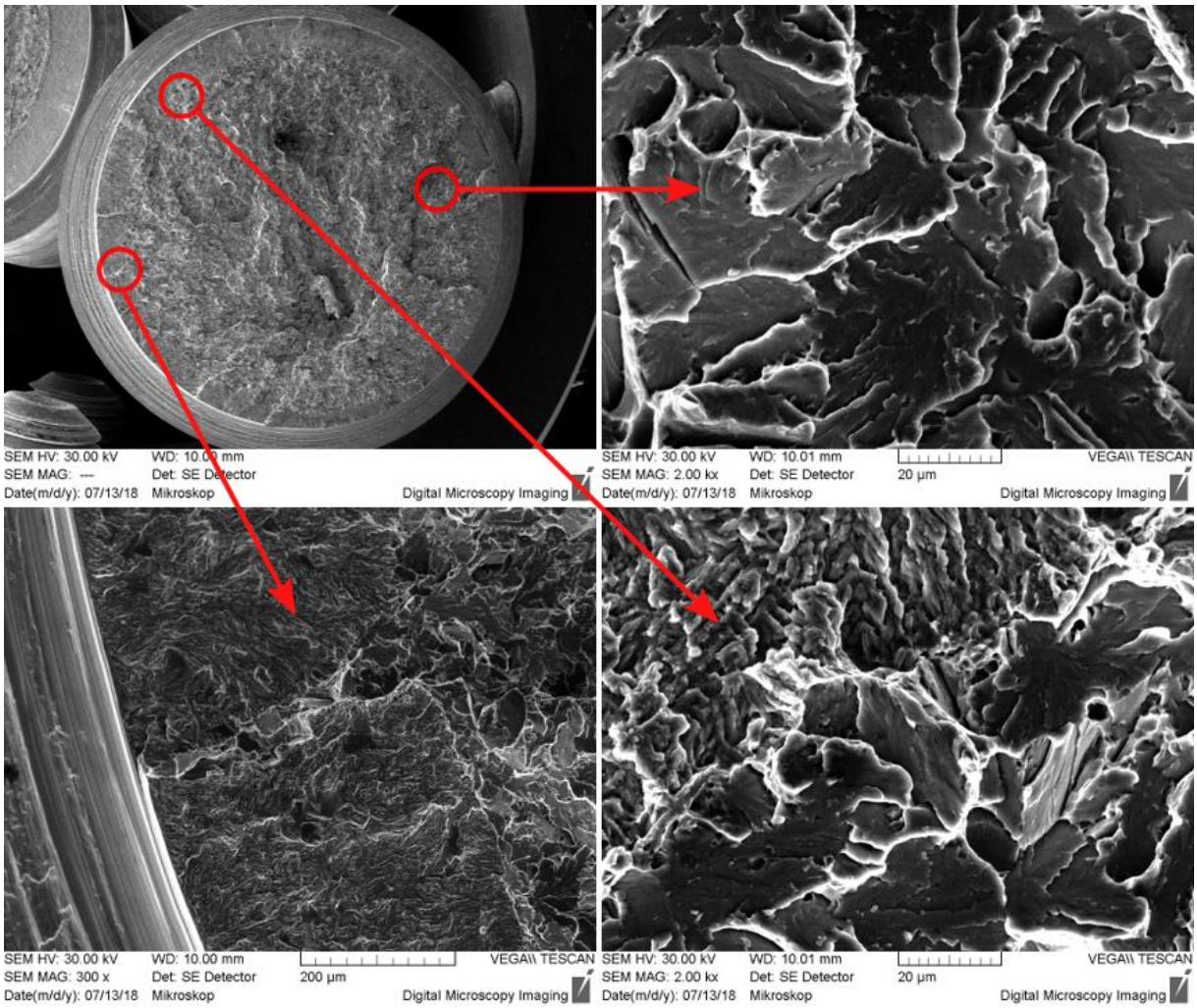

Figure 8.22 SEM image of ECCRB-02 specimen

SEM image of ED-01 experimental high strength steel specimen which was fatigue precracked and following impact tensile loaded is shown in Figure 8.23. It had almost same fracture surface with ECCRB-02 specimen. The fatigue region and unstable fracture zone due to dynamic loading can be seen clearly with the border distinguishing under 500x magnification. The region of steady crack growth had eccentricity. The possible reason of this eccentricity can be unequal machining of the notch depth. The crack propagation region was described by striations. Each striation corresponds to a load cycle. Final fracture region presented almost total brittle mechanism and entire cleavage cracking. It confirmed the validity of linear-elastic fracture mechanics preconditions. As it was same in the result of static fracture toughness test, the lowest value of dynamic fracture toughness value was obtained for experimental high strength steel. This result was supported with the SEM analysis of the fractured surface of ED-01 specimen.

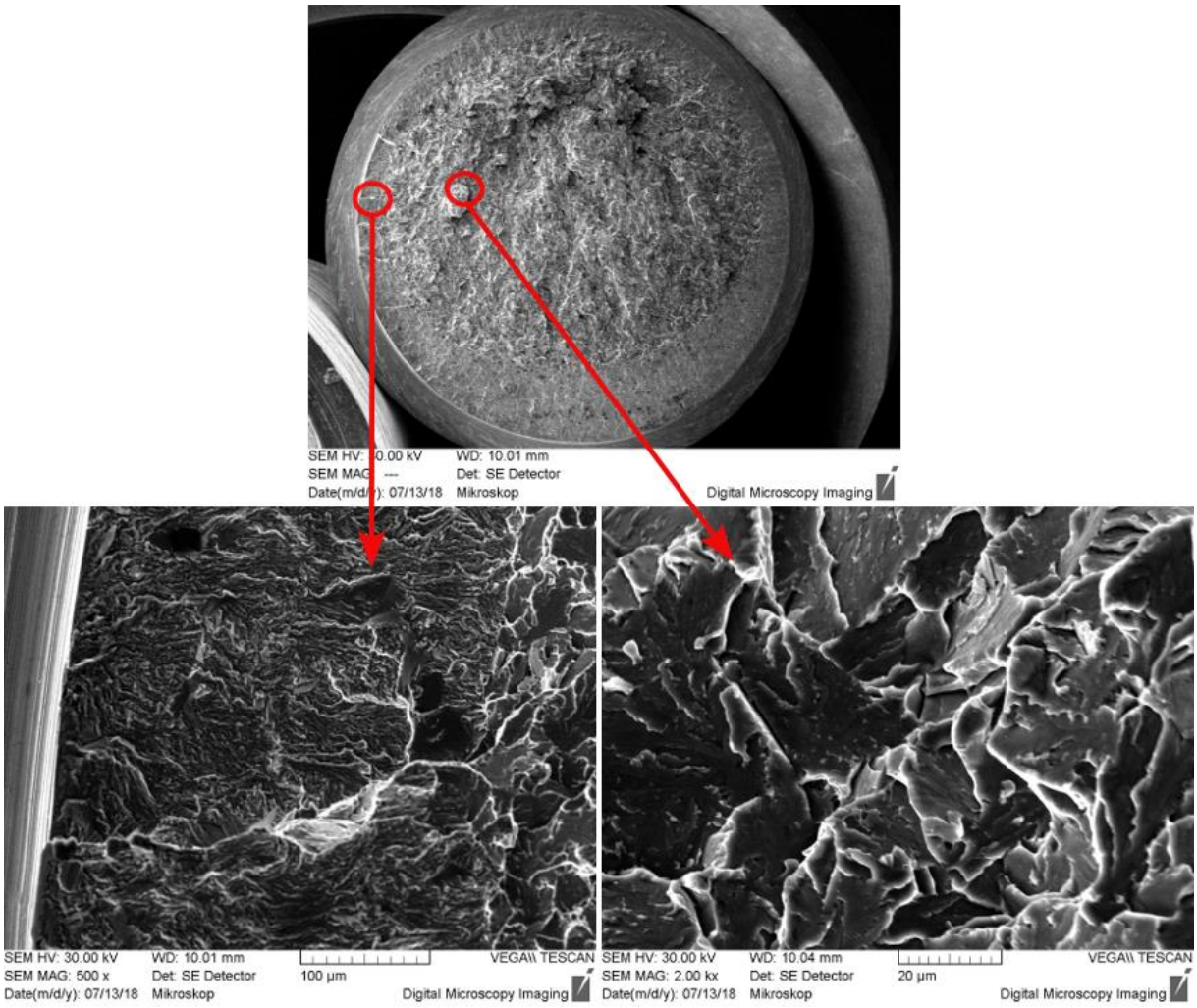

Figure 8.23 SEM image of ED-01 specimen

8.9. Influence of Loading Rate on Fracture Response

Sensitivity of compared steels on inner imperfections and passive safety capacity can be evaluated by detail examination SEM analysis of fractured specimens. The novel method was also applied for comprehensive study of every stage of crack propagation, as a tracing of prospective inner defect influence during different operational loading.

8.9.1. Standard Steel

The fractured surface of the SCCRB-05 specimen which was fatigue precracked and following static tensile loaded is given in Figure 8.24. It can be clearly seen in macroscopic scale that there are two distinct regions were existed. The first region was crack propagation zone and the macro beach marks were visible. The fatigue crack was propagated in equal distance from the machined notch tip and no eccentricity was observed through circumferential

direction. The second region was the result of the static tensile loading and it was distinctive in comparison to the crack propagation zone. This zone exhibited two different characteristics. The initial moment of the static tensile loading, fracture surface displayed undulating appearance. A number of small and big cup like depressions were observed in the fractographs. This depression were generally known as dimples. The cup like depressions shows that the material exhibits ductile fracture mechanism. In the final stage of the static tensile loading, the fracture mechanism was changed from ductile to brittle fracture type. It can be clearly seen from the figure (lower-right) final unstable part has cleavage type which is the proof of the brittle fracture mechanism.

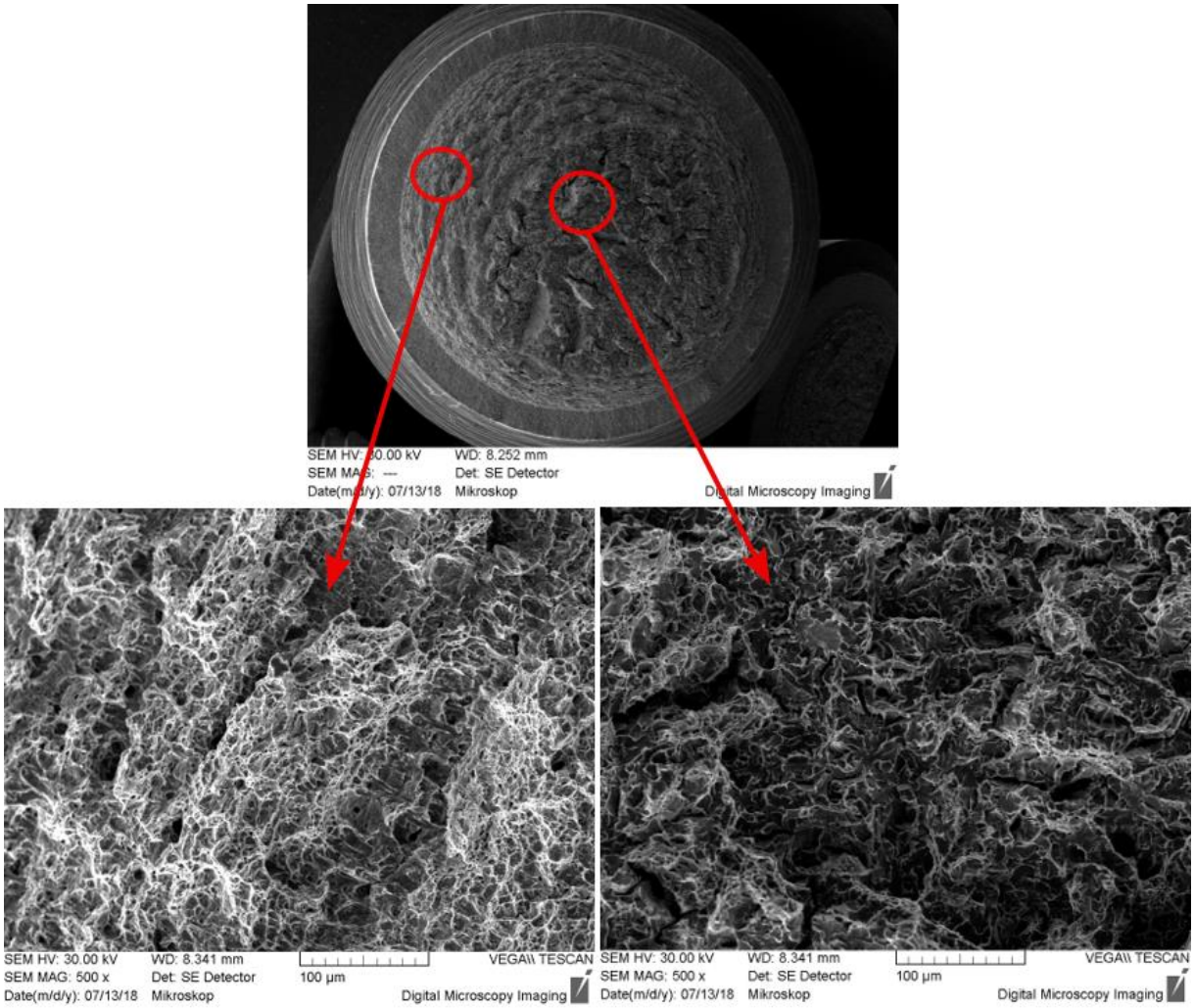

Figure 8.24 SEM image of SCCRB-05 specimen

The fractured surface of the S355D-02 specimen which was fatigue precracked and following impact tensile loaded at pendulum speed 5.23 m/s is given in Figure 8.25. The overall sectional view of the fatigue fractured surface showed smooth surface finish. In comparison to

SCCRB-05 specimen, the distance of undulating appearance (uphill and downhill steps) was narrower. The possible reason of this observation was higher loading rate. Higher strain rate did not allow time for stress redistribution and it promoted the brittle fracture type. Because of this, limited length of the ductile fracture mechanism was observed in the zone of impact tensile loading. Nevertheless, in this region a large number of dimples were seen in the fractographs. At the center of the specimen, it displayed almost full brittle fracture appearance.

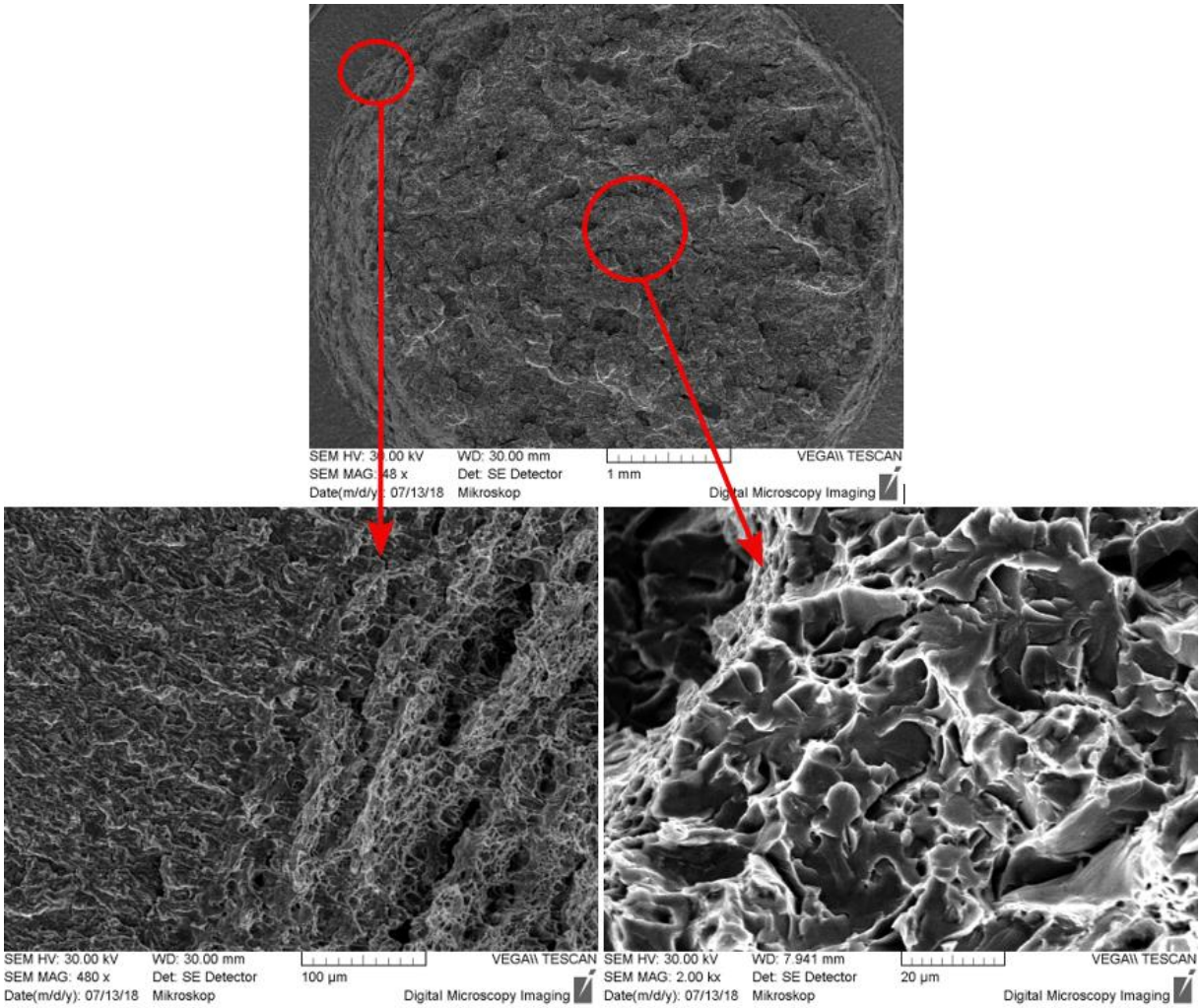

Figure 8.25 SEM image of S355D-02 specimen

The fractured surface of the S355LSD-02 specimen which was fatigue precracked and following impact tensile loaded at pendulum speed 3.48 m/s is given in Figure 8.26. The same fracture characteristics were observed with S355D-02 specimen. The zone of the fatigue precracking was very smooth and distinctive from the zone of impact tensile loading. As it was the case with higher loading rate, two different regions were existed in the region of the impact tensile loading. The length of the undulating region was narrow in comparison to the case of

the static loading but almost same as with higher loading rate. In center of the specimen, fracture mode was completely brittle, and cleavages were clearly visible.

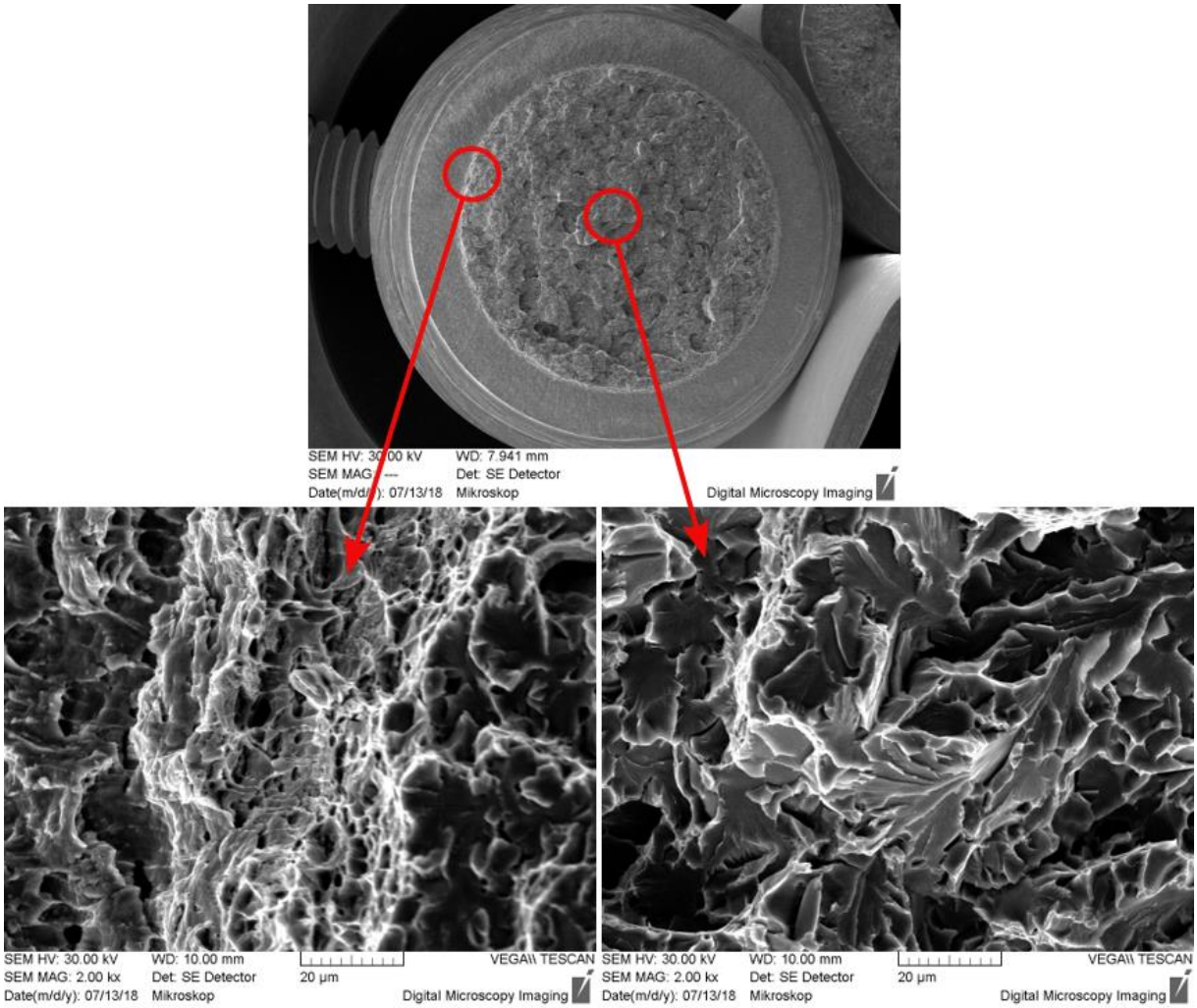

Figure 8.26 SEM image of S355LSD-02 specimen

Representative force – displacement graph is shown in Figure 8.27. S355 steel displayed an increase in fracture load with increasing loading rate. This was expected because mechanisms which easily move dislocations under low loading rates were deactivated at higher loading rates. The obtained result was consistent with the findings of previous works [51–54]. Boyce and Dilmore reported that the increase in strength with increasing strain rate is typically attributed to the reduction of diffusion limited (thermal) dislocation processes to overcome short range obstacles [52]. Increasing fracture load led to an increase in the static (K_{IC}) and the dynamic (K_{Id}) fracture toughness because of they were directly proportional to the fracture loads.

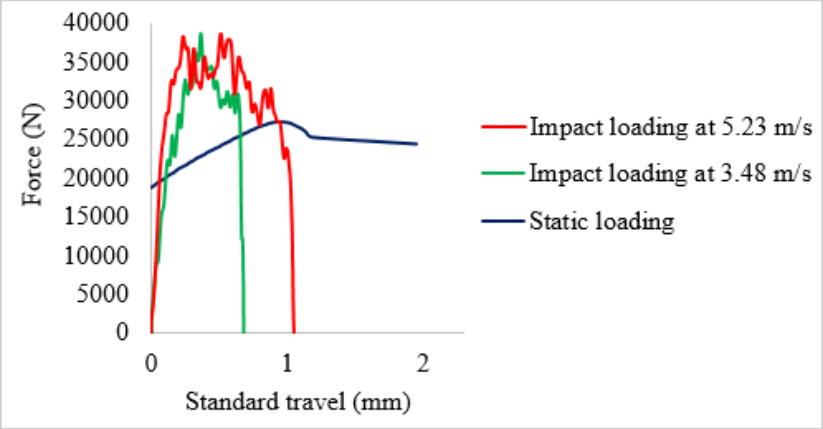

Figure 8.27 Force-displacement graph of S355 specimen at different loading rate

8.9.2. Prospective High Strength Steel

In Figure 8.28, fractographs of StxCCRB-01 specimen which was fatigue precracked and following static tensile test is performed is shown. In comparison to other tested steels, it was visible that the length of fatigue crack propagation was completely heterogeneous. It started from the tip of the machined notch, but it was not propagated equally through in circumferential direction. In the middle of the broken specimen, sharp micro hills were observed. These micro hills were existed because of the steel had internal heterogeneity. In the region of static tensile loading, the fracture mode was mixed mode. In some region, cleavage was existed and in the rest of the fractured surface, microvoid coalescence was observed. Some inclusions were seen in the structure during SEM examination. In order to understand the composition of inclusions, EDX analysis was performed and it was given in Figure G1 (Appendix G). It was observed that MnS and TiN had negative effects on fracture behaviour.

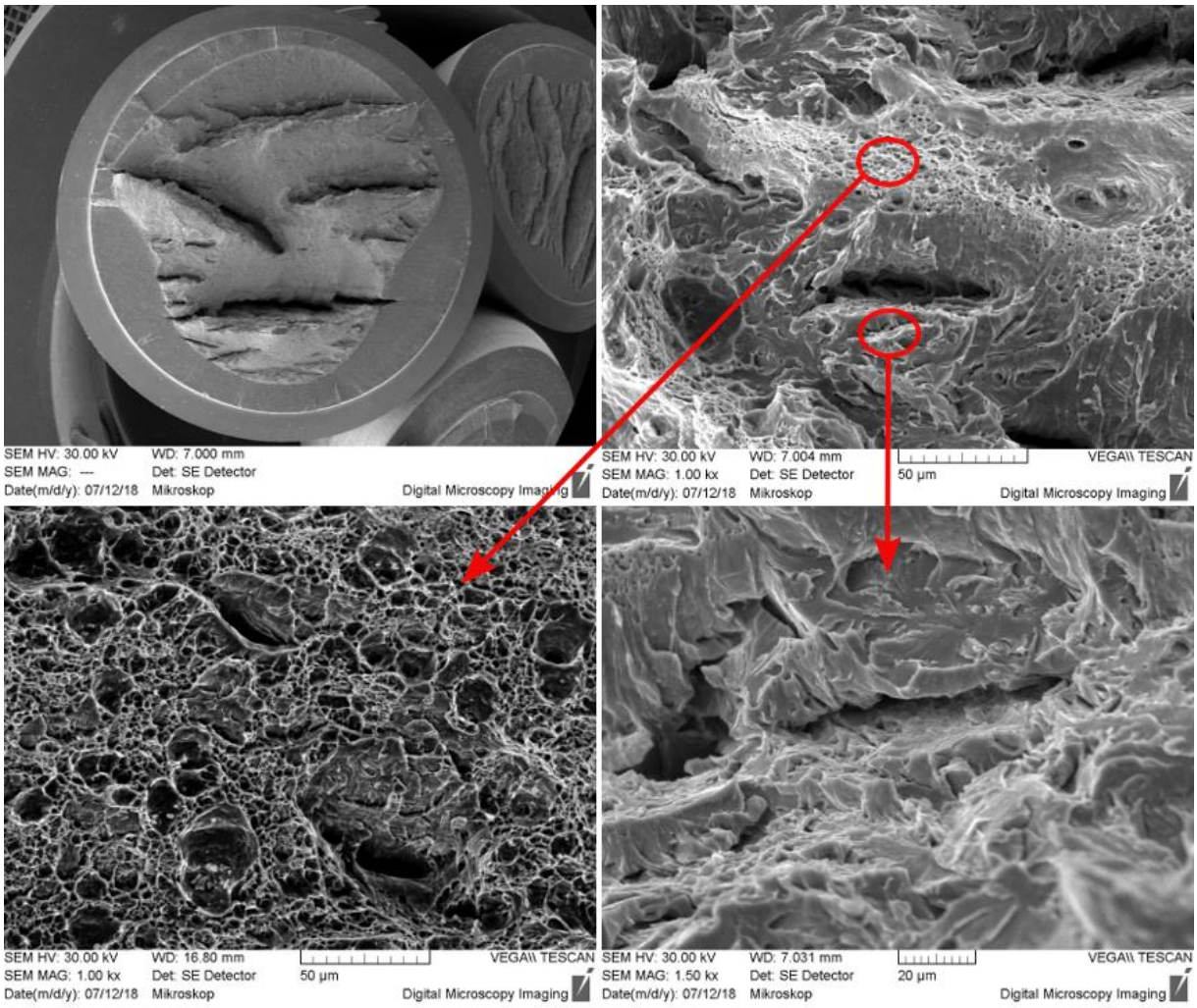

Figure 8.28 SEM image of StxCCRB-01 specimen

The SEM fractured surfaces of StxD-05 specimen and StxLSD-01 specimen are shown in Figure 8.29 and in Figure 8.30, respectively. These specimens were fatigue precracked and following impact tensile test was conducted. StxD-05 specimen and StxLSD-01 were tested at pendulum speed 5.23 m/s and 3.48 m/s, respectively. Between two different loading conditions, the region of fatigue precracking and unstable fracture were almost same. Both of them had mixed-mode ductile and brittle cracking mechanism. The most noticeable difference was the appearance of the micro hills. A large number of micro parallel hills were observed at higher pendulum speed whereas limited number of micro hills were existed at lower pendulum speed.

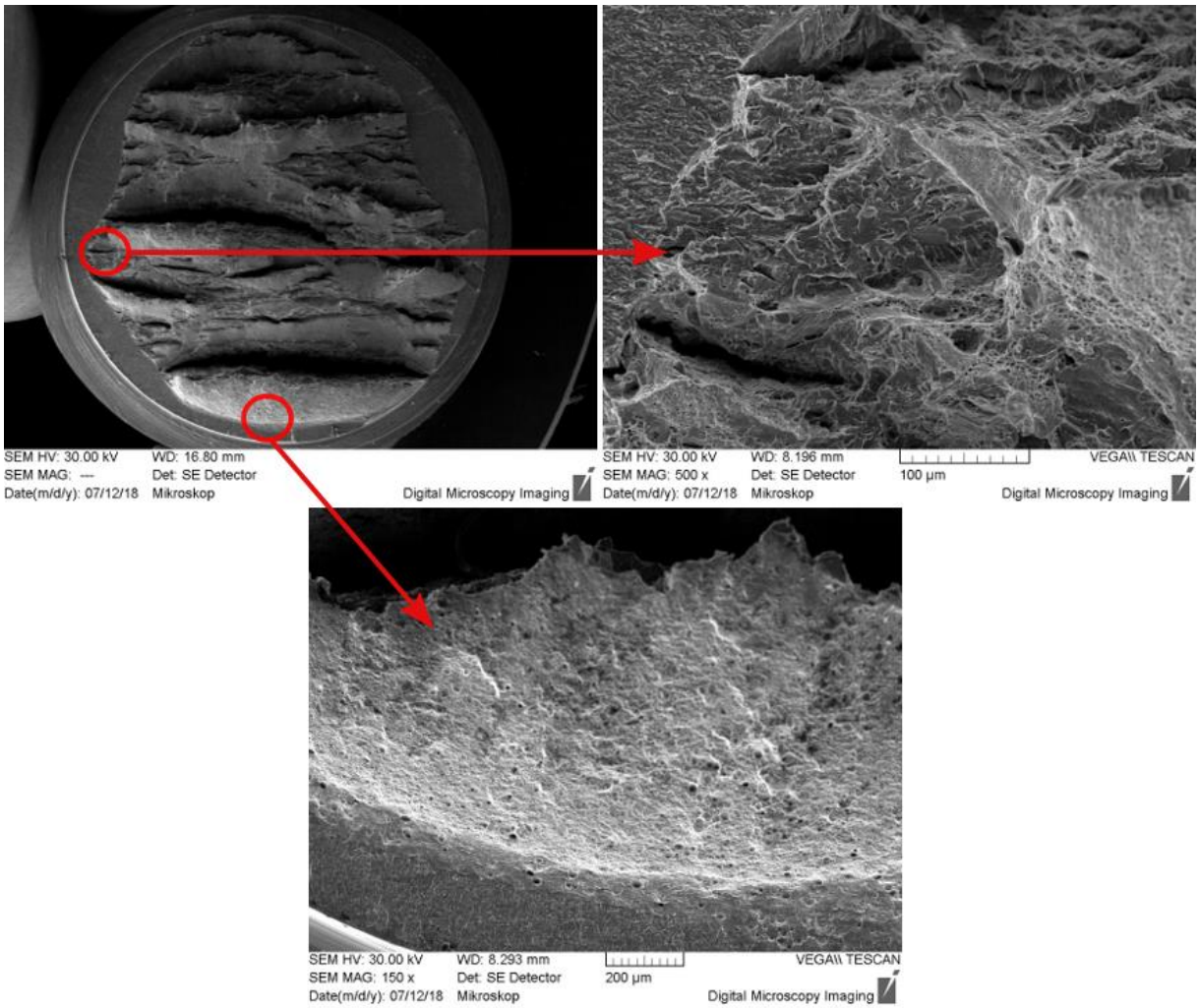

Figure 8.29 SEM image of StxD-05 specimen

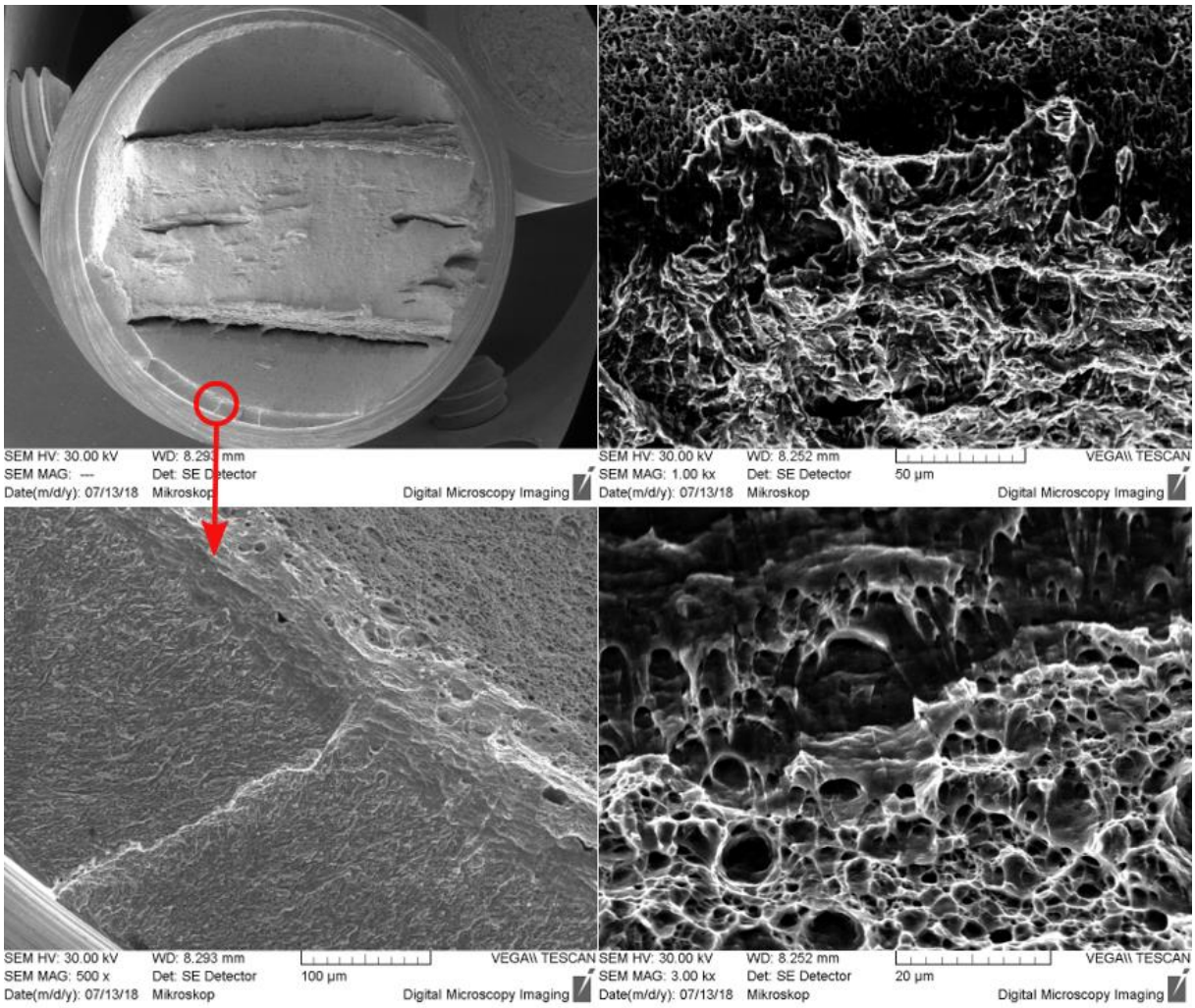

Figure 8.30 SEM image of StxLSD-01 specimen

Representative force displacement graph is shown in Figure 8.31. A similar trend which was seen in S355 steel was also observed for Strenx 700MC steel, the fracture load was increased with increasing loading rate. Strenx 700MC steel showed higher mean fracture load in comparison to S355 steel. The main mechanism attributed to grain boundary strengthening mechanism. Increasing fracture load by decreasing the grain size was consistent with the Hall – Petch relationship ($\sigma_y = \sigma_o + kd^{-1/2}$). It can be explained in terms of dislocation pile-up at grain boundaries. The number of dislocations in these pile-ups is proportional to the grain size, d. By increasing the grain size, the number of dislocations pile-ups increases and hence the stress concentration in the grain across the boundaries increases. Thus, with a larger grain size, a lower load or stress is required for the slip [51].

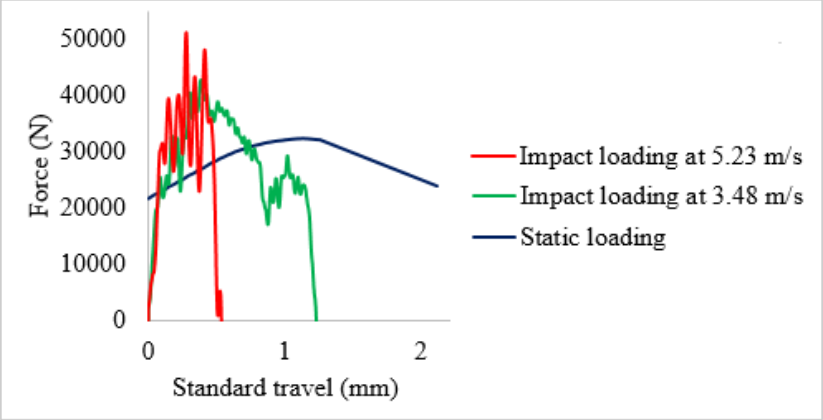

Figure 8.31 Force-displacement graph of Strenx 700MC specimen at different loading rate

8.10. Influence of Welding Process on Crack Sensitivity

The SEM fractured surfaces of StxWSCCRB-03 specimen and StxWSD-01 specimen are shown in Figure 8.32 and in Figure 8.33, respectively. Both specimens were exposed to weld thermal cycle simulation in order to investigate the effect of heat input on fracture behaviour. After fatigue precracking procedure, static tensile test was conducted for StxWSCCRB-03 specimen and impact tensile test at pendulum speed 5.23 m/s was performed for StxWSD-01 specimen. In Figure 8.32, it can be clearly seen that after fatigue precracking region, two different fracture mechanisms were observed. Firstly, resulted in a typical microvoid coalescence morphology and ductile fracture mode as expected after weld thermal cycle simulation. There were subtle differences in terms of dimple size. Secondly, the microvolume of cleavages was observed which was the proof of brittle fracture mechanism. In Figure 8.33, (upper-left) fractured surface had radial marks which were macroscopic surface features that indicate the region of crack initiation and propagation direction and also this figure revealed that the notch was not machined properly. This machining defect was resulted with heterogeneous crack propagation through the circumferential direction. Moreover, some steps were existed (lower-left). During stable crack propagation striations were clearly seen in the upper-right figure. In the region of unstable fracture, the mechanism was almost ductile manner. Representative force displacement graph is shown in Figure 8.34. The same behaviour was also observed after the weld thermal cycle simulation process. The fracture load increased by increasing loading rate.

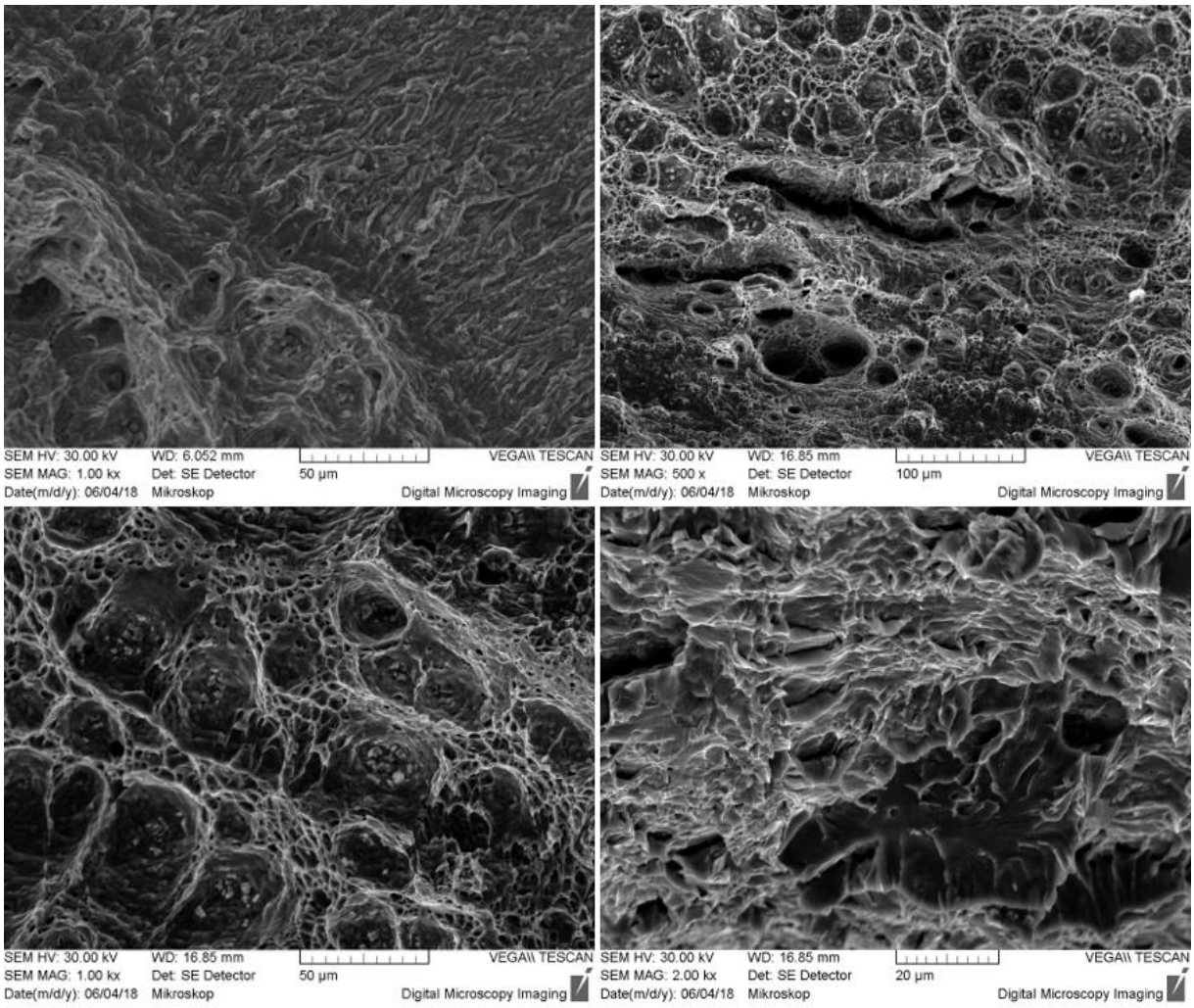

Figure 8.32 SEM image of StxWSCCRB-03 specimen

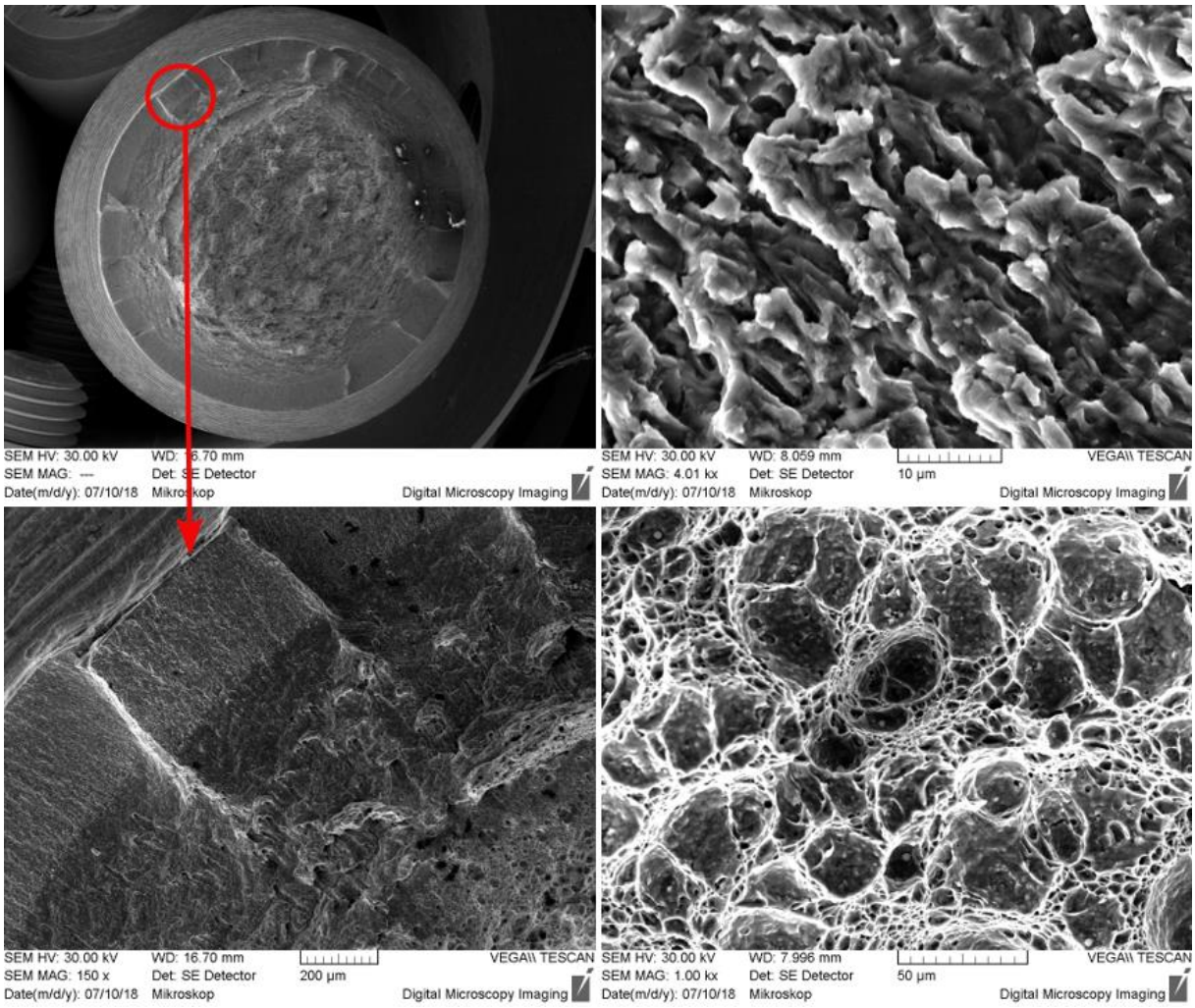

Figure 8.33 SEM image of StxWSD-01 specimen

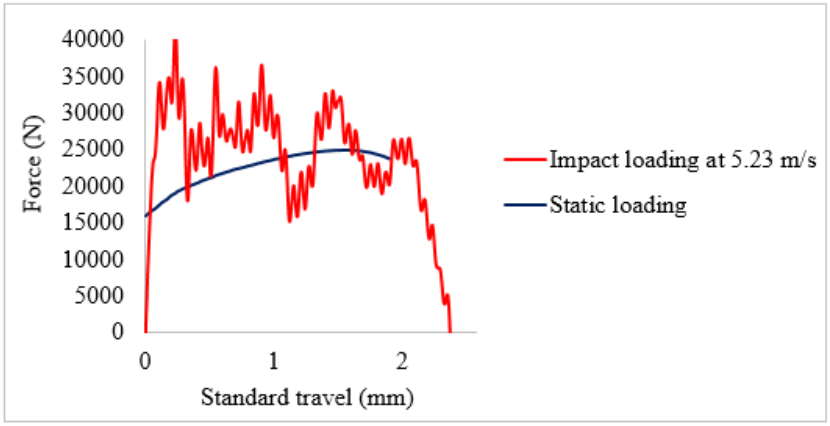

Figure 8.34 Force-displacement graph of Strenx 700MC specimen after weld thermal simulation

9. Conclusions

The main focus of this dissertation work was evaluating prospective high strength steel for construction of railway transport means hence a set of experimental works were performed. The novel methodology for safety assessment was found out as a crucial precondition to use this kind of steel.

The conducted experimental research has studied the fracture response and durability of the used high strength steel against two decisive effects:

- Degradation of primary strength and toughness of tested steel due to supplied temper influence
- Sensitivity of tested steel to internal defects in connection welding.

Above mentioned questions limit the current applications for wider particular structural parts of railway transport means. Because of the internal heterogeneities and the heterogeneous plastic response of the used high strength steel, the standard testing approaches are not suitable for feasible profiles.

9.1. Summary of Results

This experimental research study, using the standard and the novel methodology, provided a lot of particular information. The result obtained from this doctoral dissertation can be summarized as follows:

The effect of the heat input on fracture response

• To identify the degradation process, structural characterization of the experimental welding was conducted for Strenx 700MC steel and hardness measurements were performed. It indicated that the lowest value in sublayer of outer part of the grain refinement zone. It was in contradiction with generally known grain refining effect. Based on detail microstructure evaluation, it was observed that the reprecipitation of carbides has led to substantial decrease of hardness.

• The weld thermal cycle simulation was designed based on analyses of experimental welding process influence. Hardness measurement showed almost stabile values in all cross section. It

enabled to evaluate the change of fracture behaviour using both parameters – the fracture toughness and also the crack propagation resistance.

- K_{IC} value of Strenx 700MC steel specimen was found to be slightly higher than that of the specimen which was exposed to weld thermal cycle simulation. Microstructure of Strenx 700MC specimen subjected to thermal cycle simulation was combination of acicular and Widmanstatten ferrite and the suppression of the heterogeneity after weld simulation process could be reasons for decreasing in K_{IC} value.
- After conducting the weld thermal cycle simulation, the value of the calculated dynamic fracture toughness increased in comparison to the heat untreated Strenx 700MC specimen. Contrary to expectations, the heat input did not induce the degradation of crack dynamic resistance of this high strength steel.

The result of the plane strain fracture toughness (K_{IC}), the effect of diameters on K_{IC} value and the comparison of two different test methods

- The plane strain fracture toughness (K_{IC}) was determined with circumferentially notched round bar (CNRB) and circumferentially cracked round bar (CCRB) for S355, Strenx 700MC and experimental high strength steels. The highest K_{IC} value was obtained for Strenx 700MC steel, followed by S355 steel and experimental high strength steel.
- The difference of the calculated K_{IC} values between CNRB and CCRB methodologies was remarkable and it was investigated with fracture mechanics aspect. Fracture toughness determination of metallic materials with using these approaches was easy, reliable and accurate method.
- The diameter of the unnotched and notched sections had significant effect on fracture toughness even if (D/d) ratio was kept constant as 1.2. It was found that as the unnotched diameter along with notch diameter increased, the fracture toughness values were decreased.
- It was found a correlation between d_{eff}/D ratio and K_{IC} value. As the d_{eff}/D ratio increased, the fracture toughness value decreased.
- Crack Depth meter (JK – 1) was firstly introduced in the literature of CCRB methodology to estimate the crack propagation for round bar specimen.
- Fatigue crack growth rate was specified for S355 steel as $da/dN=4x10^{-9}\Delta K^{0,888}$ and for Strenx 700MC steel as $da/dN=3x10^{-17}\Delta K^{6,467}$. Strenx 700MC steel was found safer than S355 steel

from the point of the internal imperfections which is important point for application of lightweight means.

The result of the dynamic fracture toughness (K_{Id}), the effect of the loading rate on K_{Id} value and the comparison between the novel and standard test methodologies

- The new approach was used for evaluation of dynamic fracture toughness (K_{Id}) of metallic materials. Considering calculated mean dynamic fracture toughness, the highest (K_{Id}) value was obtained for S355 steel, followed by Strenx 700MC and experimental high strength steel. In higher loading rate, Strenx 700MC steel exhibited lower crack resistance in comparison to static loading conditions.
- Regardless of the grade of the steel, as the loading rate increased from 3.48 m/s to 5.23 m/s, calculated (K_{Id}) value increased for the novel methodology. All of the tested steels induced some micro plasticity at the propagated crack tip.
- The novel method was compared with ISO 26843:2015(E) standard which uses single edge notch bend specimen. The obtained results showed that the calculated K_{Id} values were very close each other for experimental high strength steel.

The analysis of the fractured surface

- The SEM analysis supported the experimental results. Experimental high strength steel with the lowest fracture toughness values, displayed totally brittle cleavage cracking while S355 and Strenx 700MC steels exhibited almost mixed-mode ductile and brittle cracking mechanism in static and dynamic loading conditions. In all specimen, crack propagation zone was visible.

9.2. Contributions of the Doctoral Dissertation

In this doctoral dissertation, the fracture behaviour of S355, Strenx 700MC and experimental high strength steels were evaluated. While S355 is generally used in structural part of rail vehicles, Strenx 700MC steel presents the prospective high strength variety for light weight construction. The production of rail transportation vehicle without the welding process is almost impossible. Vehicle crashworthiness of high strength steels are greatly influenced by welding process due to high energy input. As many metallurgical changes that take place in welded structural part, it is necessary to evaluate in terms of microstructural and mechanical properties. It is important to know that material behaviour which consists a crack during its

service life, because the crack which exists in a structure can be propagated by means of the random loading in operation. Taking into consideration basis of the fracture mechanics, the service life of the structural part can be estimated, and the precautions can be taken for safety.

The lack of information about real influence of the degradation of the primary strength and toughness of the prospective high strength steels, based on thermomechanical treatment and/or fine-grained steels like Strenx 700MC is the obstacle for application in mainly dynamic loaded parts of railway means frame. All of obtained results, reflecting the influence of welding on static and dynamic resistance to defects, present results towards to implementation in practical application. Degradation process due to welding and weld thermal cycle simulation process was conducted and evaluated for Strenx 700MC steel which has the possibility increasing safety, improving crashworthiness and reducing the total weight of the transport means. Fatigue crack growth rate was specified for S355 and Strenx 700MC steels. The impact tensile tests were performed at two different loading rates in order to examine the effect of loading rates on dynamic fracture toughness value. Particular results confirmed the prospective application of Strenx 700MC for lightweight structures.

Comprehensive understanding all of included material processes is necessary for reliable use of the suggested steels replacement (Strenx 700MC vs. S355). Performed material analysis has led to findings of substance and reach of related processes, which presents the scientific contribution of work.

Substantial part of results is connected with design and validation of novel methodology for fracture behavior testing for limited dimensions of steel profiles. In recent years, there is a great interest on simplifying the test method which determines the parameters related with fracture mechanics. In this study, attractive nonstandard test methodologies were used to specify the plane strain fracture toughness (K_{IC}) and the dynamic fracture toughness (K_{Id}) for three kinds of steels. Moreover, standardized test method was compared with novel test method for determination of dynamic fracture toughness value.

9.3. Recommendations for Future Research

- Standardized test methods can be performed on different kinds of steels and the results can be compared for the plane strain fracture toughness testing.

- In order to extend the investigation of heat input on fracture response, different heat treatment parameters can be used for the weld thermal cycle simulation.
- In order to eliminate the effect of diameters on the plane strain fracture toughness, a large number of specimens can be tested using round bar methodologies. It can be suggested a relation between the diameter and yield strength to obtain the plane strain conditions.

References

[1] I. Dincer, J. Hogerwaard, and C. Zamfirescu, 2015, Clean Rail Transportation Options, Springer Science+Business Media, New York, NY.

[2] A. Kurc-Lisiecka, J. Piwnik, and A. Lisiecki, 2017, "Laser Welding of New Grade of Advanced High Strength Steel STRENX 1100 MC," Arch. Metall. Mater., 62(3), pp. 1651–1657.

[3] R. Ulewicz, P. Szataniak, F. Novy, L. Trsko, and O. Bokuvka, 2017, "Fatigue Characteristics of Structural Steels in the Gigacycle Region of Loading," Mater. Today Proc., 4(5), pp. 5979–5984.

[4] J. Laitila, J. Larkiola, and D. Porter, 2018, "Effect of Forced Cooling on the Tensile Properties and Impact Toughness of the Coarse-Grained Heat-Affected Zone of a High-Strength Structural Steel," Weld. World, 62(1), pp. 79–85.

[5] M. Mazur, and R. Ulewicz, 2017, "Analysis of Strength and Fatigue Properties of Construction Materials for Manufacturing the Parts of Semi-Trailers," 2(1), pp. 32–37.

[6] R. Ulewicz, and P. Szataniak, 2016, "Fatigue Cracks of Strenx Steel," Mater. Today Proc., 3(4), pp. 1195–1198.

[7] J. Górka, 2015, "Weldability of Thermomechanically Treated Steels Having a High Yield Point," Arch. Metall. Mater., 60(1), pp. 469–475.

[8] M. Mazur, 2016, "Fatigue Properties of Fine-Grained Steels Applied in Components of Semitrailers," Tech. Trans. Mech., 4M/2016, pp. 9–14.

[9] J. Górka, and S. Stano, 2018, "Microstructure and Properties of Hybrid Laser Arc Welded Joints (Laser Beam-MAG) in Thermo-Mechanical Control Processed S700MC Steel," Metals, 8(2), pp. 132–147.

[10] J. Sperle, L. Hallberg, J. Larsson, and H. Groth, 2008, "The Environmental Value of High Strength Steel Structures", The Steel Eco-Cycle, Environmental Research Programme for the Swedish Steel Industry, 2004 – 2012, The Steel Eco-Cycle. Scientific Report. Phase 1, 2004 – 2008," pp. 151–171.

[11] F. Bozkurt, 2015, "Structural and Mechanical Heterogeneities of Fine Grain Steel Welded Joints Used in Construction of Rail Vehicles," Master Thesis, 96 p., University of Pardubice.

[12] K. Weman, 2012, Welding Processes Handbook, Woodhead Pub, Oxford ; Philadelphia.

[13] Md. I. Khan, 2007, Welding Science and Technology, New Age International (P) Ltd., Publishers, New Delhi.

[14] S. Kou, 2003, Welding Metallurgy, Wiley-Interscience, Hoboken, N.J.

[15] S. Kim, D. Kang, T. Kim, J. Lee, and C. Lee, 2011, "Fatigue Crack Growth Behavior of the Simulated HAZ of 800MPa Grade High-Performance Steel," Mater. Sci. Eng. A, 528(6), pp. 2331–2338.

[16] W. Liu, F. Lu, R. Yang, X. Tang, and H. Cui, 2015, "Gleeble Simulation of the HAZ in Inconel 617 Welding," J. Mater. Process. Technol., 225, pp. 221–228.

[17] J. Górka, 2012, "An Influence of Welding Thermal Cycles on Properties and HAZ Structure of S700MC Steel Treated Using Thermomechanical Method," pp. 41–44.

[18] S. Kumar, S.K. Nath, and V. Kumar, 2016, "Continuous Cooling Transformation Behavior in the Weld Coarse Grained Heat Affected Zone and Mechanical Properties of Nb-Microalloyed and HY85 Steels," Mater. Des., 90, pp. 177–184.

[19] M. Dunđer, I. Samardžić, and Š. Klarić, 2007, "Influence of Cooling Time Δt8/5 on Welded Joint Properties of the Thermal Cycle Simulated TStE 420 Specimens," Teh. Vjesn., 14(1,2), pp. 47–57.

[20] Z. Boumerzoug, E. Raouache, and F. Delaunois, 2011, "Thermal Cycle Simulation of Welding Process in Low Carbon Steel," Mater. Sci. Eng. A, 530, pp. 191–195.

[21] Y. Shi, and Z. Han, 2008, "Effect of Weld Thermal Cycle on Microstructure and Fracture Toughness of Simulated Heat-Affected Zone for a 800MPa Grade High Strength Low Alloy Steel," J. Mater. Process. Technol., 207(1–3), pp. 30–39.

[22] X. Kong, and C. Qiu, 2013, "Continuous Cooling Bainite Transformation Characteristics of a Low Carbon Microalloyed Steel under the Simulated Welding Thermal Cycle Process," J. Mater. Sci. Technol., 29(5), pp. 446–450.

[23] W. Zhao, W. Wang, S. Chen, and J. Qu, 2011, "Effect of Simulated Welding Thermal Cycle on Microstructure and Mechanical Properties of X90 Pipeline Steel," Mater. Sci. Eng. A, 528(24), pp. 7417–7422.

[24] J. Winczek, and A. Kulawik, 2012, "Dilatometric and Hardness Analysis of C45 Steel Tempering with Different Heating-up Rates," Metalurgija, 51(1), pp. 9–12.

[25] T. Vuherer, M. Dunđer, L. Milović, M. Zrilić, and I. Samardžić, 2013, "Microstructural Investigation of the Heat-Affected Zone of Simulated Welded Joint of P91 Steel," Metalurgija, 52(3), pp. 317–320.

[26] I. Samardžić, A. Stoić, D. Kozak, I. Kladaric, and M. Dunđer, 2013, "Application of Weld Thermal Cycle Simulator in Manufacturing Engineering," Manuf. Ind. Eng., 12(1–2), pp. 7–11.

[27] I. Samardžić, A. Čikić, and M. Dunđer, 2013, "Accelerated Weldability Investigation of TStE 420 Steel by Weld Thermal Cycle Simulation," Metalurgija, 52(4), pp. 461–464.

[28] T. L. Anderson, 2005, Fracture Mechanics: Fundamentals and Applications.

[29] J. M. Barsom, and S. T. Rolfe, 1999, Fracture and Fatigue Control in Structures: Applications of Fracture Mechanics, ASTM, West Conshohocken, PA.

[30] N. Perez, 2005, Fracture Mechanics, Springer London NetLibrary, Inc. [distributor, Guildford; Boulder.

[31] ASTM Designation E1820 − 17a, 2018, "Standard Test Method for Measurement of Fracture Toughness," p. 55.

[32] ASTM Designation E399 − 17, 2018, "Standard Test Method for Linear-Elastic Plane-Strain Fracture Toughness Kıc of Metallic Materials," p. 34.

[33] L. F. Jeffus, 2012, Welding and Metal Fabrication, DelmarCengage Learning, Clifton Park, NY.

[34] T. Vadholm, 2014, "Investigation of Low Temperature Toughness and Crack Initiation In Welded Structural Steels," Norwegian University of Science and Technology.

[35] A. Bayram, A. Uğuz, and A. Durmus, 2002, "Rapid Determination of the Fracture Toughness of Metallic Materials Using Circumferentially Notched Bars," J. Mater. Eng. Perform., 11(5), pp. 571–576.

[36] A. Bayram, A. Uğuz, and M. Ula, 1999, "Effects of Microstructure and Notches on the Mechanical Properties of Dual-Phase Steels," Mater. Charact., 43(4), pp. 259–269.

[37] S. Nath, and U. K. Das, 2008, "Effect of Microstructure and Notches on the Fracture Toughness of Medium Carbon Steel," J. Nav. Archit. Mar. Eng., 3(1), pp. 15–22.

[38] N. V. Londe, T. Jayaraju, C. Rajashekar, and T. K. Chandrashekar, 2015, "Determination of Fracture Toughness in Tensile Fracture and Fatigue Fracture of Steels," pp. 92–97.

[39] V.L. Neelakantha, T. Jayaraju, P. Naik, D. K. K, C.R. Rajashekar, and Mohankumar, 2015, "Determination of Fracture Toughness and Fatigue Crack Growth Rate Using Circumferentially Cracked Round Bar Specimens of Al2014T651," Aerosp. Sci. Technol., 47, pp. 92–97.

[40] F. Bozkurt, and E. Schmidová, 2018, "Fracture Toughness Evaluation of S355 Steel Using Circumferentially Notched Round Bars," Period. Polytech. Transp. Eng., pp. 1–4.

[41] B. Ule, V. Leskovšek, and B. Tuma, 2000, "Estimation of Plain Strain Fracture Toughness of AISI M2 Steel from Precracked Round-Bar Specimens," Eng. Fract. Mech., 65(5), pp. 559–572.

[42] T. K. Todkari, M. C. Swami, and P. S. Patil, 2015, "Effect of Specimen Diameter and Notch Diameter on the Fracture Toughness of AL-7075-T6 Alloy- an Experimental Approach," Int. J. Res. Eng. Technol., 04(01), pp. 66–70.

[43] N. V Londe, T. Jayaraju, and P. R. S. Rao, 2010, "Use of Round Bar Specimen in Fracture Toughness Test of Metallic Materials," Int. J. Eng. Sci. Technol., 2, pp. 4130–4136.

[44] V. Leskov, 2013, “Multi-Functional Kıc-Test Specimen for the Assessment of Different Tool- and High-Speed-Steel Properties,” Mater. Tehnol., 47(3), pp. 273–283.

[45] D. M. Li, and A. Bakker, 1997, “Fracture Toughness Evaluation Using Circumferentially-Cracked Cylindrical Bar Specimens,” Eng. Fract. Mech., 57(1), pp. 1–11.

[46] N. V. Londe, T. Jayaraju, and P. R. S. Rao, 2010, “Determination of Plane-Strain Fracture Toughness of AL 2014-T6 Alloy Using Circumferentially Cracked Round Bar Specimen,” Eng. E-Trans., 6(1), pp. 26–31.

[47] C. D. Wilson, and J. D. Landes, 2000, “Fracture Toughness Testing with Notched Round Bars,” Fatigue and Fracture Mechanics: 30th Volume, K. Jerina, and P. Paris, eds., ASTM International, 100 Barr Harbor Drive, PO Box C700, West Conshohocken, PA 19428-2959, pp. 69–82.

[48] A. F. Liu, 2005, Mechanics and Mechanisms of Fracture: An Introduction, ASM International, Materials Park, Ohio.

[49] ASM International, Lampman, S. R., and ASM International, eds., 2002, Fatigue and Fracture, ASM International, Materials Park, Ohio.

[50] ISO 26843:2015(E), “Metallic Materials - Measurement of Fracture Toughness at Impact Loading Rates Using Precracked Charpy-Type Test Pieces,” p. 35.

[51] A.R. Khalifeh, A.Dehghan Banaraki, H. Danesh Manesh, and M.Dehghan Banaraki, 2018, “Investigating of the Tensile Mechanical Properties of Structural Steels at High Strain Rates,” Mater. Sci. Eng. A, 712, pp. 232–239.

[52] B.L. Boyce, and M.F. Dilmore, 2009, “The Dynamic Tensile Behavior of Tough, Ultrahigh-Strength Steels at Strain-Rates from $0.0002s^{-1}$ to $200s^{-1}$,” Int. J. Impact Eng., 36(2), pp. 263–271.

[53] N. Tsuchida, H. Masuda, Y. Harada, K. Fukaura, Y. Tomota, and K. Nagai, 2008, “Effect of Ferrite Grain Size on Tensile Deformation Behavior of a Ferrite-Cementite Low Carbon Steel,” Mater. Sci. Eng. A, 488(1–2), pp. 446–452.

[54] N.K. Singh, E. Cadoni, M.K. Singha, and N.K. Gupta, 2011, “Dynamic Tensile Behavior of Multi Phase High Yield Strength Steel,” Mater. Des., 32(10), pp. 5091–5098.

[55] J. Fang, 2006, “Strength and Toughness Properties of Steels under Dynamic Loading,” Fracture of Nano and Engineering Materials and Structures, E. E. Gdoutos, ed., Springer Netherlands, Dordrecht, pp. 503–504.

[56] M. A. M. Daud, N. Z. Nasir, A. Rivai, and M. Z. Selamat, 2013, “Dynamic Fracture Toughness of Magnesium Alloy under Impact Loading Conditions,” Procedia Eng., 53, pp. 639–644.

[57] K. Nishioka, and K. Ichikawa, 2012, “Progress in Thermomechanical Control of Steel Plates and Their Commercialization,” Sci. Technol. Adv. Mater., 13(2), pp. 1–20.

[58] C. Baykasoglu, E. Sunbuloglu, S. E Bozdag, F. Aruk, T. Toprak, and A. Mugan, 2012, "Numerical Static and Dynamic Stress Analysis on Railway Passenger and Freight Car Models," Int. Iron Steel Symp. Karabük Turk., pp. 579–586.

[59] F. C. Campbell, ed., 2008, Elements of Metallurgy and Engineering Alloys, ASM International, Materials Park, Ohio.

[60] Cambridge University Engineering Department, 2003, Materials Data Book.

[61] F. Bozkurt, and E. Schmidová, 2018, "Effect of Notch Angle on Fracture Toughness of AISI 4340 Using Circumferentially Notched Bars," 27th Anniv. Int. Conf. Metall. Mater. Met. 2018.

[62] C. V. Kranenburg, 2010, "Fatigue crack growth in aluminium alloys," Technische Universiteit Delft.

Publications of the PhD Student

1) Bozkurt F., Schmidová E., Structural and Mechanical Heterogeneities of Fine Grain Steel Welded Joints Used in Construction of Rail Vehicles, Electronic Journal of Occupational Improvement and Research, 2015, Vol 3., 131–144, ISSN:2147-850

2) Bozkurt, F., Çakır F. H., Çelik O. N., Er Ü., Tribological Examination of Hardened Two Types Boron Steel for Railway Applications, Electronic Journal of Occupational Improvement and Research, 2015, Vol 3., 146–154, ISSN:2147-850

3) Bozkurt F., Schmidová E., Examination of The Local Mechanical Behavior After Welding, 33rd International Colloquium Advanced Manufacturing and Repair Technologies in Vehicle Industry, Zuberec – Slovakia, 2016, 25 – 28, ISBN 978 – 80 – 554 – 1214 – 6.

4) Bozkurt F., E. Schmidová, Schmid M., Culek B., Local Elastic-Plastic Response of Welding Joints of Domex 700MC Steel, 25th Anniversary International Conference on Metallurgy and Materials Metal, Brno, Czech Republic, 2016, ISBN 978-80-87294-67-3.

5) Bozkurt F., Schmidová E., Determination of Fracture Toughness of Steels Using Circumferentially Notched Round Bars, 34th International Colloquium on Advanced Manufacturing and Repairing Technologies in Vehicle Industry – Visegrád, 17 – 19 May 2017, 41 – 44, ISBN 978-963-313-258-6.

6) Bozkurt F., E. Schmidová, Determination of Fracture Toughness of Metallic Materials Using Round Bar Specimen, 26th Anniversary International Conference on Metallurgy and Materials Metal, Brno, Czech Republic, 24 – 26 May 2017, 737 – 742, ISBN 978-80-87294-79-6.

7) Bozkurt F., Schmidová E., Fracture Toughness Evaluation of S355 Steel Using Circumferentially Notched Round Bars, Periodica Polytechnica Transportation Engineering, Published Online 01/24/2018, https://doi.org/10.3311/PPtr.11560.

8) Bozkurt F., E. Schmidová, Effect of Notch Angle on Fracture Toughness of AISI 4340 Using Circumferentially Notched Bars, 27th Anniversary International Conference on Metallurgy and Materials Metal, Brno, Czech Republic, 23 – 25 May 2018, 114, ISBN 978-80-87294-83-3.

9) Bozkurt F., Yurdakul Ö., Hojka P., Routil L., Balaban E. and Artagan S. S., Mechanical Properties of Structural Steel Exposed to Passive Fire, 27th Anniversary International Conference on Metallurgy and Materials Metal, Brno, Czech Republic, 23 – 25 May 2018, 114, ISBN 978-80-87294-83-3.

Appendix A

Table A1. Functions for the determination of K_{Id}

t' (μs)	t'' = f(t') (μs)	t' (μs)	t''=f(t') (μs)
0	0	56	53
2	0	58	57
4	2	60	61
6	4	62	65
8	6	64	69
10	9	66	72
12	13	68	73
14	17	70	73
16	20	72	72
18	24	74	70
20	28	76	69
22	30	78	68
24	33	80	69
26	35	82	70
28	36	84	75
30	38	86	81
32	39	88	88
34	40	90	94
36	42	92	100
38	43	94	106
40	45	96	111
42	46	98	116
44	47	100	118
46	46	102	119
48	45	104	118
50	45	106	117
52	46	108	115
54	49	110	115

Appendix B

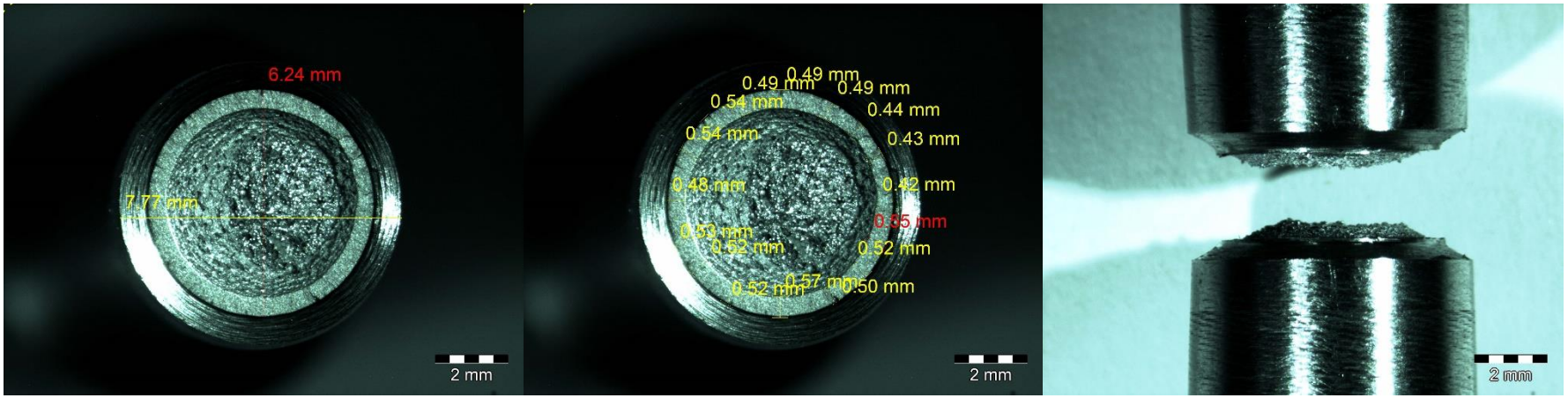

Figure B1. Cross-sectional and side view of fractured SCCRB-04

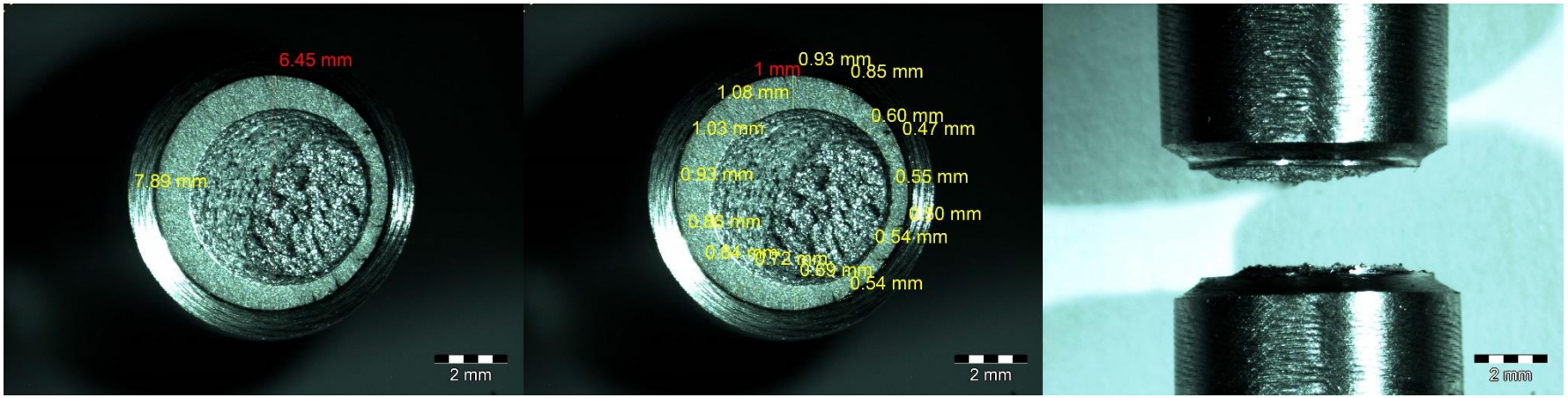

Figure B2. Cross-sectional and side view of fractured SCCRB-05

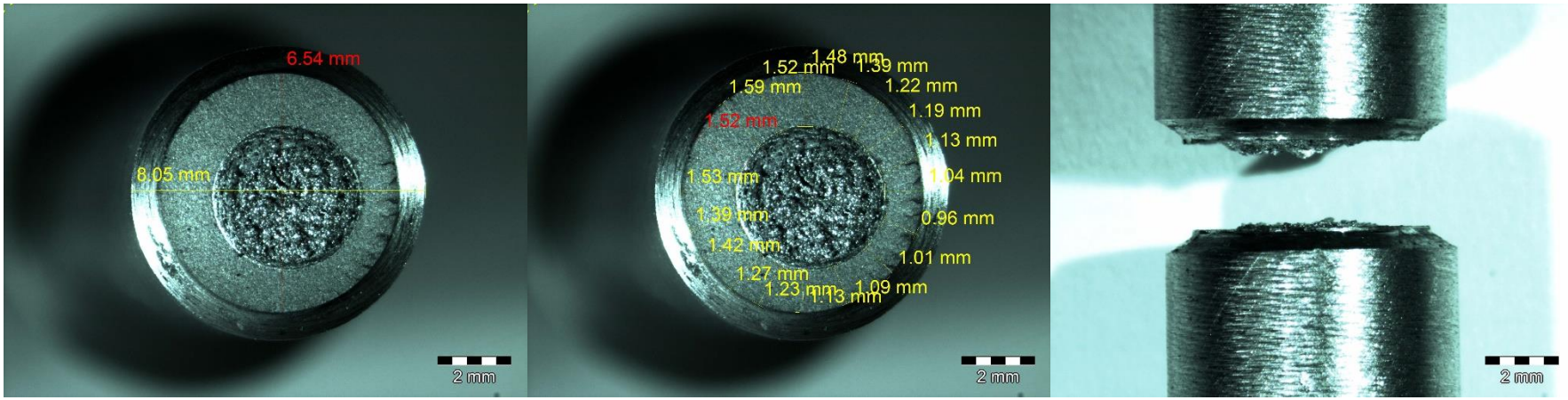

Figure B3. Cross-sectional and side view of fractured SCCRB-06

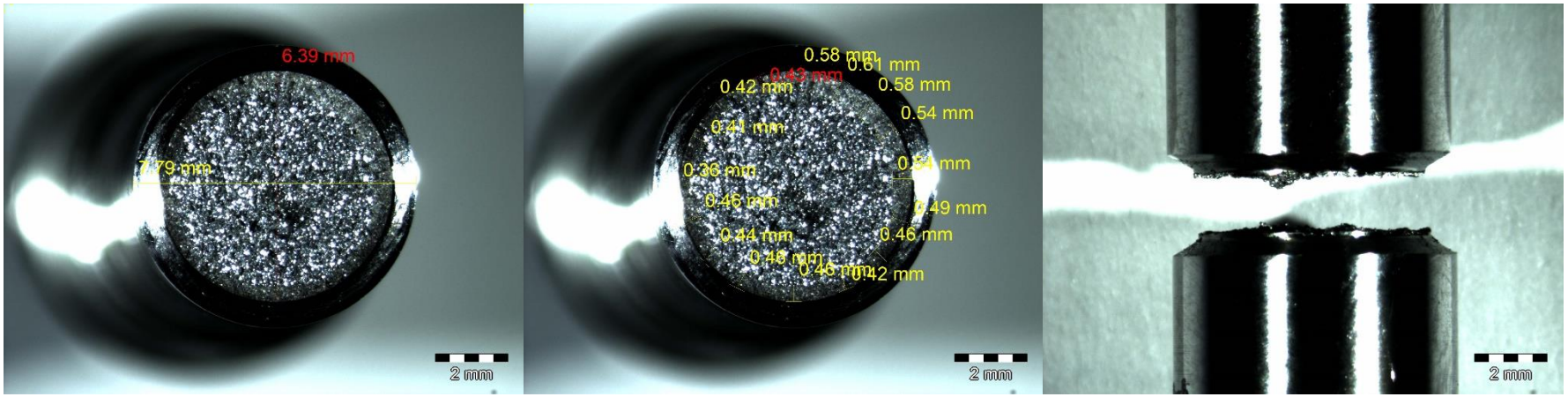

Figure B4. Cross-sectional and side view of fractured ECCRB-01

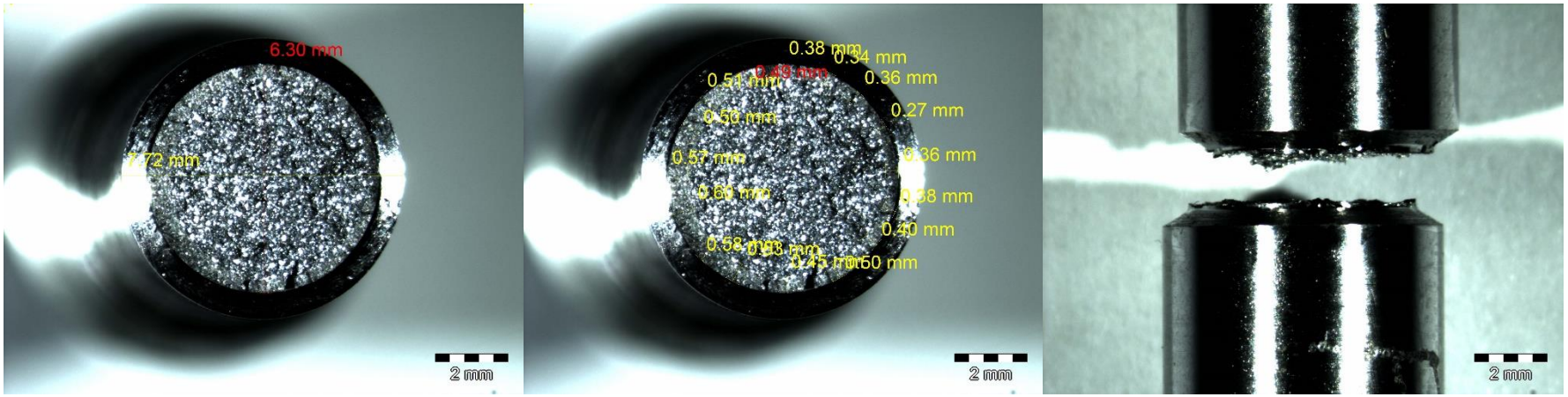

Figure B5. Cross-sectional and side view of fractured ECCRB-02

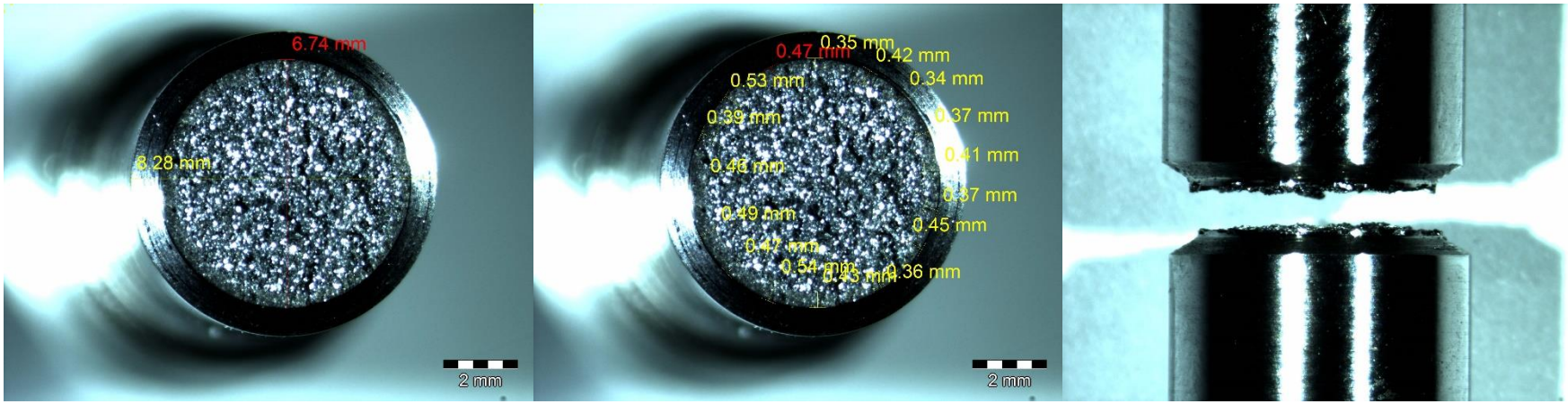

Figure B6. Cross-sectional and side view of fractured ECCRB-03

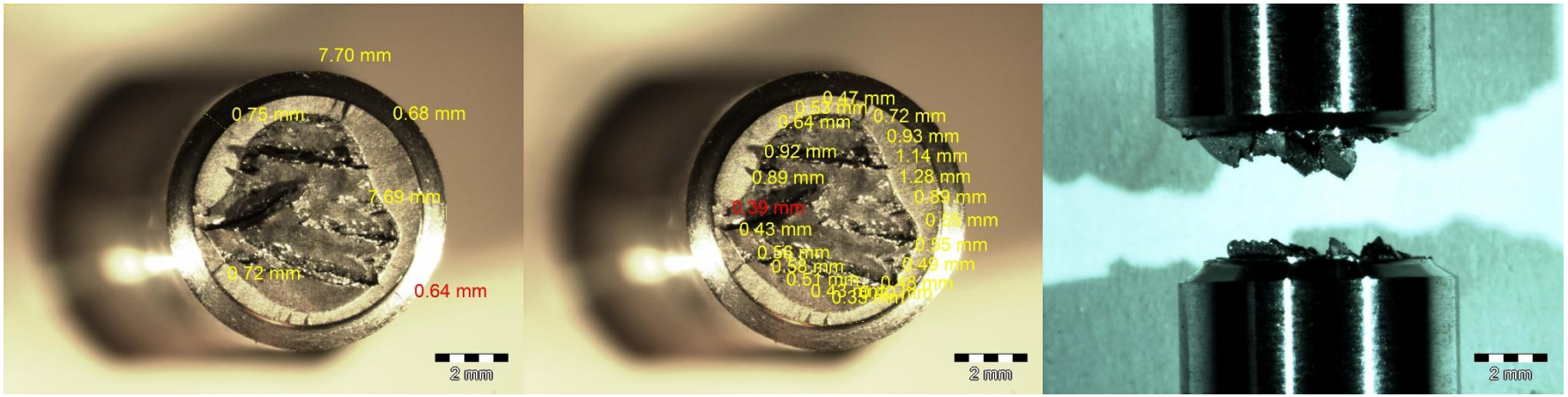

Figure B7. Cross-sectional and side view of fractured StxCCRB-01

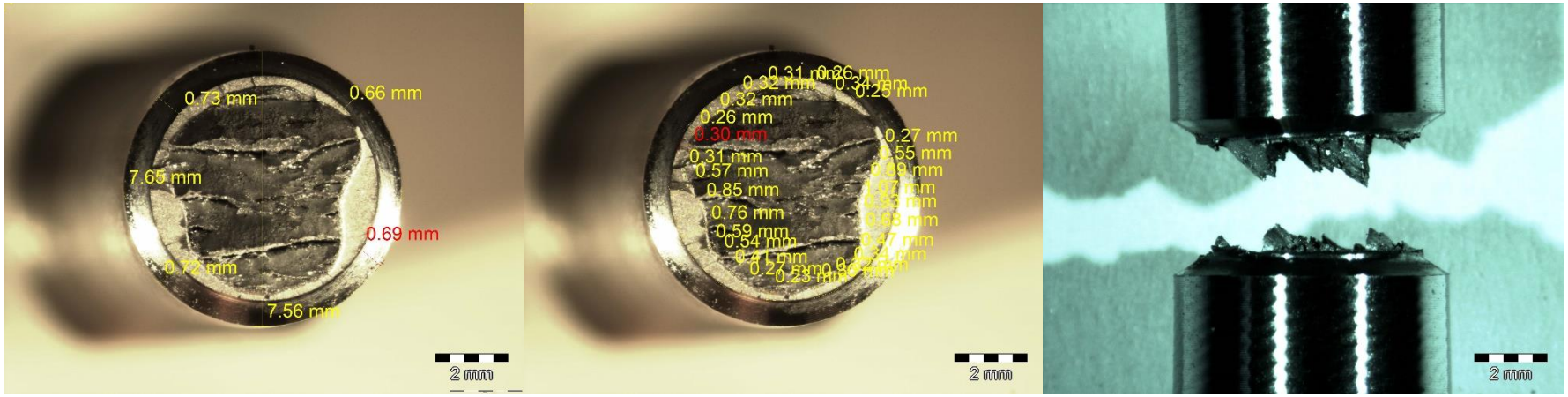

Figure B8. Cross-sectional and side view of fractured StxCCRB-02

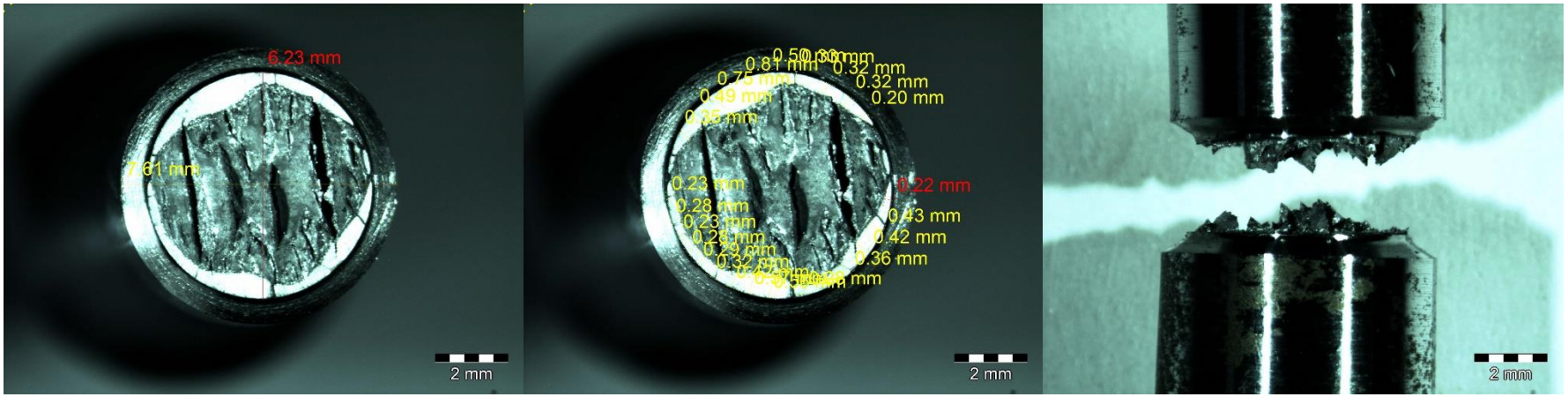

Figure B9. Cross-sectional and side view of fractured StxCCRB-03

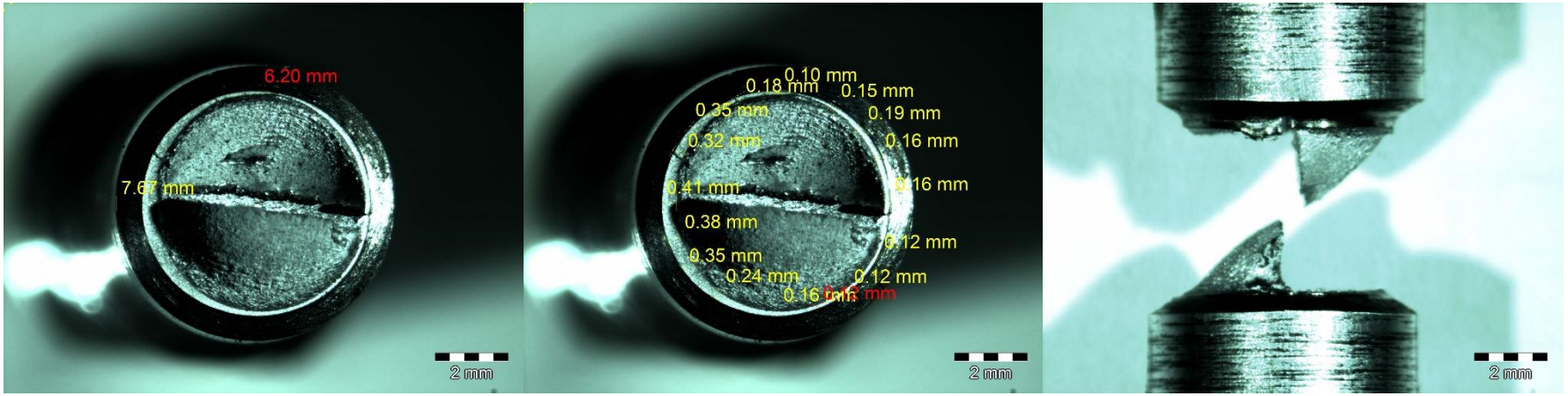

Figure B10. Cross-sectional and side view of fractured StxWSCCRB-01

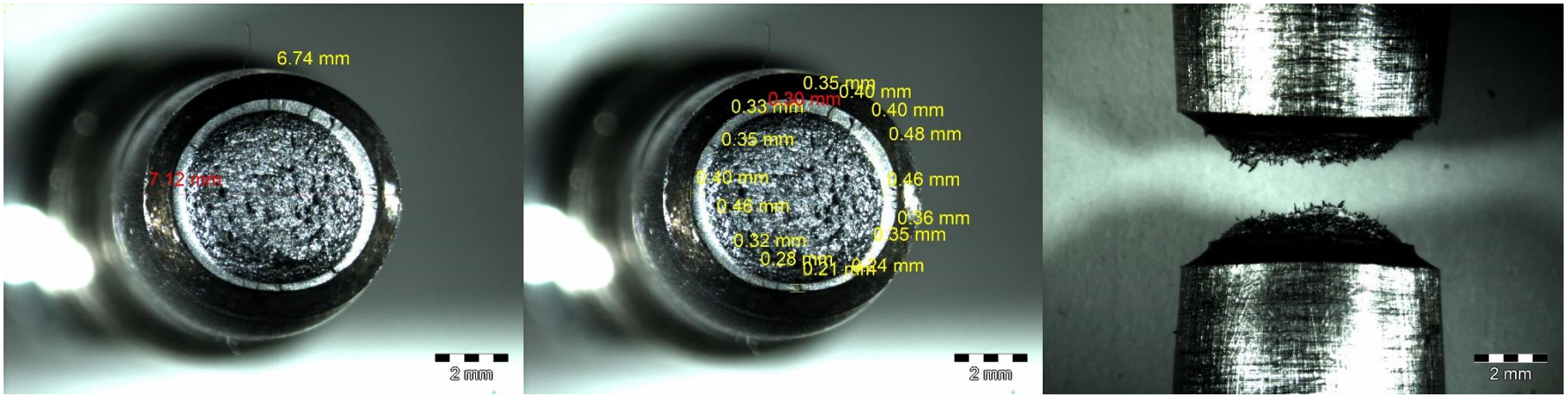

Figure B11. Cross-sectional and side view of fractured StxWSCCRB-02

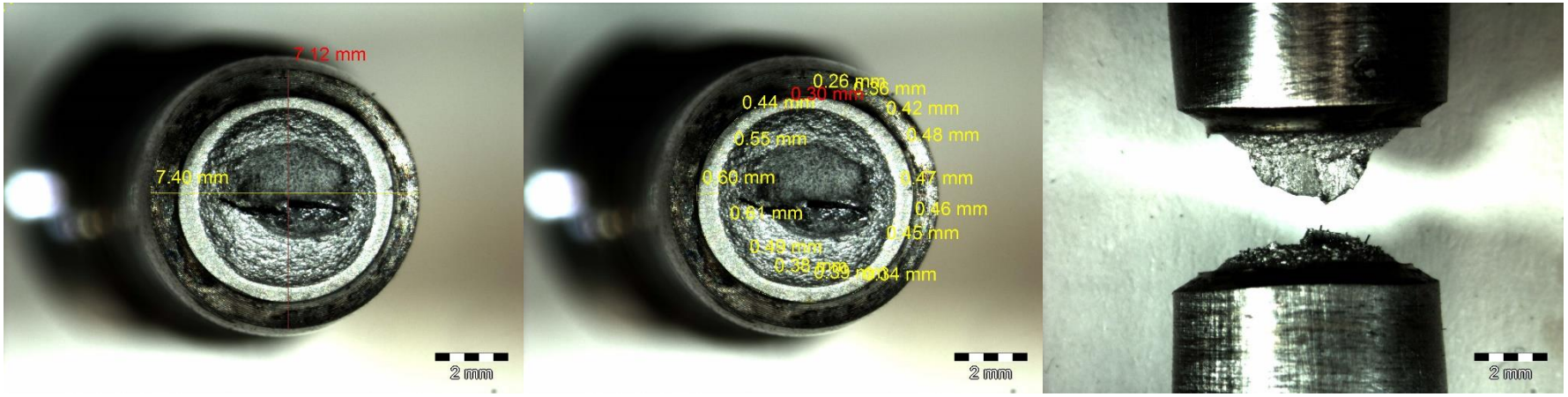

Figure B12. Cross-sectional and side view of fractured StxWSCCRB-03

Appendix C

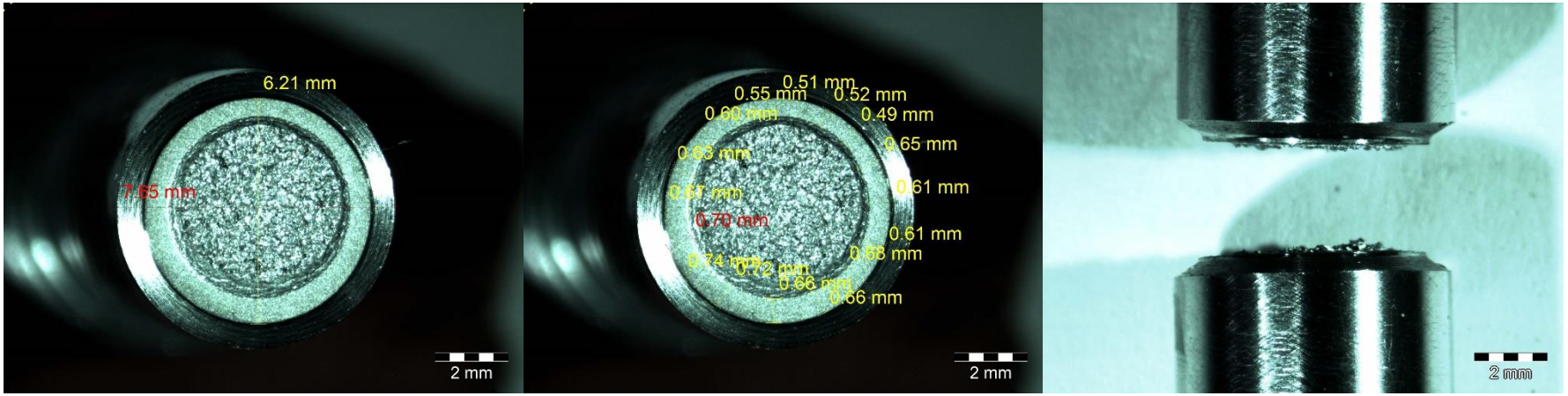

Figure C1. Cross-sectional and side view of fractured S355D-01

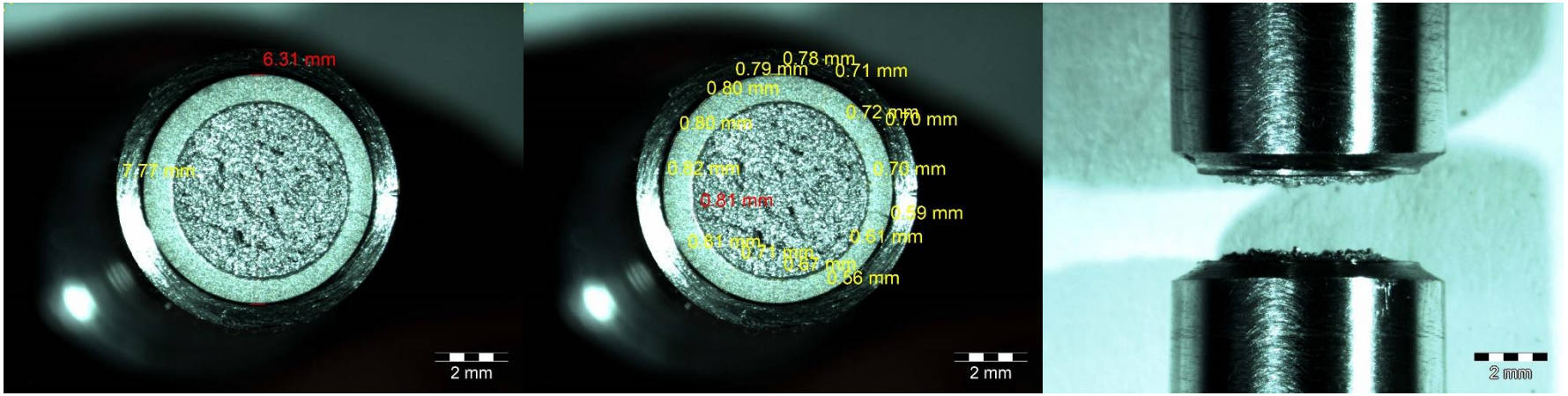

Figure C2. Cross-sectional and side view of fractured S355D-02

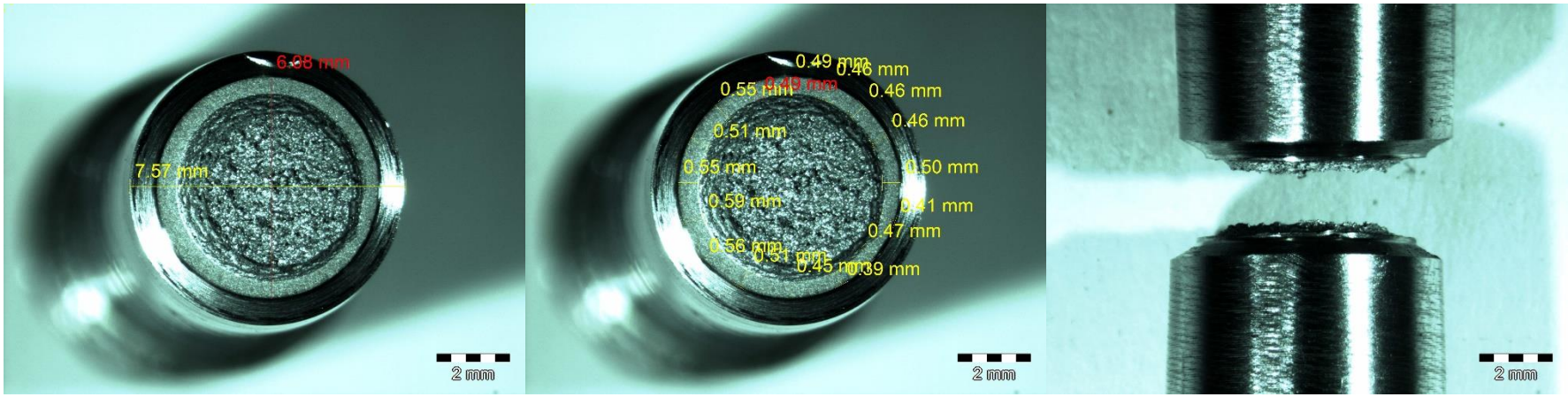

Figure C3. Cross-sectional and side view of fractured S355D-03

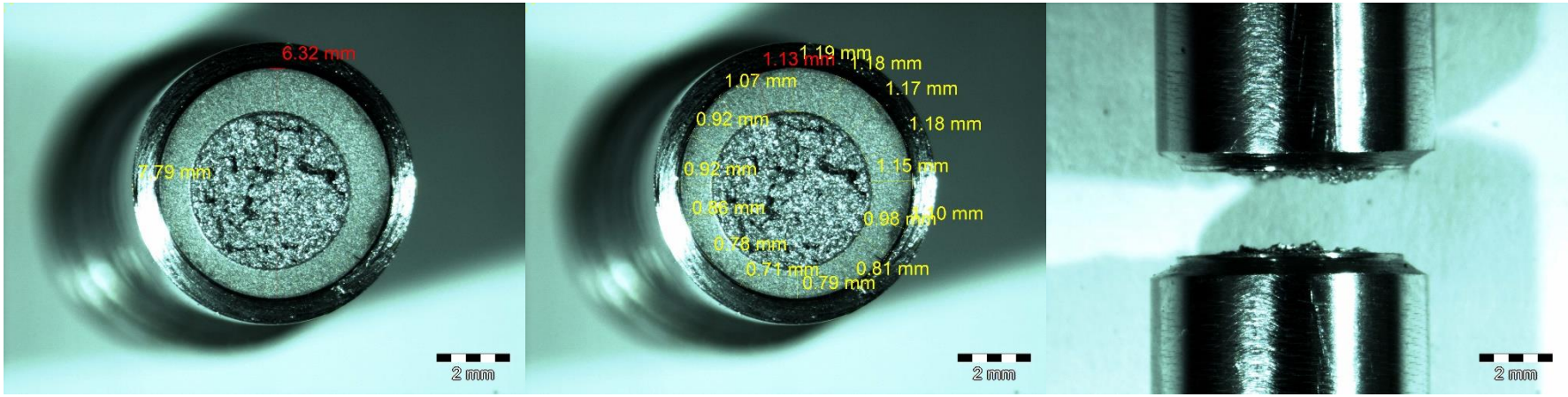

Figure C4. Cross-sectional and side view of fractured S355D-04

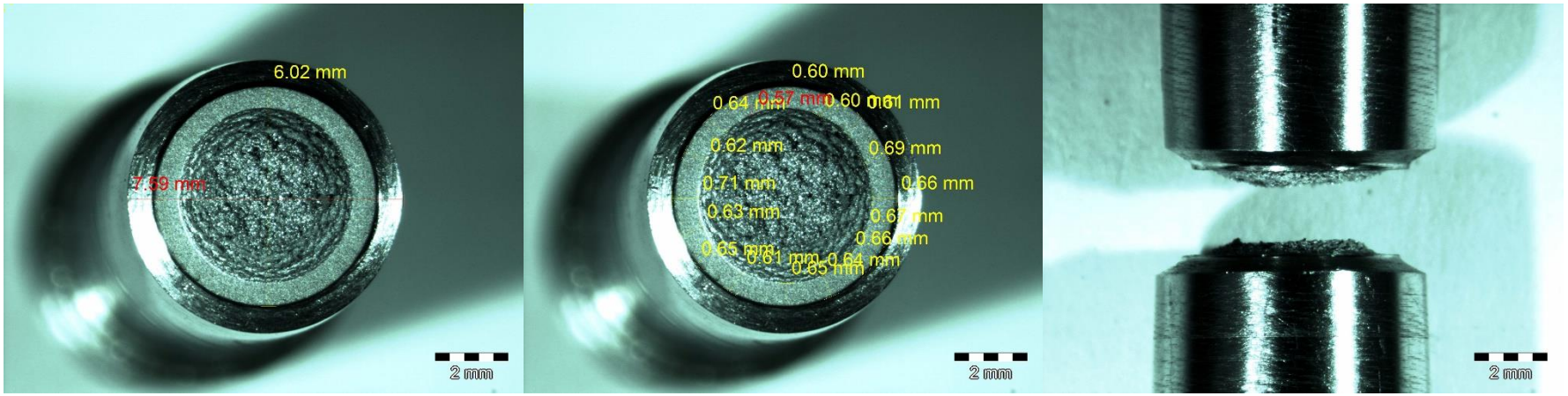

Figure C5. Cross-sectional and side view of fractured S355D-05

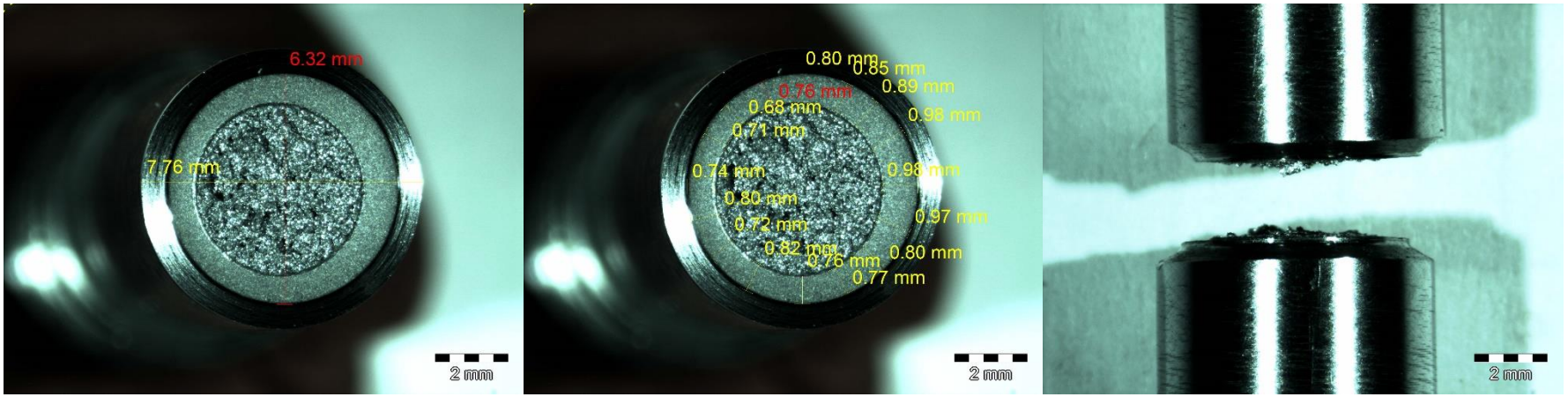

Figure C6. Cross-sectional and side view of fractured S355D-06

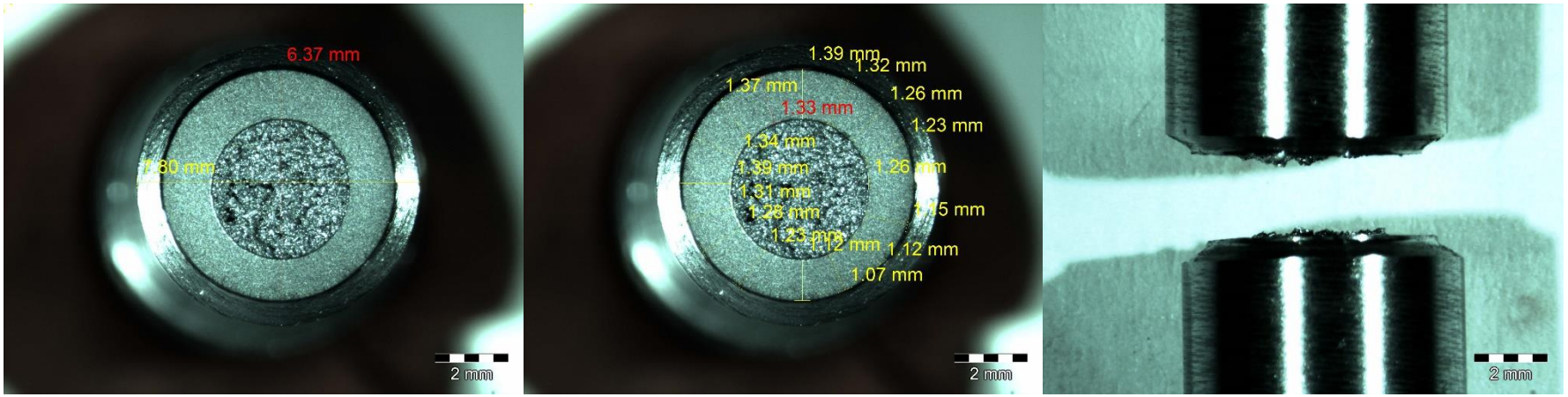

Figure C7. Cross-sectional and side view of fractured S355D-07

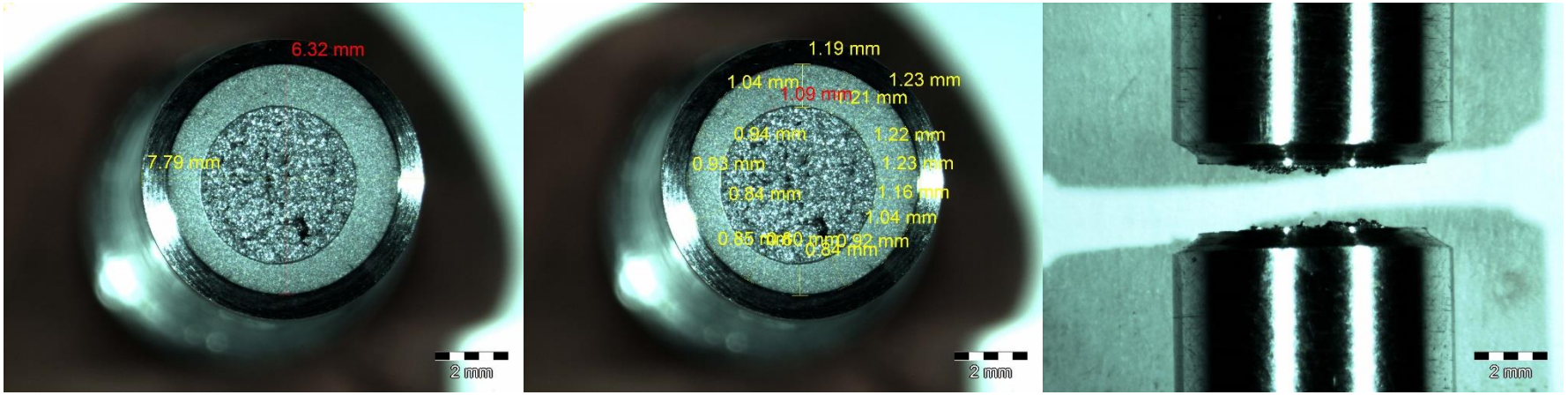

Figure C8. Cross-sectional and side view of fractured S355D-08

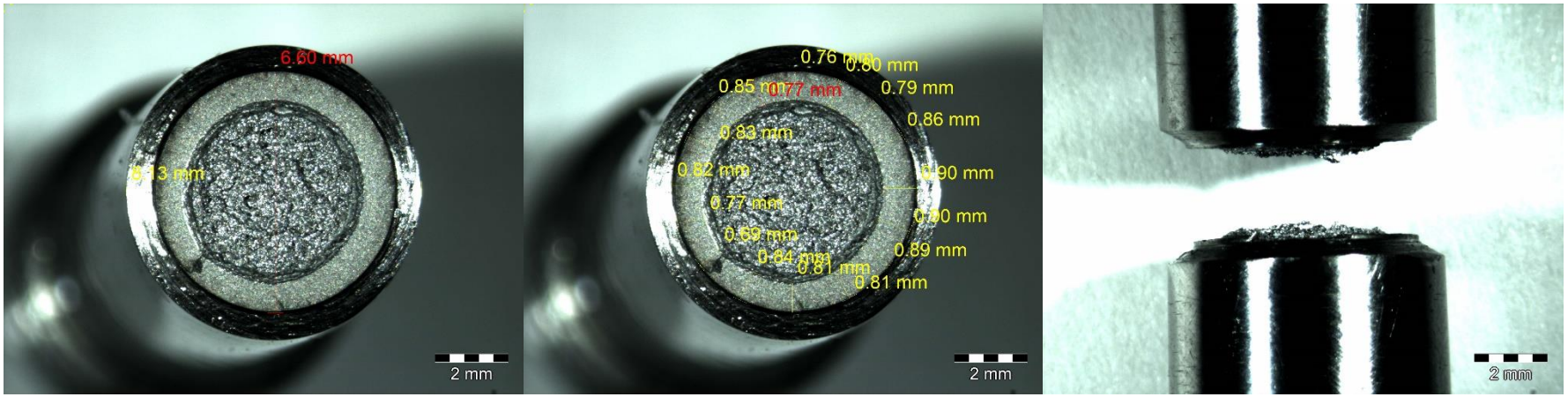

Figure C9. Cross-sectional and side view of fractured S355LSD01

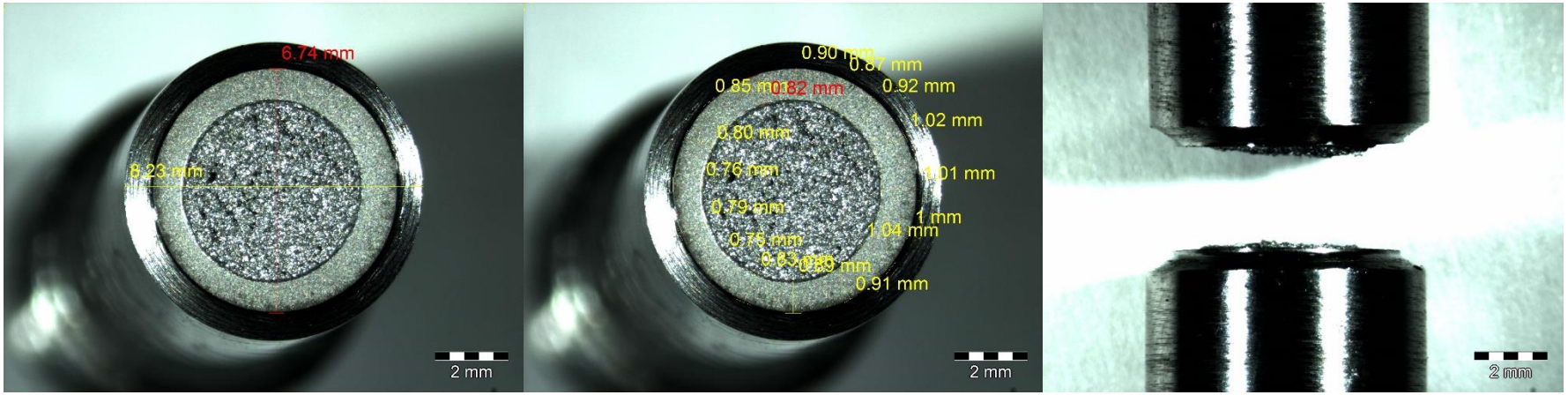

Figure C10. Cross-sectional and side view of fractured S355LSD-02

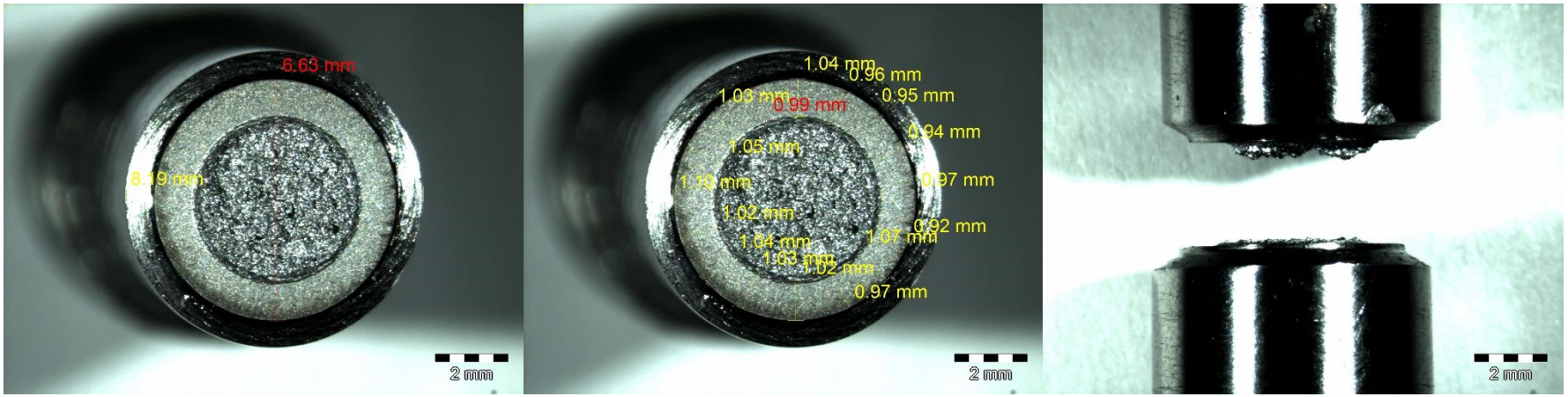

Figure C11. Cross-sectional and side view of fractured S355LSD-03

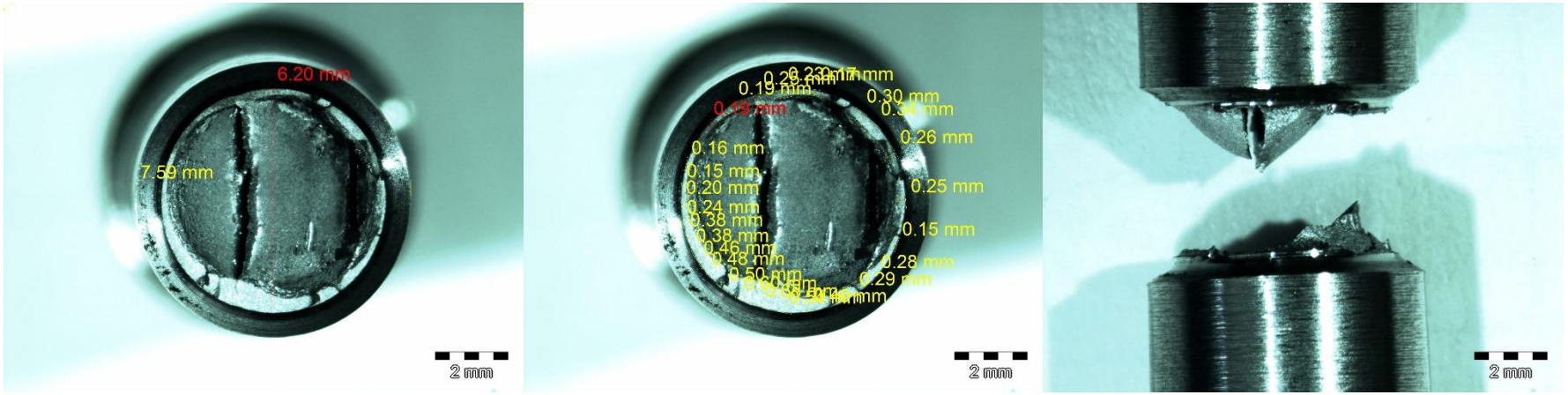

Figure C12. Cross-sectional and side view of fractured StxD-01

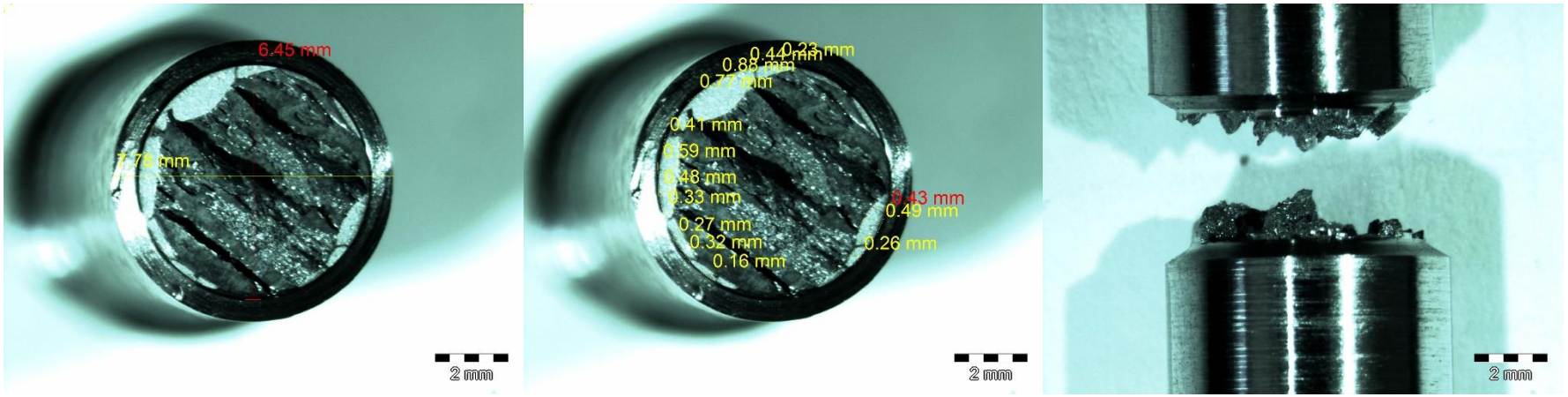

Figure C13. Cross-sectional and side view of fractured StxD-02

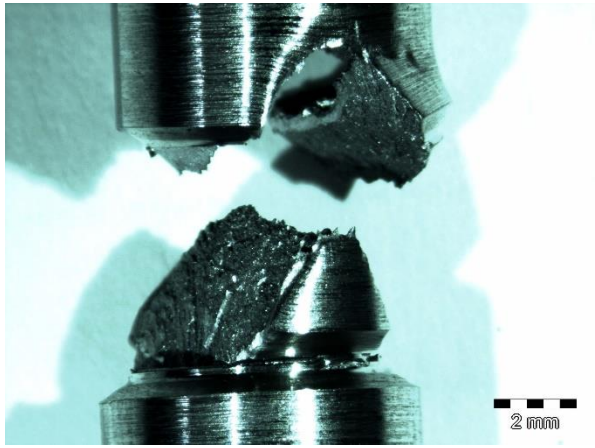

Figure C14. Side view of fractured StxD-03

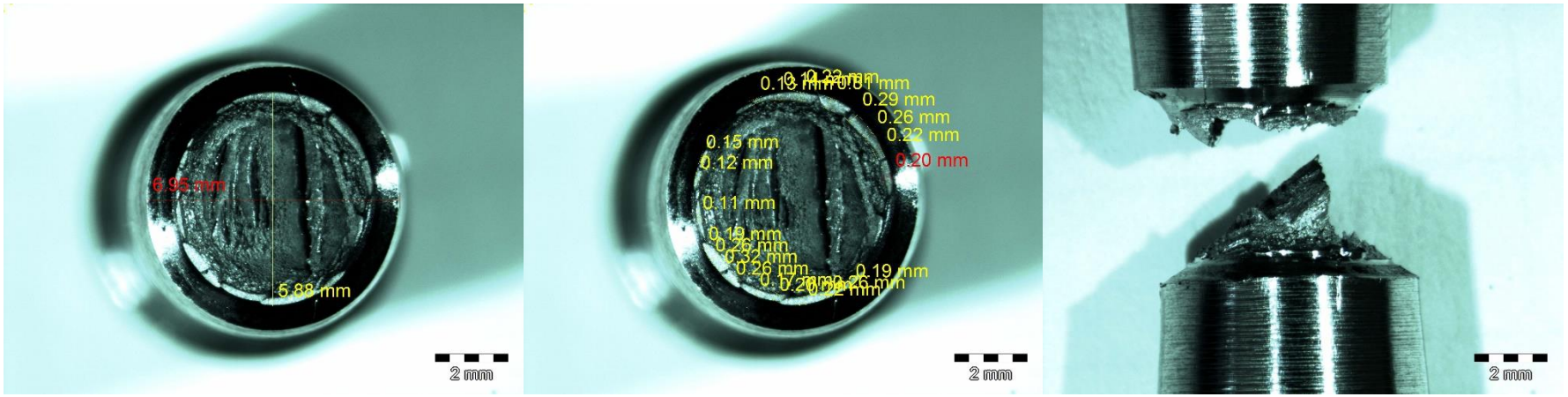

Figure C15. Cross-sectional and side view of fractured StxD-04

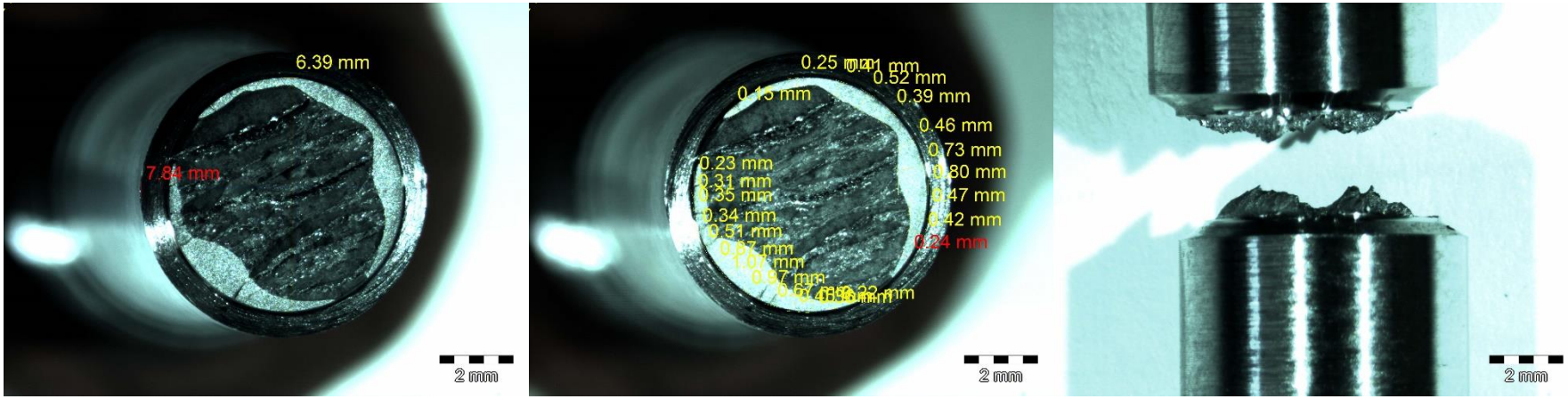

Figure C16. Cross-sectional and side view of fractured StxD-05

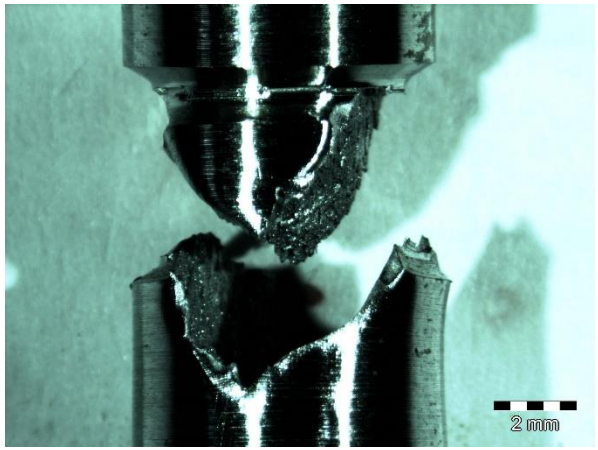

Figure C17. Side view of fractured StxD-06

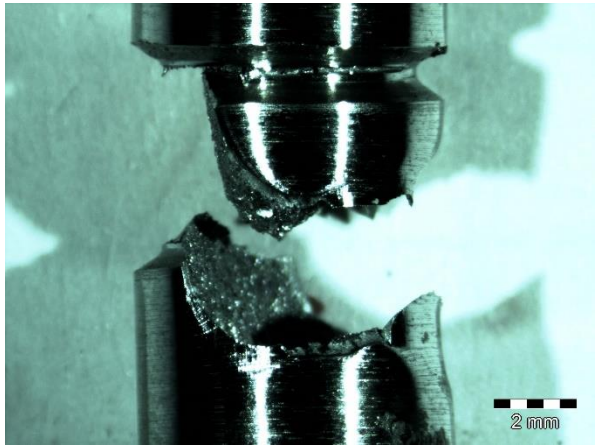

Figure C18. Side view of fractured StxD-07

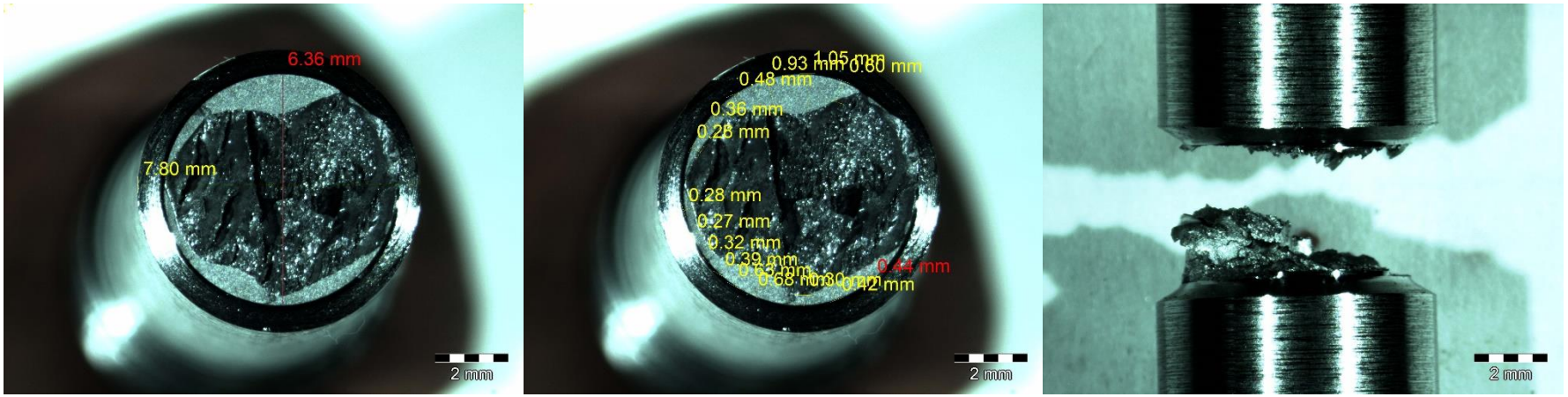

Figure C19. Cross-sectional and side view of fractured StxD-08

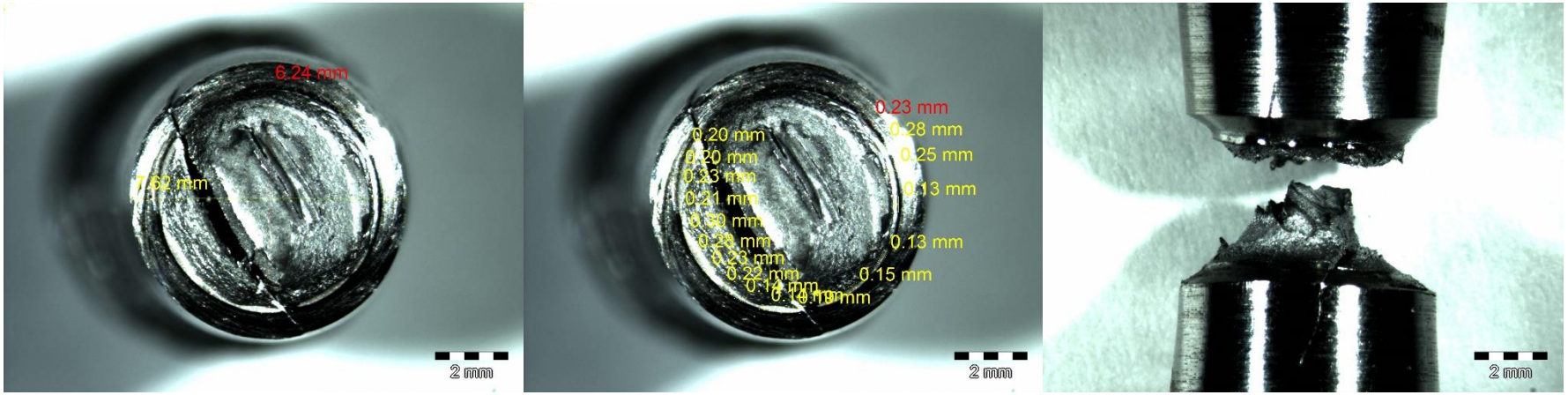

Figure C20. Cross-sectional and side view of fractured StxLSD-01

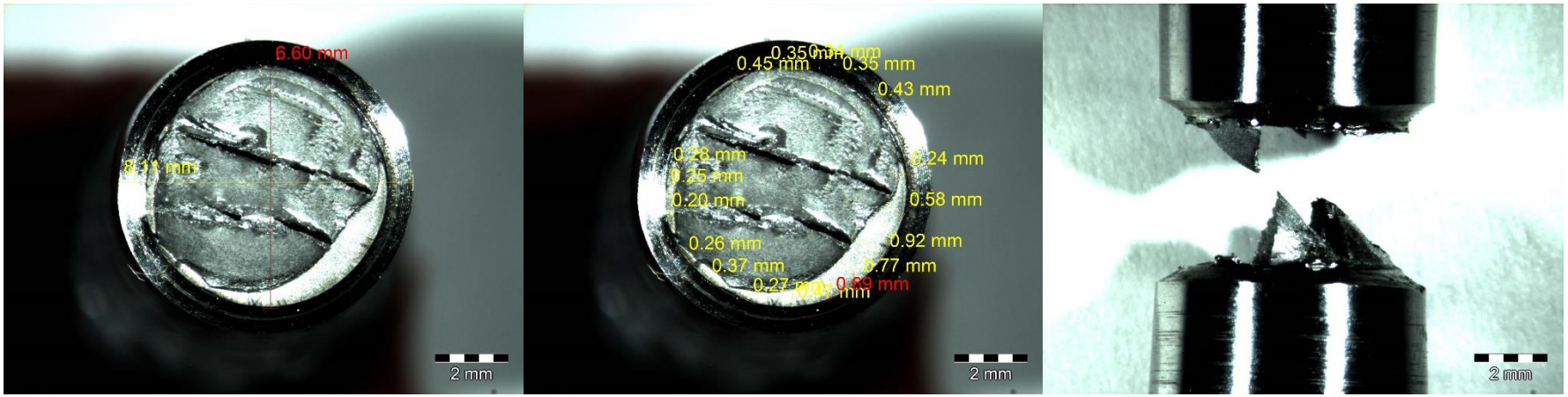

Figure C21. Cross-sectional and side view of fractured StxLSD-02

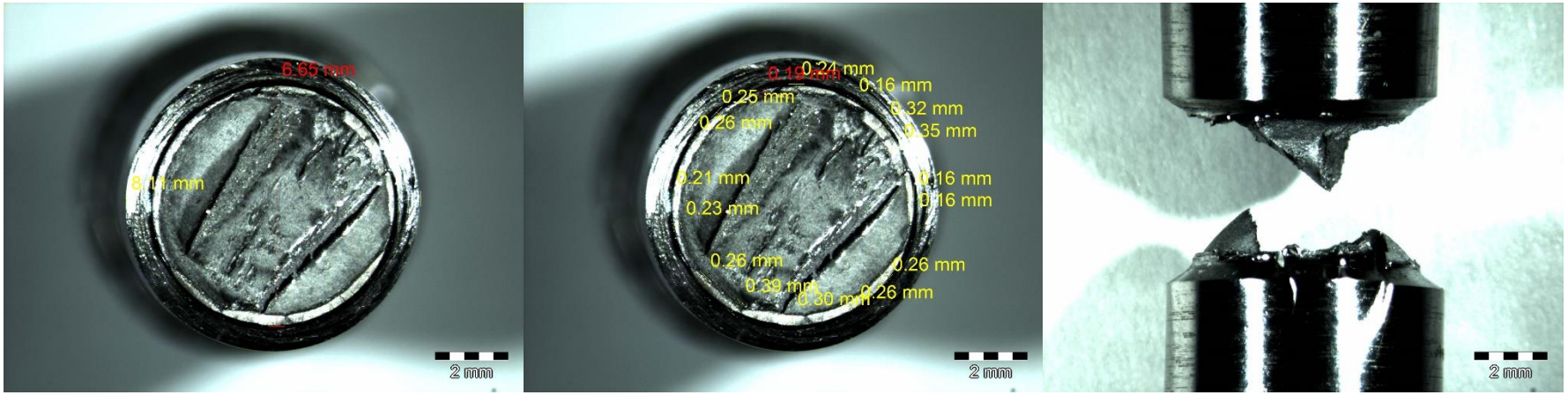

Figure C22. Cross-sectional and side view of fractured StxLSD-03

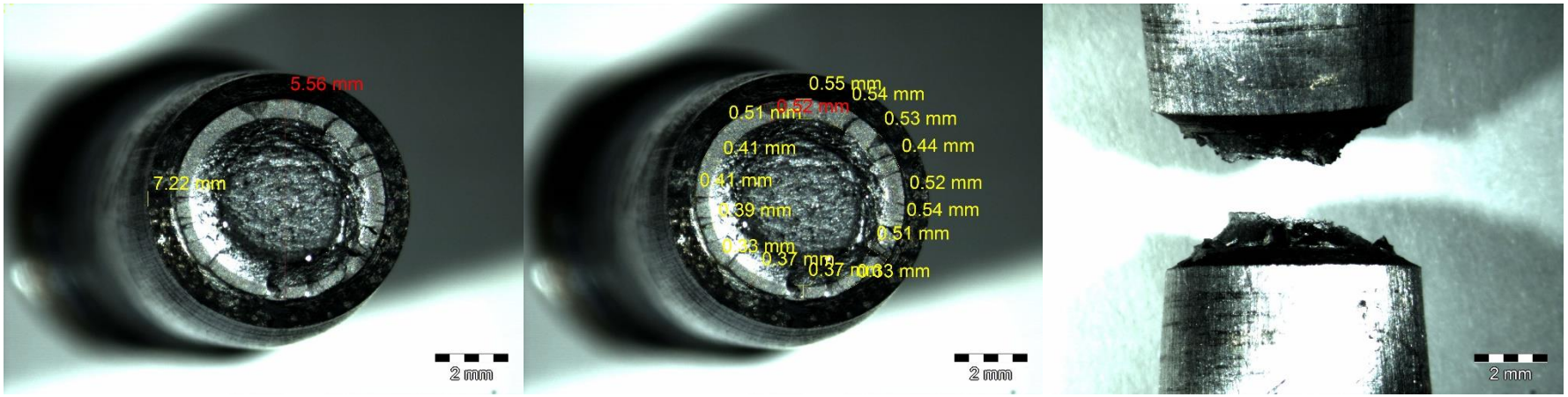

Figure C23. Cross-sectional and side view of fractured StxWSD-01

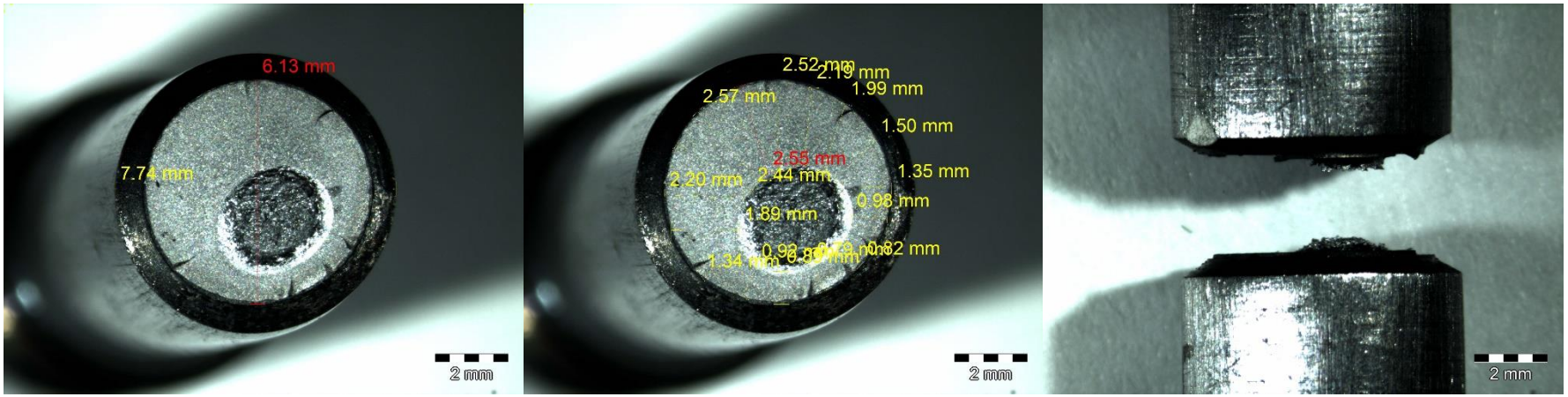

Figure C24. Cross-sectional and side view of fractured StxWSD-02

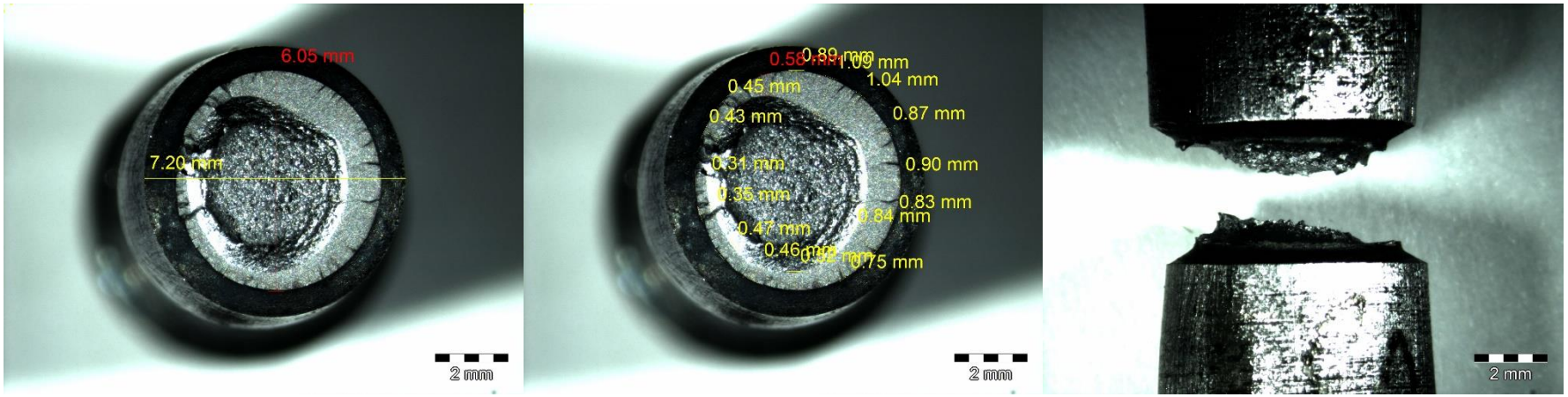

Figure C25. Cross-sectional and side view of fractured StxWSD-03

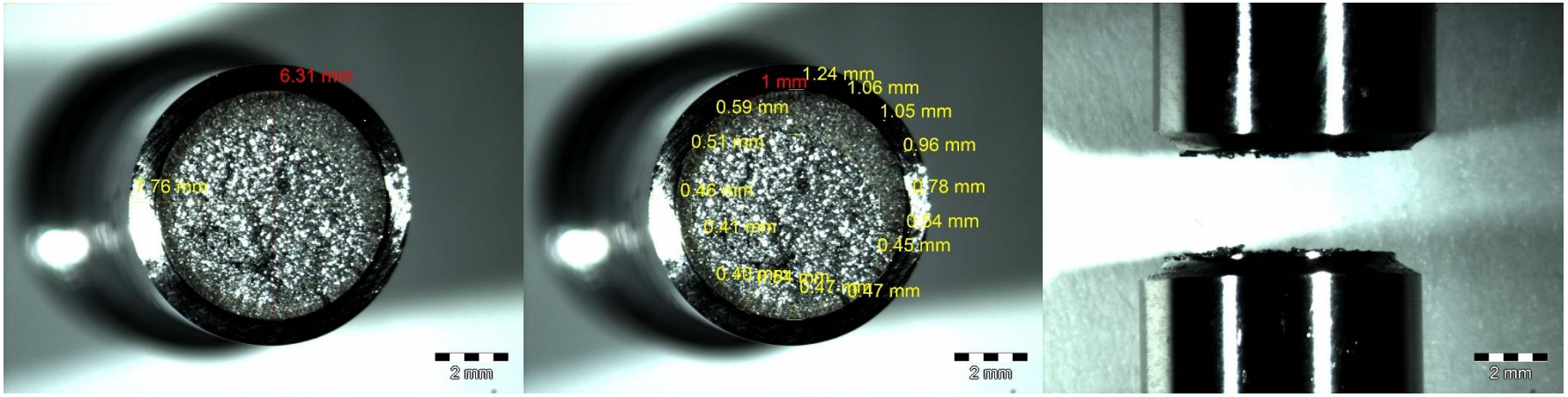

Figure C26. Cross-sectional and side view of fractured ED-01

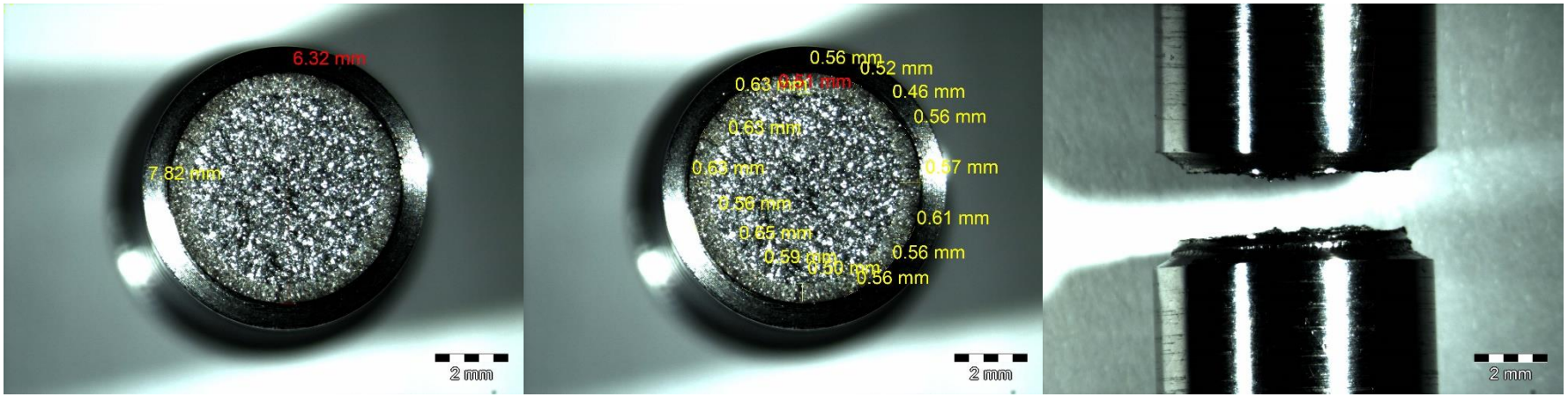

Figure C27. Cross-sectional and side view of fractured ED-02

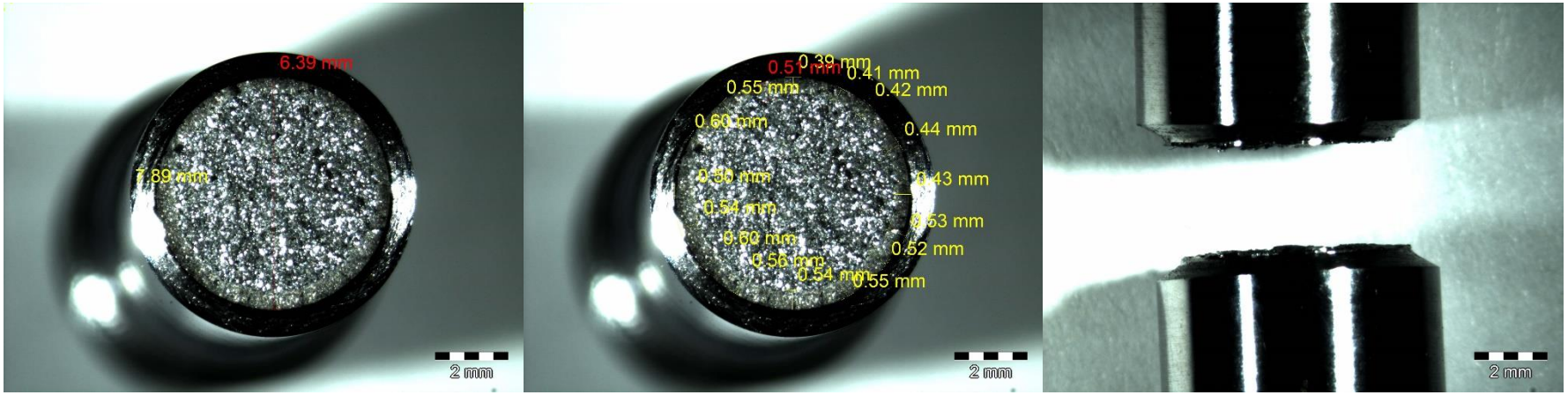

Figure C28. Cross-sectional and side view of fractured ED-03

Appendix D

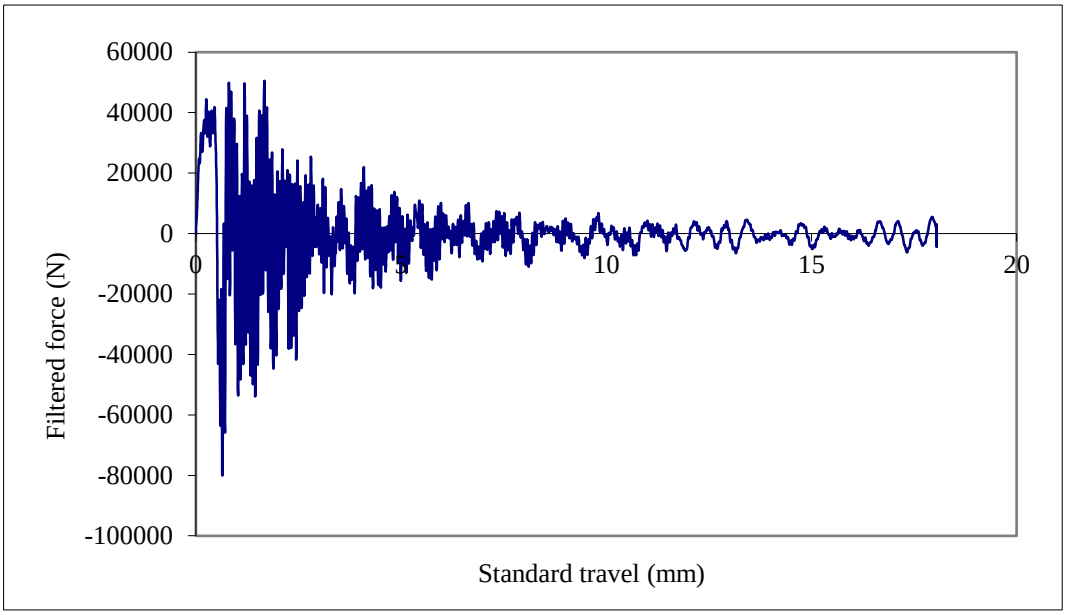

Figure D1. Force – displacement plot of S355D-01

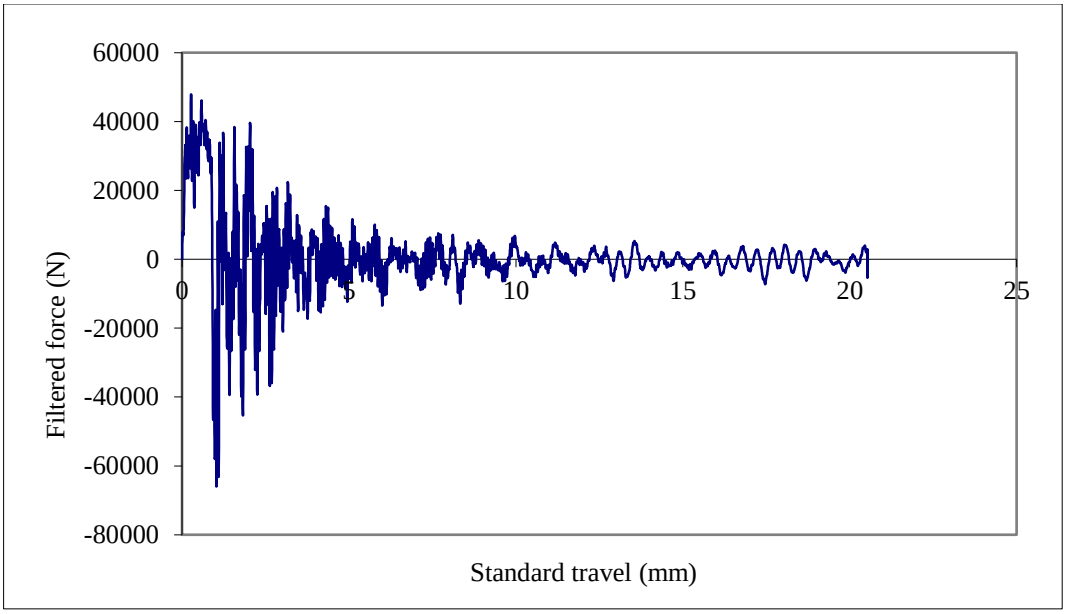

Figure D2. Force – displacement plot of S355D-02

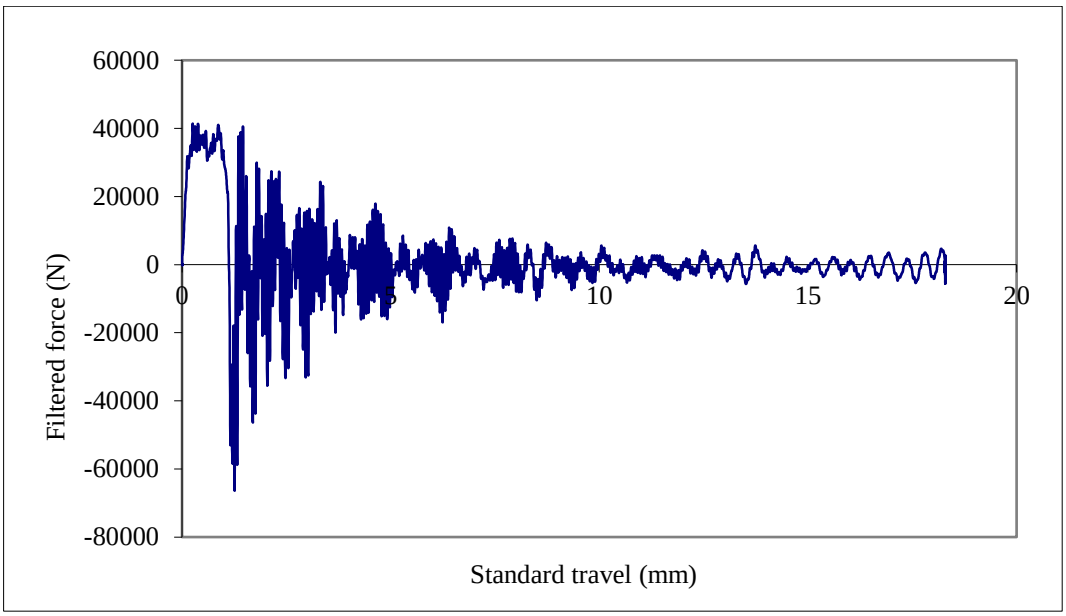

Figure D3. Force – displacement plot of S355D-03

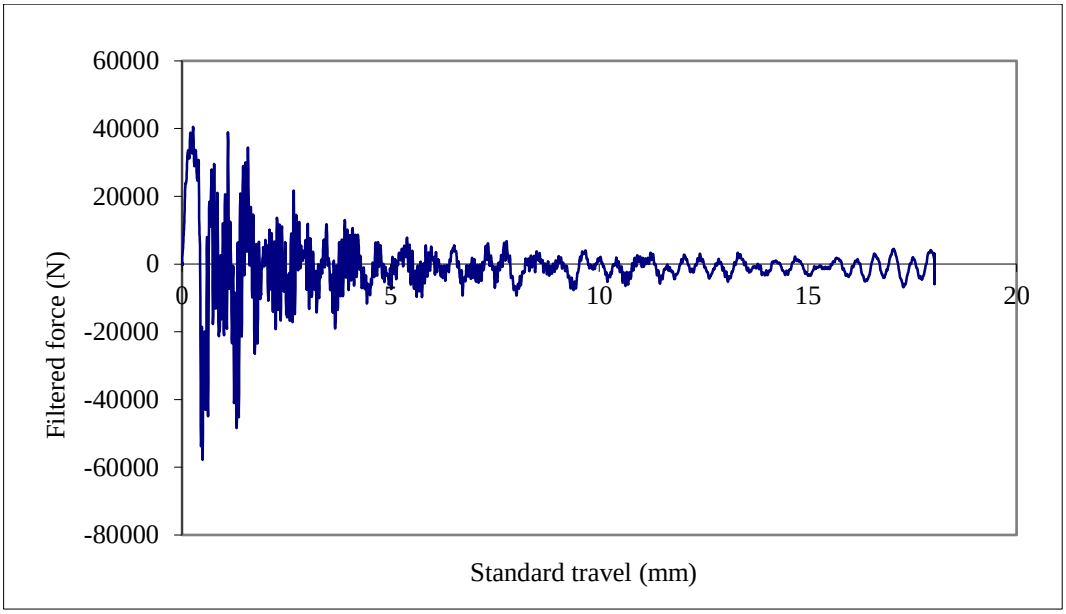

Figure D4. Force – displacement plot of S355D-04

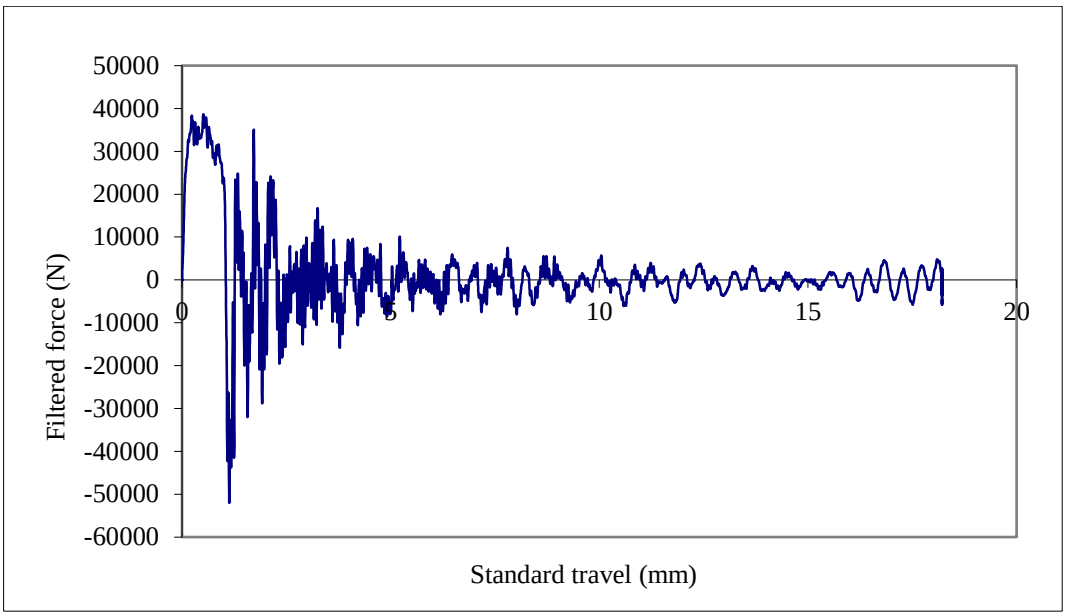

Figure D5. Force – displacement plot of S355D-05

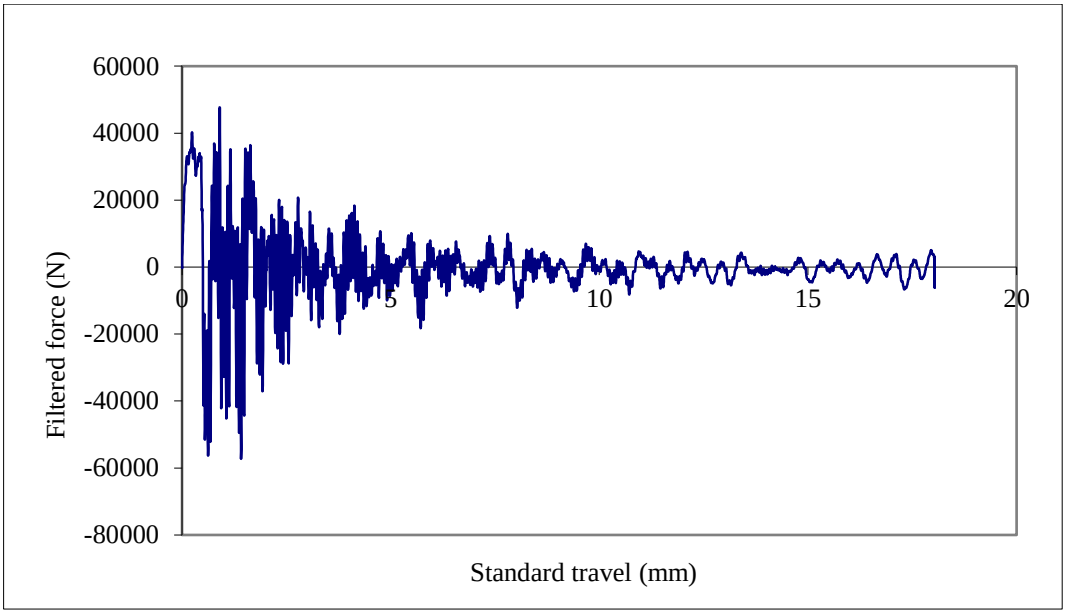

Figure D6. Force – displacement plot of S355D-06

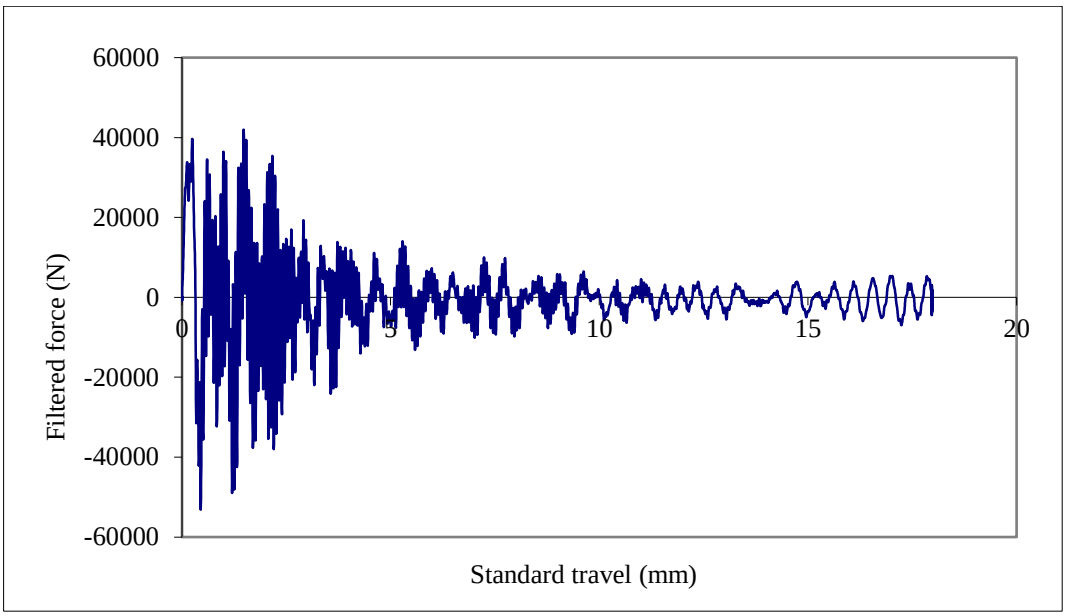

Figure D7. Force – displacement plot of S355D-07

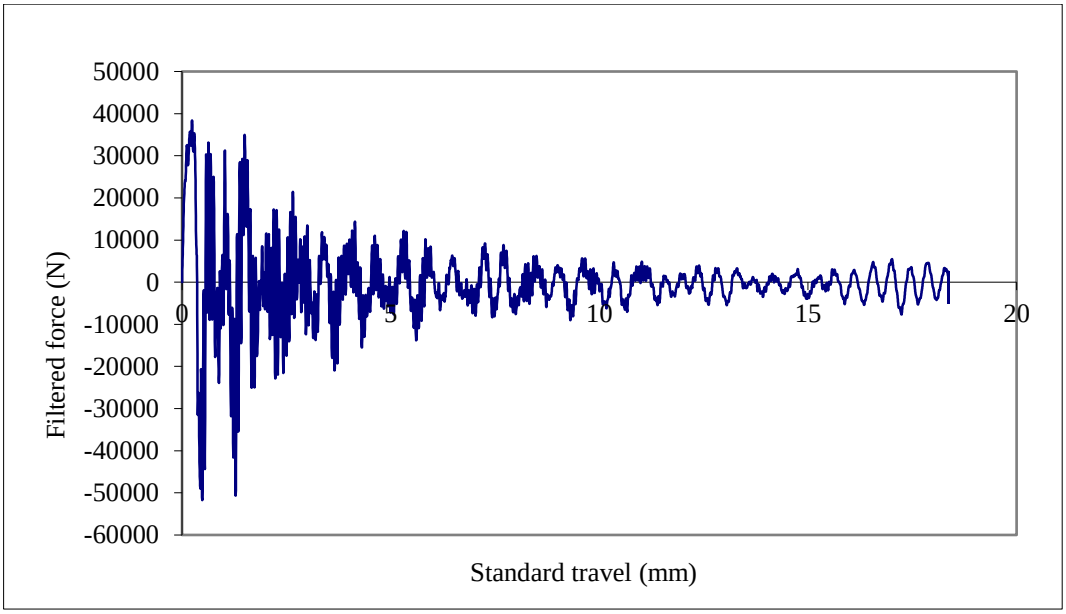

Figure D8. Force – displacement plot of S355D-08

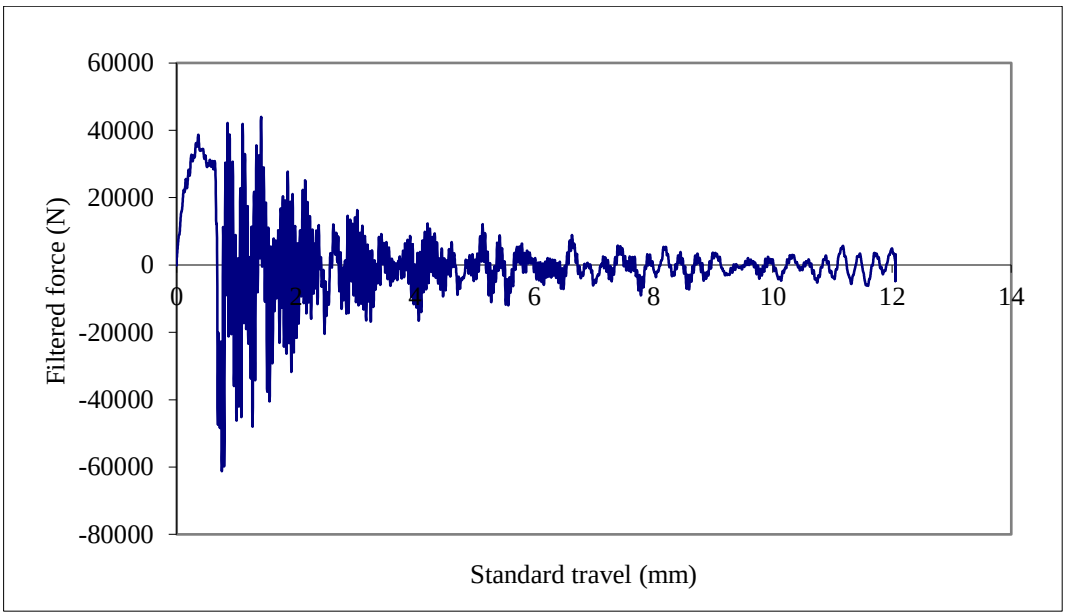

Figure D9. Force – displacement plot of S355LSD-01

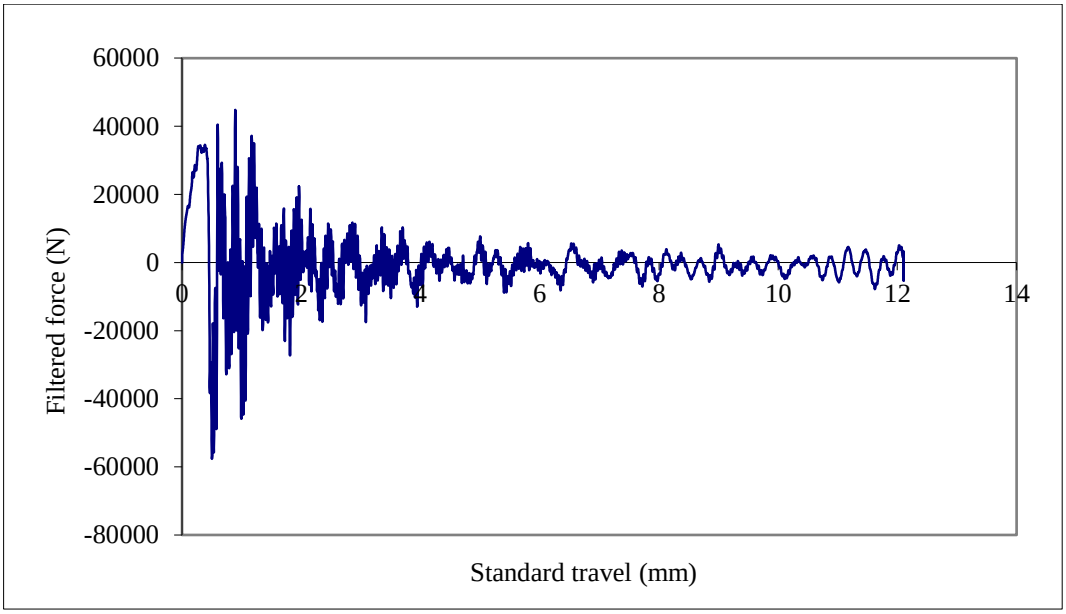

Figure D10. Force – displacement plot of S355LSD-02

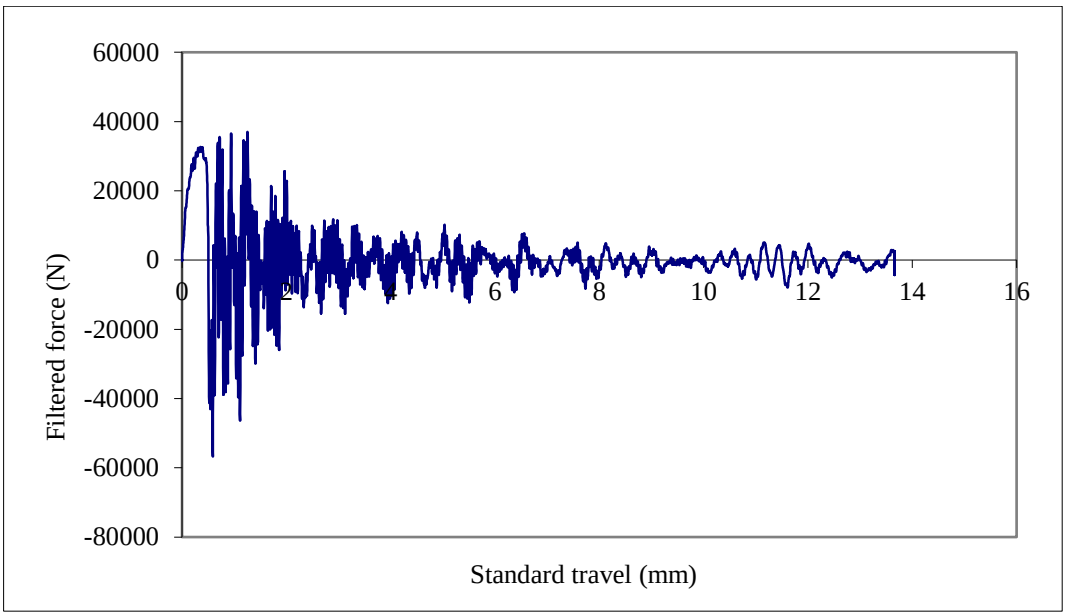

Figure D11. Force – displacement plot of S355LSD-03

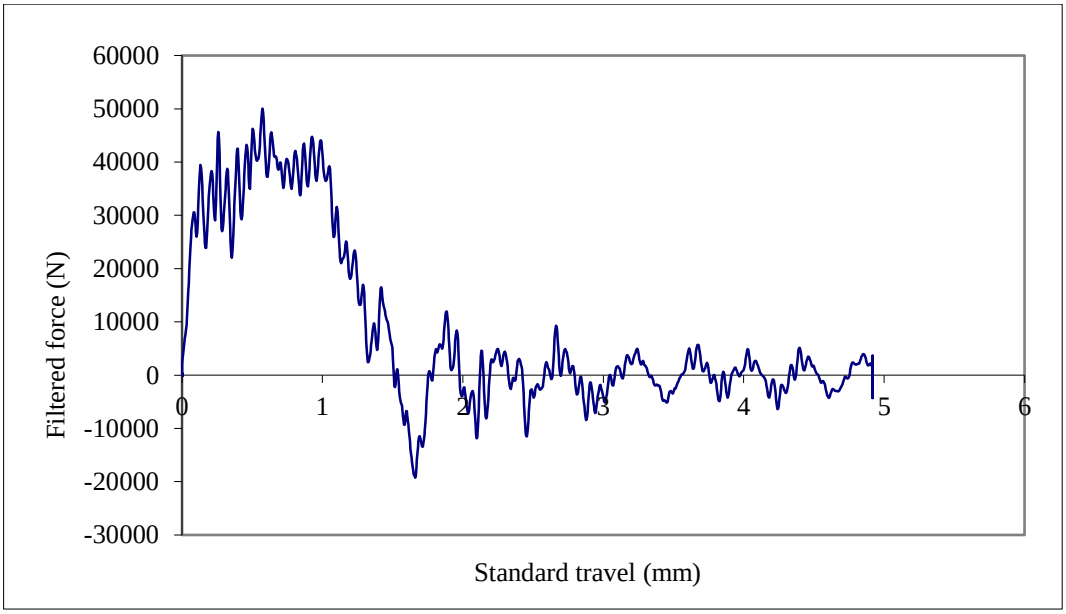

Figure D12. Force – displacement plot of StxD-01

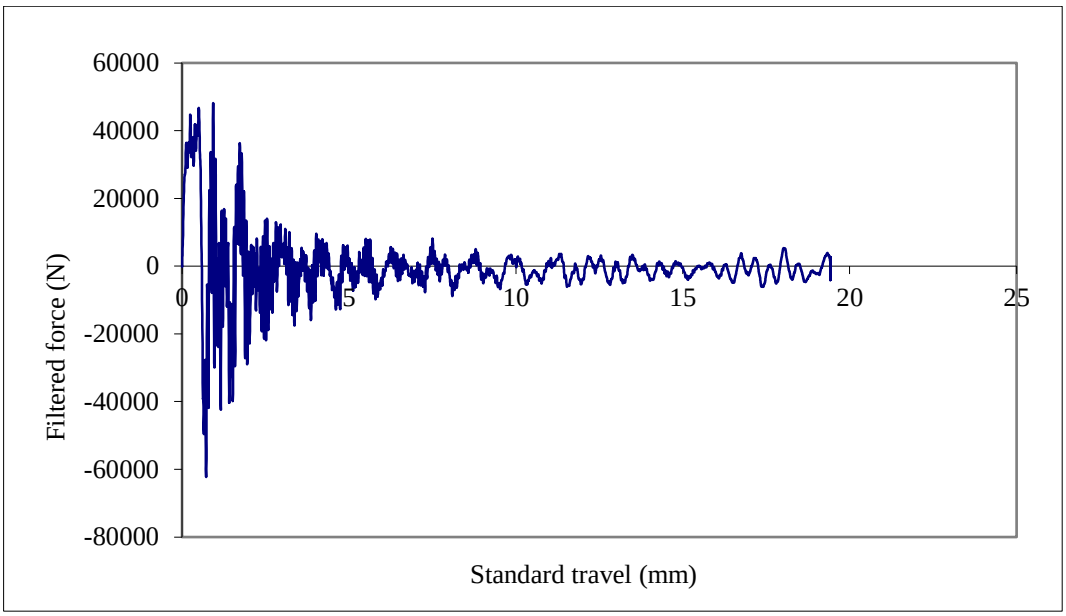

Figure D13. Force – displacement plot of StxD-02

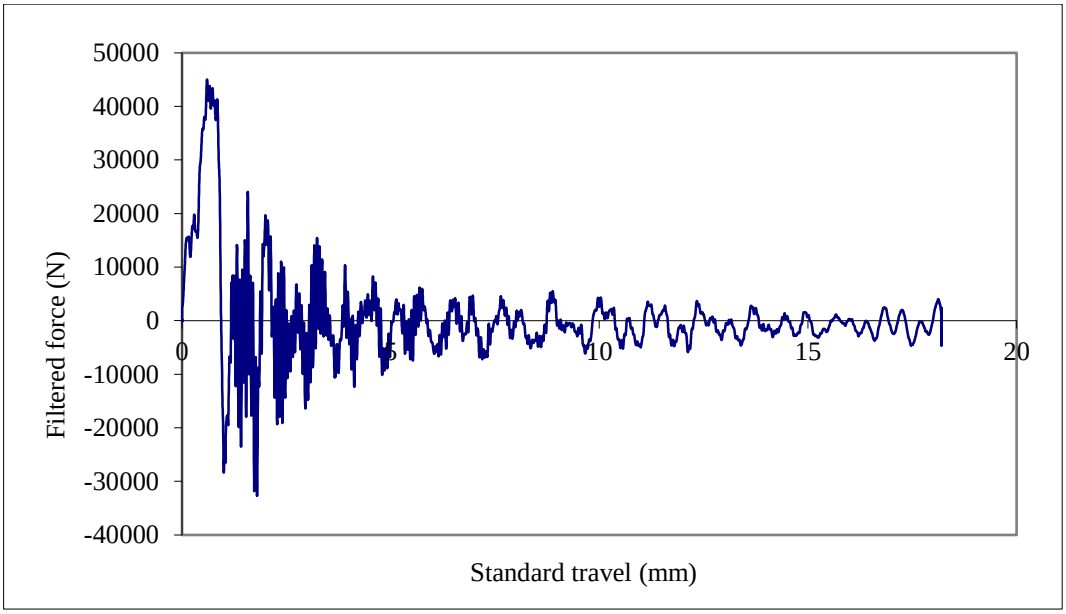

Figure D14. Force – displacement plot of StxD-03

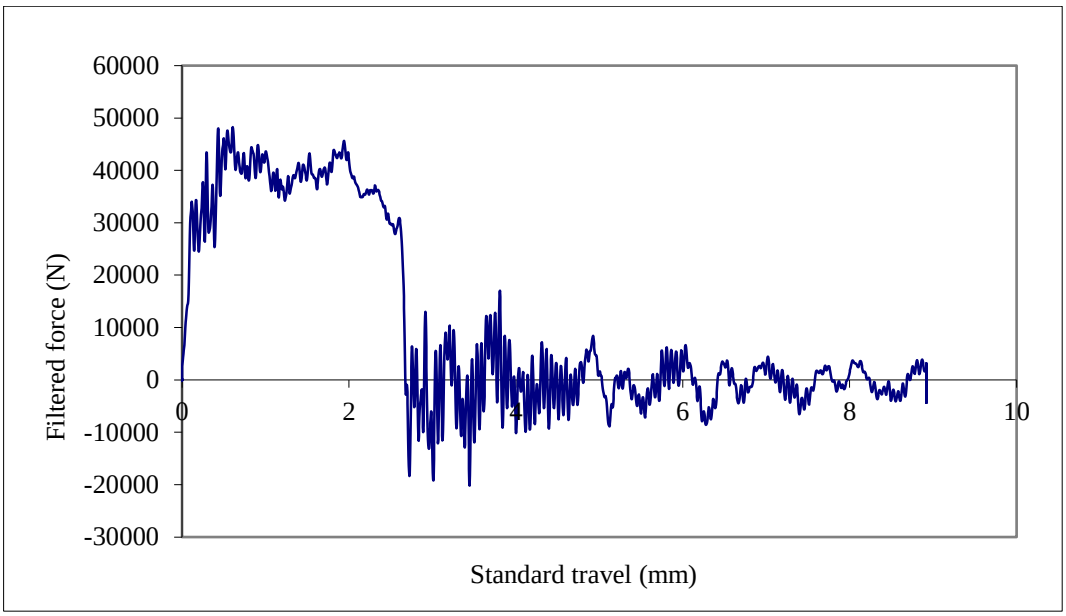

Figure D15. Force – displacement plot of StxD-04

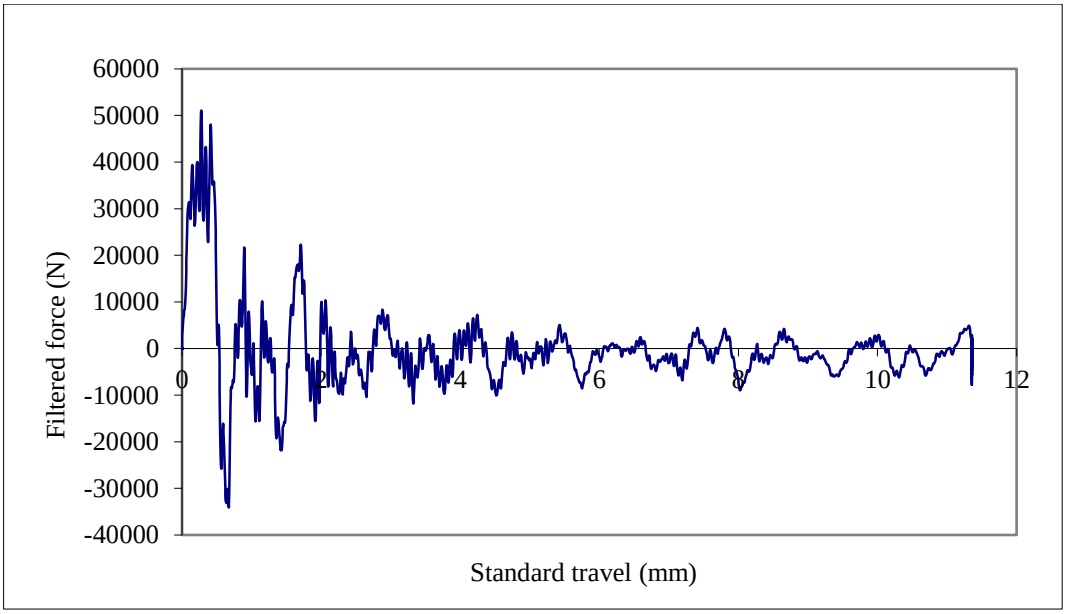

Figure D16. Force – displacement plot of StxD-05

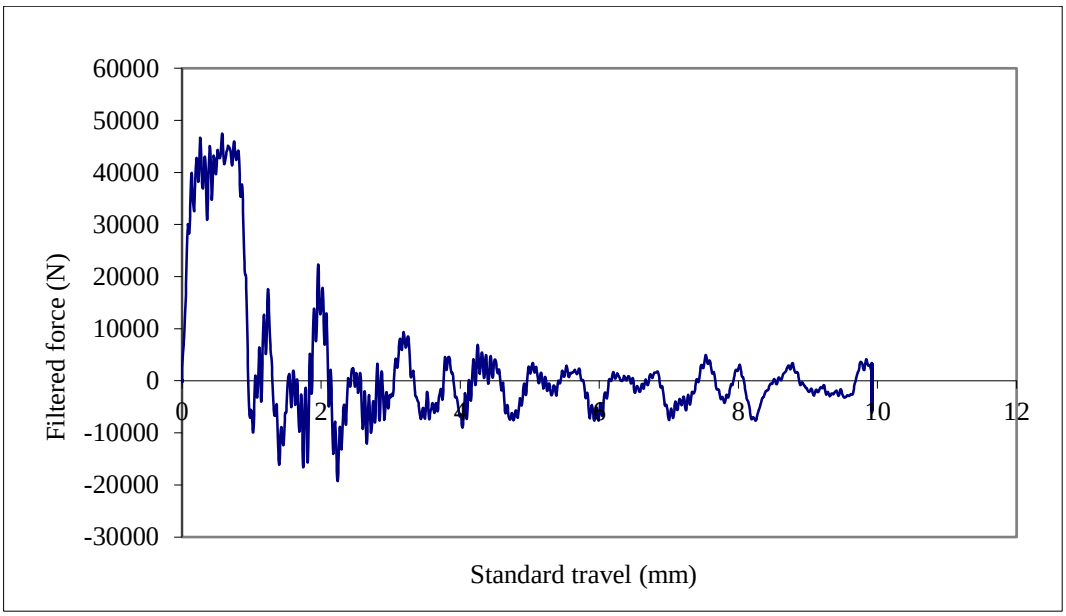

Figure D17. Force – displacement plot of StxD-06

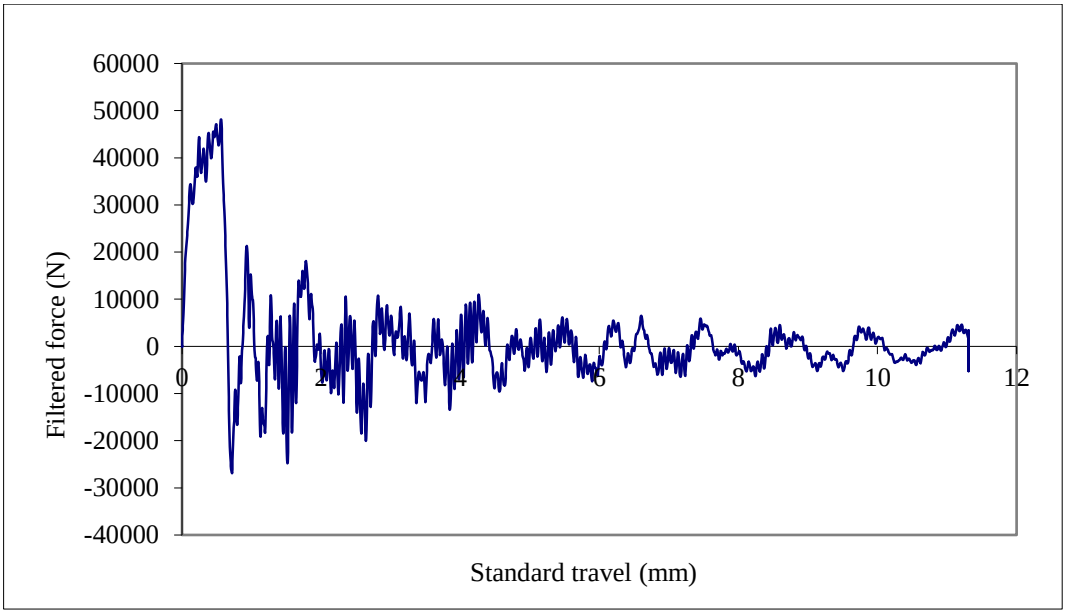

Figure D18. Force – displacement plot of StxD-07

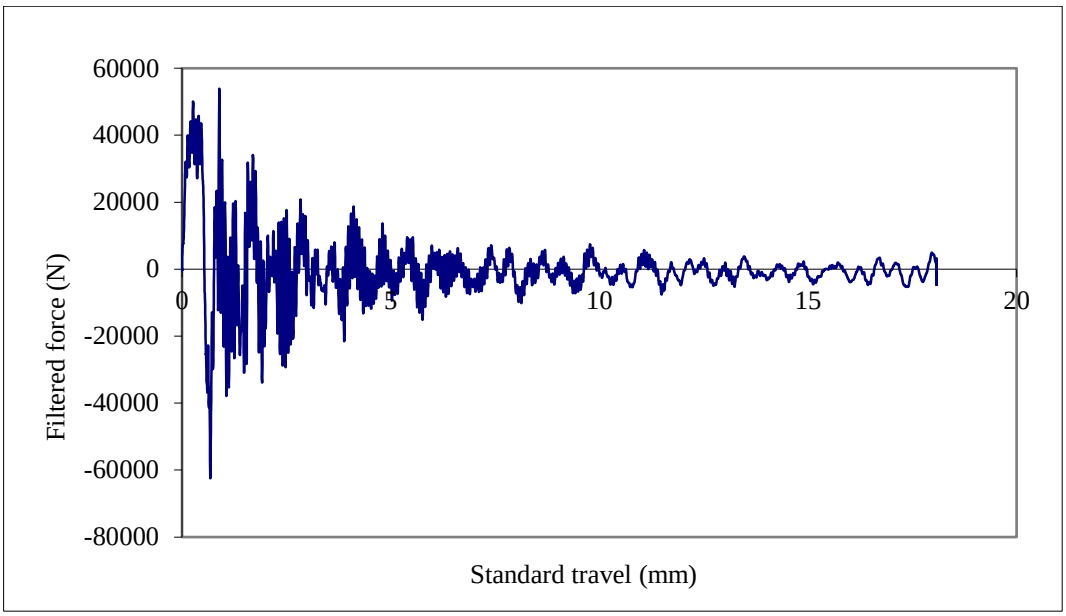

Figure D19. Force – displacement plot of StxD-08

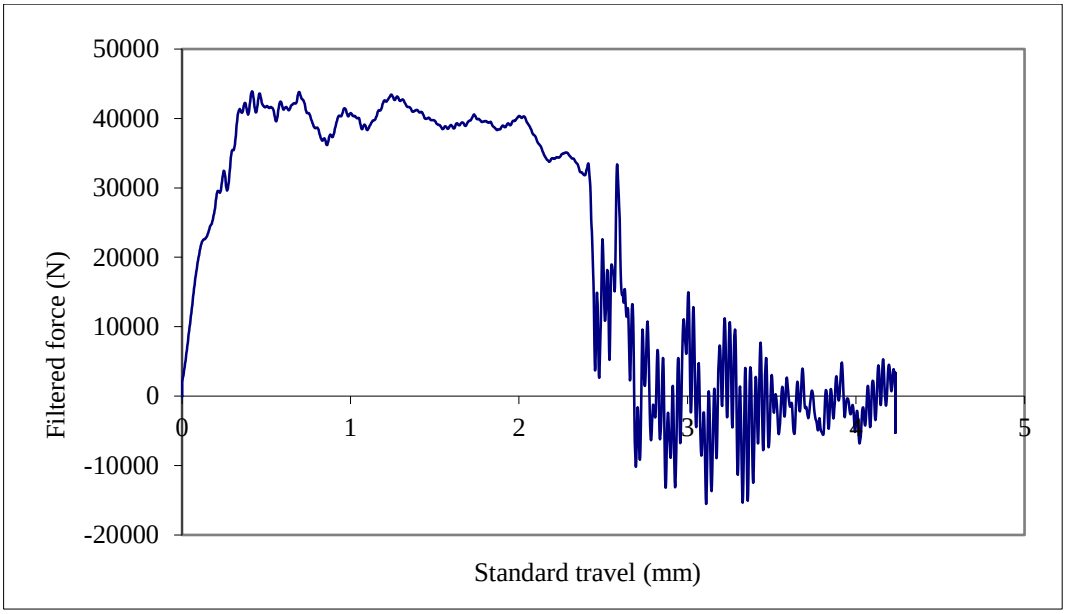

Figure D20. Force – displacement plot of StxLSD-01

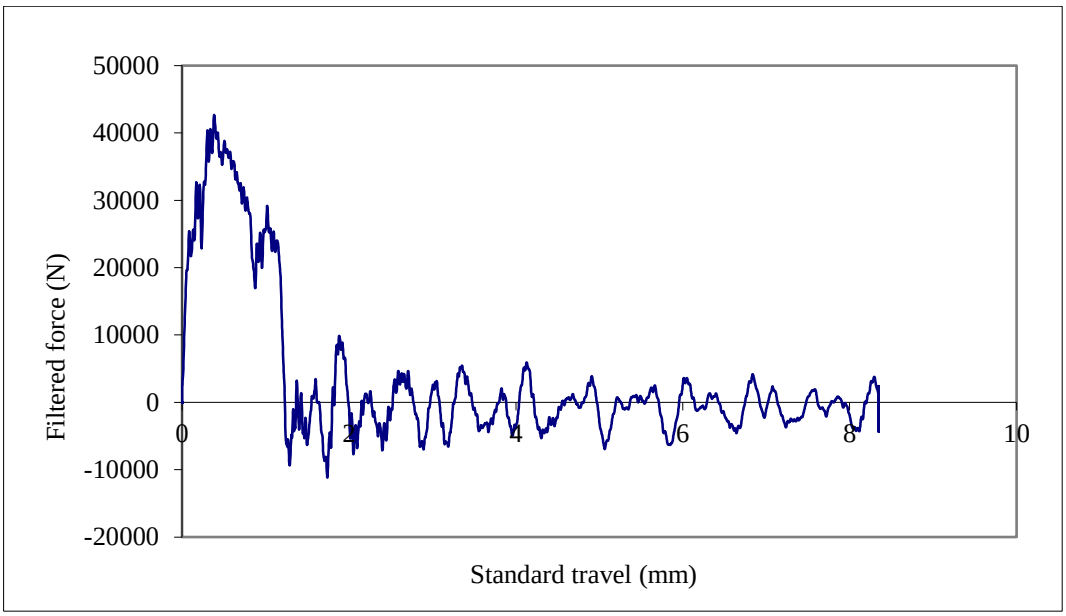

Figure D21. Force – displacement plot of StxLSD-02

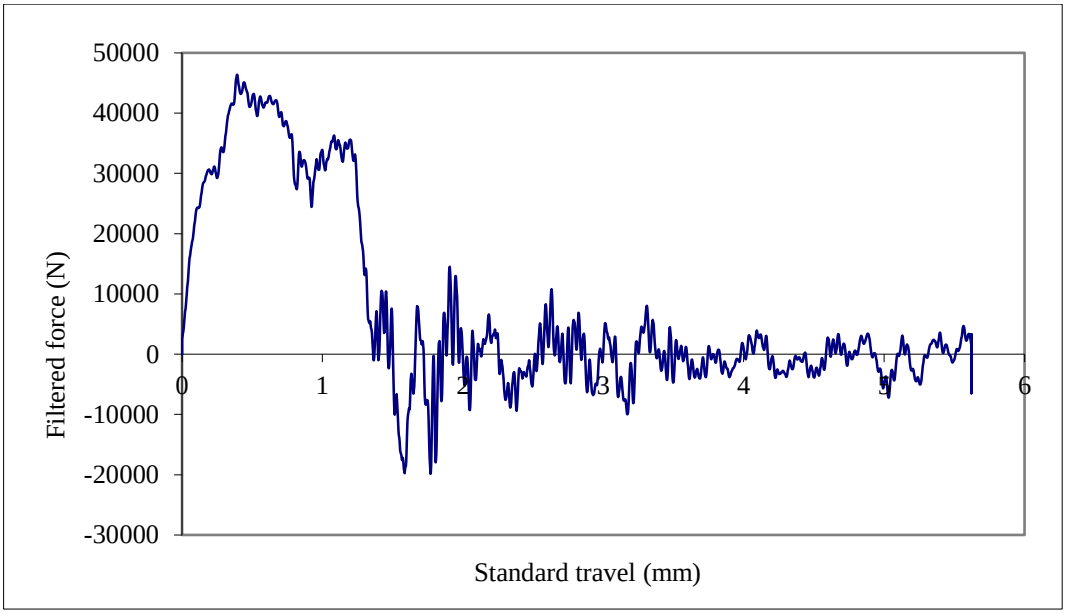

Figure D22. Force – displacement plot of StxLSD-03

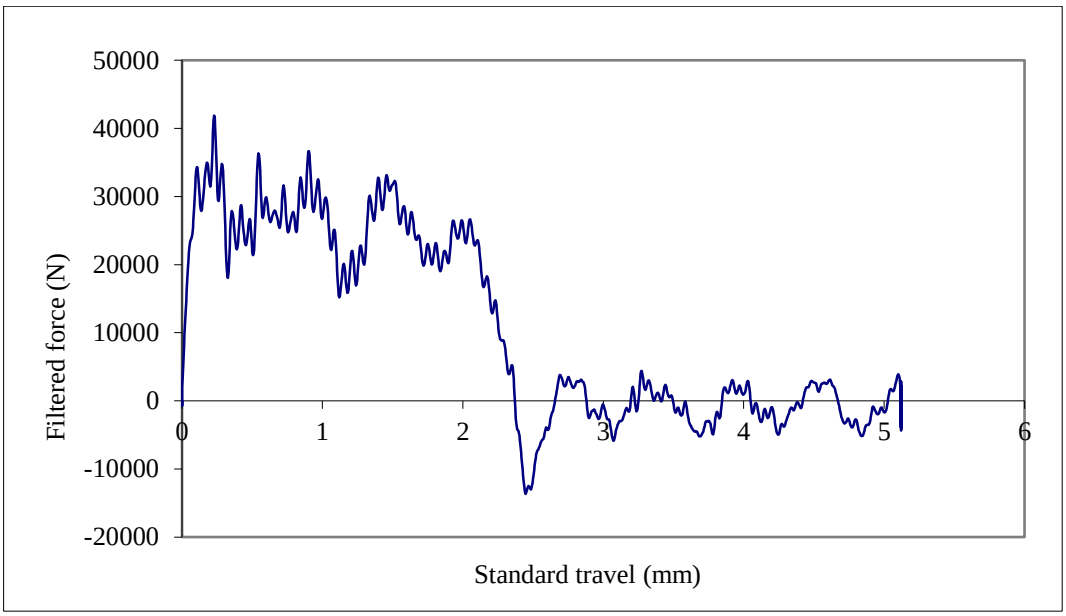

Figure D23. Force – displacement plot of StxWSD-01

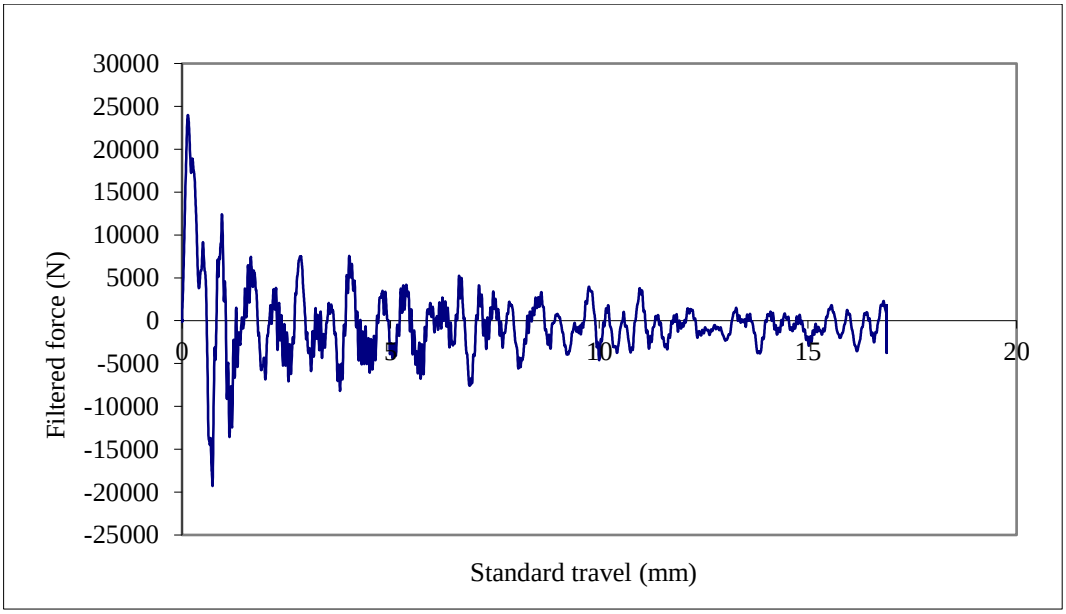

Figure D24. Force – displacement plot of StxWSD-02

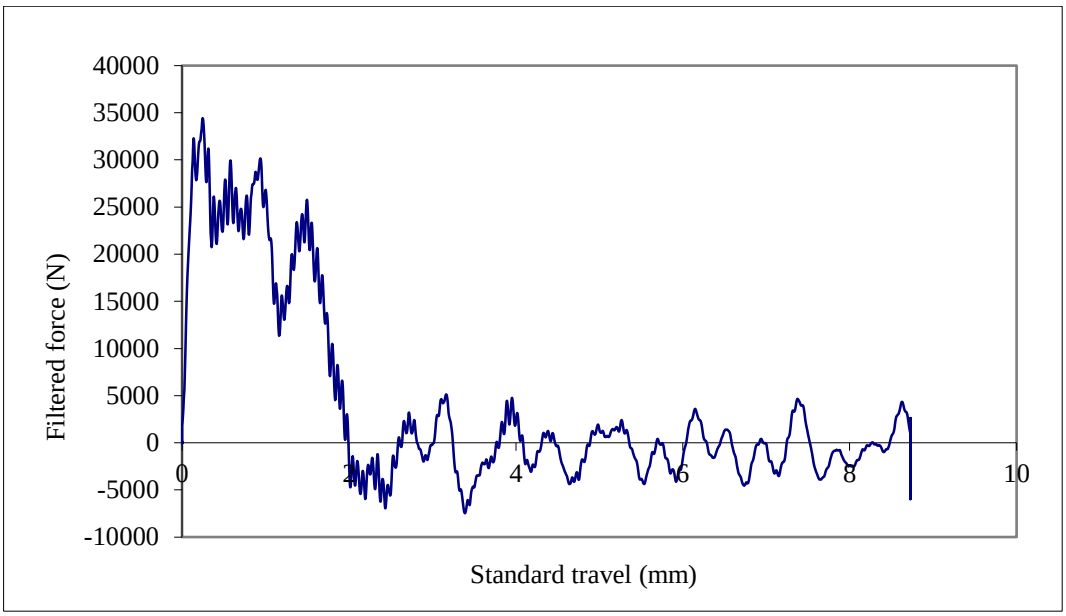

Figure D25. Force – displacement plot of StxWSD-03

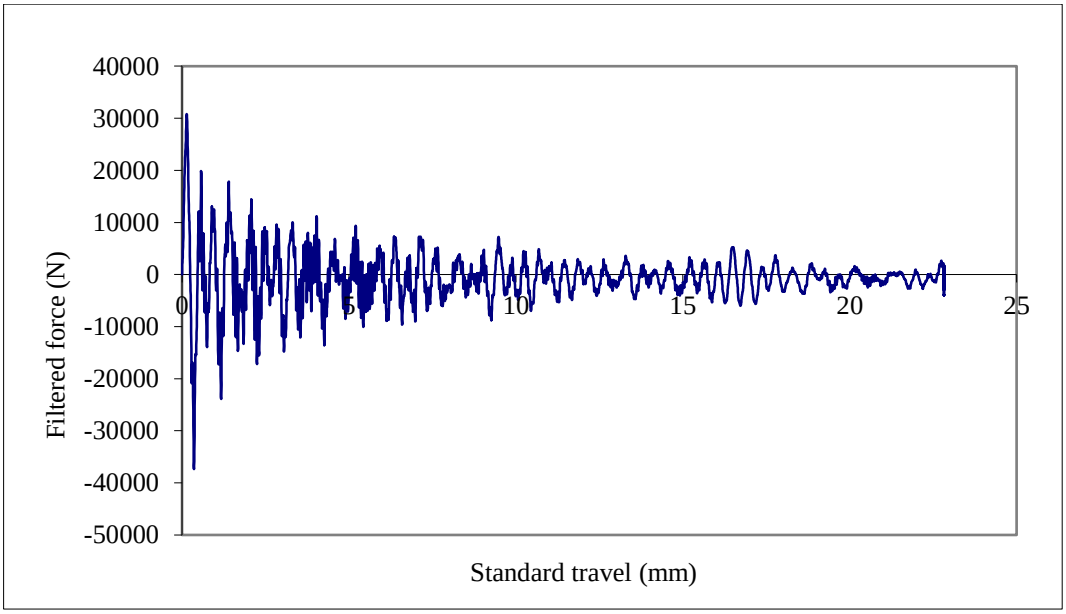

Figure D26. Force – displacement plot of ED-01

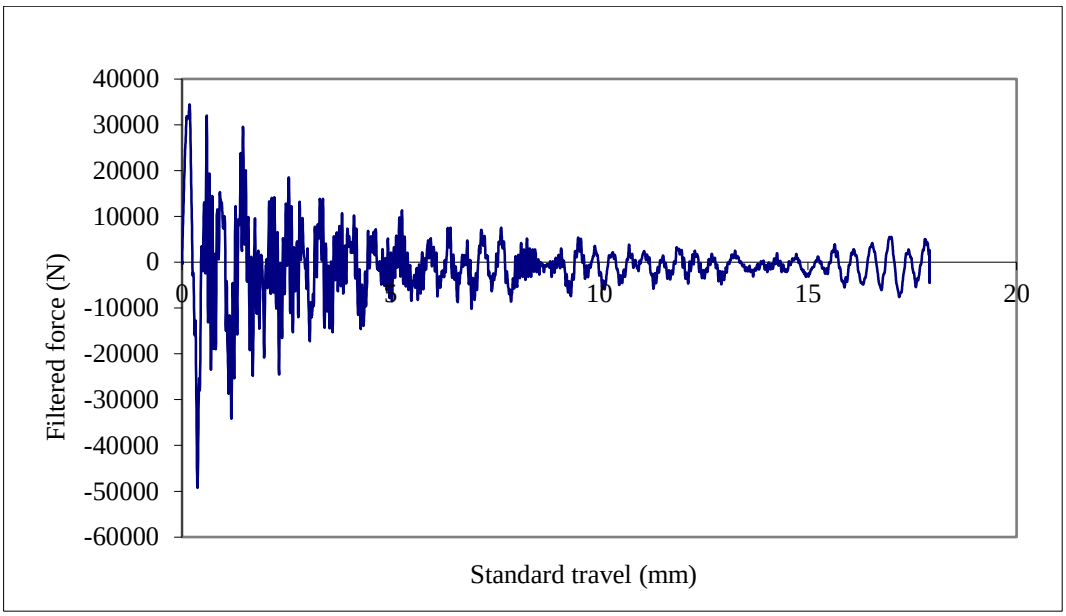

Figure D27. Force – displacement plot of ED-02

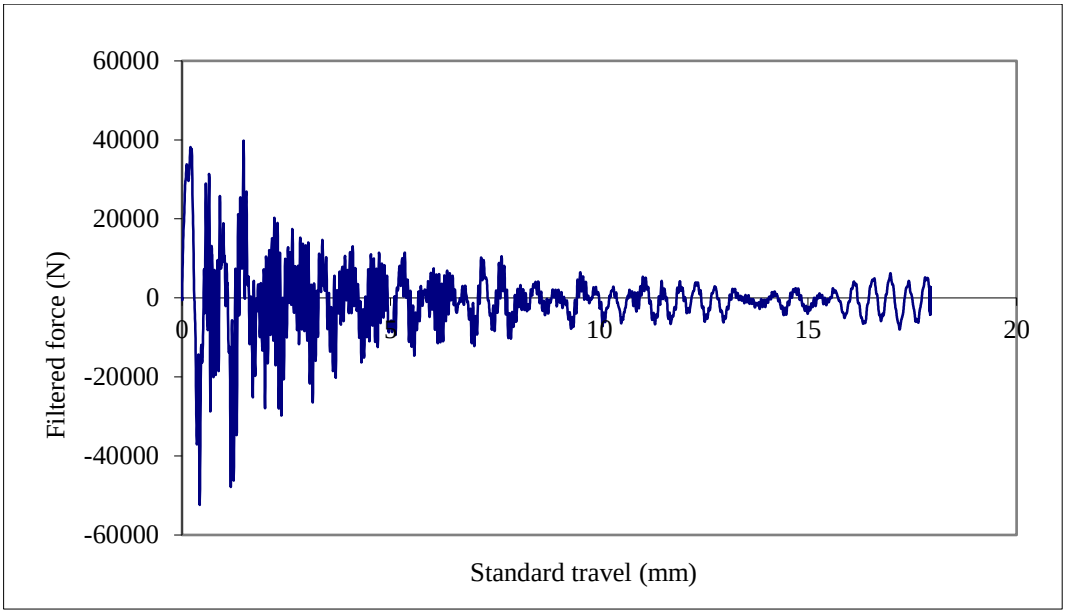

Figure D28. Force – displacement plot of ED-03

Appendix E

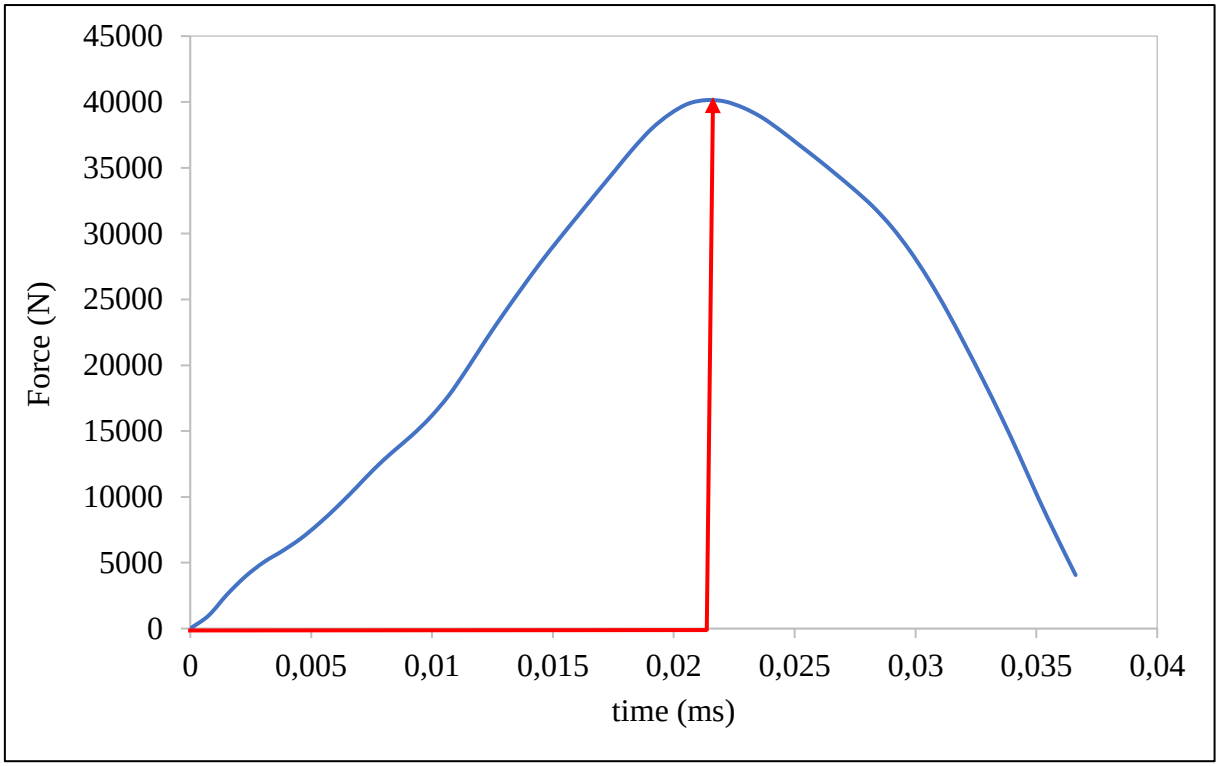

Figure E1. Force versus time plot of ESD-01

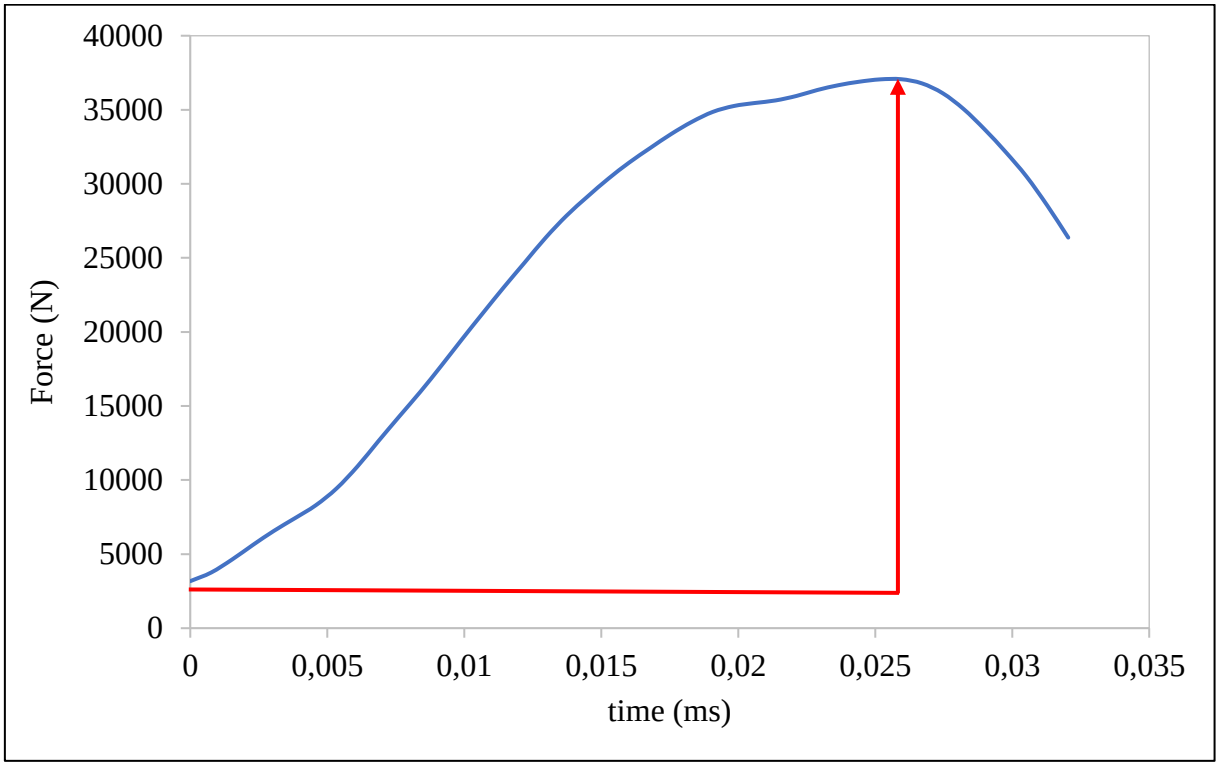

Figure E2. Force versus time plot of ESD-02

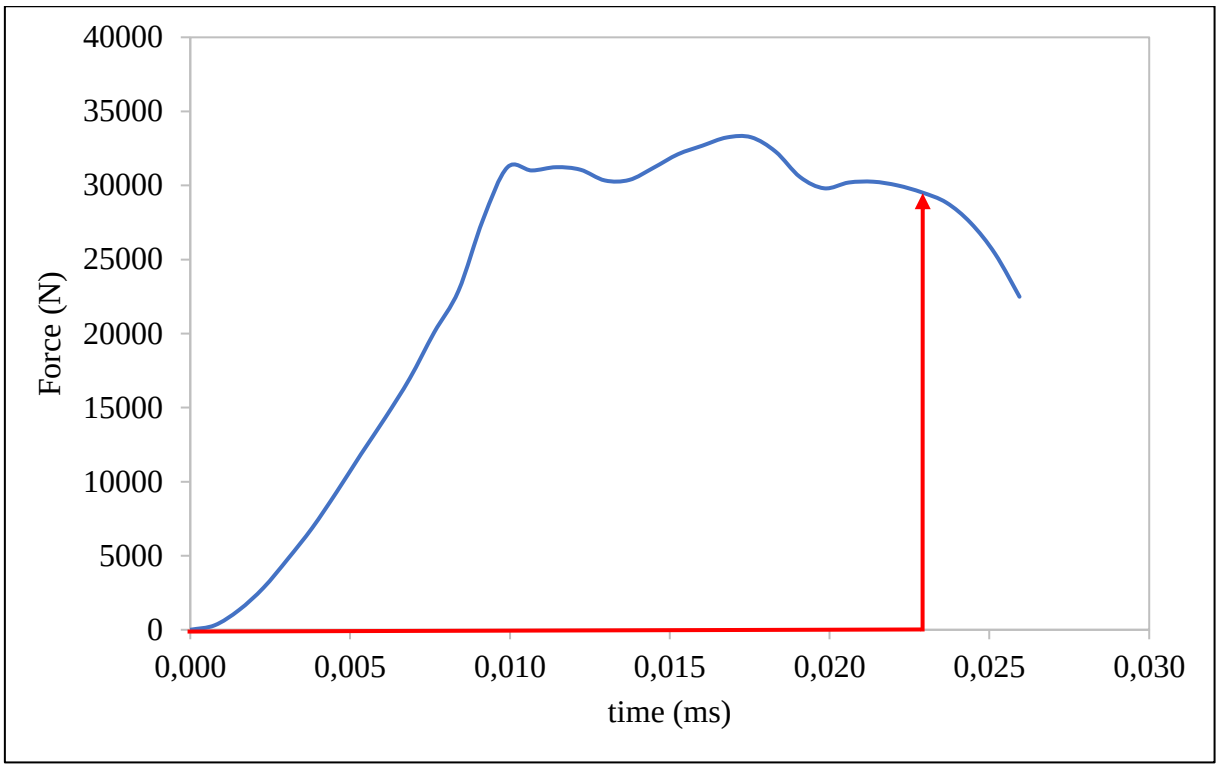

Figure E3. Force versus time plot of ESD-03

Appendix F

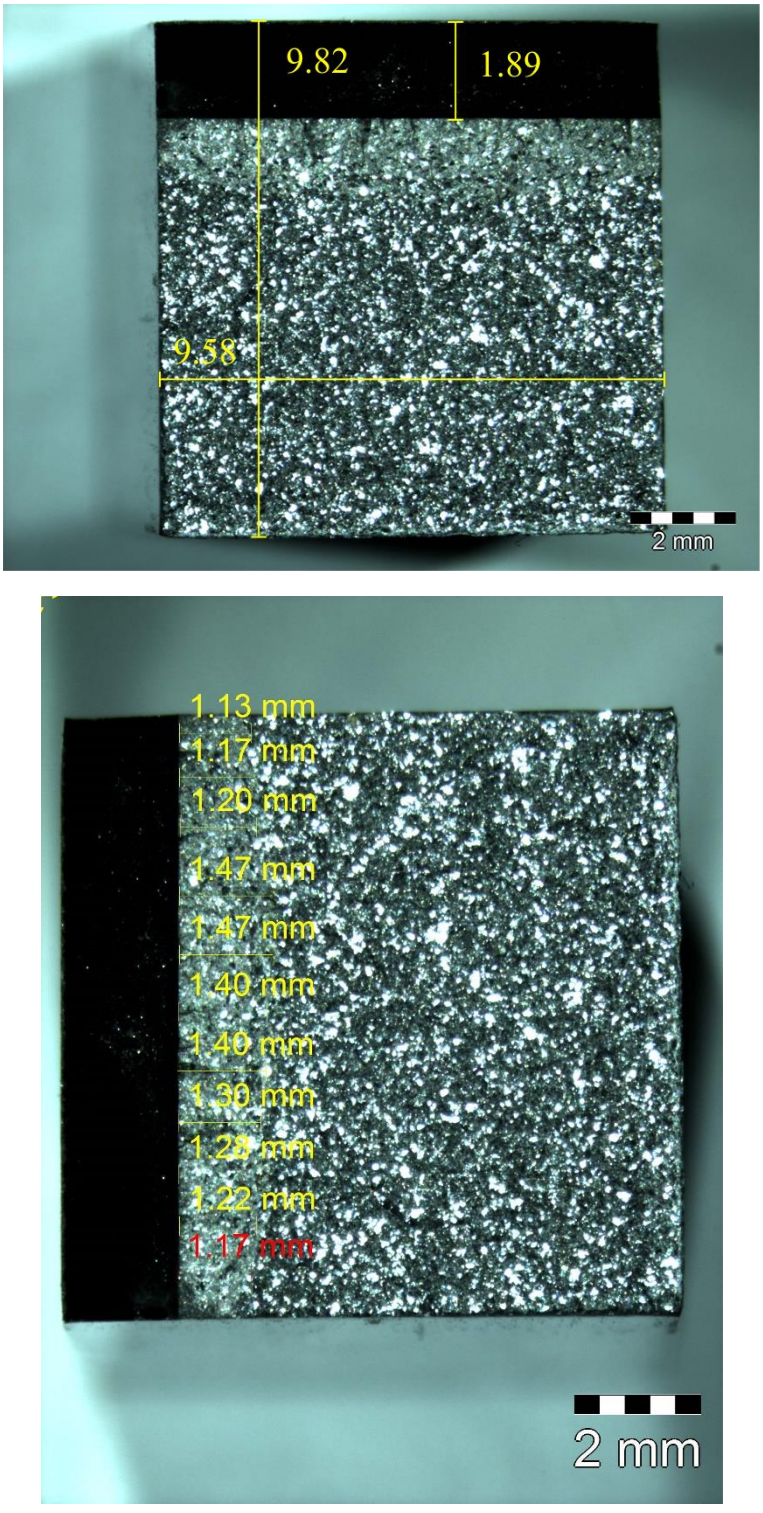

Figure F1. Fractured surface of ESD-01

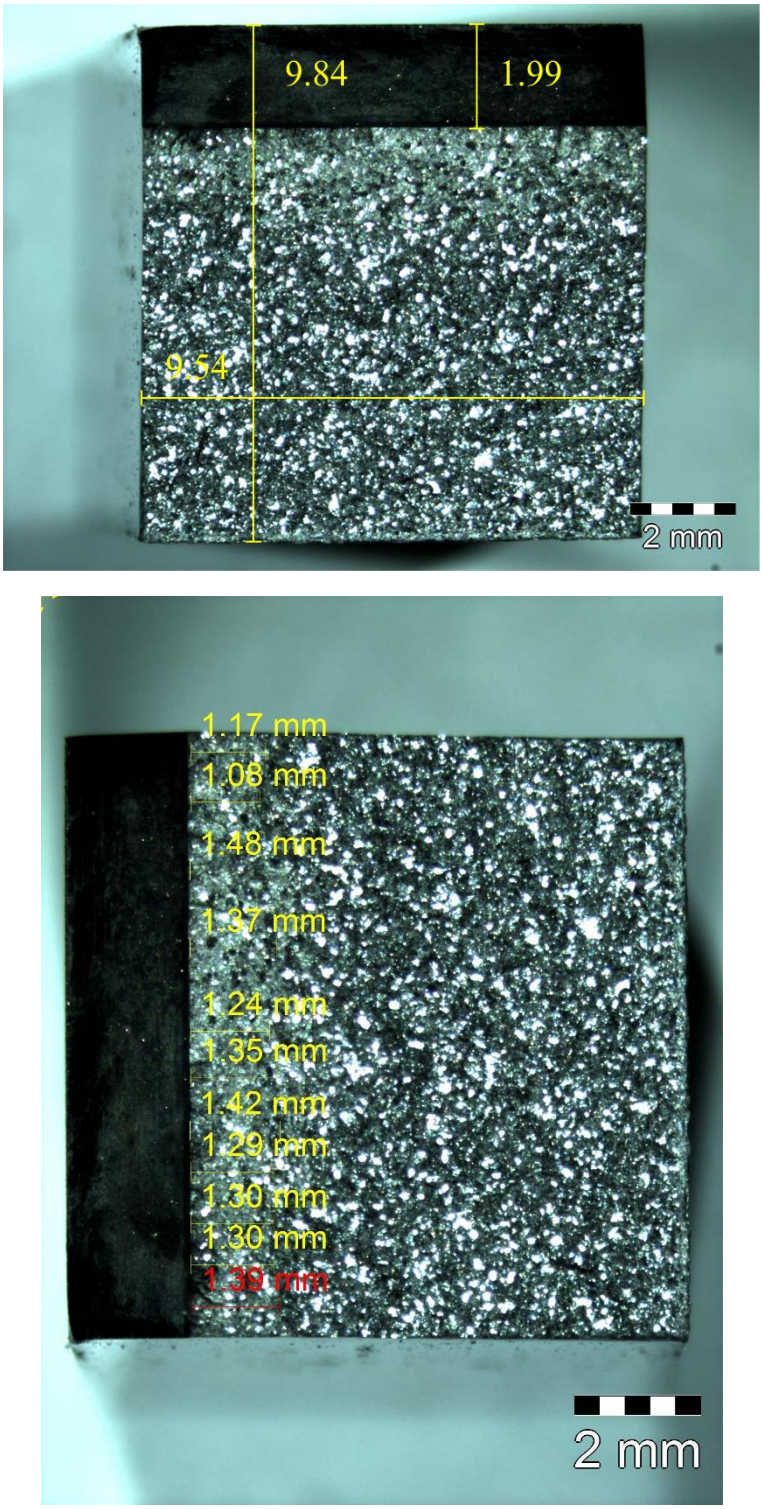

Figure F2. Fractured surface of ESD-02

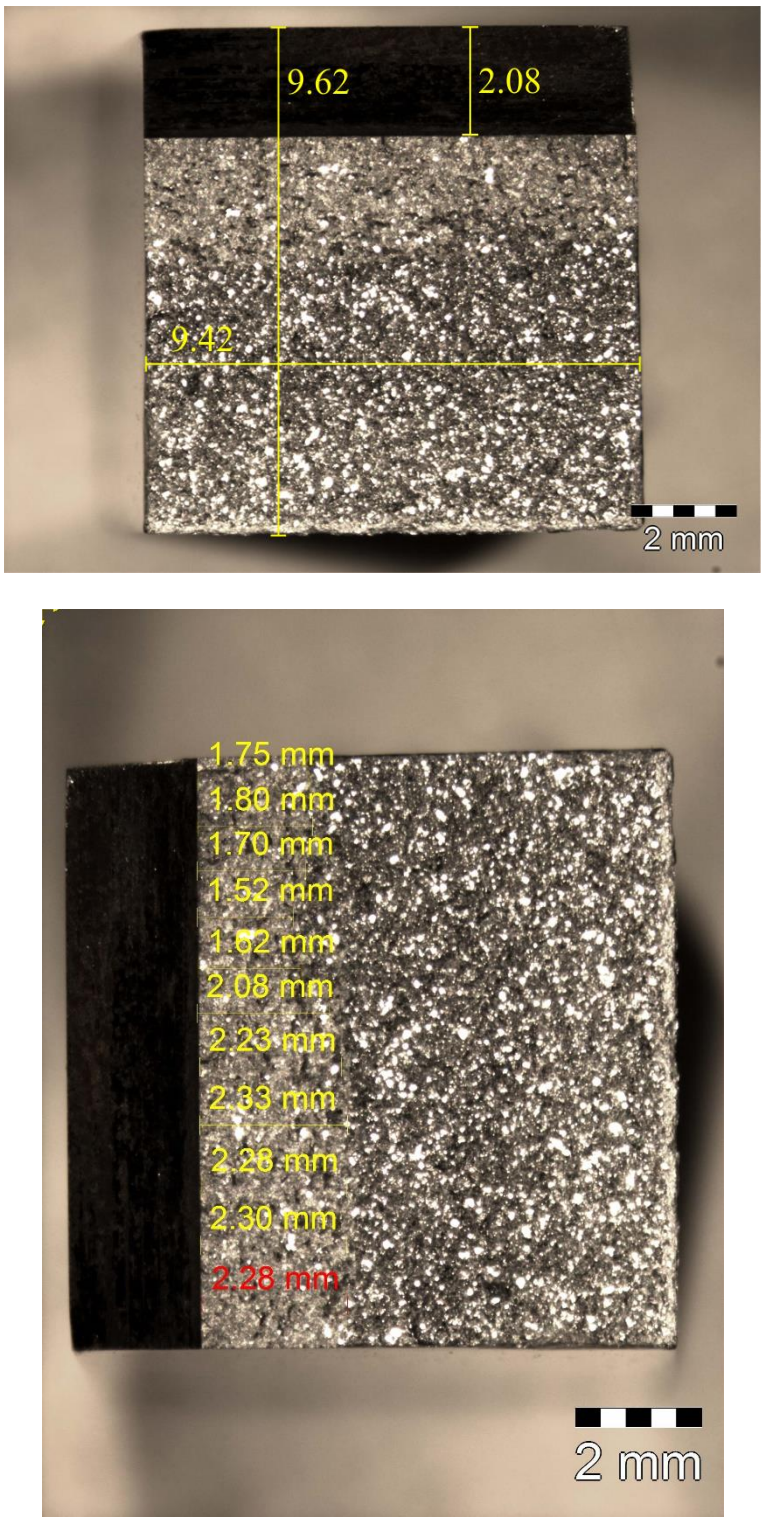

Figure F3. Fractured surface of ESD-03

Appendix G

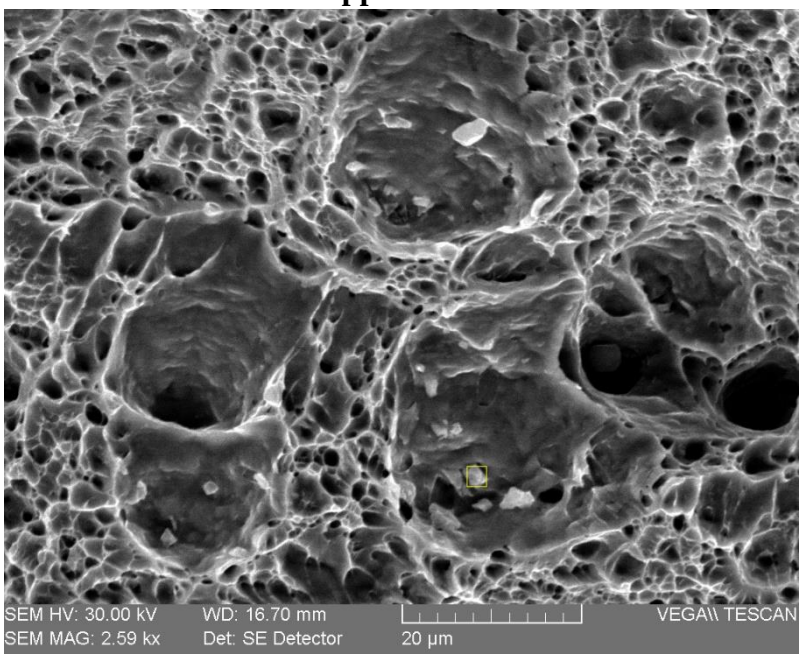

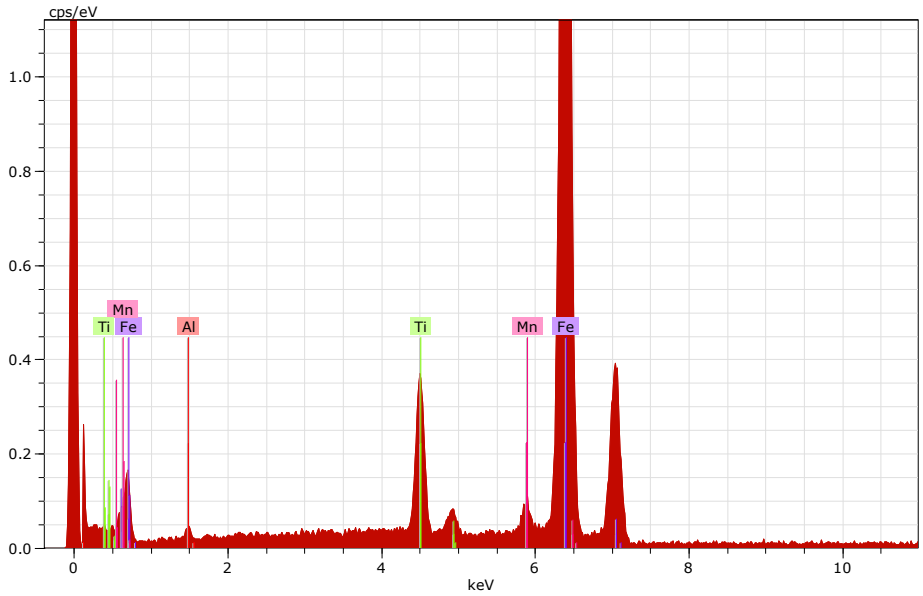

Spectrum: Acquisition 1709

El	AN	Series	unn. C [wt.%]	norm. C [wt.%]	Atom. C [at.%]	Error (1 Sigma) [wt.%]
Fe	26	K-series	96.27	91.15	89.45	2.52
Ti	22	K-series	7.22	6.83	7.82	0.26
Mn	25	K-series	1.40	1.33	1.33	0.10
Al	13	K-series	0.73	0.69	1.40	0.11
Total:			105.63	100.00	100.00	

Figure G1. EDX analysis of StxCCRB-01 specimen